

Electrokinetic Separation of Nucleic Acids in Thermoplastic Nanochannels

By

© 2020

Charuni A Amarasekara

Submitted to the graduate degree program in Department of Chemistry and the Graduate Faculty
of the University of Kansas in partial fulfillment of the requirements for the degree of
Doctor of Philosophy.

Chair: Prof. Steven A. Soper

Prof. Robert C. Dunn

Prof. Michael A. Johnson

Prof. Mikhail V. Barybin

Prof. Cory Berkland

Date Defended: 20 March 2020

The dissertation committee for Charuni A. Amarasekara certifies that this is the approved version
of the following dissertation:

**Electrokinetic Separation of Nucleic Acids in Thermoplastic
Nanochannels**

Chair: Prof. Steven A. Soper

Date Approved: 20 March 2020

ABSTRACT

Charuni A. Amarasekara: Electrokinetic Separation of Nucleic Acids in Thermoplastic Nanochannels
(Under the direction of Prof. Steven A. Soper)

Nucleic acid analysis and separation have recently become an interesting area of research due to their applicability in precision medicine. In precision medicine disease diagnosis, treatment and prevention are tailored to an individual's genetic makeup. Therefore, there is a huge demand to develop new nucleic acid separation methods that can be utilized in clinical environments. When developing separation methods for clinical applications, it is necessary to consider the growing need for reduced reagent consumption, high throughput analysis, reduced analysis time, sensitive detection and separating nucleic acids in highly complex samples with low analyte concentrations. These factors have limited the use of conventional electrophoretic and chromatographic methods in clinical settings. Therefore, bioanalytical separations have an ever-increasing need for new methods for nucleic acid separations.

Development of nucleic acid separation methods for clinical applications are trending toward miniaturization due to low sample and reagent volume consumption, ability to perform high throughput parallel analysis, and unique separation modalities observed at molecular length scales. With the advances in the design and fabrication of nanofluidic devices during the last decade, there have been numerous reports on nucleic acid separations in nanoscale. Nanofluidics offer unique separation modalities that are not observed in microscale due to increased surface interactions such as electrostatic, van de Waals interactions, hydrogen bonding and electric double layer overlap effects. However, the majority of these methods utilize glass-based nanofluidic

devices which are not suitable for the use of point of care applications because of sophisticated, time consuming, high-cost fabrication methods of these devices.

In this study, we report the use of thermoplastic nanochannels (110 nm x 110 nm depth and width, respectively) as an alternative for glass nanochannel devices for the free solution electrokinetic separation of deoxynucleotide monophosphates (dNMPs), ribonucleotide monophosphates (rNMPs) and short single stranded DNA. Thermoplastic nanofluidic devices with mixed scale micro and nanofluidic networks were fabricated using a simple, high resolution nanoimprinting lithography method and the structures were enclosed via thermal fusion bonding to a cover plate. We were able to separate ss-DNA in these thermoplastic nanochannels without any additives to the buffer and we found that the separation mechanism is electrochromatographic. In the separation of rNMPs and dNMPs we found that the separation is majorly electrophoretic but, with some impact on the separation by surface interactions of these analytes with nanochannel walls.

*To my ever-loving parents, husband, my brother and my baby Sayali ,my family and friends
for your unconditional love and encouragement throughout this journey.*

In honor of my parents:

Nimal Amarasekara and Nilanthi Amarasekara

In memory of my late grandfather:

Hemawansha Amarasekara

Acknowledgments

Firstly, I would like to express my sincere gratitude to my advisor Prof. Steven A. Soper for the continuous support of my PhD study and the related research work, for your patience, motivation, and immense knowledge. I joined the group in summer 2016, and since then I was encouraged all the time to carry out challenging research projects. I also gained a lot of knowledge on problem solving and fixing instruments since 2016. I must mention the flexibility given to us in the lab to conduct research, which inspired me to work hard on my own and think critically on developing experiments as an independent researcher. Prof. Soper let me explore a wide range of fields including engineering, biology, and chemistry. I obtained a lot of experience as a multidisciplinary researcher working in your lab. In addition, I would like to thank you for giving me time off from the lab during the time I had my baby girl. I could not have imagined having a better advisor and mentor for my PhD study. Again, thank you for your kindness, support, and encouragement throughout this journey.

Besides my advisor, I would also like to thank the rest of my thesis committee: Prof. Robert Dunn, Prof. Michael Johnson, Prof. Mikhail Barybin and Prof. Corey Berkland for your insightful comments and encouragement, but also for the hard questions, which inspired me to widen my research from various perspectives. I am extremely honored to have all of you on my thesis committee.

This journey is not possible without the support of my friends and lab mates. I cannot thank you all enough for listening to me when I was going through hard times and motivating me to move forward in my PhD. Dr. Bethany Gross and Dr. Camila Campos, thank you for all your kind

mentoring provided me when I first joined the group. Thank you, Dr. Colleen O’Neil, for training me to take over the project after you. Next, I would like to thank Dr. Kumuditha Ratnayake for helping me move forward with my research work with his valuable discussions, corrections, and constructive criticism. Jenny Conner, Dr. Nick Larkey, and Eva Mohr thank you for being there for me all the time through thick and thin. Thanks to Nick and Ian Freed for correcting my writing and giving your honest opinion. Chathurika Rathnayaka and Uditha Athapattu, thanks for helping me with finishing up some of the experiments. Thanks to Brandon Young for helping me with laser systems. Dr. Maggie Witek and Dr. Matt Hupert, thank you for all your guidance and mentoring. Lindsey Roe, your support is unforgettable; every time when I had to order things or plan travels you always helped without hesitation. I will really miss your smile. Finally, I would like to convey my thanks to all the other present and past members of the Soper group.

All of this is not possible without the immense support of my mom Mrs. Nilanthi Amarasekara and my dad Mr. Nimal Amarasekara. I was born in 1989, during the peak time of JVP insurrection in Sri Lanka. My dad being an army officer, my mom and dad had to face a lot of challenges to avoid life-threatening moments that came to us during that time with newborn me. After this tragic event, civil war started in Sri Lanka, where my dad was actively in the war field for 27 years until it ended in 2009. Even through these hard times in our lives, you always encouraged me to get a good education, and advised me to be a good person. I have no words to thank you dad for all your silent sacrifices, love, care, and humanity. Mom, you are the strongest person I have ever seen in my life. Dad being away from home for duty, you faced all the challenges raising me and my brother by yourself. You are my first teacher, my mentor, and my best friend. I remember how you held my arms and walked with me to the first grade in 1995. Since then you were there with me

like a shadow and never left me. Even today you are here taking care of me and my baby Sayali while helping me to finish my PhD. There were times I felt defeated and wanted to give up on things, but you always believed me and encouraged me, and you knew very well what I am capable of. Thank you, mom, for everything you did, and all your sacrifices and dedication are immeasurable. I also would like to thank my brother Heshan Amarasekara for helping me to achieve my dreams and taking care of mom and dad while I was away from home. I should not forget my grandparents Mr. Karunaratna Liyanage and Mrs. Mangalika Karunaratna, and Mrs. Violet Thiranagama for your true blessings given to me throughout this time. I wish you all a healthy and longer life. Hope we all can meet soon. Thank you, all my uncles and aunts, for encouraging me and showing me the value of education. Mom, dad, and my family, I made you all proud being the first in family with a PhD.

To my husband, Mahesh Abeyrathna, thank you for helping me to achieve my dreams. You gave up on your job and came here to support me. Your sacrifice is highly appreciated. Whenever I said I can't, and I wanted to give up you always believed in me and encouraged me. Thanks for staying up late with me when I was working late in the lab. I would like to thank my mother-in-law and sisters-in-law, too, for their love and care given to me through all these years.

I had my baby Sayali four months ago, and even though you cannot understand the things very well, you supported me for this too. Whenever I felt so stressed and depressed, your smile wiped out all the sadness away from me. Couple of weeks ago I felt really discouraged and thought I would not be able to finish my work, and at that time you were playing on the play mat, suddenly I noticed you were trying to roll over from front to back for the first time. You fell down many

times but finally you were able to roll over. That day you taught me the lesson of trying. You made me strong. Thank you, my little angel, I love you so much.

I tried my best to thank everyone who helped me to make this journey a success. In case if I have forgotten someone I greatly apologize. Once again thank you all!!

Table of Contents

Chapter 1. Nanofluidic Devices for Biomolecule Separation.....	1
1.1 Introduction.....	2
1.2 Unique phenomena affecting separations in nanofluidic devices	5
1.2.1 Electric double layer (EDL) and zeta potential (ζ)	6
1.2.2 Electroosmotic flow (EOF).....	11
1.2.3 Surface roughness effects.....	15
1.3 Fabrication of nanofluidic devices.....	16
1.3.1 Conventional lithography methods	17
1.3.2 High energy beam processing lithography methods	19
1.3.3 Nanoimprint lithography (NIL).....	20
1.4 Detection methods for biomolecule separations in nanofluidic devices	21
1.5 Biomolecule separations in nanofluidic devices	24
1.5.1 Electrokinetic (EK) separations of biomolecules in nanofluidic devices	24
1.5.2 Chromatographic separations of biomolecules in nanofluidic devices	36
1.6 Overall dissertation outline.....	42

1.6.1	Chapter 2. Electrokinetic transport behavior of deoxynucleotide monophosphates (dNMPs) through thermoplastic nanochannels	42
1.6.2	Chapter 3. Open tubular nanoelectrochromatographic separation of single stranded DNA in thermoplastic nanochannels	43
1.6.3	Chapter 4. Electrokinetic Separation of Ribonucleotide Monophosphates (rNMPs) in Thermoplastic Nanochannels	43
1.6.4	Chapter 5. Ongoing developments and Future directions	44
1.7	References.....	45

CHAPTER 2. Electrokinetic Transport Properties of Deoxynucleotide Monophosphates (dNMPs) through Thermoplastic Nanochannels51

2.1	Introduction.....	52
2.2	Materials and Method	56
2.2.1	Reagents and materials.....	56
2.2.2	Fluorescent labeling of dNMPs.....	57
2.2.3	Fabrication of nanochannel devices	58
2.2.4	Imaging system for nanoelectrokinetic separation experiment	59
2.2.5	Nanochannel electrokinetic transport properties of ATTO 532-labeled dNMPs	62
2.2.5	Nanochannel electrokinetic separation data analysis	62
2.3	Results and discussion	63

2.3.1	Nanochannel electrokinetic transport behavior of ATTO 532 dye	64
2.3.2	Nanochannel electrokinetics of the ATTO 532-labeled dNMPs.....	67
2.3.3	Effect of pH on the nanochannel electrokinetics of ATTO 532-labeled dNMPs.....	72
	As a matter	72
2.3.4	Effect of EDL overlap on the nanochannel electrokinetics of ATTO 532-labeled dNMPs.....	78
2.4	Conclusions.....	80
2.5	References.....	82
Chapter 3: Open-tubular Nanoelectrochromatography: (OT-NEC) Gel-free Separation of Single Stranded DNAs in Thermoplastic Nanochannels		85
3.1	Introduction.....	86
3.2	Materials and Methods.....	92
3.2.1	Reagent and Materials.....	92
3.2.2	Fabrication of microchannel devices.....	93
3.2.3	Free solution separation of oligonucleotides by microchip electrophoresis.....	93
3.2.4	Fabrication of nanochannel devices	95
3.2.5	Surface roughness measurements by AFM	99
3.2.6	EOF measurements	100

3.2.7	Detection system for the nanoelectrochromatography	100
3.2.8	Nanoelectrochromatographic separation of ssDNAs	101
3.2.9	Data analysis	102
3.3	Results and Discussion.....	104
3.3.1	Microscale separation of ssDNAs	104
3.3.2	Material effects on EOF and ssDNA separations.....	107
3.3.2.3	Separation of oligonucleotides in IM-PMMA and NIM-PMMA	116
3.3.3	Effect of column length on separation performance	121
3.4	Conclusions.....	123
3.5	References.....	125
Chapter 4. Electrokinetic Separation of Ribonucleotide Monophosphates (rNMPs) in Thermoplastic Nanochannels.....	130	
4.1	Introduction.....	131
4.2	Materials and Methods.....	138
4.2.1	Materials and reagents	138
4.2.2	Fabrication of nanochannel devices	138
4.2.3	Bond strength measurements of nanochannel devices	144

4.2.4	Evaluation of pH stability of fabricated nanochannel devices	145
4.2.5	Electroosmotic flow (EOF) measurement.....	145
4.2.6	Microscale electrophoresis of rNMPs	146
4.2.7	Electrokinetic separation of rNMPs in nanochannels	148
4.2.8	Data analysis	150
4.3	Results and discussion	151
4.3.1	Bond strength and pH stability of COC/COC devices	151
4.3.2	Water contact angle and EOF mobility of COC/COC devices	153
4.3.3	Microscale electrophoretic separation of rNMPs	157
4.3.4	Effect of material type for the nanoelectrokinetic separation of ATTO 532- labeled rNMPs.....	159
4.4	Conclusions.....	169
4.5. References:	170
Chapter 5. Summary, On-going Developments and Future Work		174
5.1	Summary	175
5.2	Ongoing developments and Future directions.....	177
5.2.1	Introduction.....	177
5.3	Ongoing developments	181

5.4	Future directions.....	182
5.5	References.....	185

List of Figures

Figure 1.1. An overview of major components of precision medicine concept (reproduced from Roda *et al.* Analytical and Bioanalytical Chemistry 2018)

Figure 1.2. A representation of materials and nanometric object at the same length scales as nanofluidics, where unique transport phenomena and effects occur. (reproduced from Xu, Y. Advanced Materials 2018)

Figure 1.3. A schematic of the Gouy-Chapman-Stern model of EDL, where a strongly bound cation layer is known as the Stern layer, while loosely bound cation later with mobile ions is known as the diffuse layer. The potential at the shear plane is named the zeta potential (ζ) (Reproduced from Pennathur *et al.* Nanotechnology understanding the small systems, CRC press, 2014).

Figure 1.4. Schematic diagram of overlapped and non-overlapped EDL in a nanochannel. **A)** When the Debye length is much smaller than critical channel dimensions, the solution towards the center of the channel becomes neutral. **B)** When there is an overlapping EDL, the solution becomes charged. **C)** Electric potential decays rapidly closer to the channel wall, and in the center, it becomes neutral in non-overlapped EDL conditions. **D)** In an overlapping EDL, the electric potential at the center of the channel does not become neutral and is influenced by surface charge. **E)** The concentration of anions (red) and cations (blue) in a non-overlapping EDL scenario is equal to the bulk concentration. **F)** In an overlapping EDL scenario, the concentration of cations (counterions) becomes much higher than the anion concentration (co-ions) (Reproduced from Napoli *et al.* Lab on a Chip 2010).

Figure 1.5. Diagram representing the transverse electromigration effects observed with overlapped EDL. In this case, faster moving +1 ions separate from slower moving +2 ions (reproduced from Pennathur *et al.* Nanotechnology understanding small systems, CRC press 2014).

Figure 1.6. A Schematic diagram of EOF in a channel with a negatively charged channel wall. (Reproduced from Pennathur,*et al.* Nanotechnology understanding small systems, CRC press 2014)

Figure 1.7. **A)** Electrokinetically driven plug-like flow profile, and **B)** pressure driven parabolic flow profile in a negatively charged channel (reproduced from <https://chem.libretexts.org>)

Figure 1.8. A schematic diagram representing an overview of nanofabrication methods. **A)** Main steps involving in photolithography[a) photoresist coated substrate is exposed to UV light. b) the removal of exposed photoresist by immersing into developer.] **B)** steps used in focused ion beam milling by using Ga^+ ions. **C)** An illustration of electron beam lithography where an electron beam is focused on a resist film to create a pattern by exposing dot by dot. **D)** An illustration of nanoimprinting lithography (left) and UV nanoimprinting lithography (right) (Reproduced from Pimpin *et al.* Engineering journal 2012

Figure 1.9. A schematic diagram representing the detection methods used in nanoscale separation studies. **A)** Laser induced wide field fluorescence imaging system equipped with a CCD (charge coupled detector). (reproduced from Pennathur *et al.* Analytical Chemistry 2007) **B)** Resistive pulse sensing of analytes migrating through a nanopore. (reproduced from Menard *et al.* ACS Nano 2012) **C)** Components in differential interference contrast thermal lens microscope. (reproduced from Shimizu *et al.* Analytical Chemistry, 2010)

Figure 1.10. **A)** The layout of the nanofilter array chip with four buffer access reservoirs(anode, cathode, sample and waste), a 1 cm separation channel and a T-shaped injector. **B)** A schematic diagram of the cross section of the separation channel in nanofilter array chip consists of thin (ds) and thick (dd) regions with equal lengths **C)** Scanning electron microscopy images of the thin regions in nanofilter array chip with different depths. **D)** Electropherograms for the separation of double stranded DNA with different lengths. 1)50bp; 2) 150 bp; 3) 300 bp; 4) 500bp; 5)766 bp at different electric field strengths. **E)** Electropherograms for the separation of SDS-protein complexes. 1) cholera toxin subunit B; 2)lectin phytomagglutinin-L; 3) low density human lipoproteins at different field strengths.(Reproduced from Fu *et al.* Journal of Applied Physics letters 2005)

Figure 1.11. **A)** A schematic diagram of the nanoslit device used for the separation and the length of the separation channel is 3-4 cm. **B)** A schematic of the cross sectional transition of DNA from its three dimensional relaxed state to squished state when forced into nanochannel in two dimensions where the molecule becomes a pancake like entity composed of sub-blobs of DNA with a diameter equal to channel height. **C)** Electropherograms showing the separation of mixture of DNA molecules in 19 nm deep separation channel. (Reproduced from Cross *et al.* Journal of Applied Physics, 2007)

Figure 1.12. **A)** Schematic of nanochannel electrophoresis of rod-like oligonucleotides. Important length scales are the depth of the channel ($2h$), the length of the dsDNA (l), and the Debye length (λD). **B)** Measured electropherograms for electrokinetic separations of fluorescein, UTP, and a 10-100 bp oligonucleotide ladder in a 100 nm deep channel. Electropherograms are shown for separations in five different concentrations of sodium borate. t_{FI} is the residence time of fluorescein in each experiment (Reproduced from Pennathur *et al.* Analytical Chemistry 2007)

Figure 1.13. **A)**The schematic illustrates the 5-port device layout, including sample wells (A and B), mixing tee, offset tee injector, and separation channel. **B)** Electropherogram of the separation of single stranded DNA (left) and electropherogram of single stranded DNA plus the double stranded DNA(right) after hybridization step. (Reproduced from Huber *et al.* Lab on a Chip 2009)

Figure 1.14. The velocity measurement of methylated and non-methylated DNA translocated inside the nanochannel. Arrows show the translocation distance of DNA in 0.03 s. **A)** Fluorescence images of translocation of methylated and non-methylated T4 DNA inside the nanochannel. Scale bars are 10 μm . **B)** translocation of methylated and non-methylated λ DNA. Scale bars are 10 μm . **C, D)**Histogram of translocation velocities of methylated and non-methylated T4 DNA molecules and λ DNA respectively for n=200.

Figure 1.15. **A)** a)Schematic diagram of the dual pore device with a 500nm flight tube. b)An SEM image of a fabricated dual nanopore device in Si master. c) An image of a fabricated dual pore device in PEGDA. **B)** Histogram of time of flight for the dNMPs at pH 8.3 in 1m KCl and 0.5X Tris borate EDTA buffer(TBE) **C)**Histogram of time of flight for the dNMPs at pH 10 in 1M KCl and 0.5 X TBE.

Figure 1.16. **A)** Schematic diagram of the crossed microfluidic channels separated by a nanometer diameter capillary array interconnect. **B)** Separation and selective collection of arginine and glutamate derivatized with FITC. The electropherogram demonstrate the separation and of three bands without collection (a); collection of glutamate band (b) ; collection of first arginine band(c); collection of second arginine band.

Figure 1.17. **A)** Schematic diagram of the experimental setup. **B)** Separation results of 5kb -10kb DNA in a nanocapillary with a radius of 500 nm and a total length of 46 cm. The separation traces represent the background tris EDTA concentrations of 50 μ M(1), 100 μ M(2), 10 mM (3), 100 mM (4) and 500 mM(5)(Reproduced from Wang *et al.* Analytical Chemistry 2008.

Figure 1.18. **A)** An Image of the microchip and the schematic diagram of the design of the extended nanochannels with 2.2 mm in length. **B)** Chromatograms of the separation of fluorescently labeled amino acids by extended nanochromatography. (Reproduced from Smirnov *et al.* Journal of Chromatography A 2015)

Figure 2.1. Reaction scheme showing the conjugation of ATTO 532 to adenosine monophosphate, dAMP. 100 μ L of each dNMP (1 mM in 100 mM HEPES pH 6.5) was mixed with 100 μ L EDC (300 mM in 100 mM HEPES) and 100 μ L of ATTO 532 (25 mM in 100 mM HEPES) and reacted overnight while shaking at 37°C.

Figure 2.2. SEM images showing the Si master (left panels), resin stamp (middle panels) and imprinted PMMA device (right panel) used for the nanochannel electrophoresis experiments

Figure 2.3. (A) Optical set-up of the fluorescence imaging system. The Gaussian beam from the laser (Nd.YAG; λ_{ex} = 532 nm; P = 0.01-5 W; 2.2 mm beam diameter) was expanded 10x using a Keplerian beam expander and the wings were knocked out with an iris that ensured uniform laser intensity in the field-of-view and complete back-filling of the objective (OBJ). The beam was focused into the back of a 100x oil immersion objective lens (OBJ) using lens (L3) after passing through a 532 nm laser line filter (F1) and reflected by a dichroic filter (DF). A collimated laser beam impinged upon the polymer nanofluidic device. The fluorescence signal was collected by the same objective, passed through the DF and spectrally selected using a longpass filter (F2). A mirror was used to steer the fluorescence signal onto the EMCCD after passing through a bandpass filter (F3) and focused using a lens (L4) ⁸. (B) Photograph of the laser excitation system shown in (A). (C) Photograph of the nanofluidic chip sitting atop the microscope objective and illuminated with the 532 nm laser.

Figure 2.4. Depiction of how the nanochannel electrokinetics and data analysis were performed. The top panel shows a fluorescently labeled dNMP being electrokinetically transported through a nanochannel with the yellow boxes indicating Position (Pos) 1 and 2. The bottom left panel shows the fluorescence intensity profile of one injection event at POS 1 and 2. The bottom right panel shows the first derivative of the intensity profile to determine the time required for each dNMP to migrate from Pos 1 to Pos 2.

Figure 2.5. Apparent mobility versus field strength for ATTO 532 injected into a nanochannel that was 110 x 110 nm (width and depth; L = 100 μ m) that were fabricated in PMMA and possessed a COC cover plate. The nanochannel electrokinetic used two different carrier electrolytes consisting of; a) 44.5 mM TB with a pH 8.3 (λ_d = 1.25 nm); and b) 0.45 mM TB pH 8.3 (λ_d = 12.5 nm). Errors bars show \pm standard deviations for the apparent mobilities.

Figure 2.6. a) Apparent mobility versus the electric field strength for ATTO 532 conjugated to dCMP, dGMP, dTMP and dAMP injected into a nanochannel that was 110 x 110 nm (width and depth; L = 100 μ m) and used PMMA as the substrate with a COC cover plate. The electrokinetic used a buffer of 44.5 mM TB at pH 8.3 (λ_d = 1.25 nm). b) Histograms of the apparent mobility for the dye-labeled dNMPs using a field strength of 342 V/cm in a 100 μ m total length nanochannel. Histograms were fit to a Gaussian function with of the apparent mobility histogram (each bin represents 2×10^{-5} cm²/Vs apparent mobility units). The error bars represent the standard deviations in the measurements.

Figure 2.7 Microscale electrophoresis of dAMP, dCMP, dTMP and dGMP at varying pH values. The electrophoresis was performed using the following conditions. Carrier electrolyte was 1 mM MgCl₂ in 89 mM TB. The applied voltage was 20 kV (310 V/cm). The separations were performed in a silica capillary that possessed an ID = 50 μ m, total length = 64.5 cm, effective length = 56 cm, pressure injection at 90 mbar* s, with UV detection at 254 nm. In this case, the nucleotides were not labeled with ATTO 532

Figure 2.8. Histogram of apparent mobilities for the dye-labeled dNMPs at field strength of 342 V/cm in a 100 μ m long nanochannel. The nanochannel electrokinetic conditions are the same as in Figure 2.7 but using a carrier electrolyte of pH = 10.3. Gaussian functions were fit to the histograms as discussed in Figure 2b.

Figure 2.9. Relative apparent mobility of the ATTO 532-labeled dNMPs with respect to carrier electrolyte pH values. Apparent mobilities have been normalized to the highest observed apparent mobility for pH 8.3, 9.3 and 10.3. (Note. data lines are connected only for ease of interpretation). The error bars represent the standard deviations in the measurements.

Figure 2.10. a) Apparent mobility versus the electric field strength for ATTO 532 conjugated to dCMP, dGMP, dTMP, and dAMP. The nanochannel electrokinetic conditions are the same as shown in Figure 2 except that the carrier electrolyte concentration was 0.45 mM TB pH 8.3 (λ_d = 12.5 nm). b) Histogram of apparent mobility for the dye labeled dNMPs with a field strength of 342 V/cm in a 100 μ m long nanochannel. The error bars represent the standard deviations in the measurements.

Figure 3.1. **A)** An image of the T-chip used for the microscale electrophoresis. The chip was made via hot embossing into PMMA. **B)** Schematic diagram of the in-house built microchip electrophoresis laser-induced fluorescence detector that utilized a 20 mW 532 nm excitation laser with edge filter. The detector contained a 560 nm long pass filter, 532 nm dichroic filter and SPCM-AQR single photon counting module within the optical train. A 100X high numerical aperture (NA = 1.3) microscope objective was used to focus the laser beam onto the microchannel and collect the fluorescence.

Figure 3.2. SEM images of the Si master, resin stamp, and imprinted device. **A)** An SEM of the Si master at 500X magnification. **B)** Enlarged area of the entrance funnel formed in the Si master. **C)** UV-imprinted nanochannel device to form the resin stamp with PUA. **D)** Enlarged nanochannel area in the resin stamp. **E)** Nanochannels thermally imprinted into PMMA substrate. **F)** Enlarged area of nanochannel imprinted into PMMA

Figure 3.3: The optical setup of the fluorescence imaging system. The Gaussian beam from the laser (Nd:YAG; $\lambda_{ex} = 532$ nm; $P = 0.01\text{-}5$ W; 2.2 mm beam diameter) was expanded 10x using a Keplerian beam expander and the wings were knocked out with an iris that ensured uniform laser intensity in the field-of view and complete backfilling of the objective (OBJ). The beam was focused into the back of a 100x oil immersion objective

Figure 3.4. Representation of how the nanochannel electrochromatography and data analysis were performed. **A)** A of picture a fluoresently labeled ss-DNA migrating through a thermoplastic nanochannel. The yellow boxes indicate Positions (Pos) 1 and 2. **B)** The fluorescence intensity profile of one injection event was enlarged at Pos1 and 2.

Figure 3.5. **A)** Image of a PMMA/COC nanochannel device (100 nm x 100 nm x 107 μm in depth, width, and length, respectively). **B)** Experimental setup for nanoelectrochromatography experiment where anode (red) is at the sample input reservoir and the cathode at the waste reservoir. **C)** Schematic of a nanochannel when an external electric field was applied. Electroosmotic flow (μ_{eof}) was from anode to cathode while the electrophoretic mobility (μ_{ep}) of negatively charged dye-labeled ssDNA was toward the anode. In addition to μ_{ep} and μ_{eof} , the ssDNA can interact with wall of the channel giving rise to μ_{eff}

Figure 3.6. **A)** Schematic diagram of experimental set up used for the microscale electrophoresis, where a T shaped microchip is used. A sample plug was electrokinetically introduced into the separation channel by applying a potential across the S and SW reservoirs. A photon avalanche detector was used to capture the fluorescence signal at the detection point. **B)** Electropherogram obtained for the free solution microchip (PMMA) electrophoresis of ssDNAs with microchannel dimensions of 50 μm x 100 μm (depth and width respectively) and 5.0 cm in length. The applied voltage for the electrophoresis was 5 kV (1000 V/cm) with a 45 mM TBE buffer (pH 8.3) used as the background electrolyte. The of ssDNAs (5 μM) were injected electrokinetically into the separation channel.

Figure 3.7. Characterization of surface roughness by AFM for IM-PMMA and NIM-PMMA surfaces before and after O₂ plasma activation. Shown are AFM images of: **A)** IM-PMMA; **B)**

NIM-PMMA; **C**) O₂ plasma treated IM-PMMA; and **D**) O₂ plasma treated NIM PMMA. Plasma activation was done at 50 mW for 1 min, which is similar to conditions used during bonding of nanochannel devices.²⁸ These images were taken by scanning an area of 3 μm x 3 μm. **E**) Comparison of the measured root mean square (RMS) roughness of both PMMA types before and after O₂ plasma activation. **F**) The measured EOF for NIM-PMMA and IM-PMMA nanochannel devices as well as the zeta potential following O₂ plasma activation (EOF measured at pH = 8.3).

Figure 3.8. A) Effective mobility of oligonucleotides vs. the field strength in NIM-PMMA (substrate) – COC 8007 (cover plate) nanochannels (100 nm depth x100 nm width and 104 μm length). B) Effective mobility of oligonucleotides vs. the field strength in IM-PMMA (substrate)-CO₈₀₀₇ (cover plate) nanochannels (100 nm depth x100 nm width and 104 nm length) C) semilog plot of effective mobility vs length of oligonucleotides in NIM-PMMA and IM-PMMA.

Figure 3.9 **A**) Histogram of effective migration time of Oligo 35, Oligo 50 and Oligo 70 at a field strength of 280 V/cm that were separated in NIM-PMMA-COC8007 device. **B**) Histogram of effective migration time of Oligo 35, Oligo 50 and Oligo 70 at a field strength of 280 V/cm that were separated in IM-PMMA-COC 8007 device. Histograms were fitted in to a Gaussian distribution and each bin represent 0.05 s for n=100 events. **C**) Calculated separation resolution between the 3 ssDNA.

Figure 3.10 **A**) Histogram of migration time for ssDNAs at an effective column length of 30 μm through a 100 nm x 100 nm NIM-PMMA nanochannel at a field strength of 280 V/cm. Histograms were fit to a Gaussian and each histogram represents 100 events. **B**) Comparison of peak resolution at an effective column length of 60 μm and 30 μm. **C**) Calculated theoretical plates for ssDNAs at effective column lengths of 30 μm and 60 μm. $N = 5.54 \left(t_m / w_{0.5} \right)^2$ was used to calculate the number of theoretical plates and $\frac{N \times 100}{\text{column length (cm)}}$ to obtained theoretical plates in units of m⁻¹

Figure 4.1. **A**) Schematic illustration of the device assembly using the Nanonex2500. **B**) Temperature-pressure process profile showing the seven stages for the imprinting and bonding cycle. An imprinting cycle is 10 min (5 min imprinting time) and bonding cycle is 25 min (15 min bonding time).

Figure 4.2. **A**) An SEM image of nanochannel replicated onto polyurethane (PUA) resin. **B**) An SEM image of nanochannel imprinted into COC5010 substrate. **C**) An SPM image of the nanochannel imprinted in to COC5010 and the depth was measured as 110 nm by SPM.

Figure 4.3. A schematic diagram of microscale electrophoresis set up with the T-shaped microchip fabricated in PMMA having the dimensions of 100 μm in width and 50 μm depth. The length of the separation channel is 5 cm.

Figure 4.4. (A) Optical set-up of the fluorescence imaging system. The Gaussian beam from the laser (Nd:YAG; $\lambda_{\text{ex}} = 532$ nm; P = 0.01-5 W; 2.2 mm beam diameter) was expanded 10x using a Keplerian beam expander and the wings were knocked out with an iris that ensured uniform laser intensity in the field-of view and complete back-filling of the objective (OBJ). The beam was focused into the back of a 100x oil immersion objective

Figure 4.5. **A)** The bond strength calculated for thermally bonded COC/COC devices and NIM-PMMA/COC devices. Bonding of COC/COC devices was done without plasma treatment and NIM-PMMA/COC was done by treating both substrate and coverplate under 50 mW O₂ plasma for 1 min Standard deviation is given for n=5 measurements. **B)** pH stability of NIM-PMMA/COC devices with time. **C)** pH stability of COC/COC devices with time. All fluorescence images were adjusted to the same intensity scale.

Figure 4.6. **A)** Water contact angle of COC 5010 surface measured at different UV/O₃ exposure times at 22 mW/cm². The data points named as with cover plate were obtained by keeping a cover plate on top of the substrate and then exposing it with UV/O₃. After exposure, the contact angle of the underlying substrate was measured. **B)** EOF mobility of COC/COC nanochannel devices. The dimensions of the nanochannels were 110 nm x 110 nm depth and width respectively (length – 107 μm). Substrate is COC5010 and sealed with COC8007 coverplate. The activation was done through the coverplate side. Error bars represent the standard deviation of contact angle and EOF for n=5.

Figure 4.7. **A)** The electropherogram for the separation of rNMPs by microscale electrophoresis in PMMA microchannels having dimensions of 50 μm x 100 μm (depth and width, respectively) with 5 cm separation length. **B)** Calculated apparent mobilities of rNMPs using equation (4.5). **C)** Resolutions (R) calculated for adjacent peak pairs using the electropherogram shown in (A). R= 1.18(t_{m2}-t_{m1})/ (w_{0.5}+w_{0.5}) where t_{m1} and t_{m2} are migration times and w₁ and w₂ corresponds to the peak widths at the base of the peaks.

Figure 4.8 **A)** Apparent mobility vs electric field strength of rNMPs in 110 nm x 110 nm nanochannels fabricated in NIM-PMMA/COC nanochannels using 1X NE buffer 3 at pH 7.9 as carrier electrolyte. **B)** Schematic diagram of rNMPs with attached dye and the pKa of the nucleobases. **C)** Histogram of apparent mobilities of rNMPs at 280 V/cm in 110 x 100 nm NIM-PMMA/COC nanochannel devices using 1X NE buffer 3 at pH 7.9 as the carrier electrolyte. The histograms were fit in to gaussian function and each bin represent 2 x 10⁻⁶ cm²/Vs. **C)** The resolution of peaks was calculated using R= 1.18 (Δμ/w_{0.5} + w_{0.5}) where w_{0.5} correspond to the full width at half maximum of the gaussian peaks. **D)** Identification accuracies of rNMPs calculated from

Figure 4.9. **A)** Apparent mobility vs electric field strength of rNMPs in 110 nm x 110 nm nanochannels fabricated in COC/COC nanochannels using 1X NE buffer 3 at pH 7.9 as the background carrier electrolyte **B)** Histogram am of apparent mobilities of rNMPs at 934 V/cm in 110 x 100 nm COC/COC nanochannel devices using 1X NE buffer 3 at pH 7.9 as the carrier electrolyte. The histograms were fit into gaussian function and each bin represent 2 x 10⁻⁶ cm²/Vs. **C** The resolution of peaks was calculated using R = 1.18 (Δμ/w_{0.5} + w_{0.5}) where w_{0.5} correspond to the full width at half maximum of the gaussian peaks. **D)** Identification accuracies of rNMPs calculated from Gaussian peak overlap. Identification accuracy was calculated as mentioned in Figure 4.8.

Figure 4.10. **A)** Histogram of apparent mobilities of rNMPs at 934 V/cm in 110 x 100 nm COC/COC nanochannel devices using 1X NE buffer 3 at pH 10.3 as the carrier electrolyte. The

histograms were fit to Gaussian functions and each bin represents $2 \times 10^{-6} \text{ cm}^2/\text{Vs}$. **B)** The resolution of peaks at pH 10.3 was calculated using $R = 1.18 (\Delta\mu/w_{0.5} + w_{0.5})$, where $w_{0.5}$ correspond to the full width at half maximum of the Gaussian peaks. **C)** Identification accuracies of rNMPs calculated from Gaussian peak overlap. Identification accuracy = area of non-overlapped/total peak area at pH 10.3.

Figure 5.1. **A)** A schematic diagram of X-ToF. **B)** An enlarged area of X-ToF with the fluidic network. **C)** Expanded region of the bioreactor where enzyme digestion of RNA occurs. **D)** Expanded RNA enriching area of the X-ToF.

Figure 5.2. **A)** Tapestation traces showing the digestion of 60 mer RNA molecule by XRN-1 tethered to microfluidic solid phase bioreactor. Lanes: (1) Size markers; 60mer in absence of XRN-1(2) and presence (3) of XRN-1; 60mer containing a ^{6}mA residue in absence of (4) and presence (5) of XRN-1. **B)** Immobilization of XRN-1 using direct EDC/NHS coupling to a surface. **C)** Tapestation traces of the FLuc IVT in the absent of (left) and presence of (right) XRN-1.

Figure 5.3. **A)** An SEM image of the footprint of X-ToF fabricated in Si using photolithography and FIB milling. **B)** An enlarged area of the bioreactor in Si master where the XRN-1 will be immobilized in X-ToF sensor.

List of Tables

Table 2.1: The net charges of dNMPs at pH 8.3 and pH 10.3

Table 2.2 Separation resolution between ATTO 532-dNMP pairs at pH 8.3 and 44.5 mM TB (taken from Figure 2b) were calculated using $R = \Delta\mu/w_{avg}$ where $\Delta\mu$ is the difference in the average apparent mobility (determined from the centroid of the Gaussian fit to each histogram) for each peak pair and w_{avg} is the average full width of the two peaks, which is related to the standard deviation of the Gaussian.

Table 2.3. Resolution between ATTO532-dNMPs pairs at pH 10.3 and 44.5 mM TB (taken from Figure 2.8 and calculated as in Table 2.2

Table 2.4. Identification accuracy for all ATTO 532-dNMPs at pH 10.3 and were calculated using the peak overlap between Gaussian fits to the histogram of apparent mobilities at pH 10.3

Table 2.5. Resolution of ATTO 532-dNMPs pairs at pH 8.3 and 0.45 mM TBE (from Figure 2.10B) and were calculated the same procedure as described in Table 2.1

Table 3.1. Conditions used to imprint nanochannel devices on two different PMMA substrates using the Nanonex 2500.

Table 3.2. Bonding conditions used to seal the nanochannel devices imprinted on two different PMMA substrates with COC8007 cover plate in Nanonex2500. Both cover plate and substrate were oxygen plasma treated prior to bonding.

Table 3.3. Calculated bond strength by crack test for IM-PMMA and NIM-PMMA using equation (3.1).

Table 3.4. Calculated radius of gyration of ssDNA by using the equation $R_g = \sqrt{\sigma L/3}$ where σ is the persistence length (5 nm)⁷¹ of the ssDNA and L is the contour length. [L= number of nucleotides x length per (0.43 nm)].

Table 3.5. Retention factors of oligonucleotides in IM-PMMA and NIM-PMMA.

Table 4.1. The optimized imprinting conditions for NIM-PMMA and COC5010 110 x110 nm nanochannels in Nanonex 2500; Width and depth of the imprinted nanochannel measured by SEM (Hitachi SU8230 Field emission scanning electron microscopy)and SPM (Schimadzu SPM-9700HT), respectively.

Table 4.2. Optimized bonding conditions for NIM-PMMA and COC 5010 110 x110 nm nanochannels using the Nanonex 2500.

Table 4.3. Chemical composition of 1X NE buffer 3.

Chapter 1. Nanofluidic Devices for Biomolecule Separation

1.1 Introduction

Precision medicine combines disease diagnosis, treatment, and prevention tailored to a patients' individual variability of genes, environment, and lifestyle.¹ Unlike the one-size-fits-all concept of medicine, in precision medicine drug selection, treatment protocols, and prevention plans will minimize harmful side effects and ensure outcomes that are more successful for a particular patient's molecular makeup of their disease. In precision medicine, most patients are classified by specific molecular biomarkers such as proteins, nucleic acids, and metabolites.^{2, 3} Therefore, bioanalytical chemistry has become a major contributor to precision medicine for the development of analytical techniques tailored for medical diagnostics and therapeutics that seek to discover the unique molecular composition of a patient's disease.^{1, 2, 4}

In particular, analytical separations can be viewed as a general method to determine the results of molecular biological reactions that generate products (*i.e.*, biomolecules) dependent on the composition of one's disease. Conventional electrophoresis and chromatography are used for qualitative and quantitative analyses of these biomolecules. Chromatographic methods can separate molecules, but typically require large input sample volumes. Electrophoresis uses a smaller sample volume, but typically analyzes only charged molecules, and in many cases, requires sieving matrices to do the separation, for example in the case of DNAs. Thus, the implementation of precision approaches to determine the molecular composition of a patient's disease will require novel, rapid, robust, and cost-effective techniques that can detect and identify even a few molecules secured from a given biomarker in small volume samples with high throughput and/or multiplexing capabilities (see Figure 1.1).

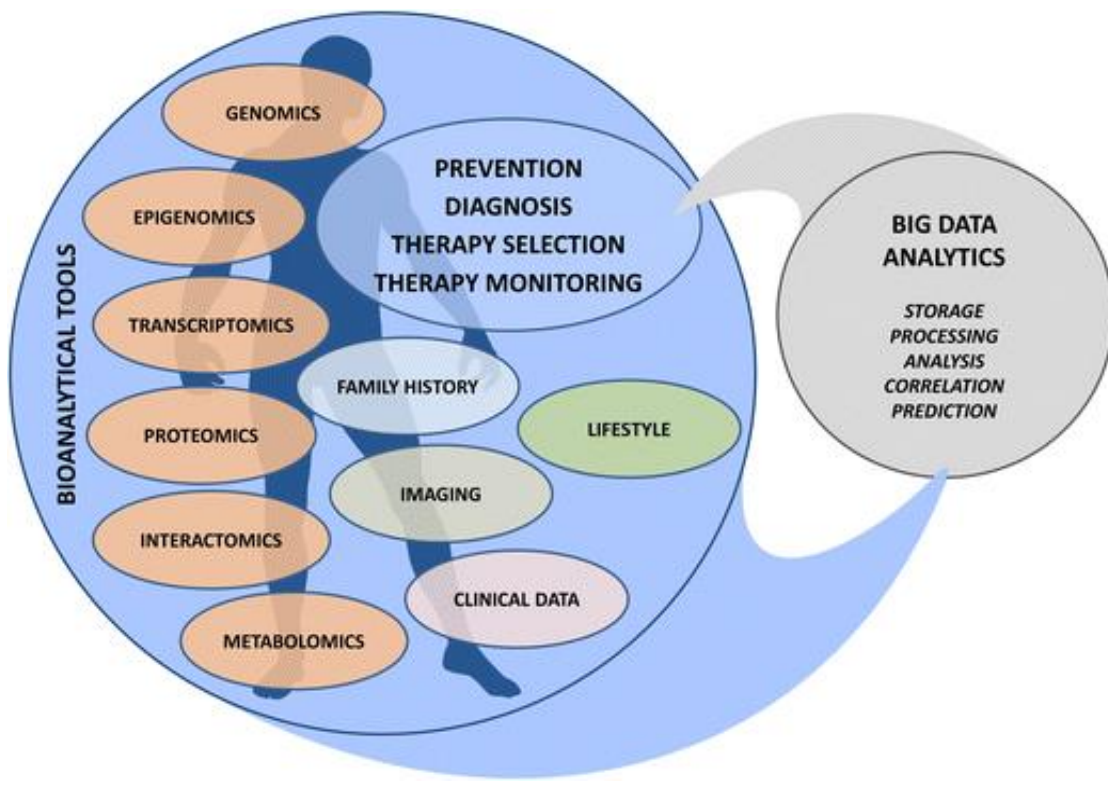


Figure 1.1. An overview of the major components comprising the precision medicine concept (reproduced from Roda *et al.* Analytical and Bioanalytical Chemistry 2018).

Miniaturization of analytical separations has potential benefits for clinical applications. These benefits are: (i) low sample and reagent volume requirements; (ii) the ability to perform parallel analyses with high throughput; (iii) separations at molecular length scales that provide unique separation modalities; and (iv) the ability to integrate the separation with lab-on-a-chip (LOC) components that can perform sample preparation. Miniaturization and LOC devices could be ideal platforms for point-of-care testing, as these tests can be done in resource-limited settings without the need of highly qualified personnel.^{4, 5}

In the past decades, there have been impressive developments in the field of microfluidics for diagnostic applications and several concepts have been commercialized as well.^{6, 7} Although

microfluidics has been useful in several applications, the story of nanofluidics is quite different due to the unique nanoscale phenomena arising from nano-confinement.

Unique separation modalities are observed in nanofluidics due to phenomena that occur only on the nanometer scale, including increased surface area-to-volume ratio, EDL overlap, surface charge dominating flow, and effects of surface roughness.⁸ Therefore, nanofluidics has garnered a significant amount of attention in the field of biomolecule separations including electrokinetic and chromatographic separations.^{8, 10}

Nanofluidics involves flow in channels with dimensions ranging from 1 nm to 1000 nm including classical (1-100 nm) and extended nanoscale (10 – 1000 nm) separations.¹¹ With the development of new technologies for both inspection and creation of nanostructures, such as atomic force microscopy (AFM), scanning tunneling microscopy (STM), electron beam lithography, and ion beam milling that can permit the patterning of sub-100 nm structures. In addition, nanomachining techniques such as nanoimprint lithography and soft lithography provide the ability to replicate nanometer structures into a variety of materials. With the advent of these techniques, new insights into the applications of nanofluidics in a variety of fields including bioengineering, medicine, and chemistry have been realized.¹² Furthermore, a significant development in molecular dynamic simulations have become a useful tool for the elucidation of the ion transport, separation behavior of analytes, and surface effects within nanochannels.^{13, 14}

A unique feature of nanofluidics is that the relevant length scale is comparable with the range of surface and interfacial forces in fluids, such as van der Waals forces, and electrostatic and steric interactions. When a fluidic channel's dimensions approach the classical nanoscale regime, changes in the dominating forces together with the transport dynamics deviate from typical micro- and macroscale descriptions.^{15, 16} In addition, due to increased surface area-to-volume ratio in

nanochannels, surface charge governed transport becomes apparent.⁹ Wall adsorption and desorption of molecules is another important aspect in nanofluidics that arises. These adsorption and desorption events can be reversible or irreversible depending on the magnitude of the interaction energy and are utilized by many chromatographic separations developed in nanoscale fluidic channels.^{10, 17}

Herein we summarize the state-of-the-art technologies for biomolecule separations in the nanoscale. Unique transport phenomena in nanofluidics related to biomolecular separations will be discussed as well as the different devices used and their fabrication discussed. The detection methods widely used in biomolecular separations will also be presented. Finally, the application of nanofluidics for biomolecule separations with the emphasis on nano-electrophoresis and nano-chromatography will be discussed in this chapter as well.

1.2 Unique phenomena affecting separations in nanofluidic devices

Nanofluidics is the study of fluid behavior inside or around objects of which at least one dimension (depth/width or length) is < 100 nm. In many cases, the nanometer relevant length scale can be extended to fall in the range if 10 – 1000 nm known as extended nanofluidics.¹⁸ Unique physical phenomena not observed in the micro- and macroscale can dominate in the nanoscale, opening up an innovative territory of research and applications. The illustrative phenomena and effects that have been revealed include nonlinear transport such as concentration polarization, ion current rectification, and altered liquid properties. These are mostly stemming from ultrahigh surface area-to-volume ratio, surface charge, electroosmotic flow and EDL overlap (see Figure 1.2). Herein the relevant parameters and unique nanoscale phenomena that influence nanoseparations are discussed.

Length Scales	1 nm	10 nm	100 nm	1000 nm
Regimes*		Classical Nanofluidics		Extended Nanofluidics
Phenomena and effects		Surface charge Ultrahigh surface-to-volume ratios Electric double layer overlap Nonlinear transport Altered liquid properties		
Representative materials at the length scales	Ions Water Small molecules	Lipids Proteins	Ribosomes Exosomes	Viruses Microvesicles Bacteria
		DNA	Lipid vesicles/Liposomes	
		Nanoparticles /Submicron particles		
		Nanotubes/Nanowires/Polymers/Fibers		
		2D materials, eg., Graphene		

Figure 1.2. A representation of materials and nanometric objects at the same length scales as nanofluidics, where unique transport phenomena and effects occur. (reproduced from Xu, Y. Advanced Materials 2018)

1.2.1 Electric double layer (EDL) and zeta potential (ζ)

Almost every surface is electrically charged when in contact with an electrolyte. This charge is gained through either dissociation or association of ions covalently bound to the surface or

through non-covalent adsorption of ions. Ions in solution with the opposite charge compared to the surface charge (counter-ions) are attracted to the surface while ions with similar charges compared to surface charge (co-ions) are repelled from the surface. When this attraction combined with Brownian diffusion of ions occurs, this will result in two layers of ions next to the surface. A fixed layer of ions is called the Stern layer and a mobile layer of ions is called the diffuse layer. These two layers together are called the electrical double layer, EDL. Ions in the Stern layer are tightly bound to the surface. Therefore, can think of these ions as a part of the surface itself, but this layer does not completely shield off the surface charge. Hence, more ions from the solution get attracted to shield this surface charge, but these ions do not get bound tightly. Instead, these ions move freely due to Brownian motion creating a layer of mobile ions known as the diffuse layer (see Figure 1.3) ¹⁹

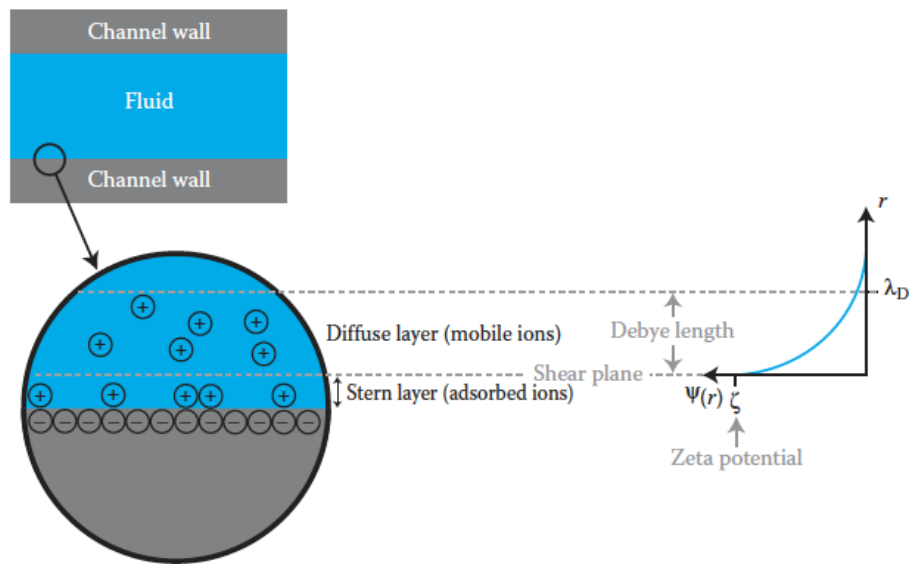


Figure 1.3. A schematic of the Gouy-Chapman-Stern model of the EDL, where a strongly bound cation layer is known as the Stern layer, while loosely bound cation layer with mobile ions is known as the diffuse layer. The potential at the shear plane is named the zeta potential (ζ) (reproduced from Pennathur *et al.* Nanotechnology: understanding the small systems, CRC press, 2014).

The thickness of EDL, which is known as the Debye length, can be described by equation 1.1;

$$\lambda_D = \left(\frac{\epsilon k_B T}{e^2 \sum_{i=1}^n Z_i n_{\infty,i}} \right)^{1/2} \quad (1.1)$$

where ϵ is the electric permittivity of the liquid, k_B is the Boltzmann constant, T is the absolute temperature, e is the charge of an electron, Z_i is the charge of ions, and n_i is the number density of ions.²⁰ The interface between the Stern layer and the diffuse layer is known as the shear plane. The electric potential at the shear plane is the ζ -potential, which measures the electric charge developed on a solid surface in contact with an aqueous solution. Further, it is a property that depends on the ion concentration, ion valency, size of the ion, pH, and temperature of the solution. As a result, each solid-liquid interface has its unique zeta potential. Mathematical expression of the ζ -potential is given by equation 1.2;^{21, 22}

$$\zeta = \frac{2kT}{e} \ln \left[\frac{2e\sigma_s \lambda_D}{\epsilon_0 \epsilon_r k_B T} + \sqrt{1 + \frac{(2e\sigma_s \lambda_D / \epsilon_0 \epsilon_r k_B T)^2}{4}} \right] \quad (1.2)$$

where σ_s is the surface charge and k is the Boltzmann constant. Sze *et al.* reported that the ζ -potential for surfaces in KCl and LaCl₃ aqueous solutions varied between -88 to -66 mV and -110 to -68 mV for glass and PDMS surfaces, respectively, independent of the channel size and driving voltage. Uba *et al.*²² reported the ζ -potential for PMMA nanochannels and nanoslits modified with NH₂ and O₂ plasma, which were 38 mV and -59 mV, respectively.

The ratio of the channel height (h) and thickness of EDL (λ_d) can be used to describe the state of electroneutrality of the bulk solution within a nanochannel/slit. When $h/\lambda_D \gg 1$, the solution towards the center of the channel becomes electrically neutral and has an equal number of co-ions and counter-ions within the channel with a neutral electric potential. The flow profile becomes classically observed as plug-like flow. However, for $h/\lambda_D \approx 1$ there is an overlap of EDL leading to the loss of electroneutrality with excess counter-ions. In this case, the flow profile becomes parabolic in shape and is known as Poiseuille-like flow (see Figure 1.4).²³

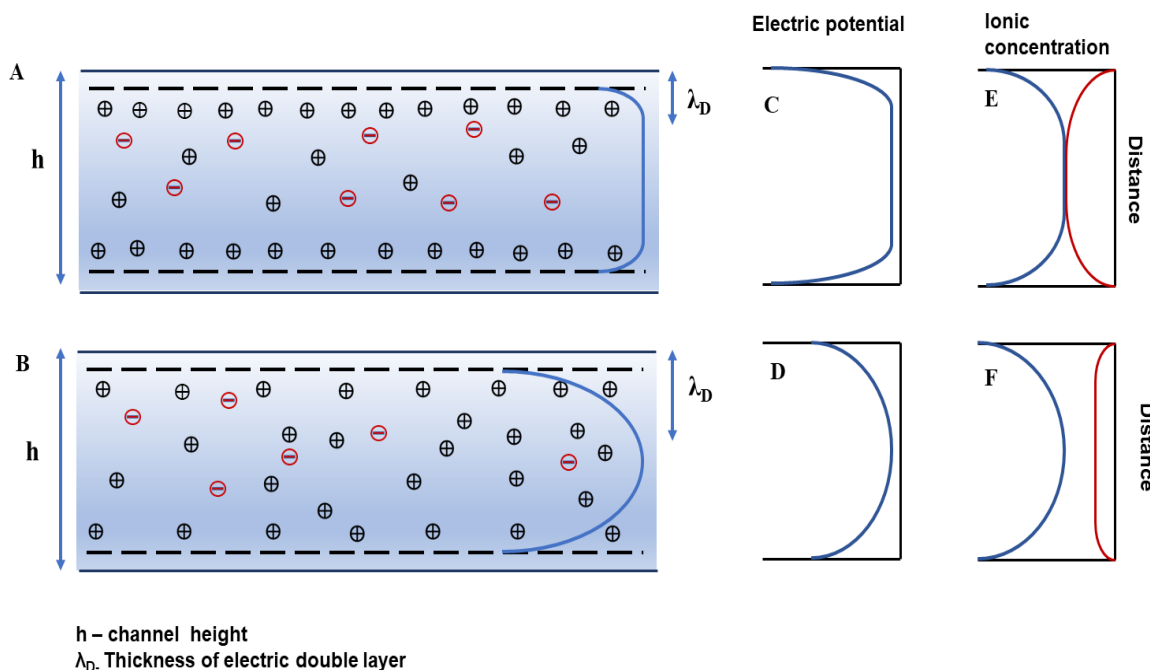


Figure 1.4. Schematic diagram of overlapped and non-overlapped EDL in a nanochannel. **A)** When the Debye length is much smaller than critical channel dimensions, the solution towards the center of the channel becomes neutral. **B)** When there is an overlapping EDL, the solution becomes charged. **C)** Electric potential decays rapidly closer to the channel wall, and in the center, it becomes neutral in non-overlapped EDL conditions. **D)** In an overlapping EDL, the electric potential at the center of the channel does not become neutral and is influenced by surface charge. **E)** The concentration of anions (red) and cations (blue) in a non-overlapping EDL scenario is equal to the bulk concentration. **F)** In an overlapping EDL scenario, the concentration of cations (counterions) becomes much higher than the anion concentration (co-ions) (Reproduced from Napoli *et al. Lab on a Chip* 2010).

For conditions when there is plug flow, two ions with the same electrophoretic mobility but with different charges move at the same speed.²⁰ However, when the EDL is thick compared to the channel dimensions, there is a non-uniform distribution of ions along the channel due to repulsions from the walls. This combined with the parabolic flow make ions move at different velocities depending on their charge. For parabolic flow, the centerline has a higher velocity than near the channel wall, and therefore the more negatively charged ions are repelled from the wall and move more towards the middle of the channel and thus, possess a higher velocity. However, less negatively charged ions or more positively charged ions move closer to the channel wall and, thus, have a lower velocity through the channel. This can lead to novel separation modalities that can only be achieved in the nanoscale (see Figure 1.5).^{20, 24, 25}

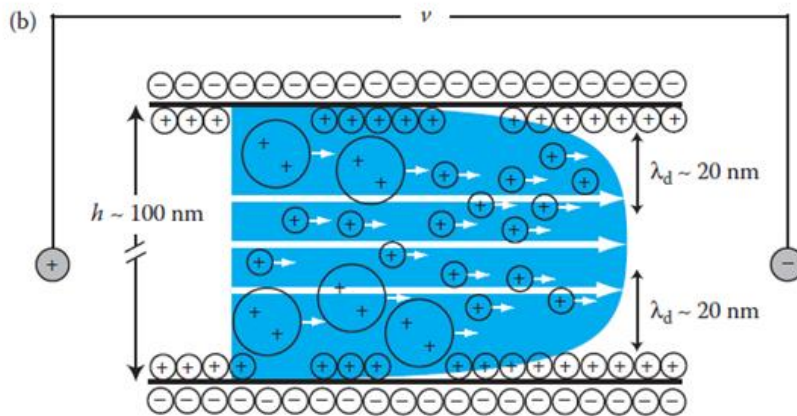


Figure 1.5. Diagram representing the transverse electromigration effects observed with overlapped EDL. In this case, faster moving +1 ions separate from slower moving +2 ions (reproduced from Pennathur *et al.* Nanotechnology understanding small systems, CRC press 2014).

1.2.2 Electroosmotic flow (EOF)

Studies on EOF have been reported as early as the 18th century, where Reuss first discovered that flow in capillaries could be induced by clay particles in water under an external electric field.²⁶ Wiedmann reported fundamental theories of electrokinetics from his studies after a couple of decades to support the findings by Reuss.²⁷ Since then, several theories have evolved for the EOF, which has become a fundamental aspect in electrokinetic separations. Scientists such as Helmholtz (1879), and Smoluchowickz (1903) derived the electrical double layer theory, which occurs under electrokinetic transport phenomena.^{28,29} When the channel wall is negatively charged, negatively charged ions (co-ions) in solution are attracted to the anode while positively charged ions (counter ions) are attracted to the cathode. The movement of the excess counter ions results in a viscous drag of the surrounding liquid creating a bulk flow in the presence of an external electric field, which creates the EOF (Figure 1.6).

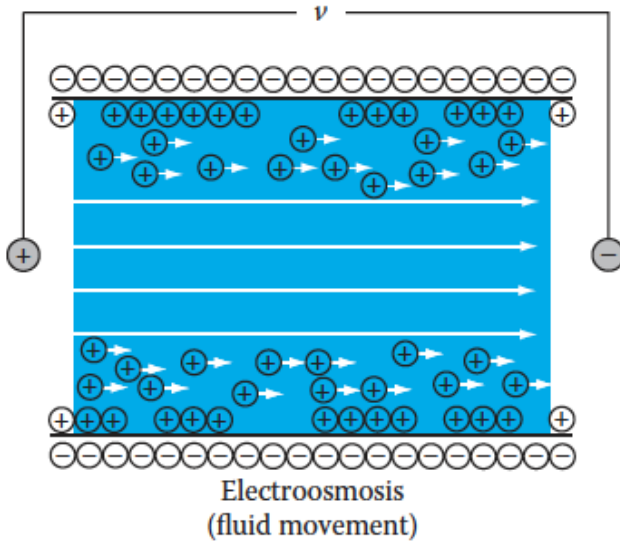


Figure 1.6: A Schematic diagram of EOF in a channel with a negatively charged channel wall. (Reproduced from Pennathur,*et al.* Nanotechnology understanding small systems, CRC press 2014)

When the EDL is thin or when the EOF occurs in a large channel, the EOF has a flat flow profile while in the case of hydrodynamic flow, the flow profile is parabolic (Figure 1.7A, B).³⁰ The advantage of a flat EOF flow profile is that molecules in the channel experience the same velocity regardless of their radial position in the channel, which has been reported to result in high-efficiency electrokinetic separations due to significant reductions in Taylor dispersion.³¹⁻³³

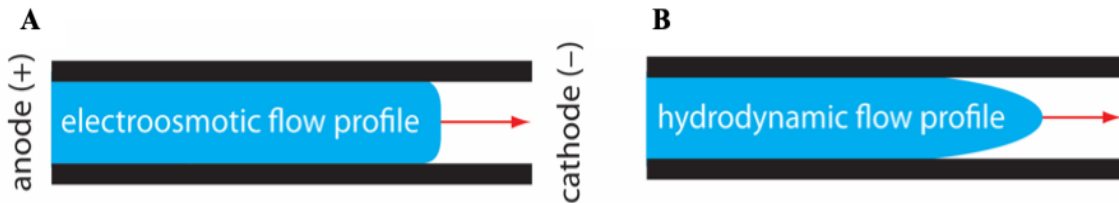


Figure 1.7 A) Electrokinetically driven plug-like flow profile, and B) pressure driven parabolic flow profile in a negatively charged channel (reproduced from <https://chem.libretexts.org>).

The EOF velocity can be described by equation (1.3), where ϵ is the dielectric constant of the buffer, ζ is the zeta potential, E is the applied electric field, and η is the viscosity of the buffer. The EOF is given by equation (1.4) and depends solely on buffer characteristics such as the dielectric constant, viscosity, pH, and concentration, but is independent of the applied electric field.³⁰

$$V_{eof} = \epsilon \zeta E / 4\pi\eta \quad (1.3)$$

$$\mu_{eof} = \epsilon \zeta / 4\pi\eta \quad (1.4)$$

Several studies have reported the EOF of nanochannels optically by monitoring the transport time of zwitterionic dyes like Rhodamine B^{25, 34} and the current monitoring method.^{22, 35-37} In the current monitoring method an electrolyte solution is replaced with another solution of the same electrolyte with slightly higher (~5% higher) ionic concentration. During the replacement of this difference concentration electrolyte from the other generates a change in the current. The time taken for this change is taken to obtain EOF velocity.³⁵

Jacobson *et al.*³⁴ measured the EOF of in nanochannels as small as 98 nm in depth by using the travel time of Rhodamine B, which is a neutral dye molecule and thus, travels at a rate determined by the magnitude of the EOF. The EOF in glass nanochannels was compared to the EOF in microchannels. They observed a 35% decrease in the EOF associated with nanochannels compared to microchannels with decreasing concentration of the carrier electrolyte. They claimed that EDL overlap occurred in nanochannels compared to microchannels and that was responsible for the decrease in the EOF.

Uba *et al.*²² measured the EOF for O₂ and NH₂ modified PMMA nanochannels using the current monitoring method. The values obtained for O₂ modified and NH₂ modified PMMA nanochannels were $1.02 \pm 0.02 \times 10^{-4} \text{ cm}^2/\text{Vs}$ and $-0.75 \pm 0.02 \times 10^{-4} \text{ cm}^2/\text{Vs}$, respectively. They stated that these values were lower than the EOF values obtained for the PMMA microfluidic channel (O₂ modified = $4.43 \pm 0.58 \times 10^{-4} \text{ cm}^2/\text{Vs}$ and NH₂ modified = $-1.34 \pm 0.21 \times 10^{-4} \text{ cm}^2/\text{Vs}$, respectively). The authors suggest that the low EOF observed in PMMA nanofluidic devices is due to low ζ .

Peng *et al.*³⁷ investigated the EOF of single PDMS nanochannels having depths ranging from 20 nm to 250 nm and compared those values to a 5 μm deep channel. They investigated the effects of channel dimensions, the concentration of carrier electrolyte, and the electric field strength for the EOF using the current monitoring method. According to their observations, when the EDL was thin (0.01 M KCl, EDL \sim 3nm), the EOF does not vary with channel dimensions. The d/λ_D for this electrolyte concentration ranged from 10-80. (channel dimensions ranged from 32 nm -240 nm). In contrast, at low electrolyte concentrations (0.001 M KCl, EDL \sim 10 nm), they observed a decrease in the EOF for nanochannels with depths smaller than 100 nm where EDL overlap occurred (d/λ_D for ranged from 3-10 for channel dimension of 30 nm -104 nm). When the electrolyte concentration decreased, the thickness of EDL increases. Therefore, the overlap of the EDL can occur depending on the nanochannel dimensions. Here they observed that for a very small nanochannel, decreasing the electrolyte concentration led to a decrease in the EOF due to EDL overlap (for nanochannels smaller than 89 nm).

1.2.3 Surface roughness effects

Surface roughness is ubiquitous in many nanofluidic and microfluidic devices, which can occur either during fabrication or due to adhesion of molecules to the surface. As channel dimensions decrease, the surface area-to-volume ratio increases (For 100 μm cube surface area-to-volume ratio is 6×10^4 while for 100 nm cube it is 6×10^7). Therefore, compared to microscale channels strong fluid-wall interactions are observed in nanochannels, and the effect of surface roughness to the fluid flow is expected to be significant.³⁸⁻⁴⁰ In general, surface activation steps not only modify the surface chemically, but also induce sub-nanometer and nanometer roughness to the surface, changing the surface morphology.³⁸

Molecular dynamic (MD) studies have discovered that surface roughness has a considerable influence on the EOF and surface wettability depending on the magnitude of the roughness height (h_r).⁴¹ There is significant distortion in the EOF velocity profile and ion distribution when the roughness amplitude and thickness of the EDL are of the same magnitude; the effect becomes insignificant when the thickness of the EDL is much larger than the roughness.³⁹ According to Zhang *et al.*,⁴² the fluid flow experiences high resistance on rough surfaces causing molecules to stick onto the surface of the nanochannel, requiring more time to escape from rough regions. In addition, their simulations showed a decrease in ζ and EOF with increasing roughness amplitude, which is similar to other MD simulations.^{39,41} Furthermore, the surface roughness can strongly influence the resolution of electrokinetic separations performed in nanochannels. Surface roughness can induce dielectrophoretic trapping and fluid recirculation within the channel leading to field-dependent mobilities and higher variances in mobilities.^{22,44-46} However, roughness effects

on separations are more prominent at lower electric field strengths than higher electric field strengths.⁴⁴⁻⁴⁶

1.3 Fabrication of nanofluidic devices

Fabrication of nanochannels is a critical component in the utilization of nanofluidic devices for a variety of areas, including analytical separations. Besides, the mode of fabrication can determine the performance of the nanofluidic device for analytical separation. For example, if the fabrication method generated rough walls in the nanofluidic channels, it could reduce the separation resolutions as these rough surfaces tend to create dielectrophoretic trappings and cause molecules to stick to the wall while they move through the channels. Therefore, nanofabrication methods have evolved significantly during the last decade. Several review papers have extensively discussed various techniques that can be utilized to fabricate nanochannel devices.^{11, 47, 48} However, the choice of fabrication method is determined by the desired nanostructure dimensions and the substrate of choice such as inorganic, elastomeric, or thermoplastic.¹¹

In general, nanofabrication methods are divided into two major categories according to the process involved in creating nanostructures, “top-down” and “bottom-up” methods. In the top-down approach various lithography methods are used to pattern nanoscale structures where it includes serial and parallel techniques for patterning features typically in two-dimensions (2D) over lengths scales that are larger in 4 orders of magnitude than an individual structure.⁴⁸ In this method, nanofabrication tools that are controlled by external experiment parameters are used to create nanostructures.^{49, 50} In contrast, the bottom-up approaches use molecular or atomic components built up into more complex nanoscale assemblies or directed self-assemblies based on

complex mechanisms and technologies.⁵¹ In this method, atoms and smaller molecules are used as the building blocks for the fabrication of multilevel nanostructures. Herein we focus on summarizing the top-down approaches that are widely used in nanofluidic device fabrication. These methods include conventional lithographic methods, high energy beam processing methods, and nanoimprint lithography methods.⁵²

1.3.1 Conventional lithography methods

Conventional photolithography involves the use of light to generate a pattern in a photoresist spun over a Si wafer with a mask used to define the pattern on Si (see Figure 1.8A) and followed by reactive ion etching to etch the exposed substrate following resist development from the sample to form the desired nanochannels. After nanochannels are shaped on Si, sealing of the device is done using glass cover plates. In these methods the lateral dimension is limited by the diffraction limit of UV light used in photolithography. The minimum feature size (l_m) generated can be calculated by the equation given below (equation 1.5)⁵² where k_1 is a constant that depends on the optics, photo resists and process latitude, λ is the wavelength of the UV light and NA is the numerical aperture of the lens used. For a wavelength of 400 nm, k_1 of 0.4 and NA of 0.6 the minimum feature size calculated is 266 nm.

$$l_m = k_1 \frac{\lambda}{NA} \quad (1.5)$$

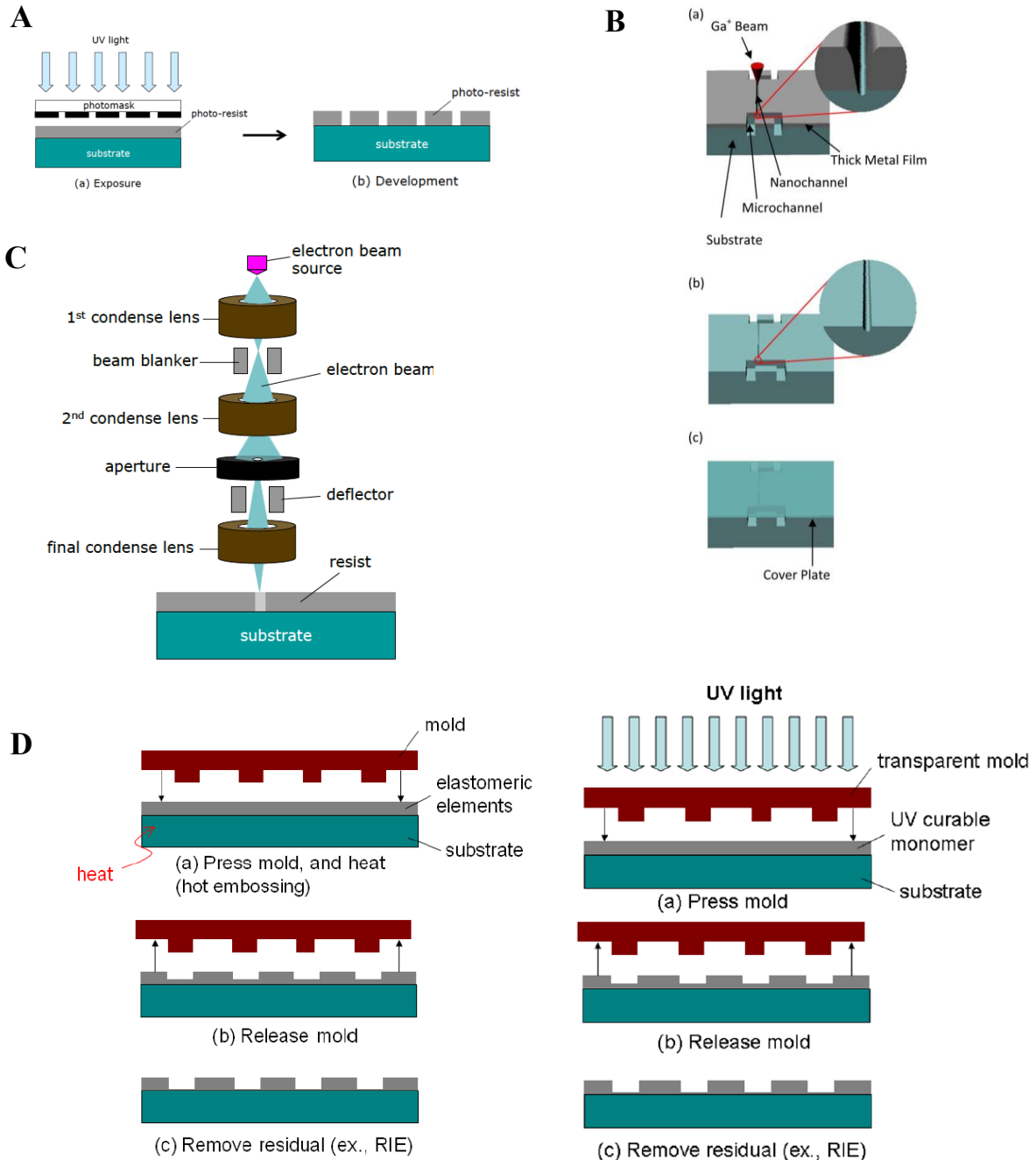


Figure 1.8. Schematic diagrams representing an overview of nanofabrication methods. **A)** Main steps involving in photolithography: a) photoresist coated substrate is exposed to UV light; b) the removal of exposed photoresist by immersing into developer. **B)** Steps used in focused ion beam milling by Ga^+ ions. **C)** An illustration of electron beam lithography where an electron beam is focused onto a resist film to create a pattern by exposing dot-by-dot. **D)** An illustration of nanoimprinting lithography (left) and UV nanoimprinting lithography (right) (Reproduced from Pimpin *et al. Engineering Journal*, 2012).

Therefore, this method is widely used in fabricating planer nanochannels that have only one-dimension in the nanoscale, which is the depth of the channel and is determined by the dose and rate of reactive ion etching. Most of the pioneering research work on biomolecule separations are done in nanofluidic channels fabricated by these methods.^{48, 53-56} Conventional photolithography followed by reactive ion etching has some advantages, such as ease of fabrication, and good reproducibility. A disadvantage of this method is that the nanoscale fabrication is only in the depth direction.

1.3.2 High energy beam processing lithography methods

High energy beam processing is another top-down approach where the nanofluidic structures are obtained through direct writing on the substrate by electron, proton, or focused ion beams. Electron beam lithography (EBL) and focused ion beam milling (FIB) are prominently used for nanofluidic structure fabrication among the high energy beam processing methods. In EBL, nanopatterns are initially defined in a thin layer of electron beam (e-beam) reactive resist using a beam of focused electrons. This focused e-beam interacts with the resist and modify the resist's property to make it soluble/insoluble during a subsequent development step. The very first e-beam reactive resist is known as PMMA, which was developed in the 1960s.⁵⁷ Then, these patterns are transferred to the underlying substrate by wet or reactive ion etching, which is carried out following resist development. Nanostructures as small as 10 nm have been fabricated using EBL.⁵⁸

FIB has become an attractive method for fabrication of nanostructures and uses a focused beam of high energy Gallium (Ga) ions to sputter atoms from the substrate. By optimizing the beam current and utilizing thick conductive sacrificial metal layers, this method has been able to

fabricate sub-5 nm structures.⁵⁸ The overview of these two processes are given in Figure 1.8B and 1.8C.

Over the years, several research groups have utilized EBL followed by dry etching or FIB to develop nanofluidic structures in inorganic substrates, such as glass and fused silica for biomolecule separations, analysis and the evaluation of transport properties though nanofluidic channels have been reported.^{36, 60, 61} Although these high energy beam process methods can produce high quality nanofluidic channels even below 10 nm, these methods rely on sophisticated equipment to make each device via a direct write method. In addition, processing can only be done in a serial manner, which results in high manufacturing cost and low production rates. Thus, these methods are not the best to mass produce nanofluidic devices.

1.3.3 Nanoimprint lithography (NIL)

Nanoimprint lithography is a high-resolution parallel patterning method, which has mainly been targeted towards applications requiring high throughput production of nanoscale devices.^{62,}⁶³ In NIL, a hard mold with the desired nanostructures is used to imprint the structures into a polymer film using a thermal process. Polymers are heated above their glass transition temperature to enable material flow, allowing the filling of the mold structures. Then, its temperature is lowered to solidify the replicated patterns, and finally, the mold is removed carefully. The mold with the nanostructures is first manufactured by conventional photolithography, EBL, or FIB. The use of a hard mold for the fabrication retains the nanofluidic features with minimum deformation. Although NIL has made significant progress, there are a few limitations that need to be resolved. Heating/cooling cycles and high pressures applied during thermal NIL cause stress and wear on

the hard molds. The viscosity of the imprinted material is also an issue that limits the minimum feature size and feature density. However, to overcome these issues, introduction of low viscosity UV-curable resins can be used as a compliant layer, which enhances the fluidity of the imprinted material. This process is known as UV-NIL (Figure 1.8D).⁶⁴ Most of the thermoplastic and elastomeric (PDMS) nanofluidic devices are fabricated by modifying the principles of NIL.^{65, 66}

1.4 Detection methods for biomolecule separations in nanofluidic devices

Decreasing the dimensions of devices to the nanoscale results in ultra-small amounts of analytes that must be detected and demands high sensitivity detection. When channel dimensions are decreased, the number of analytes present in the confined volume decreases proportionately, and most of them can even approach the single molecule level. The probability (P_v) of molecule(s) occupying the probe volume can be calculated using equation 1.6;

$$P_v = CN_A P \quad (1.6)$$

where C is the molecular concentration (mol L^{-1}), N_A is Avogadro's number, and P is the probe volume size (L).⁶⁶ As given by equation 1.6, decreasing probe volume size decreases the probability of a molecule occupying the probe volume. For an example, the volume of a 100 nm cube is 1 aL. When the concentration of an analyte is 1 μM , the number of analyte molecules in the cube is 0.6 molecules.

The other considerations are that the nanochannel dimensions are nearly equal or shorter than the wavelength of visible light, and path lengths are decreased. Therefore, conventional absorbance methods and optical methods using geometrical optics including reflection and refraction optics

cannot be used for the detection in nanochannel dimensions.^{10, 68} Among the various detection methods that have been used for nanochannel detection, laser-induced fluorescence (LIF), thermal lens spectrometry (TLS), and resistive pulse sensing are widely used in nanofluidic studies.¹⁰ A summary and diagram of some of these detection methods are shown in Figure 1.9.

Laser-induced fluorescence (LIF) is widely used because fluorophores can be excited and detected selectively with low limits-of-detection, even at the single-molecule level. In addition, when the detection volume is decreased the sensitivity of fluorescence is enhanced significantly due to reduced background signals generated by impurities and Rayleigh and Raman scattering.⁶⁹ For the majority of separation experiments, wide-field epifluorescence systems are used (see Figure 1.9A).^{22, 70, 71} However, for high resolution single-molecule experiments in the nanoscale, LIF-confocal microscopy is often used to detect signals from analytes in a particular focal volume. This single molecule method is widely used in the analysis of DNA molecules in nanochannels.⁷²

Resistive pulse sensing (RPS) is another method that is widely used in nanofluidics (see Figure 1.9B). When an analyte enters a three-dimensional nano-constriction known as a nanopore, the analyte displaces a sufficient fraction of electrolyte ions and results in a measurable change in the pore resistance, which corresponds to a change in current. Nanopore RPS is widely used for single molecule detection, particularly in third generation nanopore-based DNA sequencing.⁷³ There have also been numerous electrokinetic separations performed that utilized in-plane, solid-state nanopores for virus capsid separations or nucleotide separations.^{68, 74}

Thermal lens spectrometry (TLS) is another sensitive method that has been developed as an analytical tool for microfluidic applications to detect non-fluorescent analytes.⁷⁵ However, conventional TLS cannot be applied directly to nanoscale experiments as the principle is based on

refraction of light. Shimizu *et al.*⁷⁶ modified conventional TLS and developed a new TLS detector known as a differential interference contrast thermal lens microscope (DIC-TLM). DIC-TLM exploits a local change in the refractive index of a solution and is used to detect the concentration of non-fluorescent analytes in nanochannels (500 nm in depth and 5 μm in width) with a 250 aL detection volume (see Figure 1.9C). Non-labeled bovine serum albumin (BSA) were detected by this method in extended nanochannels.⁷⁷

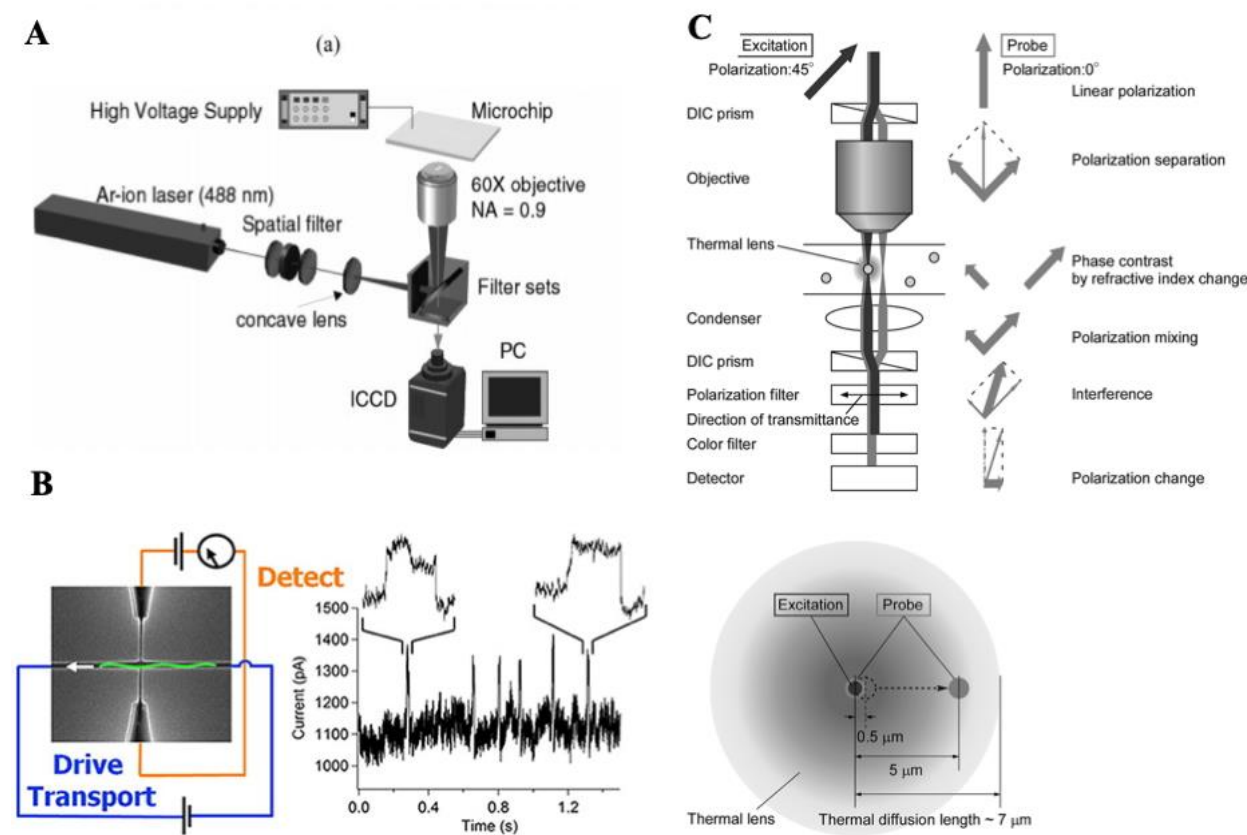


Figure 1.9. A schematic diagram representing the detection methods used in nanoscale separation studies. **A)** Laser induced wide field fluorescence imaging system equipped with a CCD (reproduced from Pennathur *et al.* Analytical Chemistry 2007). **B)** Resistive pulse sensing of analytes migrating through a nanopore (reproduced from Menard *et al.* ACS Nano 2012). **C)** Components in differential interference contrast thermal lens microscope (reproduced from Shimizu *et al.* Analytical Chemistry, 2010).

1.5 Biomolecule separations in nanofluidic devices

Nanofluidic devices can offer unique separations due to nanoscale phenomena. For example, microscale separations of DNA make use of either a gel or a solution of hydrophilic polymers to serve as a separation medium.^{78, 79} In contrast, gel-free separations of DNA can be achieved in nanofluidic devices.⁹ These gel-free separations can significantly reduce the cost and time for separation making these methods applicable for clinical applications. In addition, due to the increased surface area-to-volume ratio, several chromatographic methods are feasible when using nanofluidic devices when open tubular columns are used. The advantages of nanoscale chromatography are high efficiency, fast separation, and the use of extremely small sample volumes, femtoliter (fL) or attoliter (aL) scale.⁸⁰ In this section, the electrokinetic separation of biomolecules and nanoscale chromatographic methods utilized for biomolecule separations are reviewed.

1.5.1 Electrokinetic (EK) separations of biomolecules in nanofluidic devices

Recent review articles have presented an overview on the theories and experimental studies for electrokinetic (EK) separations in nanochannels.^{9, 24, 81} Compared to microscale electrophoretic separations, separations in nanoscale requires a different perspective for studying the separation phenomena as the separation can be altered by EDL effects and surface effects (surface interactions, surface roughness).⁹ As stated, the effects of EDL become prominent in nanochannels due to EDL overlap, which can create a parabolic flow profile. EDL overlap can induce non-uniform electric fields and result in ionic concentration gradients due to the equilibrium between electromigration and diffusion of ions. This transverse concentration gradient not only depends on

the EDL thickness but also depends on surface charge density, valence number of ions, and temperature.^{24, 25} Another factor that affects EK motion of molecules in nanochannels is channel dimension. In nanoslits, Taylor dispersion of neutral molecules across the channel width cannot be neglected compared to that across the channel depth as molecules tend to spend a long time across the channel widths.⁸¹ However for charged molecules in nanochannels, the equilibrium between electromigration of molecules and diffusion affect their dispersion as molecular diffusion can be constrained by the non-uniform electric field within the EDL.

The first efforts on EK separations in nanoscale focused primarily on DNA separations because DNA separations have numerous applications in biotechnology, such as sequencing for mutation detection, forensics, biometric fingerprinting, and identification of pathogens. Therefore, developing methods that can separate and quantify DNA depending on their length is vital to biotechnology and precision medicine. In addition to DNA separations, there are a few studies on protein and amino acid separations as well. In the next section, several efforts on the EK separation of biomolecules in nanofluidic devices are discussed.

One of the first EK DNA separations reported in nanoscale involved using an entropic trap fabricated by shaping a microchannel with an alternating sequence of shallow (75-100 nm) and deep (300 nm) wells. The shallow regions were designed to have depths smaller than the radius of gyration of DNA. When DNA molecules were electrokinetically driven through the microchannel, they got trapped temporarily at the entrance of the shallow wells.⁸³ Surprisingly, longer molecules had higher escape rates from the traps as they have a larger surface area in contact with the boundary of the nano-region, thereby increasing their probability of entry.^{54, 83} The separation efficiency in nanochannels using entropic trap arrays was higher at higher field strengths.⁵⁴

Fu *et al.*⁵³ further developed the entropic trapping using a device geometry with symmetric wells (Figure 1.10A, B) that addressed the problem of separating small DNA molecules. In their study, they were able to separate five different lengths of DNA in ~10 min over a 5 mm long channel (see Figure 1.10 D). The basic device geometry used in their previous study was integrated into a two-dimensional nanofluidic filter array, which allowed for different separation mechanisms other than entropic trappings, such as Ogston and electrostatic sieving.⁸⁴ Furthermore, this device was able to separate biomolecules over a broad range of sizes in a continuous flow format.

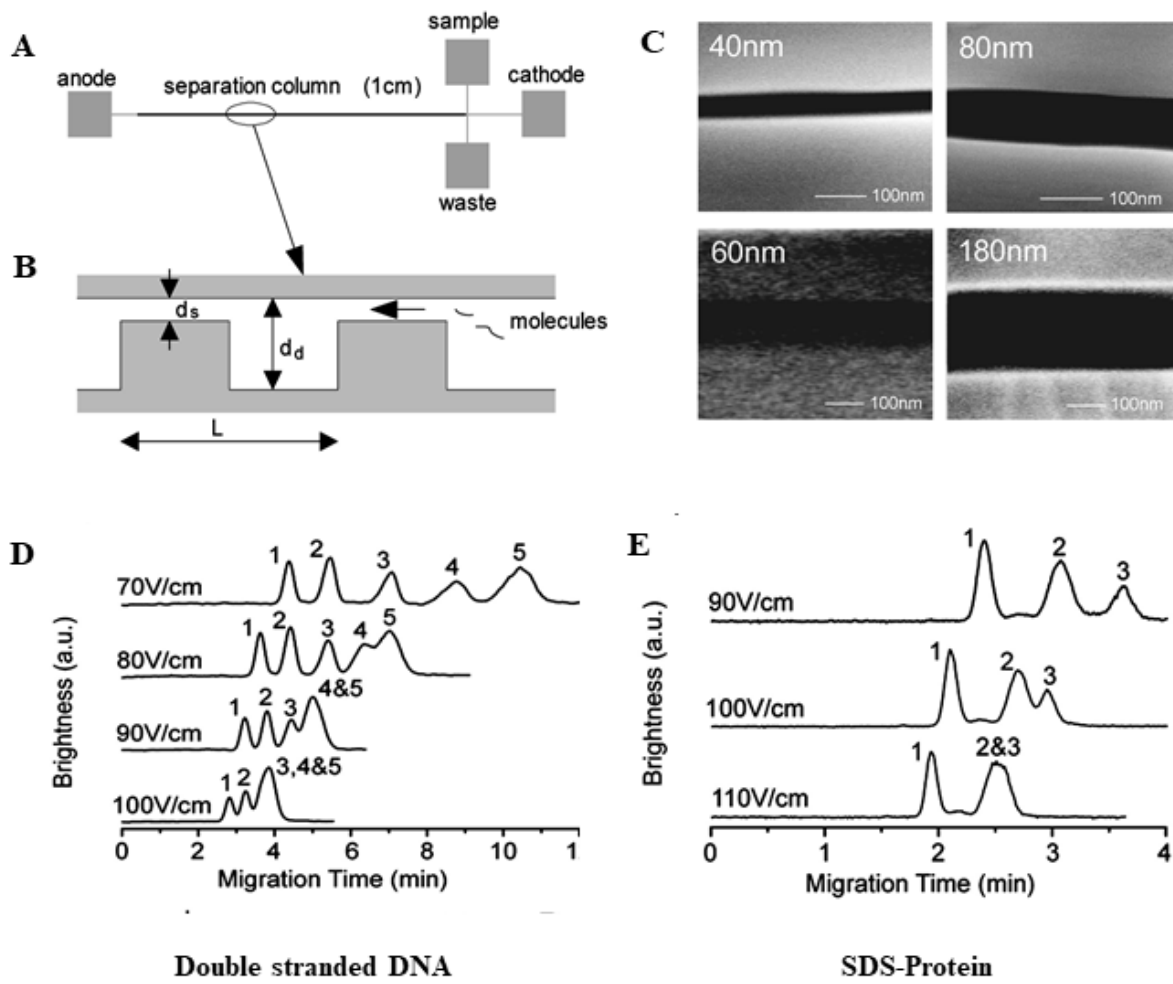


Figure 1.10. **A)** The layout of the nanofilter array chip with four buffer access reservoirs(anode, cathode, sample and waste), a 1 cm separation channel and a T-shaped injector. **B)** A schematic diagram of the cross section of the separation channel in nanofilter array chip consists of thin (ds) and thick (dd) regions with equal lengths **C)** Scanning electron microscopy images of the thin regions in nanofilter array chip with different depths. **D)** Electropherograms for the separation of double stranded DNA with different lengths. 1)50bp; 2) 150 bp; 3) 300 bp; 4)500bp; 5)766 bp at different electric field strengths. **E)** Electropherograms for the separation of SDS-protein complexes. 1) cholera toxin subunit B; 2)lectin phytomagglutinin-L; 3) low density human lipoproteins at different field strengths.(Reproduced from Fu *et al.* Journal of Applied Physics letters 2005)

Cross *et al.*⁸⁵ showed the free solution separation of DNA traveling through nanoslits with depths of 19 and 70 nm. The device used in the experiment consisted of two microfluidic channels,

coupled to nanoslits (Figure 1.11). Fluorescence measurements revealed length-dependent separation of DNA strands (2000 – 10000 bp) that were electrokinetically driven through the nanoslits. When channel dimensions were on the same order as the size of the molecules migrating through the channel, steric interactions influenced the separation. They suggested that surface interactions with channel walls due to confinement led to length-dependent mobility of DNA in free solution.

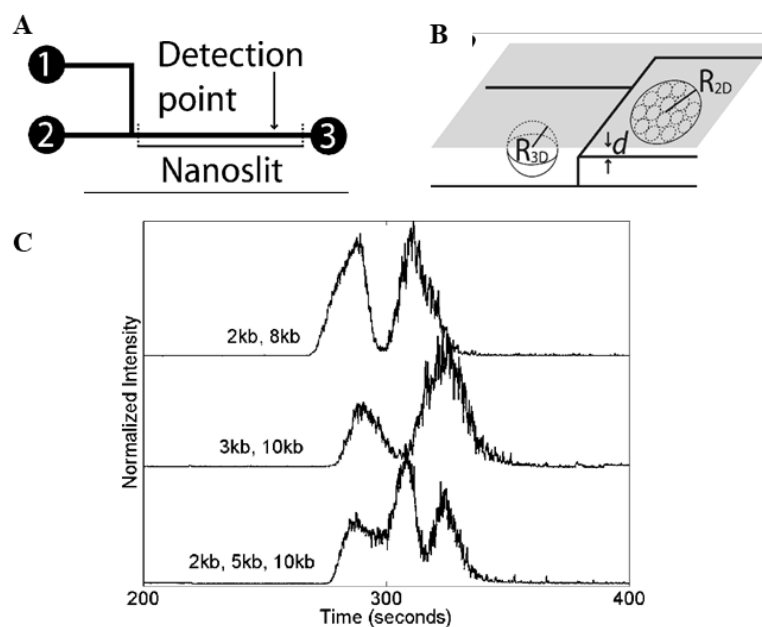


Figure 1.11. **A)** A schematic diagram of the nanoslit device used for the separation and the length of the separation channel is 3-4 cm. **B)** A schematic of the cross sectional transition of DNA from its three dimensional relaxed state to squished state when forced into nanochannel in two dimensions where the molecule becomes a pancake like entity composed of sub-blobs of DNA with a diameter equal to channel height. **C)** Electropherograms showing the separation of mixture of DNA molecules in 19 nm deep separation channel. (Reproduced from Cross *et al.* *Journal of Applied Physics*, 2007)

Pennathur *et al.*⁷⁰ were able to achieve free solution separation of DNAs in nanometer sized channels. A mixture of fluorescently labeled double stranded DNAs with sizes of 10, 25, 50, and

100 bp, fluorescein, and fluorescein-12-UTP were separated in fused silica nanoslits having different depths (40, 100, and 1560 nm). In their study, they investigated the effect of carrier electrolyte concentration on the separation by varying sodium borate buffer concentrations, which ranged from 1 – 100 mM with the best separation resolution obtained at 10 mM buffer concentration. The authors observed a length dependent migration order, which was influenced by the thickness of the EDL. The thickness (λ_D), λ_D/h , and l/h parameters were varied to explore the optimal conditions for the separation. At 10 mM ($\lambda_D/h \approx 3\%$) the elution order was Fluorescein (FL), UTP, and 10, 25, 50 and 100 bp oligonucleotides as a result of their mobility order; $\mu_{FL} < \mu_{UTP} < \mu_{10bp} < \mu_{25bp} < \mu_{50bp} < \mu_{100bp}$. The authors observed the same order for the 5 mM ($\lambda_D/h \approx 4\%$) case too. Even though the elution order was the same, poor separation resolution was observed for 20 mM and 100 mM carrier electrolyte concentrations. At low buffer concentration, 1 mM sodium borate ($\lambda D/h \approx 0.10$), the order of elution was changed compared to high ionic strengths, which was FL, UTP and 100, 50, 10, and 25 bp oligonucleotides. At low ionic strength, the effects of ion density, and EDL coupling compete with each other to determine the net axial migration rate. Hence, transverse electromigration in the axial and transverse directions and steric-wall interactions play a role in determining the EK resolution.(see Figure 1.12 A and B)

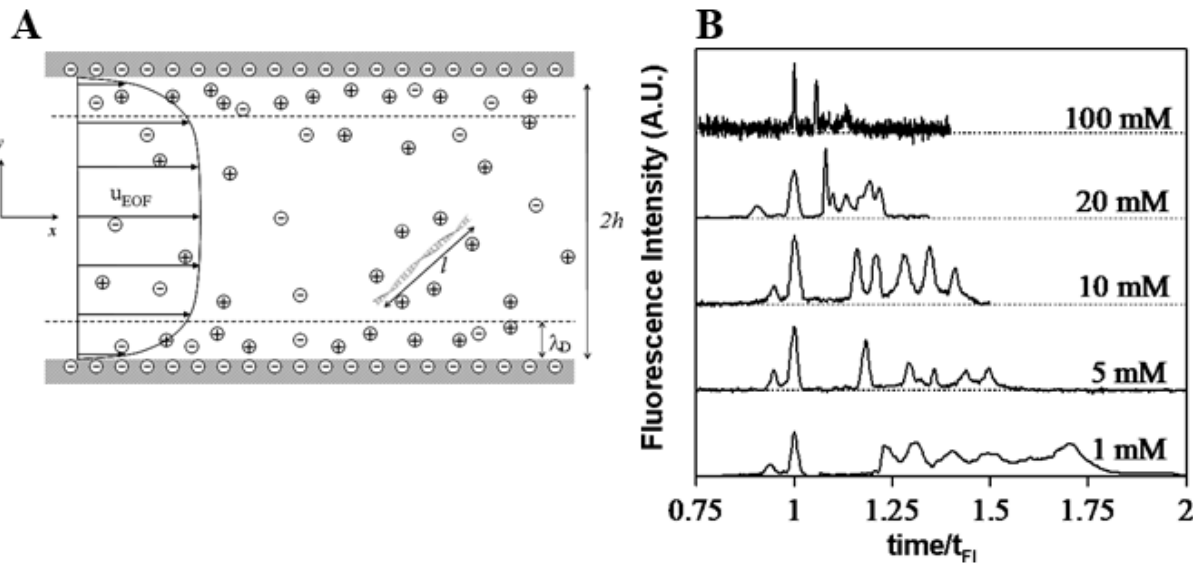


Figure 1.12. A) Schematic of nanochannel electrophoresis of rod-like oligonucleotides. Important length scales are the depth of the channel ($2h$), the length of the dsDNA (l), and the Debye length (λ_D). B) Measured electropherograms for electrokinetic separations of fluorescein, UTP, and a 10-100 bp oligonucleotide ladder in a 100 nm deep channel. Electropherograms are shown for separations in five different concentrations of sodium borate. t_{FI} is the residence time of fluorescein in each experiment (reproduced from Pennathur *et al.* Analytical Chemistry 2007).

In 2009, Huber *et al.*⁸⁶ performed free solution DNA hybridization and separation of single stranded and double stranded DNA in a 200 nm deep nanoslit. As depicted in Figure 1.13A, the device consisted of a 5-ports variation on the common cross-injection chip. Instead of a single sample port there were two sample ports (A and B) as supply channels that were intersecting at a mixing T. The primary oligonucleotide probe with a sequence of 5'TCTCCTTGCTCTCTTCTC3' was labeled with Alexa Flour 488 and an LIF fluorescence microscope system with EMCCD camera was used for detection. The solutions were electrokinetically driven through the initial T for mixing and hybridization was allowed to occur upon mixing and continued as the sample passed through the channel into the injection region. A small sample plug was driven to the separation via the EOF. As seen in Figure 1.13B, there was a clear separation of single stranded

DNA and double stranded DNA in free solution in these nanoslit devices. According to their results, the single stranded unhybridized oligonucleotide migrated faster than the hybridized double stranded DNA. Moreover, they performed a kinetic study on the hybridization of DNA over time and observed the depletion of the single stranded peak in the electropherogram while obtaining the hybridized double stranded DNA peak.

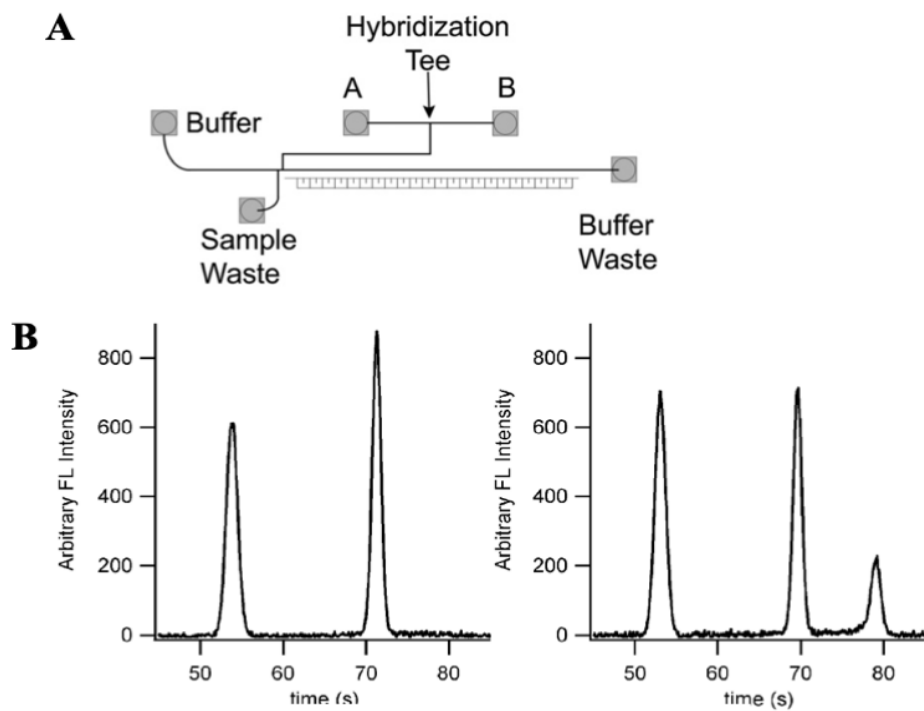


Figure 1.13. **A)** The schematic illustrates the 5-port device layout, including sample wells (A and B), mixing tee, offset tee injector, and separation channel. **B)** Electropherogram of the separation of single stranded DNA (left) and electropherogram of single stranded DNA plus the double stranded DNA(right) after hybridization step (reproduced from Huber *et al. Lab on a Chip* 2009).

Sun *et al.*⁸⁷ observed a velocity difference between methylated and non-methylated DNA in quartz glass nanochannels with dimensions of 300 x 300 nm (depth and width, respectively). They used λ -DNA and T4-DNA methylated and non-methylated labeled with YOYO-1 dye. As depicted

in the fluorescence images in Figure 1.14A and B, there was a clear distinction in translocation velocity of methylated and non-methylated T4-DNA and λ -DNA. They observed that methylated DNA migrated faster than unmethylated DNA. They suggested that the coefficient of friction of methylated DNA was lower than that of non-methylated DNA, allowing methylated DNA to transit the nanochannel faster than non-methylated DNA.

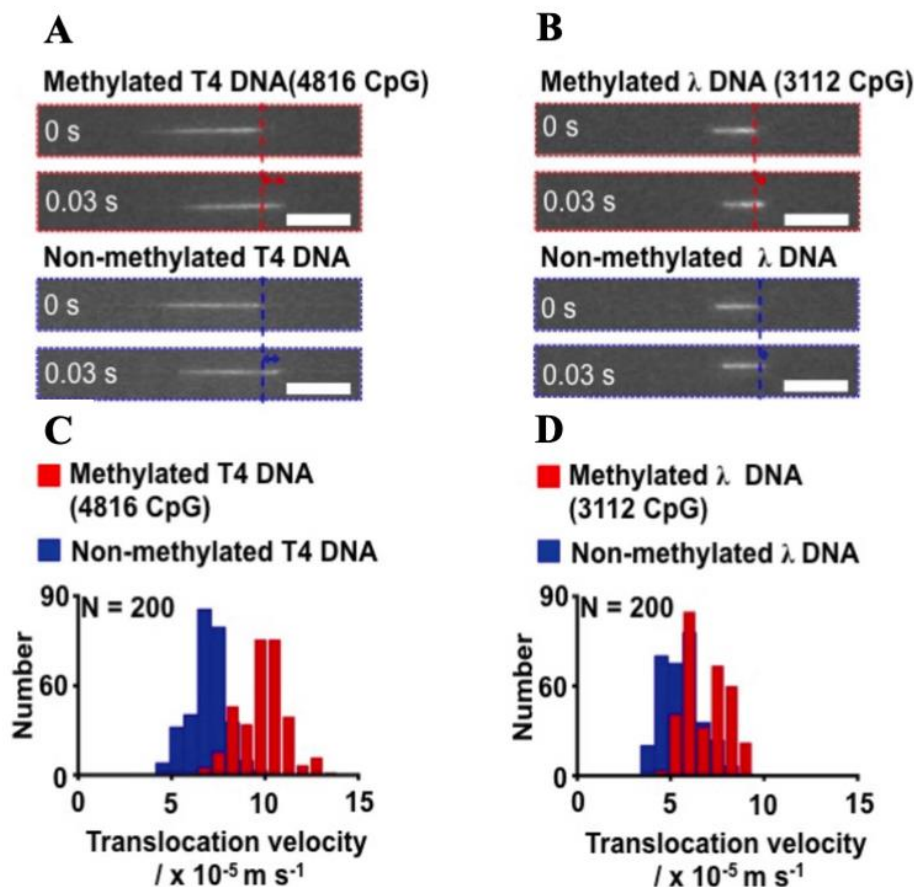


Figure 1.14. The velocity measurement of methylated and non-methylated DNA translocated inside the nanochannel. Arrows show the translocation distance of DNA in 0.03 s. **A)** Fluorescence images of translocation of methylated and non-methylated T4 DNA inside the nanochannel. Scale bars are 10 μm . **B)** translocation of methylated and non-methylated λ DNA. Scale bars are 10 μm . **C, D**)Histogram of translocation velocities of methylated and non-methylated T4 DNA molecules and λ DNA respectively for n=200.

Jia *et al.*⁷⁴ showed separation of deoxynucleotide monophosphates (dNMPs) using a thermoplastic nanofluidic device consisting of two in-plane pores connected with a 500 nm nanochannel fabricated in polyethylene glycol diacrylate (PEGDA) using nanoimprinting lithography (Figure 1.15A) The dNMPs were electrokinetically driven through the nanofluidic device. Translocation of dNMPs through the first nanopore generated a current blockade signal from one pore and then electrokinetically migrated through the nanochannel and entered the other in-plane pore generating another current blockade signal. The time difference between these two signals were taken as the flight time of each dNMP, with each dNMP having a unique flight time. Differences in the flight time of these dNMPs were investigated by varying the carrier electrolyte pH, and the length of the nanochannel. The authors observed better differences in the flight times at pH 10. However, the migration order remained the same at pH 8.3 and 10, which was dTMP < dCMP < dAMP < dGMP. At this pH, they claimed the average identification efficiency of the dNMPs was 55%. When the nanochannel length was increased from 500 nm to 1 μ m, they observed an increase in the average identification accuracy, which was found to be 75%.

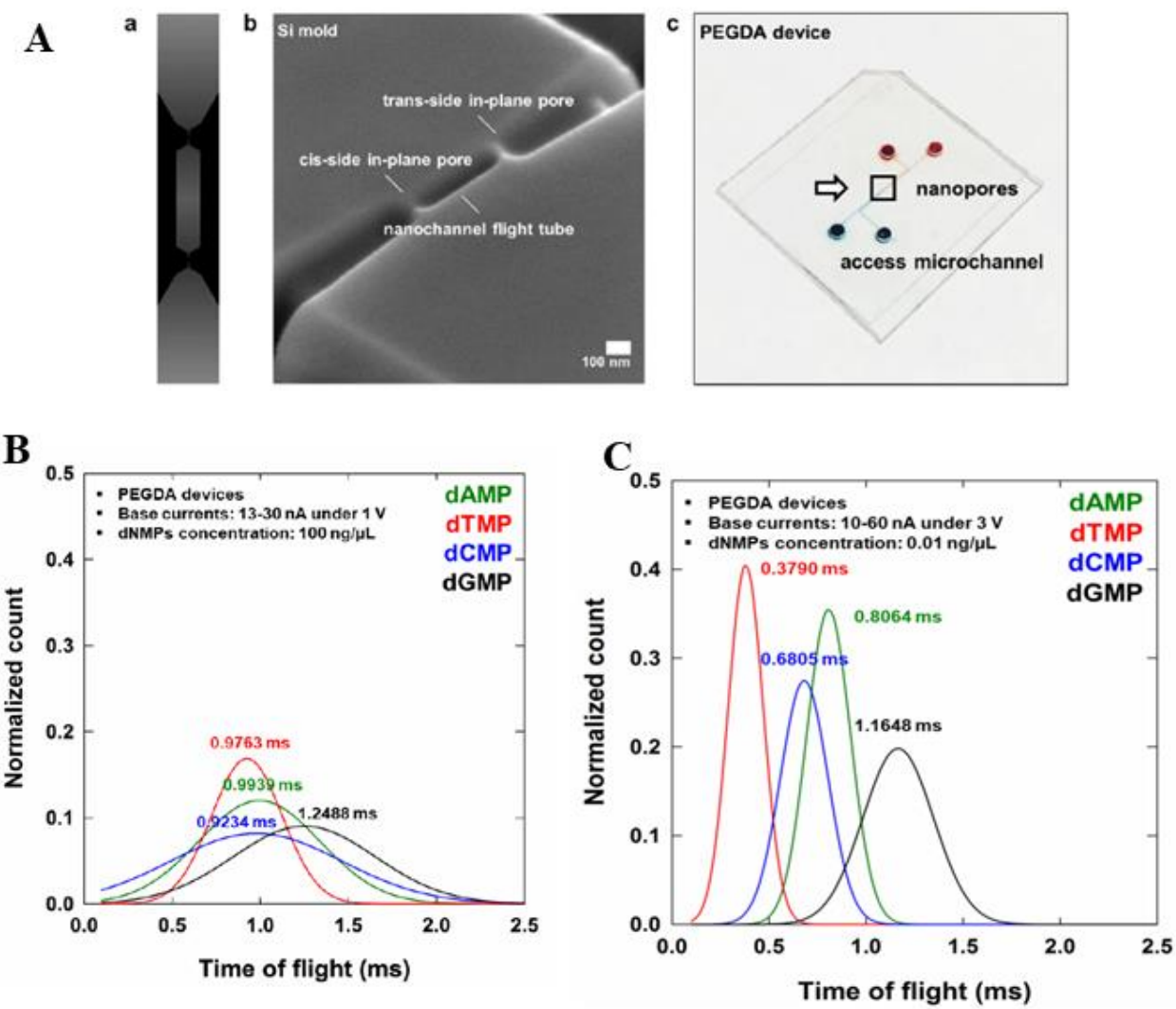


Figure 1.15. **A)** a) Schematic diagram of the dual pore device with a 500 nm length flight tube. b) SEM image of a fabricated dual nanopore device in a Si master. c) Image of a fabricated dual pore device in PEGDA. **B)** Histogram of the time-of-flight for the dNMPs at pH 8.3 in 1 M KCl and 0.5X Tris borate EDTA buffer (TBE). **C)** Histogram of the time-of-flight for the dNMPs at pH 10 in 1 M KCl and 0.5 X TBE.

Even though a majority of separations in the nanoscale are on DNA separations, there are a few efforts on protein separations. Fu *et al.*⁵³ were able to separate a mixture of three SDS protein

complexes based on their molecular weights in a nanofluidic device possessing channels, which were 60 nm in the shallow area and 300 nm in the deep region (Figure 1.10E). Interestingly, the smaller proteins migrated faster, which is opposite to what was previously demonstrated in DNA separation experiments. The resulting separation occurred at a length scale of 570 μm and a time of 30 s. Schoch *et al.*⁸⁸ showed the separation of proteins by utilizing diffusion characteristics of charged molecules in a Si-based nanofluidic device having 50 nm nanochannels. When pH of the solution was changed, the charge of the protein was changed to be either negative or positive ($\text{pH} < \text{pI}$ – positive net charge; $\text{pH} > \text{pI}$ – negative net charge), which is known as the Donnan effect. Using this approach, the authors managed to separate three lectin proteins by varying the pH from 6 to 11; the lectins had the same molecular weight, but different pI values. Electrostatic interactions became significant with increasing surface charges in the nanochannel, thus providing a mechanism for separation based on different diffusion coefficient values.

Kuo *et al.*⁸⁹ proposed a different separation device where vertically stacked microchannels were connected by nano-porous membranes (Figure 1.16A). These membranes were arrays of nanochannels where the transport properties depended on the surface charge density that could be controlled by applying an external voltage. Under normal operation, separation on the main microchannel followed standard electrophoresis principles. The gating voltage could then be timed to allow the transport of a specific analyte through the membrane and to the collection channel. By applying this principle, the authors showed the separation of a mixture of amino acids (Figure 1.16B).

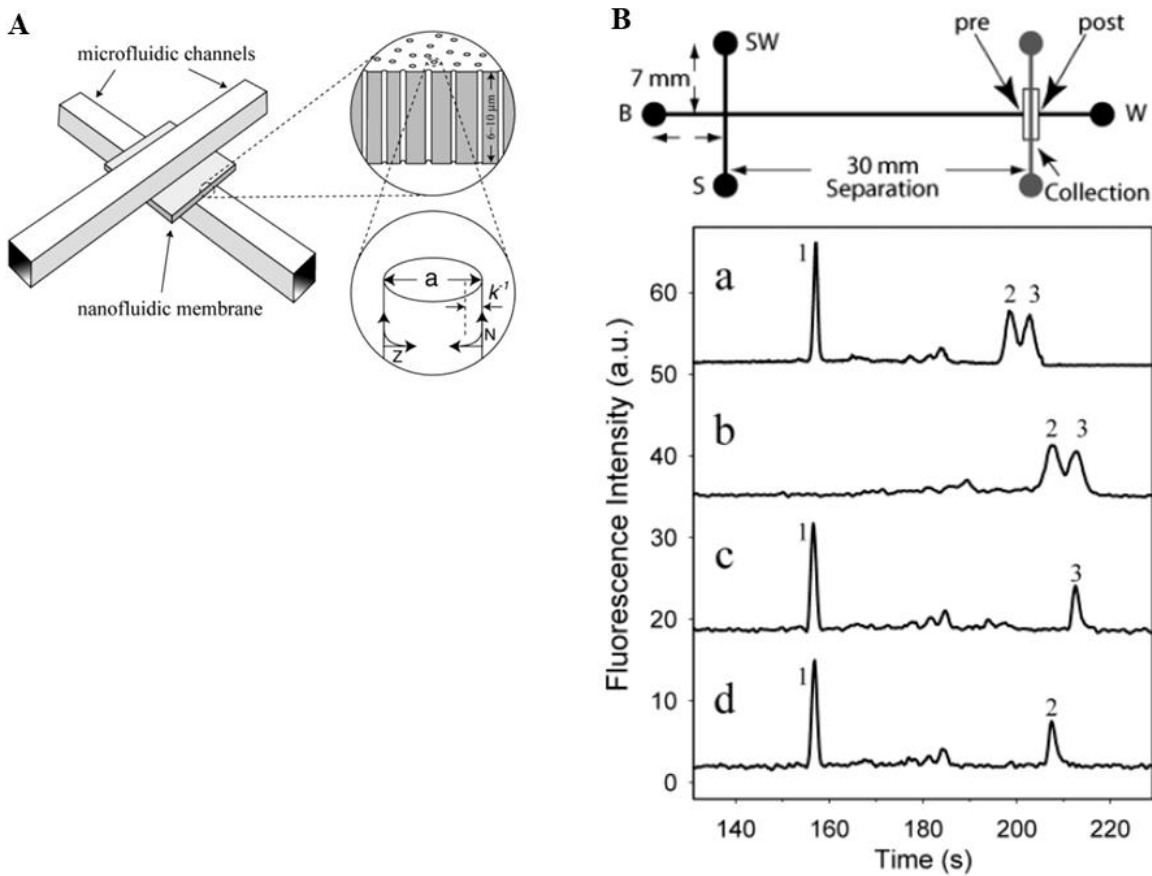


Figure 1.16. **A)** Schematic diagram of the crossed microfluidic channels separated by a nanometer diameter capillary array interconnect. **B)** Separation and selective collection of arginine and glutamate amino acids derivatized with FITC. The electropherogram demonstrated the appearance of three bands without collection (a); collection of glutamate band (b); collection of first arginine band (c); collection of second arginine band (d).

1.5.2 Chromatographic separations of biomolecules in nanofluidic devices

In the nanoscale as a consequence of higher surface-area-to-volume ratios, interfacial forces such as surface tension become dominant over the forces resulting from pressure, inertia and viscosity in microscale. As a result, fluid transport in the nanoscale becomes difficult via pressure driven flow, but easier to utilize EK transport. Conlisk *et al*¹⁶ in 2005, studied about the pressure

drop and applied voltage as a function of the channel height. According to their study, as the height of a nanochannel decreased from 80 nm to 10 nm, at a flow rate of 1 μ L/min, the pressure drop in the nanochannel increased from 0.006 atm to 3 atm (~50,000%), while the voltage drop increased by ~560% from 0.05 V to 0.33 V. At this low flow rate, such a high pressure drop creates practical challenges to utilize pressure driven flows in nanofluidic channels compared to electrokinetic driven flows. Therefore, EOF driven separations are common in the nanoscale. However, there are a few studies involving pressure driven nanoscale chromatographic separations.

Many of the nano-chromatographic separations utilize open nanochannels with coated walls to avoid the limitations that exist from packed columns.⁸⁸ Utilizing open channels has an advantage over packed columns by eliminating the need for a packing material and the process of packing the column. In the absence of a packing material, Eddie diffusion, which reduces the separation efficiency, can be avoided.^{91,92} Tsukahara *et al.*⁹³ developed a pressure driven fluidic control method that can be utilized by nanofluidic systems. They used an air pressure-based fluidic control system and was able to control the flow in a 100 nm channel on a chip within a pressure range of 0.003 – 0.4 MPa, a flow rate of 0.16 – 21.2 pL/min and the residence time of solutions in nanochannel ranged from 24 – 32.4 ms.

Efforts in nano-chromatographic separations were carried out using a bare nano-capillary with a radius of 500 nm and 46 cm in length for the separation of short oligonucleotides ranging between 5 – 20 bp, long DNA molecules ranging from 0.5 – 10 kbp, and DNAs of 75 bp – 20 kbp, all of which were fluorescently labeled.⁹⁴ The authors utilized a three valve system for pressure injection as seen in Figure 1.17A. They were able to obtain baseline separation for DNA in free solution and the separation was affected using nano-capillary chromatography. In a fused silica nano-capillary

with a negatively charged surface, cations were enriched near the wall while anions were concentrated towards the center of the nano-capillary due to electrostatic attractions and repulsion between the ions and charged surface. When the pressure driven flow was introduced to the capillary, the solution at the center flowed faster than the solution closer to the channel wall as the pressure driven flow was generating a parabolic flow profile. Therefore, more negatively charged large DNAs eluted earlier than smaller ones (Figure 1.17B). Moreover, they studied the effect of buffer concentration, capillary radius, and elution pressure on the separation. When the channel radius was increased from 500 nm to 800 nm and then to 1000 nm, they observed poorer separation resolution with larger column radius. Optimal separations were obtained at 50 μM buffer concentration; however, when buffer concentration was high ($>100 \mu\text{M}$) separation resolution decreased.

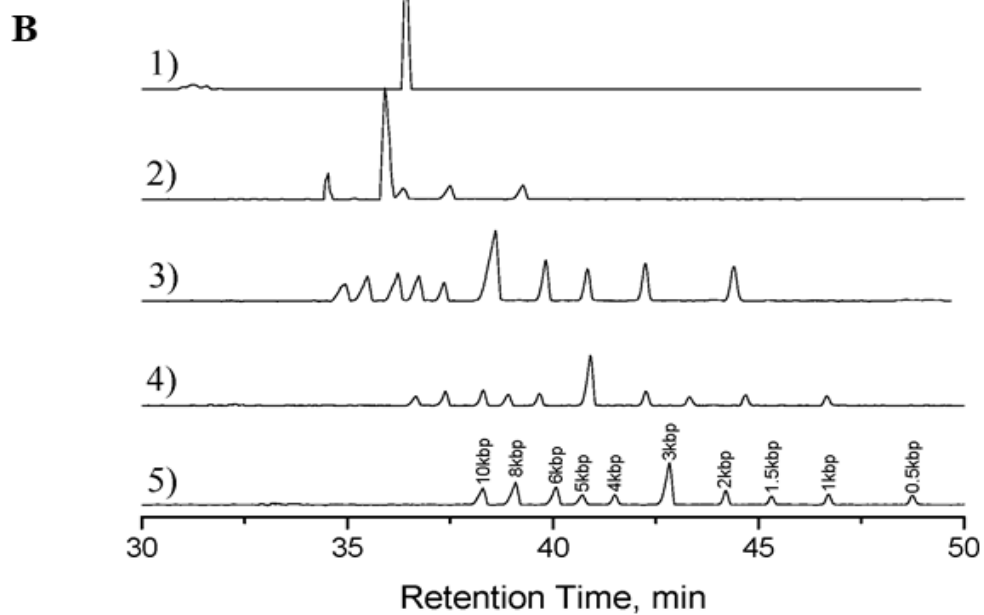
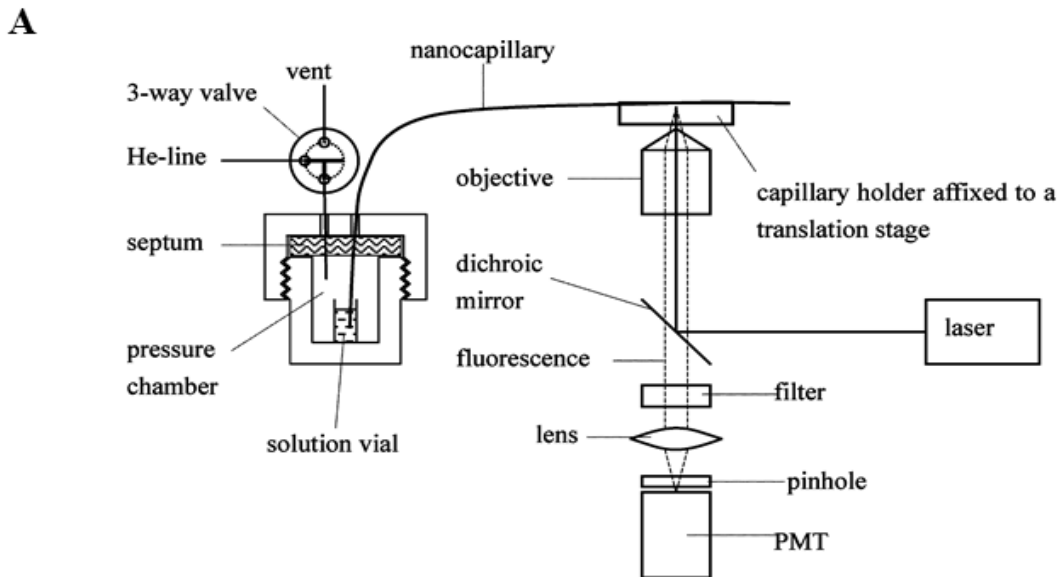


Figure 1.17. **A)** Schematic diagram of the experimental setup for performing pressure-driven nano-capillary chromatography. **B)** Separation results of 5kb – 10 kb DNAs in a nano-capillary with a radius of 500 nm and a total length of 46 cm. The separation traces represent the background TRIS EDTA concentrations of 50 μ M(1), 100 μ M (2), 10 mM (3), 100 mM (4) and 500 mM (5) (reproduced from Wang *et al. Analytical Chemistry*, 2008).

Kitamori *et al.*⁹⁵ introduced a novel chromatographic separation method named femto-liquid chromatography (flc), for the separation of negatively charged dye molecules including fluorescein (-2 charge) and sulforhodamine B (-1 charge) using pressure driven flow. They were able to separate these molecules within 30 s and fluorescein, with a higher negative charge, eluting later than sulforhodamine B, which has less negative charge. They claimed that the EDL thickness in the nanochannel had a significant effect on the velocity of the analyte migrating through the nanochannel. The authors demonstrated that the velocity difference of analytes depended on the ratio of the channel dimensions to the thickness of the EDL (λ_D). When the ratio was too large (large channel size and small λ_D) or too small (small channel size and large λ_D), the charged solutes spread throughout the channel or localized to the channel center due to electrostatic forces resulting in no difference in their velocities.

Modifying the above method, Smirnova *et al.*^{91, 96} developed a reverse-phase chromatographic method for the separation of amino acids in extended nanospace. A fluidic chip consisted of nanochannels fabricated in quartz by EBL and plasma etching. The walls of the nanochannels were modified with a C18 monolayer to obtain the stationary phase. Dimensions of their fluidic channel were 800 nm x 200 nm width and depth with a 2 mm length. Additionally, a longer channel had a length of 10 mm and a depth and width of 470 nm x 2,000 nm, respectively. Figure 1.18A shows an image of the fluidic device they used. LIF was used to detect the signal of fluorescently-labeled amino acids (serine, alanine, proline, and valine). They were successful in separating a 30 aL-labeled amino acid mixture with a high number of theoretical plates, N ($2 - 4 \times 10^3$ plates) and a short separation time (20 s) by using a nanochannel that had been extended to 10 mm in length. The

longer nanochannel showed better separation efficiency compared to the shorter one under the same amount of applied pressure (Figure 1.18B).

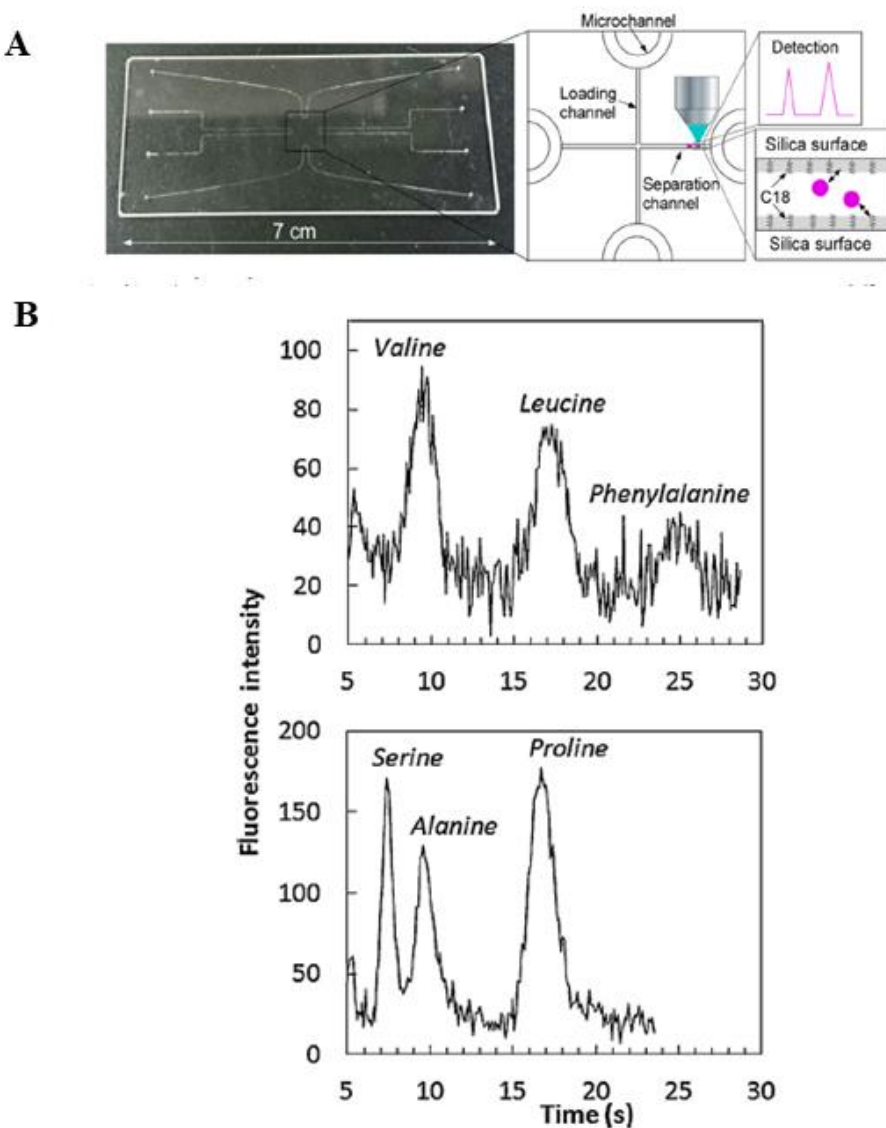


Figure 1.18. **A)** An Image of the microchip and the schematic diagram of the design of the extended nanochannels with 2.2 mm in length. **B)** Chromatograms of the separation of fluorescently labeled amino acids by extended nano-chromatography top -separation of valine, leucine, phenylalanine, serine, alanine, and proline.

leucine and phenylalanine; bottom-serine, alanine and proline (reproduced from Smirnov *et al.* *Journal of Chromatography A*, 2015)

1.6 Overall dissertation outline

A summary of the chapters in this dissertation is presented below.

1.6.1 Chapter 2. Electrokinetic transport behavior of deoxynucleotide monophosphates (dNMPs)through thermoplastic nanochannels.

In this chapter, we report the EK separation of dNMPs through thermoplastic nanochannels. Mixed scale hybrid thermoplastic nanofluidic device was fabricated in PMMA substrate sealed with COC cover plate after oxygen plasma treatment of both substrate and cover plate. In free solution, we were able to separate these four dNMPs with identification accuracies higher than 99.9 % at pH 10.3. The separation resolution was sensitive to background electrolyte pH and ionic strength of background electrolyte. Field dependent apparent mobilities were observed at lower electric field strengths leading to intermittent motions caused by surface heterogeneity, surface roughness effects.

This chapter is based on following manuscript.

O'Neil, C.; Amarasekara, C. A.; Weerakoon-Ratnayake, K. M.; Gross, B.; Jia, Z.; Singh, V.; Park, S.; Soper, S. A., Electrokinetic transport properties of deoxynucleotide monophosphates (dNMPs) through thermoplastic nanochannels. *Analytica Chimica Acta* 2018, 1027, 67-75.

1.6.2 Chapter 3. Open tubular nanoelectrochromatographic separation of single stranded DNA in thermoplastic nanochannels.

Herein we report the free solution separation of single stranded DNA oligonucleotides in thermoplastic nanochannel devices. Mixed scale nanofluidic devices were fabricated using thermal nanoimprinting lithography in PMMA substrates and sealed with COC coverplate. We investigated the effect of surface roughness for the EOF for different PMMA materials. In addition, we explored the use of different materials for the nanofluidic channels and their influence on the separation. We observed length based separation of these ss-DNA oligonucleotides in these nanochannels, where the separation resolution was influenced by the length of nanochannel and the type of material. We introduced the separation mechanism we observe here as nanoelectrochromatography. In agreement with the molecular dynamic studies, the EOF mobility changed with the surface roughness.

1.6.3 Chapter 4. Electrokinetic Separation of Ribonucleotide Monophosphates (rNMPs) in Thermoplastic Nanochannels.

In this chapter, we report the free solution separation of ribonucleotide monophosphates(rNMPs) in thermoplastic nanochannel under optimal working conditions of exoribonuclease 1 enzyme(XRN-1). Mixed scale nanofluidic devices were fabricated using thermal nanoimprinting lithography in NIM-PMMA (non-impact modified PMMA) substrates and sealed with COC 8007 coverplate. Besides PMMA nanodevices we fabricated monolithic COC/COC nanofluidic devices(COC5010 as the substrate and COC8007 as the coverplate). The COC/COC devices were UV/O₃ treated after thermal bonding. Therefore, we investigated the

magnitude of EOF with UV/O₃ dose. We compared the nanoscale separation with free solution microchip electrophoresis. Furthermore, separation is compared in monolithic COC/COC devices and NIM- PMMA/COC devices. Moreover, the effect of pH on the separation is investigated. According to our observations, the separation of rNMPs occurs primarily through electrophoresis in COC/COC devices and NIM-PMMA/COC devices. However, surface interactions also partially contribute for the separation in both of these materials.

1.6.4 Chapter 5. Ongoing developments and Future directions

In this chapter, we present a proposed sequencing scheme involving the use of dual nanopores for sequencing based on the flight times (ToF) of the enzymatically digested nucleotide monophosphates by solid phase bioreactor. These mononucleotides are electrokinetically introduced into a separation nanochannel with two in-plane nanopores. We also describe ongoing work involving the development of the solid phase bioreactor consist of exoribonuclease-1 (XRN-1) tethered to thermoplastic pillars and are developing the fabrication scheme of integrated RNA/DNA sequencing platform that will be utilized for the proof of concept of the proposed method.

1.7 References

1. What is precision medicine. <https://ghr.nlm.nih.gov/primer/precisionmedicine/definition> (accessed 09/15/2019).
2. AL-Dewik, N. I.; Qoronfleh, M. W., Genomics and Precision Medicine: Molecular Diagnostics Innovations Shaping the Future of Healthcare in Qatar. *Advances in Public Health* **2019**, 2019.
3. Ziegler, A.; Koch, A.; Krockenberger, K.; Grosshennig, A., Personalized medicine using DNA biomarkers: a review. *Hum Genet* **2012**, 131 (10), 1627-1638.
4. Roda, A.; Michelini, E.; Caliceti, C.; Guardigli, M.; Mirasoli, M.; Simoni, P., Advanced bioanalytics for precision medicine. *Analytical and Bioanalytical Chemistry* **2018**, 410 (3), 669-677.
5. Sonker, M.; Kim, D.; Egatz-Gomez, A.; Ros, A., Separation Phenomena in Tailored Micro- and Nanofluidic Environments. *Annual Review of Analytical Chemistry* **2019**, 12 (1), 475-500.
6. Haggi, M.; Thurow, K.; Stoll, R., Wearable Devices in Medical Internet of Things: Scientific Research and Commercially Available Devices. *Healthc Inform Res* **2017**, 23 (1), 4-15.
7. Chiu, D. T.; deMello, A. J.; Di Carlo, D.; Doyle, P. S.; Hansen, C.; Maceiczyk, R. M.; Woottton, R. C. R., Small but Perfectly Formed? Successes, Challenges, and Opportunities for Microfluidics in the Chemical and Biological Sciences. *Chem* **2017**, 2 (2), 201-223.
8. Napoli, M.; Eijkel, J. C.; Pennathur, S., Nanofluidic technology for biomolecule applications: a critical review. *Lab on a Chip* **2010**, 10 (8), 957-985.
9. Baldessari, F.; Santiago, J. G., Electrophoresis in nanochannels: brief review and speculation. *Journal of Nanobiotechnology* **2006**, 4 (1), 12.
10. Mawatari, K.; Kazoe, Y.; Shimizu, H.; Pihosh, Y.; Kitamori, T., Extended-nanofluidics: fundamental technologies, unique liquid properties, and application in chemical and bio analysis methods and devices. ACS Publications: 2014.
11. Abgrall, P.; Nguyen, N. T., Nanofluidic devices and their applications. *Analytical chemistry* **2008**, 80 (7), 2326-2341.
12. Eijkel, J. C.; Van Den Berg, A., Nanofluidics: what is it and what can we expect from it? *Microfluidics and Nanofluidics* **2005**, 1 (3), 249-267.
13. Li, Y.; Xu, J.; Li, D., Molecular dynamics simulation of nanoscale liquid flows. *Microfluidics and nanofluidics* **2010**, 9 (6), 1011-1031.
14. Chen, M.; Chen, Y.; Zhong, W.; Yang, J., Molecular dynamics simulation of ion transport in a nanochannel. *Science in China Series E: Technological Sciences* **2008**, 51 (7), 921-931.
15. GAD-EL-HAK, M., The Fluid Mechanics of Micro-devices-The Freeman Scholar Lecture. *ASME Journal of Fluids Engineering* **1999**, 121, 5-33.
16. Conlisk, A. T., The Debye-Hückel approximation: Its use in describing electroosmotic flow in micro-and nanochannels. *Electrophoresis* **2005**, 26 (10), 1896-1912.
17. Wang, X.; Cheng, C.; Wang, S.; Zhao, M.; Dasgupta, P. K.; Liu, S., Nanocapillaries for open tubular chromatographic separations of proteins in femtoliter to picoliter samples. *Analytical chemistry* **2009**, 81 (17), 7428-7435.
18. Xu, Y., Nanofluidics: A New Arena for Materials Science. *Advanced Materials* **2018**, 30 (3), 1702419.

19. Lyklema, J., Fundamentals of interface and colloid science. Volume 2: Solid-liquid interfaces. With special contributions by A. de Keizer, BH Bijsterbosch, GJ Fleer and MA Cohen Stuart. **1995**.
20. Rogers, B.; Adams, J.; Pennathur, S., *Nanotechnology: understanding small systems*. Crc Press: 2014.
21. Chai, J.; Lu, F.; Li, B.; Kwok, D. Y., Wettability interpretation of oxygen plasma modified poly (methyl methacrylate). *Langmuir* **2004**, *20* (25), 10919-10927.
22. Uba, F. I.; Pullagurla, S. R.; Sirasunthorn, N.; Wu, J.; Park, S.; Chantiwas, R.; Cho, Y.-K.; Shin, H.; Soper, S. A., Surface charge, electroosmotic flow and DNA extension in chemically modified thermoplastic nanoslits and nanochannels. *Analyst* **2015**, *140* (1), 113-126.
23. Burgreen, D.; Nakache, F., Electrokinetic flow in ultrafine capillary slits1. *The Journal of Physical Chemistry* **1964**, *68* (5), 1084-1091.
24. Pennathur, S.; Santiago, J. G., Electrokinetic Transport in Nanochannels. 1. Theory. *Analytical Chemistry* **2005**, *77* (21), 6772-6781.
25. Pennathur, S.; Santiago, J. G., Electrokinetic transport in nanochannels. 2. Experiments. *Analytical Chemistry* **2005**, *77* (21), 6782-6789.
26. Reuss, F. F., Sur un nouvel effet de l'électricité galvanique. *Mem. Soc. Imp. Natur. Moscou* **1809**, *2*, 327-337.
27. Wiedemann, G. t., Ueber die Bewegung von Flüssigkeiten im Kreise der geschlossenen galvanischen Säule. *Annalen der Physik* **1852**, *163* (11), 321-352.
28. Helmholtz, H. v., Studies of electric boundary layers. *Wied. Ann* **1879**, *7*, 337-382.
29. Smoluchowski, M., Krak. Anz: 1903.
30. Beale, S. C., Capillary Electrophoresis By Dale R. Baker (Hewlett-Packard, Boulder, CO). Wiley: New York. 1995. xx+ 244 pp. \$49.95. ISBN 0-471-11763-3. ACS Publications: 1996.
31. Jorgenson, J. W.; Lukacs, K. D., Zone electrophoresis in open-tubular glass capillaries. *Analytical Chemistry* **1981**, *53* (8), 1298-1302.
32. Rice, C. L.; Whitehead, R., Electrokinetic flow in a narrow cylindrical capillary. *The Journal of Physical Chemistry* **1965**, *69* (11), 4017-4024.
33. Paul, P.; Garguilo, M.; Rakestraw, D., Imaging of pressure-and electrokinetically driven flows through open capillaries. *Analytical Chemistry* **1998**, *70* (13), 2459-2467.
34. Haywood, D. G.; Harms, Z. D.; Jacobson, S. C., Electroosmotic flow in nanofluidic channels. *Analytical chemistry* **2014**, *86* (22), 11174-11180.
35. Huang, X.; Gordon, M. J.; Zare, R. N., Current-monitoring method for measuring the electroosmotic flow rate in capillary zone electrophoresis. *Analytical chemistry* **1988**, *60* (17), 1837-1838.
36. Menard, L. D.; Ramsey, J. M., Electrokinetically-driven transport of DNA through focused ion beam milled nanofluidic channels. *Analytical chemistry* **2012**, *85* (2), 1146-1153.
37. Peng, R.; Li, D., Electroosmotic flow in single PDMS nanochannels. *Nanoscale* **2016**, *8* (24), 12237-12246.
38. Hu, Y.; Werner, C.; Li, D., Electrokinetic Transport through Rough Microchannels. *Analytical Chemistry* **2003**, *75* (21), 5747-5758.
39. Qiao, R., Effects of molecular level surface roughness on electroosmotic flow. *Microfluidics and Nanofluidics* **2007**, *3* (1), 33-38.
40. Lu, P.; Liu, X.; Zhang, C., Electroosmotic flow in a rough nanochannel with surface roughness characterized by fractal cantor. *Micromachines* **2017**, *8* (6), 190.

41. Kim, D.; Darve, E., Molecular dynamics simulation of electro-osmotic flows in rough wall nanochannels. *Physical Review E* **2006**, 73 (5), 051203.
42. Zhang, C.; Lu, P.; Chen, Y., Molecular dynamics simulation of electroosmotic flow in rough nanochannels. *International Communications in Heat and Mass Transfer* **2014**, 59, 101-105.
43. Qiao, R.; Aluru, N. R., Atomistic simulation of KCl transport in charged silicon nanochannels: Interfacial effects. *Colloids and Surfaces A: Physicochemical and Engineering Aspects* **2005**, 267 (1), 103-109.
44. Weerakoon-Ratnayake, K. M.; Uba, F. I.; Oliver-Calixte, N. J.; Soper, S. A., Electrophoretic separation of single particles using nanoscale thermoplastic columns. *Analytical chemistry* **2016**, 88 (7), 3569-3577.
45. O'Neil, C. E.; Jackson, J. M.; Shim, S.-H.; Soper, S. A., Interrogating surface functional group heterogeneity of activated thermoplastics using super-resolution fluorescence microscopy. *Analytical chemistry* **2016**, 88 (7), 3686-3696.
46. O'Neil, C.; Amarasekara, C. A.; Weerakoon-Ratnayake, K. M.; Gross, B.; Jia, Z.; Singh, V.; Park, S.; Soper, S. A., Electrokinetic transport properties of deoxynucleotide monophosphates (dNMPs) through thermoplastic nanochannels. *Analytica chimica acta* **2018**, 1027, 67-75.
47. Chen, X.; Zhang, L., Review in manufacturing methods of nanochannels of bio-nanofluidic chips. *Sensors and Actuators B: Chemical* **2018**, 254, 648-659.
48. Xia, D.; Yan, J.; Hou, S., Fabrication of Nanofluidic Biochips with Nanochannels for Applications in DNA Analysis. *Small* **2012**, 8 (18), 2787-2801.
49. Gates, B. D.; Xu, Q.; Stewart, M.; Ryan, D.; Willson, C. G.; Whitesides, G. M., New Approaches to Nanofabrication: Molding, Printing, and Other Techniques. *Chemical Reviews* **2005**, 105 (4), 1171-1196.
50. Mailly, D., Nanofabrication techniques. *The European Physical Journal Special Topics* **2009**, 172 (1), 333-342.
51. Ariga, K.; Hill, J. P.; Lee, M. V.; Vinu, A.; Charvet, R.; Acharya, S., Challenges and breakthroughs in recent research on self-assembly. *Science and Technology of Advanced Materials* **2008**, 9 (1), 014109.
52. Biswas, A.; Bayer, I. S.; Biris, A. S.; Wang, T.; Dervishi, E.; Faupel, F., Advances in top-down and bottom-up surface nanofabrication: Techniques, applications & future prospects. *Advances in colloid and interface science* **2012**, 170 (1-2), 2-27.
53. Fu, J.; Mao, P.; Han, J., Nanofilter array chip for fast gel-free biomolecule separation. *Applied Physics Letters* **2005**, 87 (26), 263902.
54. Han, J.; Craighead, H. G., Separation of long DNA molecules in a microfabricated entropic trap array. *Science* **2000**, 288 (5468), 1026-1029.
55. Hamblin, M. N.; Xuan, J.; Maynes, D.; Tolley, H. D.; Belnap, D. M.; Woolley, A. T.; Lee, M. L.; Hawkins, A. R., Selective trapping and concentration of nanoparticles and viruses in dual-height nanofluidic channels. *Lab on a Chip* **2010**, 10 (2), 173-178.
56. Fu, J.; Yoo, J.; Han, J., Molecular sieving in periodic free-energy landscapes created by patterned nanofilter arrays. *Phys Rev Lett* **2006**, 97 (1), 018103-018103.
57. Con, C., Nanolithography on non-planar surfaces and self-assembly of metal salt-polymer nanomaterials. **2016**.
58. Broers, A. N.; Hoole, A. C. F.; Ryan, J. M., Electron beam lithography—Resolution limits. *Microelectronic Engineering* **1996**, 32 (1), 131-142.

59. Menard, L. D.; Ramsey, J. M., Fabrication of Sub-5 nm Nanochannels in Insulating Substrates Using Focused Ion Beam Milling. *Nano Letters* **2011**, *11* (2), 512-517.
60. Tegenfeldt, J. O.; Prinz, C.; Cao, H.; Chou, S.; Reisner, W. W.; Riehn, R.; Wang, Y. M.; Cox, E. C.; Sturm, J. C.; Silberzan, P., The dynamics of genomic-length DNA molecules in 100-nm channels. *Proceedings of the National Academy of Sciences* **2004**, *101* (30), 10979-10983.
61. Cabodi, M.; Turner, S. W.; Craighead, H. G., Entropic recoil separation of long DNA molecules. *Analytical chemistry* **2002**, *74* (20), 5169-5174.
62. Tang, M.; Chen, Z. C.; Huang, Z. Q.; Choo, Y. S.; Hong, M. H., Maskless multiple-beam laser lithography for large-area nanostructure/microstructure fabrication. *Appl. Opt.* **2011**, *50* (35), 6536-6542.
63. Pease, R. F.; Chou, S. Y., Lithography and other patterning techniques for future electronics. *Proceedings of the IEEE* **2008**, *96* (2), 248-270.
64. Pimpin, A.; Srituravanich, W., Review on micro-and nanolithography techniques and their applications. *Engineering Journal* **2012**, *16* (1), 37-56.
65. Chantiwas, R.; Park, S.; Soper, S. A.; Kim, B. C.; Takayama, S.; Sunkara, V.; Hwang, H.; Cho, Y.-K., Flexible fabrication and applications of polymer nanochannels and nanoslits. *Chemical Society Reviews* **2011**, *40* (7), 3677-3702.
66. Uba, F. I.; Hu, B.; Weerakoon-Ratnayake, K.; Oliver-Calixte, N.; Soper, S. A., High process yield rates of thermoplastic nanofluidic devices using a hybrid thermal assembly technique. *Lab on a Chip* **2015**, *15* (4), 1038-1049.
67. Soper, S. A.; Mattingly, Q. L.; Vegunta, P., Photon burst detection of single near-infrared fluorescent molecules. *Analytical Chemistry* **1993**, *65* (6), 740-747.
68. Kovarik, M. L.; Jacobson, S. C., Nanofluidics in lab-on-a-chip devices. ACS Publications: 2009.
69. Dittrich, P. S.; Manz, A., Single-molecule fluorescence detection in microfluidic channels—the Holy Grail in μTAS? *Analytical and Bioanalytical Chemistry* **2005**, *382* (8), 1771-1782.
70. Pennathur, S.; Baldessari, F.; Santiago, J. G.; Kattah, M. G.; Steinman, J. B.; Utz, P. J., Free-solution oligonucleotide separation in nanoscale channels. *Analytical chemistry* **2007**, *79* (21), 8316-8322.
71. Uba, F., Development of Nanofluidic Devices for Single-Molecule DNA Diagnostics. **2014**.
72. Cipriany, B. R.; Zhao, R.; Murphy, P. J.; Levy, S. L.; Tan, C. P.; Craighead, H. G.; Soloway, P. D., Single molecule epigenetic analysis in a nanofluidic channel. *Analytical chemistry* **2010**, *82* (6), 2480-2487.
73. Schneider, G. F.; Dekker, C., DNA sequencing with nanopores. *Nature biotechnology* **2012**, *30* (4), 326.
74. Jia, Z., Development of Polymer-Based In-Plane Nanopore for DNA Sequencing. **2018**.
75. Kitamori, T.; Tokeshi, M.; Hibara, A.; Sato, K., Peer Reviewed: Thermal Lens Microscopy and Microchip Chemistry. *Analytical Chemistry* **2004**, *76* (3), 52 A-60 A.
76. Shimizu, H.; Mawatari, K.; Kitamori, T., Sensitive determination of concentration of nonfluorescent species in an extended-nano channel by differential interference contrast thermal lens microscope. *Analytical chemistry* **2010**, *82* (17), 7479-7484.

77. Shimizu, H.; Miyawaki, N.; Asano, Y.; Mawatari, K.; Kitamori, T., Thermo-optical Characterization of Photothermal Optical Phase Shift Detection in Extended-Nano Channels and UV Detection of Biomolecules. *Analytical chemistry* **2017**, 89 (11), 6043-6049.
78. McDonell, M. W.; Simon, M. N.; Studier, F. W., Analysis of restriction fragments of T7 DNA and determination of molecular weights by electrophoresis in neutral and alkaline gels. *Journal of molecular biology* **1977**, 110 (1), 119-146.
79. Viovy, J.-L., Electrophoresis of DNA and other polyelectrolytes: Physical mechanisms. *Reviews of Modern Physics* **2000**, 72 (3), 813.
80. Ishibashi, R.; Mawatari, K.; Kitamori, T., Highly Efficient and Ultra-small Volume Separation by Pressure-Driven Liquid Chromatography in Extended Nanochannels. *Small* **2012**, 8 (8), 1237-1242.
81. Yuan, Z.; Garcia, A. L.; Lopez, G. P.; Petsev, D. N., Electrokinetic transport and separations in fluidic nanochannels. *Electrophoresis* **2007**, 28 (4), 595-610.
82. Ajdari, A.; Bontoux, N.; Stone, H. A., Hydrodynamic dispersion in shallow microchannels: the effect of cross-sectional shape. *Analytical Chemistry* **2006**, 78 (2), 387-392.
83. Han, J.; Turner, S.; Craighead, H. G., Entropic trapping and escape of long DNA molecules at submicron size constriction. *Phys Rev Lett* **1999**, 83 (8), 1688.
84. Fu, J.; Schoch, R. B.; Stevens, A. L.; Tannenbaum, S. R.; Han, J., A patterned anisotropic nanofluidic sieving structure for continuous-flow separation of DNA and proteins. *Nature Nanotechnology* **2007**, 2 (2), 121-128.
85. Cross, J. D.; Strychalski, E. A.; Craighead, H., Size-dependent DNA mobility in nanochannels. *Journal of Applied Physics* **2007**, 102 (2), 024701.
86. Huber, D. E.; Markel, M. L.; Pennathur, S.; Patel, K. D., Oligonucleotide hybridization and free-solution electrokinetic separation in a nanofluidic device. *Lab on a Chip* **2009**, 9 (20), 2933-2940.
87. Sun, X.; Yasui, T.; Yanagida, T.; Kaji, N.; Rahong, S.; Kanai, M.; Nagashima, K.; Kawai, T.; Baba, Y., Effect of DNA Methylation on the Velocity of DNA Translocation through a Nanochannel. *Analytical Sciences* **2017**, 33 (6), 727-730.
88. Schoch, R. B.; Bertsch, A.; Renaud, P., pH-controlled diffusion of proteins with different pI values across a nanochannel on a chip. *Nano letters* **2006**, 6 (3), 543-547.
89. Kuo, T.-C.; Cannon, D. M.; Chen, Y.; Tulock, J. J.; Shannon, M. A.; Sweedler, J. V.; Bohn, P. W., Gateable nanofluidic interconnects for multilayered microfluidic separation systems. *Analytical Chemistry* **2003**, 75 (8), 1861-1867.
90. Ishibashi, R.; Mawatari, K.; Kitamori, T., Highly Efficient and Ultra-small Volume Separation by Pressure-Driven Liquid Chromatography in Extended Nanochannels. *Small* **2012**, 8 (8), 1237-1242.
91. Smirnova, A.; Shimizu, H.; Mawatari, K.; Kitamori, T., Reversed-phase Chromatography in an Extended Nanospace: Separating Amino Acids in Short and Long Nanochannels. *Analytical Sciences* **2015**, 31 (11), 1201-1204.
92. Shimizu, H.; Morikawa, K.; Liu, Y.; Smirnova, A.; Mawatari, K.; Kitamori, T., Femtoliter high-performance liquid chromatography using extended-nano channels. *Analyst* **2016**, 141 (21), 6068-6072.
93. Tsukahara, T.; Mawatari, K.; Hibara, A.; Kitamori, T., Development of a pressure-driven nanofluidic control system and its application to an enzymatic reaction. *Analytical and bioanalytical chemistry* **2008**, 391 (8), 2745-2752.

94. Wang, X.; Wang, S.; Veerappan, V.; Byun, C. K.; Nguyen, H.; Gendhar, B.; Allen, R. D.; Liu, S., Bare nanocapillary for DNA separation and genotyping analysis in gel-free solutions without application of external electric field. *Analytical chemistry* **2008**, *80* (14), 5583-5589.
95. Kato, M.; Inaba, M.; Tsukahara, T.; Mawatari, K.; Hibara, A.; Kitamori, T., Femto liquid chromatography with attoliter sample separation in the extended nanospace channel. *Analytical chemistry* **2009**, *82* (2), 543-547.
96. Smirnova, A.; Shimizu, H.; Mawatari, K.; Kitamori, T., Reversed-phase chromatography in extended-nano space for the separation of amino acids. *Journal of Chromatography A* **2015**, *1418*, 224-227.

**Chapter2. Electrokinetic Transport Properties of Deoxynucleotide Monophosphates
(dNMPs) through Thermoplastic Nanochannels**

This chapter is based on the following manuscript

O'Neil, C.; Amarasekara, C. A.; Weerakoon-Ratnayake, K. M.; Gross, B.; Jia, Z.; Singh, V.; Park, S.; Soper, S. A., Electrokinetic transport properties of deoxynucleotide monophosphates (dNMPs) through thermoplastic nanochannels. *Analytica Chimica Acta* 2018, 1027, 67-75.

2.1 Introduction

Electrokinetic transport of molecules in nanochannels is influenced by several physical parameters unique to the nanoscale such as electric double layer (EDL) overlap and the high surface-to-volume ratio of nanochannels. In particular, surface mediated effects can affect the electrokinetic transport properties of charged molecules through nanochannels that is not observable in microchannels, such as surface roughness. Also, partial overlap in the EDL can occur in nanochannels. The EDL thickness (λ_d), is defined by;

$$\lambda_d = \sqrt{\frac{\epsilon_0 \epsilon_r R T}{2 F^2 c}} \quad (2.1)$$

where R is the gas constant, ϵ_r is the dielectric constant of the medium, F is the Faraday constant, T is the temperature, and c is the concentration of the electrolyte solution ¹⁻⁵. As λ_d approaches the channel dimensions, EDL overlap can occur, which introduces a parabolic flow profile rather than the classically observed plug-like flow typically seen in microscale channels creating interesting transport properties ⁴⁻⁶. For example, it has been shown that double stranded DNA (dsDNA) fragments have different mobilities in nanochannels in the absence of a sieving medium when the channel dimensions are on the order of λ_d ⁴. By comparison, dsDNA has the same mobility irrespective of their size in microscale channels.

The increased surface area-to-volume ratio in nanoscale channels allows for solute/wall interactions that can influence electrokinetic transport as well. Potential interactions of solutes with walls include intermittent motion, which can cause mobilities that are electric field strength

dependent, and is produced by surface roughness ⁷⁻⁹. These intermittent motions can be induced by dielectrophoretic trapping generated by surface roughness on the nanoscale producing an inhomogeneous electrical field. Additional wall effects include molecular retardation, friction, and relaxation forces ⁷. Viscous retardation forces depend on the solute's radius and Debye length and arise from solute interactions with a non-conducting boundary ¹⁰. Frictional forces are those arising from drag between the direction of bulk fluid flow and the channel wall. The relaxation effects, or EDL distortions, arise from a greater charge density behind the solute compared to the front as the ions comprising the EDL "lag" as the solute is transported through the nanochannel ^{11, 12}.

Another phenomenon that can be observed in nanochannels is adsorption/desorption events between the solute and wall, which can be more prevalent in nanochannels compared to microchannels due to scaling effects (*i.e.*, smaller diffusional distances in the case of nanochannels). Electrostatic, van der Waals, and hydration interactions between molecules and channel walls contributes to the interactions of molecules with channel walls that will affect the transport properties of the molecules. Depending on the magnitude of the interaction, adsorption events can be classified as reversible or irreversible. In a computational study by Moldovan and coworkers, the adsorption/desorption behavior of deoxynucleotide monophosphates (dNMPs) traveling through polymer nanochannels was found to depend on the hydrophobicity of the dNMPs ¹³⁻¹⁵.

The electrokinetic transport of silver nanoparticles (AgNPs) through poly(methylmethacrylate), PMMA, nanoslits (only one dimension in the nanoscale) was shown recently ⁷. The authors were able to demonstrate size-dependent mobilities of AgNPs in buffer only, which was not possible using microscale columns. Optimal differences in the mobilities were

observed for 60 and 100 nm AgNPs at high electric field strengths, where no intermittent motion was evident. O’Neil *et al.* showed differences in the electromigration of 20 nm polystyrene (PS) beads traveling through PMMA nanoslits at varying electric field strengths⁸. At low electric field strengths (200 V/cm), the PS beads showed intermittent transport properties resulting in field-dependent apparent mobilities and high dispersion in the mobilities, a result of this intermittent motion. Further, the standard deviations in the mobilities in general were found to be higher at lower electric field strengths due to flow recirculation that resulted from non-uniform surface charges when using thermoplastic nanochannels⁸. In both cases, the apparent mobilities were found to be electric field dependent until a “critical” field strength was reached at which point, the apparent mobilities were electric field independent as classically seen in microchannels.

Due to the unique transport properties offered by nanochannels, we sought to explore the electrokinetic transport behavior of dNMPs through polymer nanochannels. To undertake this, we used fluorescence tracking of the dNMPs by labeling the dNMPs with a common reporter such that the transport properties could be associated with differences in the chemical properties of the dNMPs only. The ability to efficiently identify dNMPs for applications such as single-molecule sequencing (SMS).

One approach for SMS is nanopore sequencing, which uses naturally occurring pores such as α -hemolysin¹⁶. For nanopore sequencing, an intact DNA molecule is electrically transported through the pore and produces a characteristic modulation of ionic current through which the nucleotides can be identified¹⁷. However, base calling accuracy is ~80% for several reasons, including the fact that 10-15 nucleotides are resident within the nanopore at any one time¹⁸⁻²¹.

An alternative approach for SMS involves disassembling an intact DNA molecule into its discrete monomer units (*i.e.*, mononucleotides or dNMPs) using an exonuclease immobilized at the inlet of the nanopore, which addresses the issue of multiple nucleotide occupancy within a single pore²². A challenge with this approach is that each nucleotide is still identified using the amplitude of a current blockage event only and thus, generates high error rates.

To address these issues, we are developing an innovative SMS strategy that enzymatically cleaves DNAs using a surface-immobilized processive exonuclease to generate the dNMPs²³⁻²⁵. The released dNMPs are electrokinetically transported through a nanochannel and identification of the nucleobases is carried out using the unique apparent mobility (*i.e.*, mobility matching) of each dNMP electrokinetically traveling through a nanochannel. Thus, a thorough understanding of the electrokinetic properties of dNMPs through nanochannels along with parameters that affect separation resolution between the dNMP apparent mobilities, which is correlated to the base call accuracy, will be required to realize this SMS approach. We investigated various experimental parameters that may differentially affect the electrokinetic transport properties of the dNMPs, such as electrolyte pH and λ_D values as well as the electric field strength to optimize the ability to identify dNMPs based on their apparent mobilities. To thoroughly understand the electrokinetic properties of the dNMPs, fluorescence detection was used by labeling each dNMP with the same fluorescence reporter (ATTO 532) and thus, any differences in the mobilities resulted from the dNMP.

2.2 Materials and Method

2.2.1 Reagents and materials.

Silicon <100> (Si) wafers were purchased from University Wafers (Boston, MA). Poly(methylmethacrylate), PMMA, substrates and cover plates were purchased from Good Fellow (Berwyn, PA) and cyclic olefin copolymer (COC 8007 and 6017) was purchased from TOPAS Advanced Polymers (Florence, KY). An anti-adhesion monolayer of (Tridecafluoro-1,1,2,2-tetrahydrooctyl) Tricholorosilane (T-Silane) was purchased from Gelest, Inc. (Morrisville, PA). Tripropylene glycol diacrylate (TPGA), trimethylolpropane triacrylate (TMPA), Irgacure 651 (photo-initiator), 1-ethyl-3-[dimethylaminopropyl] carbodimide hydrochloride (EDC), thymidine 5'-monophosphate disodium salt, 5-methylcytosine monophosphate disodium salt, cytidine 5'-monophosphate disodium salt, adenosine 5'- monophosphate disodium salt and guanosine 5'-monophosphate disodium salt, triethylammonium acetate (TEAA), (4-(2-hydroxyethyl)-1-piperazineethanesulfonic acid, 2-amino-2-methyl-1-propanol (AMP), and methanol (MeOH) were purchased from Sigma-Aldrich (St. Louis, MO). Tris-borate buffer and sodium hydroxide (NaOH) was obtained from Fisher Scientific (Houston, TX). ATTO 532 dye was purchased from Atto-Tec (Siegen, Germany). All required dilutions were performed using 18 MΩ/cm MilliQ water (Millipore technologies) and all measurements were performed at 25 °C unless specified otherwise.

2.2.2 Fluorescent labeling of dNMPs.

Since fluorescence is used as the detection method, it is necessary to label the dNMPs with a fluorescent dye reporter. This was done through a modification of method described by Cornelius et al. 1mM dNMP solutions, 300 mM EDC and 100mM ATTO532 were prepared in 100mM HEPES ((4-(2-hydroxyethyl)-1-piperazineethanesulfonic acid) buffer at pH 6.5 100 μ L of each dNMPs were mixed with 100 μ L of EDC and 100 μ L of ATTO532 dye. These reaction mixtures were allowed to react overnight in dark while shaking at 37°C. Then separation of dye labeled dNMPs and free dye was done by HPLC purification. Jasco HPLC with Jasco FP-2020 fluorescence detection system was used with a ODS Hypersil RP18 prep column (10 mm ID, 150 mm length and particle size 5 μ m). Gradient separation was done using 0-35% acetonitrile (1% per min) in 0.1 M triethylammonium acetate (TEAA), pH 7 at a flow rate of 5 mL/min. Collected fractions were then concentrated using and Eppendorf concentrator 5301 at 30°C with vacuum for 24 h. Finally, the concentrated samples were confirmed with ESI-MS by NanoMate Quattro ii mass spectrometer. All samples were stored at -20°C until required for use.

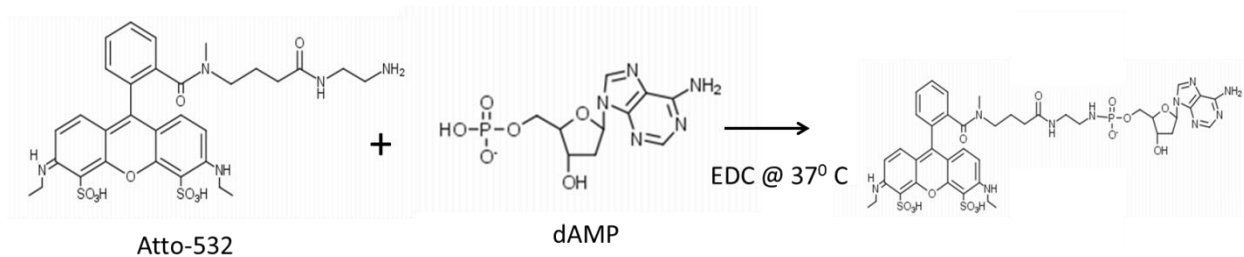


Figure 2.1: Reaction scheme showing the conjugation of ATTO 532 to adenosine monophosphate, dAMP. 100 μ L of each dNMP (1 mM in 100 mM HEPES pH 6.5) was mixed with 100 μ L EDC (300 mM in 100 mM HEPES) and 100 μ L of ATTO 532 (25 mM in 100 mM HEPES) and reacted overnight while shaking at 37°C.

2.2.3 Fabrication of nanochannel devices

Fabrication of thermoplastic nanochannel devices were done according to a method described by our group. Initially patterning of the two access mirochannels (55 μm wide, 12 μm deep, 1.5 cm long) through standard photolithography followed by wet etching with 45% KOH. Then 110 nm x100 nm (depth and width respectively) nanochannels were milled by focused ion beam (FIB) milling. (Helios NanoLab 600 dual beam instrument-FEI, Hillsboro, OR)). Then anti adhesion monolayer of (Tridecafluoro-1,1,2,2-Tetrahydrooctyl) Tricholrosilane was applied on to the Si master with nanochannels. After that resin stamp was made using UV-curable polymeric blend consist of 68 wt% TPGA (tripropylene glycol diacrylate) as the base, 28% TMPA(Trimethyl propane diacrylate) as crosslinking agent and Irgacure 651 as the photoinitiator. This UV curable resin was then sandwiched between COC6017 plate and Si master and UV cured by exposing to 365 nm UV lamp (10 J/m^2) for 7 minutes in ultraviolet crosslinker (UVP, LLC, Upland, CA). Next the cured resin stamp was demolded carefully from Si master and thermal imprinting was done via nanoimprinting lithography (NIL) at a pressure of 2888 kN/m^2 for 120 s into 1.5 mm thick PMMA sheet. During the process of imprinting the temperature of top and bottom plates of Hex03, thermal imprinter was maintained at 95 °C. Once temperature reached to this set temperature, the set pressure was applied and maintained during the entire process of imprinting until the system was cooled down to 45 °C. Then sealing of the devices were done by using 100 μm thick COC8007 coverplate. Before sealing, both coverplate and imprinted device were exposed to oxygen plasma at a 50 mW for 1 minute to generate highest possible carboxylic acid groups and sealed with same NIL imprinter by applying a pressure of 977 kN/m^2 at 70 °C for 900 s as explained by *Uba et al.*

SEM images of the Si master, resin stamp, and imprinted thermoplastic device can be seen in Figure 2.2.

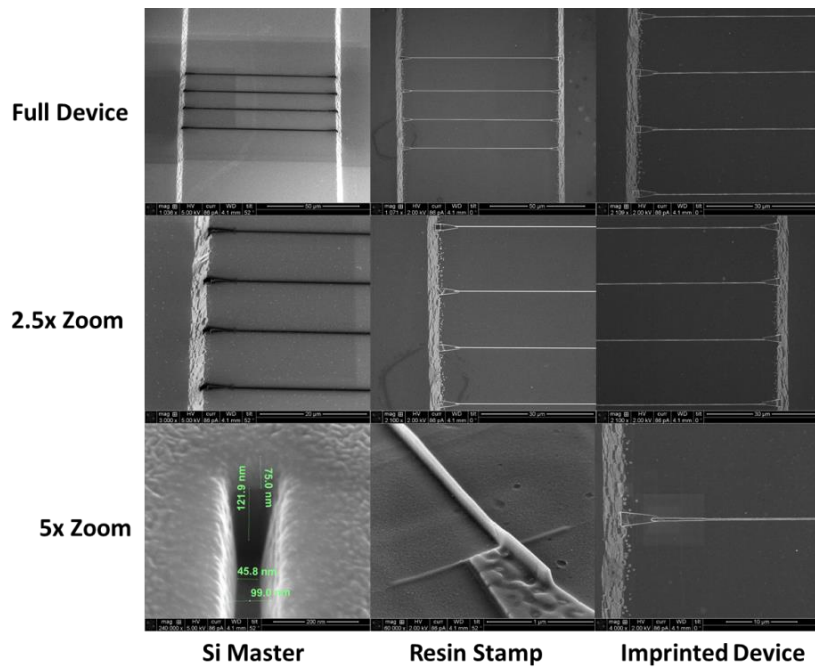


Figure 2.2: SEM images showing the Si master (left panels), resin stamp (middle panels) and imprinted PMA device (right panel) used for the nanochannel electrophoresis experiments.

2.2.4 Imaging system for nanoelectrokinetic separation experiment

All fluorescence imaging was performed using an Axiovert 35 inverted microscope (Carl Zeiss AG, Oberkochen, Germany) equipped with a 100× oil immersion objective (NA 1.3). A Gaussian laser beam (Nd:YAG; $\lambda_{\text{ex}} = 532 \text{ nm}$; $P = 0.01\text{-}5 \text{ W}$; 2.2 mm beam diameter) was expanded with a 10X Keplerian beam expander to completely back-fill the objective and the wings were knocked out with an iris to ensure uniform laser intensity in the microscope's field-of-view. The beam was focused using a lens into the back of a microscope objective to allow irradiation of the entire field-

of-view and passed through a 532 nm laser line filter and dichroic filter. The emission signal was collected by the objective, passed through a dichroic filter, spectrally selected using longpass and bandpass filters, and imaged onto an iXon3 897 EMCCD camera (Andor Technology Ltd., Belfast, United Kingdom) (see Figure 2.3)

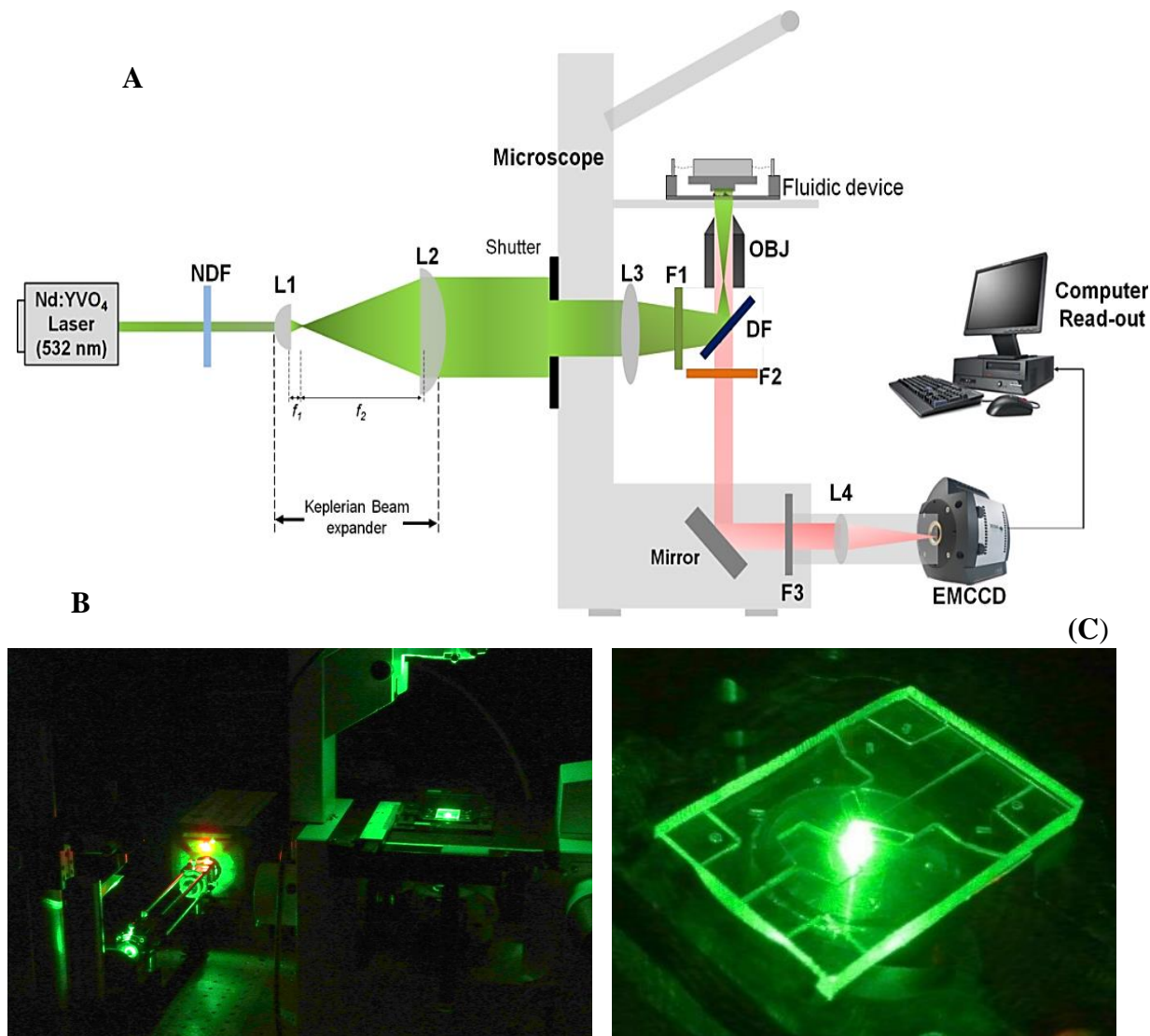


Figure 2.3: A) Optical set-up of the fluorescence imaging system. The Gaussian beam from the laser (Nd:YAG; $\lambda_{\text{ex}} = 532 \text{ nm}$; $P = 0.01\text{-}5 \text{ W}$; 2.2 mm beam diameter) was expanded 10x using a Keplerian beam expander and the wings were knocked out with an iris that ensured uniform laser intensity in the field-of-view and complete back-filling of the objective (OBJ). The beam was focused into the back of a 100x oil immersion objective lens (OBJ) using lens (L3) after passing through a 532 nm laser line filter (F1) and reflected by a dichroic filter (DF). A collimated laser beam impinged upon the polymer nanofluidic device. The fluorescence signal was collected by the same objective, passed through the DF and spectrally selected using a longpass filter (F2). A mirror was used to steer the fluorescence signal onto the EMCCD after passing through a bandpass filter (F3) and focused using a lens (L4)⁸. B) Photograph of the laser excitation system shown in A). C) Photograph of the nanofluidic chip sitting atop the microscope objective and illuminated with the 532 nm laser.

2.2.5 Nanochannel electrokinetic transport properties of ATTO 532-labeled dNMPs

Assembled nanochannel devices were activated using $21.85 \text{ mW/cm}^2 \text{ UV/O}_3$ through a $100 \mu\text{m}$ COC cover plate for 15 min. After activation, chips were primed using 50 % MeOH for 5 min. The MeOH was evacuated from the nanofluidic device and it was then filled with 50 mM Tris-Borate (TB) buffer at the desired pH and allowed to equilibrate for 10 min. ATTO 532-labeled dNMPs samples (200 nM) were prepared in the carrier electrolyte and introduction of the sample was done by removing the priming carrier electrolyte from the reservoir on chip and filled with the dNMP solution. The carrier electrolyte was then removed from the opposite reservoir to allow for pressure injection of dye-labeled dNMP solution into the access microchannels. Once the access microchannels were filled, all reservoirs were filled with equal volumes of the carrier electrolyte. Electrodes were placed in opposite access reservoirs to allow a drive voltage to drop across the nanochannels. A square wave voltage (V_{pp}) was applied using an ATTEN ATF20B function waveform generator for a period of 5 s to allow for injection of the dye-labeled dNMPs into the nanochannel. Events were recorded for 5,000 frames allowing multiple events to be analyzed.

2.2.5 Nanochannel electrokinetic separation data analysis

Fiji (a version of ImageJ) software²⁶ was used to analyze the nanochannel electrokinetic separation data. Videos of events were imported into Fiji and $1 \mu\text{m}^2$ “detection windows” were placed at the entrance and exit of the nanochannel. In the Fiji software, these detection windows recorded the fluorescence intensity over time. This data was exported into Origin 8.5 and the first derivative was taken of each data set to produce two peaks indicating the time at both the entrance

and exit of the nanochannel. The time between peak 1 and peak 2 was assigned a Δt value for each dNMP and the apparent mobility of the dye and dye-labeled dNMPs could be determined from Δt , the applied voltage (V) and the distance between the input point and output points of the column. (see Figure 2.4)

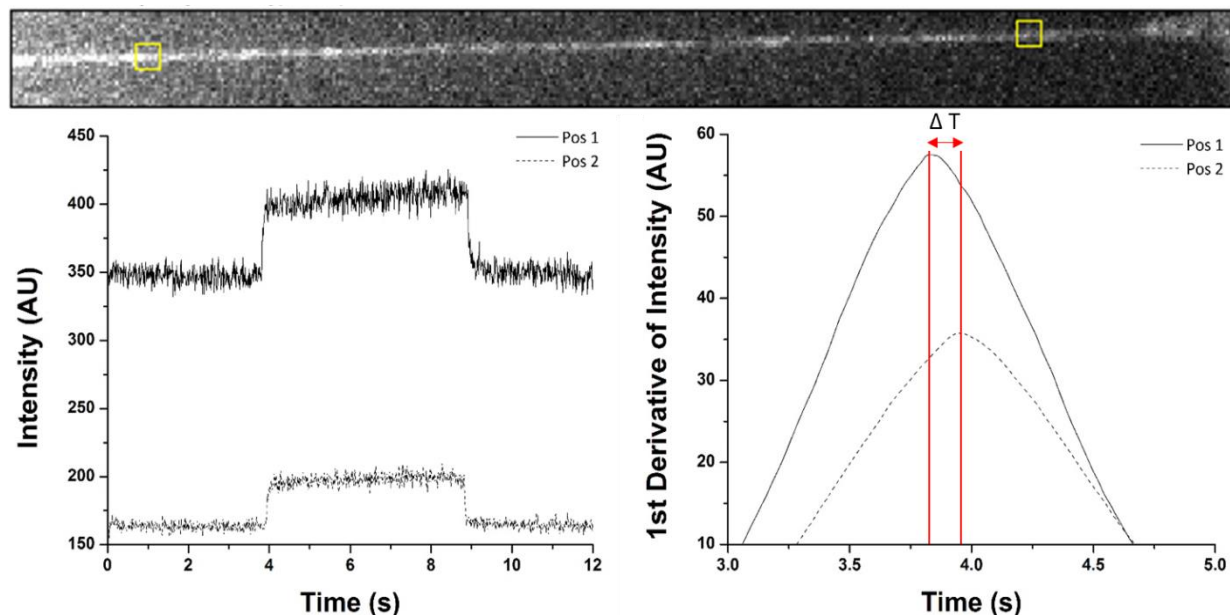


Figure 2.4. Depiction of how the nanochannel electrokinetics and data analysis were performed. The top panel shows a fluorescently labeled dNMP being electrokinetically transported through a nanochannel with the yellow boxes indicating Position (Pos) 1 and 2. The bottom left panel shows the fluorescence intensity profile of one injection event at POS 1 and 2. The bottom right panel shows the first derivative of the intensity profile to determine the time required for each dNMP to migrate from Pos 1 to Pos 2.

2.3 Results and discussion

Theory and experimental studies for the electrokinetic transport of charged molecules through nanoslits has appeared in recent reviews^{1, 27, 28}. For ion transport with d/λ_D ratios (d = channel width/depth) ranging from 1-10, anomalous transport behavior has been observed, such as charge-dependent ion speeds due to transverse electromigration resulting from solute/wall electrostatic

effects^{4, 6, 29, 30}. Pennathur and Santiago determined that electrokinetic transport in nanoslits made from glass was dependent on ion valence, ζ (zeta potential), ion mobility, and λ_D ^{4, 6}. For example, Garcia *et al.* illustrated the electrokinetic transport of the fluorescent dyes Alexa 488 (negatively charged) and rhodamine B (neutral) in Si nanoslits of various depths ranging from 35 to 200 nm³. The apparent mobilities of the dyes were dependent on their charge and extent of interaction(s) with channel walls.

Here, we explored the use of nanochannels (2 dimensions in the nanometer domain), specifically thermoplastic nanochannels, as opposed to nanoslits (only 1 dimension within the nanometer domain) on the electrokinetic transport properties of fluorescently labeled dNMPs. We also investigated how the carrier electrolyte composition would affect the transport properties of the four naturally occurring nucleotide monophosphates, dGMP, dAMP, dCMP, and dTMP, and the methylated cytosine (mdCMP) residue. The monophosphate form of these molecules was selected because these are generated upon cleavage of DNAs by λ -exonuclease, which is the focus of our SMS approach^{23, 24}.

2.3.1 Nanochannel electrokinetic transport behavior of ATTO 532 dye.

To initiate this study, fluorescence tracking of the ATTO 532 dye was undertaken. Because we intended to use ATTO 532 as a reporter for tracking the electrokinetic motion of the dNMPs through the polymer nanochannels, we sought to understand the mobility of this dye alone. Nanochannel electrokinetic experiments of the dye at varying electrolyte concentrations were performed, because changing the carrier electrolyte concentration modulates the EDL thickness and can introduce different EOF profiles under certain conditions. With a carrier electrolyte

concentration of 44.5 mM, λ_d was 1.25 nm and at an electrolyte concentration of 0.45 mM, λ_d was 12.5 nm (see Equation (2.1)). To determine the extent of EDL overlap, κa was used as an operational metric, where a is the channel radius and κ is the inverse of λ_d ;

$$\kappa = \sqrt{\frac{8\pi n e^2}{\epsilon K T}}$$

where n is the bulk ion concentration ³¹, e is the elementary charge of an electron, ϵ is the dielectric constant, K is Boltzmann's constant and T is temperature. If $\kappa a \gg 1$, there is negligible EDL overlap and thus, the EOF profile should be classically plug-like; however, for cases where $\kappa a \approx 1$, significant EDL overlap occurs and the EOF profile is predicted to resemble Poiseuille-like flow ⁵. For a buffer concentration of 44.5 mM and λ_d of 1.25 nm with the nanochannels possessing a width and height of ~110 nm ($a = 55$ nm), the κa value was ~44 indicating primarily plug-like flow. For a buffer concentration of 0.45 mM and $\lambda_d = 12.5$ nm, the κa value was 4.4 indicating partial EDL overlap and thus, more parabolic-like flow (see Equations (2.1) and (2.2)).

As can be seen in Figure 2.5, for both carrier electrolyte concentrations a field-dependent apparent mobility of the dye was observed until a “critical” electric field strength was reached, where the apparent mobility became field independent. Microscale electrokinetics would predict that the mobility of the solute be independent of field strength (e.g. we assumed that the EOF is constant for each electrolyte concentration) and thus, changes in the apparent mobility, which is the sum of the EOF and the electrophoretic mobility of the dye, are due to changes in the electrophoretic mobility of the dye ³². The field strength dependency of the apparent mobility has been reported for the electrokinetic transport of molecules in nanochannels and arises from

intermittent motion⁷⁻⁹. We also note that the thermoplastic nanochannels we are using have non-uniform surface charges generating solute recirculation due to inhomogeneous charge distribution of the channel walls, which is also electric field strength dependent⁸.

At a “critical” electric field strength, the apparent mobility becomes independent of the applied electric field strength. As seen in Figure 1, this critical field strength was dependent on the electrolyte concentration. For a carrier electrolyte concentration of 44.5 mM, the critical field strength for the ATTO 532 dye was 479 V/cm, while for an electrolyte concentration of 0.45 mM, the critical field strength was 273 V/cm. Above these critical electric field strength values, the apparent mobility of ATTO 532 was $\sim 5.0 \times 10^{-5}$ cm²/V s for both electrolyte concentrations. Thus, as the electric field is increased, the effects of intermittent motion and recirculation become less, resulting in an increase in the electrophoretic mobility of the dye and as seen in Figure 1, a decrease in the apparent mobility. Above the critical field strength, the effects of intermittent motion and recirculation become inconsequential to the apparent mobility and a field independent mobility is observed.

As we have seen in our previous work on nanoscale electrokinetics⁷⁻⁹, when intermittent motion and recirculation occur, the standard deviations in the measured mobilities are large, consistent with the data displayed in Figures 2.5 a and b. At higher electric field strengths, the standard deviations in the measured apparent mobilities becomes smaller.

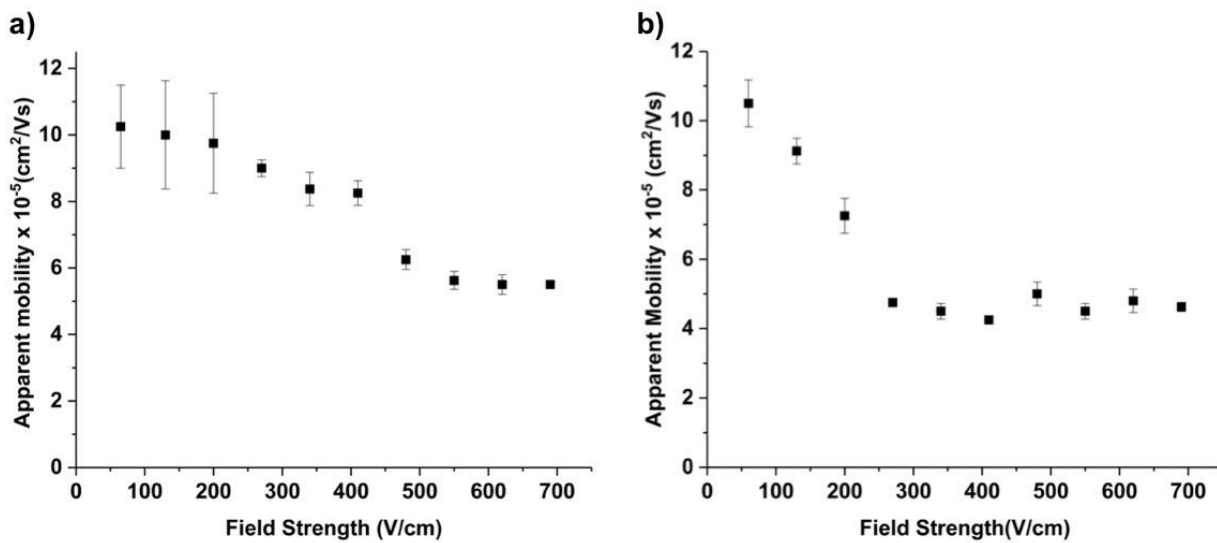


Figure 2.5: Apparent mobility versus field strength for ATTO 532 injected into a nanochannel that was 110 x 110 nm (width and depth; L = 100 μ m) that were fabricated in PMMA and possessed a COC cover plate. The nanochannel electrokinetic used two different carrier electrolytes consisting of; a) 44.5 mM TB with a pH 8.3 (λ_d = 1.25 nm); and b) 0.45 mM TB pH 8.3 (λ_d = 12.5 nm). Errors bars show \pm standard deviations for the apparent mobilities.

2.3.2 Nanochannel electrokinetics of the ATTO 532-labeled dNMPs.

Because the same dye reporter was covalently attached to each of the dNMPs, differences in the apparent mobilities of the dNMPs were assumed to arise from the identity of the nucleobase. This was necessary to study, because in our SMS approach, we will be identifying the dNMPs from their characteristic apparent mobility in a label-free approach. Labeling is not be possible post-cleavage due to reaction time limitations and building full complements of DNA strands using modified nucleotides is problematic as well. The charge of the dNMPs is based on the phosphate group, the ATTO 532 dye label, and the nucleobase. Deprotonation of the phosphate group (contributes -1 net charge) occurred at all pH values investigated (pH 8.3 – 10.3) as well as the sulfonate groups of the dye label (contributes -2 charge) and as such, all of the dNMPs are negatively charged. Changes in the net charge of the dNMPs over the pH range investigated is

primarily due to the nucleobase, which can affect their apparent mobility³³. Guanine and thymine have a pK_a of 9.3 and 10.4, respectively, and therefore these dNMPs can change over the pH range investigated (Table 2.1)³³.

Table 2.1: The net charges of dNMPs at pH 8.3 and pH 10.3

Nucleotide	Net charge at pH 8.3	
dAMP	-3	-3
dGMP	-3	-4
dCMP	-3	-3
dTMP	-3	-4

Figure 2.6a shows the apparent mobility versus electric field strength for the four dNMPs using a 110 x 110 nm nanochannel with a carrier electrolyte consisting of 44.5 mM TB at pH 8.3. At pH 8.3, all ATTO 532-labeled dNMPs have a net charge of -3; the ATTO-532 dye contributes a -2 charge for all dNMPs and the phosphate is -1 (Table 2.1) with all nucleobases not carrying a charge at this pH. The apparent mobility is a sum of the EOF (μ_{eof}) and the electrophoretic mobility of the dNMP (μ_{ep}). In this case, the electrophoretic mobility of the dye/dNMP conjugate is opposite in direction to the EOF and an increase in μ_{ep} results in a decrease in the apparent mobility.

We observed a smaller apparent mobility of the dye-labeled dNMPs compared to the free dye due to the increased negative charge of the conjugates compared to the free dye arising from the additional negative charge of the phosphate group. From Figure 2a, there were differences in the apparent mobilities of the 4 dNMPs in spite of the fact that they all carried the same net charge at this pH. Moreover, all of the nucleotides showed an apparent mobility that was dependent on the

electric field. Because the EOF mobility does not change as a function of the electric field strength^{7, 8}, changes in the apparent mobility were assumed to arise from differences in the apparent mobility of the dNMPs at different field strengths due to intermittent motion and/or recirculation as was seen for the free dye.

Figure 2.6 b shows histograms of the apparent mobility for the ATTO 532-labeled dNMPs at 342 V/cm, which was selected because it provided optimal separation resolution between the dNMPs. The resolution for these dNMPs was determined from the Gaussian fits to the histograms. Table 2.2 shows the separation resolutions between dNMP Gaussian fit pairs at pH 8.3 using 44.5 mM TB buffer. The apparent mobility order, dAMP < dTMP < dGMP < dCMP was in close agreement with the hydrophobicity order of the dNMPs (dGMP < dCMP < dAMP < dTMP)^{24, 34}. The hydrophobic nature of dAMP and dTMP likely generates more solute/wall interactions and will thus show a lower apparent mobility, while the less hydrophobic dGMP and dCMP will have larger apparent mobilities. This suggests that the apparent mobility order using these conditions (pH 8.3, $\lambda_d = 1.25$ nm), may not only depend on the differences in charges and/or sizes of the dNMPs, but also on the extent of solute/wall interactions; the walls of these devices consist of PMMA/COC carrying a partial negative charge resulting from O₂ plasma activation, which also generates nanoscale surface roughness giving rise to intermittent motion. As we have shown, specific surface areas lack charges following activation creating unmodified polymer with a low surface energy that can promote hydrophobic/hydrophobic interactions as well as recirculation⁸.

Taylor dispersion resulting from Joule heating can contribute to variances in the apparent mobilities of the dNTPs. This variance shows a strong dependency on column radius (R^6) and results in the optimum field strength for microscale experiments to be only a few hundred V/cm

^{32, 35, 36}. However, nanochannels with their reduced channel dimensions allows for the use of much higher electric field strengths without observing deleterious effects arising from Joule heating. The consequence of this is also reduced variances due to longitudinal diffusion ³⁵⁻³⁷. Variances in the observed apparent mobilities (see Figure 2.6) for thermoplastic nanochannels can also arise from non-uniform distribution of surface charged groups following O₂ plasma activation giving rise to recirculation ⁸; control of the dose used for activation can lead to an optimal surface charge density with higher charge densities correlated to lower surface charge heterogeneity and thus, lower variances in the apparent mobility.

Furthermore, utilizing COMSOL simulations to reconstruct fluid flow profiles in nanochannels with a heterogeneous distribution of point charges, the simulations indicated that there were regions of fluid recirculation leading to both positive and negative velocities. The results indicated that when the electric field strength was high (≥ 300 V/cm), intermittent motion as well as recirculation were significantly reduced, which was observed when the apparent mobility became independent of the electric field strength, Figure 2.6A ⁸. Also, in general the variances in the apparent mobilities became less when the mobilities became independent of field strength due to minimal contributions of intermittent motion and recirculation on the solute's mobility.

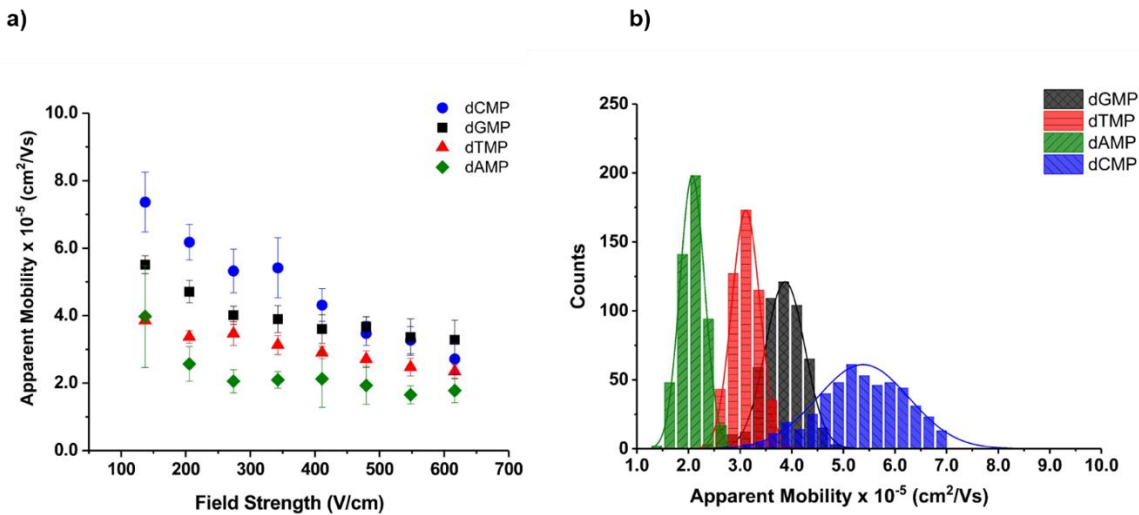


Figure 2.6: a) Apparent mobility versus the electric field strength for ATTO 532 conjugated to dCMP, dGMP, dTMP and dAMP injected into a nanochannel that was $110 \times 110 \text{ nm}$ (width and depth; $L = 100 \mu\text{m}$) and used PMMA as the substrate with a COC cover plate. The electrokinetic used a buffer of 44.5 mM TB at $\text{pH } 8.3$ ($\lambda_d = 1.25 \text{ nm}$). b) Histograms of the apparent mobility for the dye-labeled dNMPs using a field strength of 342 V/cm in a $100 \mu\text{m}$ total length nanochannel. Histograms were fit to a Gaussian function with of the apparent mobility histogram (each bin represents $2 \times 10^{-5} \text{ cm}^2/\text{Vs}$ apparent mobility units). The error bars represent the standard deviations in the measurements.

We calculated the separation resolution between the ATTO 532-dNMPs at a field strength of 342 V/cm and $\text{pH } 8.3$ TB (44.5 mM), the result of which are summarized in Table 2.2. For these conditions, we noted the separation resolution ranged from $0.73 - 2.13$. These were determined from the average mobility values and the standard deviations in the Gaussian fits (Figure 2.6 b) to the histograms of apparent mobilities for the dNMPs.

Table 2.2 Separation resolution between ATTO 532-dNMP pairs at pH 8.3 and 44.5 mM TB (taken from Figure 2b) were calculated using $R = \Delta\mu/w_{avg}$ where $\Delta\mu$ is the difference in the average apparent mobility (determined from the centroid of the Gaussian fit to each histogram) for each peak pair and w_{avg} is the average full width of the two peaks, which is related to the standard deviation of the Gaussian.

Resolution	dAMP	dTMP	dGMP	dCMP
dAMP	-	0.97	2.13	1.47
dTMP	0.97	-	0.85	0.98
dGMP	2.13	0.85	-	0.73
dCMP	1.47	0.98	0.73	-

2.3.3 Effect of pH on the nanochannel electrokinetics of ATTO 532-labeled dNMPs.

As a matter of comparison between microscale electrophoresis of the dNMPs and the nanoscale electrokinetics in terms of pH effects, we carried out microscale separations of the dNMPs using a capillary ($id = 50 \mu m$; effective length = 56 cm). We explored the free solution electrophoretic of the dNMPs in a buffer consisting of 89 mM TB at different pH values as seen in Figure 2.7. The dNMPs migrated from anode to cathode in spite of their anionic nature at all pH values due to the high electroosmotic flow, EOF ($EOF = 7.2 \times 10^{-4}$; pH 9.3). Regardless of the pH, co-migration of dAMP and dCMP was seen most likely due to the lack of a pH-sensitive group on the nucleobases. At pH = 9.3, dGMP showed the highest electrophoretic mobility and thus, migrated the slowest (*i.e.*, dGMP had the lowest apparent mobility). At this pH, guanine's electrophoretic mobility was $-3.72 \times 10^{-4} \text{ cm}^2/\text{V}\cdot\text{s}$ while thymine had an electrophoretic mobility of $-3.22 \times 10^{-4} \text{ cm}^2/\text{Vs}$. When

the pH was changed to 12, well above the pKa for both dTMP and dGMP, the electrophoretic mobility increased for both molecules. Guanine's electrophoretic mobility at pH = 12 was -4.55×10^{-4} cm²/V*s and thymine's was -4.35×10^{-4} cm²/V*s, most likely due to further deprotonation of the nucleobases at this high pH value.

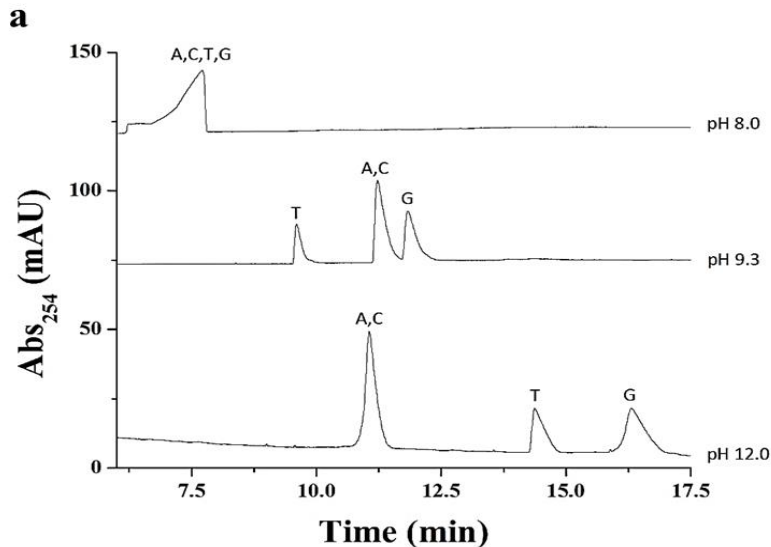


Figure 2.7 Microscale electrophoresis of dAMP, dCMP, dTMP and dGMP at varying pH values. The electrophoresis was performed using the following conditions: Carrier electrolyte was 1 mM MgCl₂ in 89 mM TB. The applied voltage was 20 kV (310 V/cm). The separations were performed in a silica capillary that possessed an ID = 50 μ m, total length = 64.5 cm, effective length = 56 cm, pressure injection at 90 mbar*s, with UV detection at 254 nm. In this case, the nucleotides were not labeled with ATTO 532.

Figure 2.8 shows histograms of the apparent mobilities for the ATTO 532-dNMPs within a nanochannel (44.5 mM TB) at pH 10.3 and a field strength of 342 V/cm. In Figure 4 a summary of the pH-dependent mobility of the ATTO 532-dNMPs is shown. Over the pH range investigated (pH 8.3 – 10.3), the EOF remains constant due to the low pKa (~5) of the surface-confined carboxylic acids ^{9, 38-41}, and thus, the observed changes in the apparent mobilities arise from differences in the electrophoretic mobilities of the ATTO 532-dNMPs conjugates. In addition, the

reporter fluorescent dye (ATTO 532) does not change its charge state within the investigated pH range indicating that the change in apparent mobility is associated with the chemical properties of the nucleobases. The increase in the pH could have a two-fold effect on the apparent mobilities of the dNMPs: 1) Changing the negative charge state of the dNMP nucleobase due to the presence of weak acid/base groups; and/or 2) altering potential solute/wall interactions due primarily to changes in the charge states of the nucleobase.

All nucleotides, except for dGMP, showed a larger apparent mobility at pH 9.3 and 10.3 compared to pH 8.3 when using a 44.5 mM carrier electrolyte concentration. The different apparent mobility order compared to pH 8.3 arose from differences in the electrophoretic mobility of dGMP as a result of pH changes. The mobility for dGMP decreased with an increased pH from 8.3 to 10.3 resulting from an increase in the net negative charge of dGMP from -3 (pH 8.3) to -4 (pH 10.3; see Table 2.1). Additionally, we show a histogram of the apparent mobilities for mdCMP (Figure 2.8), which showed a larger apparent mobility compared to the other nucleotides. Fitting of a Gaussian function to the histogram in this case was poorer ($R^2 > 0.94$) compared to the non-methylated dNMPs ($R^2 > 0.999$), which may have been due to different adducts present in the methylated cytosine sample. In spite of this observation, the large differences in the apparent mobility of the mdCMP compared to the other dNMPs suggests that mobility matching could be used as an identification approach for detecting epigenetic modifications in genomic DNA without requiring bisulfite conversion.

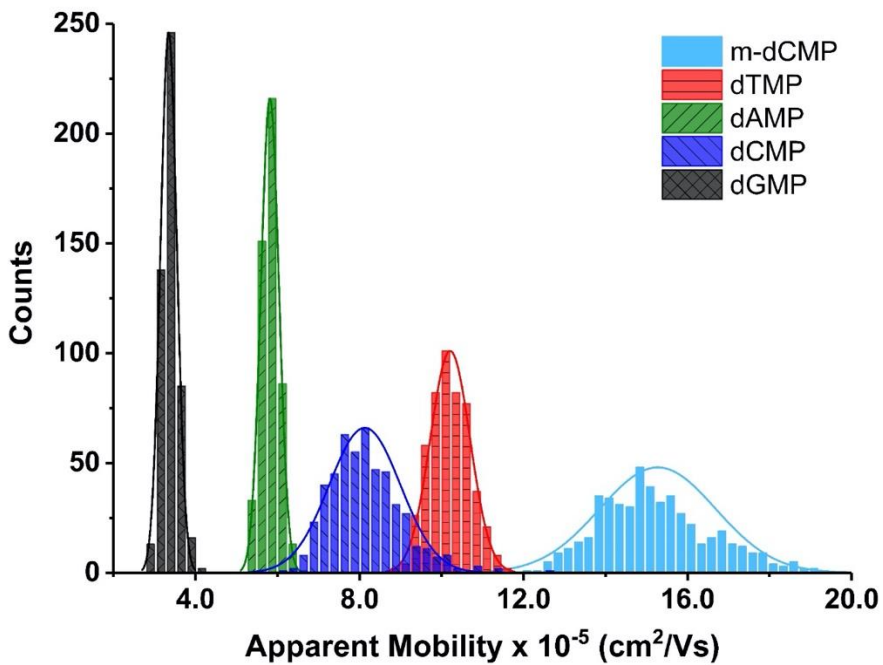


Figure 2.8: Histogram of apparent mobilities for the dye-labeled dNMPs at field strength of 342 V/cm in a 100 μm long nanochannel. The nanochannel electrokinetic conditions are the same as in Figure 2.7 but using a carrier electrolyte of pH = 10.3. Gaussian functions were fit to the histograms as discussed in Figure 2.7b.

Figure 2.9 shows the relative apparent mobilities of the nucleotides as a function of pH. At lower pH values, larger differences in the apparent mobilities were observed. However, at higher pH values, we observed an increase in the overall separation resolution between the nucleobases (see Table 2). The poorer overall resolution observed at lower pH values was a result of the higher standard deviations seen in the measured apparent mobilities for all of the dNMPs as compared to the higher pH values (see Figure 4). One trend that emerged from this data is that dCMP was not very sensitive to pH changes while the other three nucleotides were.

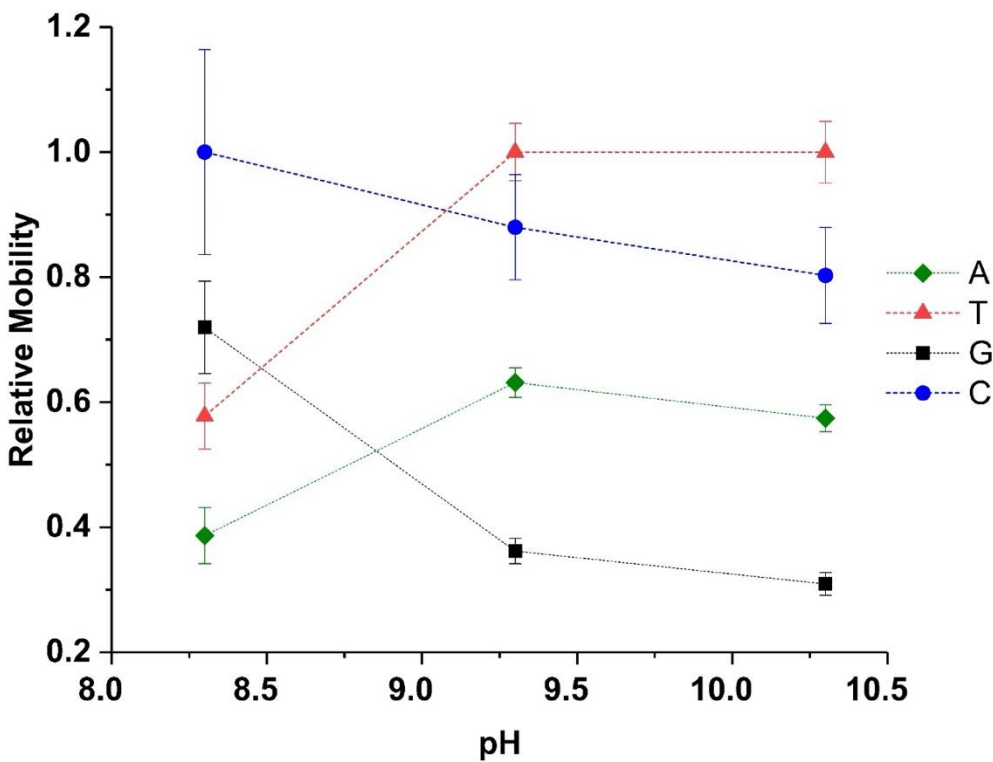


Figure 2.9. Relative apparent mobility of the ATTO 532-labeled dNMPs with respect to carrier electrolyte pH values. Apparent mobilities have been normalized to the highest observed apparent mobility for pH 8.3, 9.3 and 10.3. (Note: data lines are connected only for ease of interpretation). The error bars represent the standard deviations in the measurements.

Another important metric for the utilization of mobility matching for the identification of mononucleotides is the identification or base call accuracy, which is related to the separation resolution between the nucleotides. We define the “identification accuracy” as the amount of overlap of two adjacent Gaussian fits to the histograms of the ATTO 532-dNMPs’ apparent mobilities. With a pH value of 10.3 and a field strength of 342 V/cm ($\lambda_d = 1.25$ nm), the separation resolution between the dNMPs ranged from 0.80 – 4.84 (Table 2.3). A resolution of 0.5 has a classification accuracy of 68%, which is based on the degree of overlap in the Gaussian fits. A resolution of 1.0 has a classification accuracy of 96%. Table 2.4 shows the calculated identification

accuracies for the nucleotides at pH 10.3. As can be seen from this data, the base call accuracy is >95% in all cases, except for the dTMP/dCMP pair, which was determined to be 87%. There are a number of experimental conditions that can be altered to potentially improve the base call accuracy, such as using higher electric field strengths, increasing the channel length or removing the dye reporter.

Table 2.3. Resolution between ATTO 532-dNMPs pairs at pH 10.3 and 44.5 mM TB (taken from Figure 2.8) and calculated as in Table 2.2

Resolution	dAMP	dTMP	dGMP	dCMP
dAMP	-	0.97	2.13	1.47
dTMP	0.97	-	0.85	0.98
dGMP	2.13	0.85	-	0.73
dCMP	1.47	0.98	0.73	-

Table 2.4. Identification accuracy for all ATTO 532-dNMPs at pH 10.3 and were calculated using the peak overlap between Gaussian fits to the histogram of apparent mobilities at pH 10.3

Identification Accuracy	dAMP	dTMP	dGMP	dCMP
dAMP	-	>99.9 %	>99.9 %	97.0 %
dTMP	>99.9 %	-	>99.9 %	87.0 %
dGMP	>99.9 %	>99.9 %	-	>99.9 %
dCMP	97.0 %	87.0%	>99.9 %	-

2.3.4 Effect of EDL overlap on the nanochannel electrokinetics of ATTO 532-labeled dNMPs.

In the region of EDL overlap, the flow profile becomes more parabolic⁴⁻⁶. Due to high surface-to-volume ratios on the nanoscale, electrostatic forces induced by a charged wall can place charged particles within a particular flow streamline allowing for mobility differences of molecules that may show no difference on the microscale; this has been called Transverse electromigration, TEM⁴²⁻⁴⁴. EDL overlap may also prevent the injection of co-ions into the nanochannel due to concentration polarization⁵. To observe how EDL thickness affected the electrokinetic transport properties of the dye-labeled dNMPs, studies on the transport of the ATTO 532-dNMPs with a carrier electrolyte concentration of 0.45 mM TB (pH 8.3) under varying electric field strengths was undertaken (Figure 2.10). We did not observe concentration polarization of the dye-labeled nucleotides at any EDL thickness evaluated herein. The overall magnitude of the apparent mobility was higher for the dNMPs when compared to the case of the 44.5 mM carrier electrolyte, which possessed a thinner EDL. dCMP did show a field strength dependence on its apparent mobility while the other dNMPs did not; the cause for this is currently being investigated.

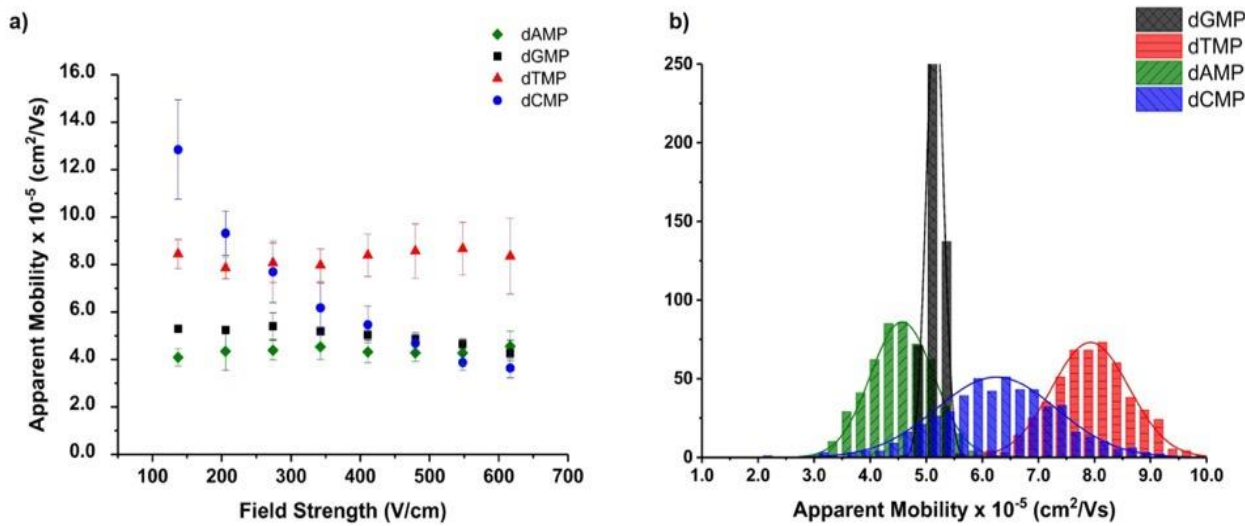


Figure 2.10: a) Apparent mobility versus the electric field strength for ATTO 532 conjugated to dCMP, dGMP, dTMP, and dAMP. The nanochannel electrokinetic conditions are the same as shown in Figure 2 except that the carrier electrolyte concentration was 0.45 mM TB pH 8.3 ($\lambda_d = 12.5$ nm). b) Histogram of apparent mobility for the dye labeled dNMPs with a field strength of 342 V/cm in a 100 μm long nanochannel. The error bars represent the standard deviations in the measurements.

Furthermore, a decrease in separation resolution of the mononucleotides was observed with the thicker EDL (0.45 mM TB) as compared to the carrier electrolyte consisting of 44.5 mM and a more compressed EDL. As seen in Figure 5, the separation resolution dropped to as low as 0.25 with the highest being 2.33 (Table 2.5). In addition, increases in the standard deviation in the Gaussian fits to the apparent mobility histograms was also observed.

Table 2.5. Resolution of ATTO 532-dNMPs pairs at pH 8.3 and 0.45 mM TBE (from Figure 2.10B) and were calculated the same procedure as described in Table 2.1

Resolution	dAMP	dTMP	dGMP	dCMP
dAMP	-	2.33	0.25	0.51
dTMP	2.33	-	1.64	0.75
dGMP	0.25	1.64	-	0.29
dCMP	0.51	0.75	0.29	-

2.4 Conclusions

In all cases and consistent with our previous papers dealing with nanoslit electrokinetics of charged particles, higher electric field strengths provided lower standard deviations in the apparent mobilities (see Figure 1)^{7, 8}. This was due to the prevalence of intermittent motion and recirculation at low electric field strengths, both of which can cause higher variances in the apparent mobilities. The effects of intermittent motion and recirculation could be minimized when employing higher electric field strengths.

We determined that electrokinetic transport of the dNMPs was sensitive to the pH and ion concentration of the carrier electrolyte. Separation resolutions ranging from 0.73- 2.13 were achieved at pH = 8.3 and at a pH = 10.3; resolutions to 4.84 were observed. While higher pH values may further improve mobility-based identification, it was not possible to carry out these experiments at pH values >10.3 due to delamination of the nanofluidic device cover plate from the substrate.

Furthermore, it was determined that buffer concentrations that affect the degree of EDL overlap can affect separation resolution as well. For example, decreased resolution of the dNMPs was observed for cases where the EDL was significantly overlapped compared to the case with a lower degree of EDL overlap. For cases where there is partial EDL overlap, more parabolic flow would be expected that can, under the action of TEM, improve resolution. However, we did not observe for our studies most likely due to the fact that the devices used herein were hybrid devices (PMMA-to-COC) that have different surface chemistries and thus, would have different EOF values ⁹. For hybrid-type devices, the flow profile can be distorted, which may cause higher variances in the apparent mobilities compared to monolithic devices (e.g., COC-to-COC), especially with thicker EDLs ⁴⁵.

In these studies, we utilized dye-labeled dNMPs to allow for tracking of the molecules during their transport through the nanoscale channel. However, in our envisioned single-molecule sequencing approach, labeling of the mononucleotides either before or after exonuclease digestion would be problematic ⁴⁶. Therefore, single-molecule detection of the dNMPs using a non-labeling approach would be preferable to allow for identification of single nucleotides following exonuclease cleavage using mobility matching. We are currently developing such a strategy that employs in-plane pores poised at the input and output ends of a nanochannel column and are fabricated via nanoimprinting in polymers ⁴⁷. While this detection format is desirable for our proposed single-molecule sequencing strategy, it cannot track the transport properties of the dNMPs through the nanochannel. Thus, the use of dye-labeled dNMPs and fluorescence tracking provided a viable approach to carefully understand the transport properties of the dNMPs to guide optimization of experimental conditions and nanochannel geometry for optimal identification of the dNMPs.

2.5 References

1. Baldessari, F.; Santiago, J., Electrophoresis in nanochannels: brief review and speculation. *Journal of Nanobiotechnology* **2006**, 4 (1), 12.
2. Daiguji, H., Ion transport in nanofluidic channels. *Chemical Society Reviews* **2010**, 39 (3), 901-911.
3. Garcia, A. L.; Ista, L. K.; Petsev, D. N.; O'Brien, M. J.; Bisong, P.; Mammoli, A. A.; Brueck, S. R. J.; Lopez, G. P., Electrokinetic molecular separation in nanoscale fluidic channels. *Lab on a Chip* **2005**, 5 (11), 1271 - 1276.
4. Pennathur, S.; Santiago, J. G., Electrokinetic Transport in Nanochannels. 2. Experiments. *Analytical Chemistry* **2005**, 77, 6782-6789.
5. Piruska, A.; Gong, M.; Sweedler, J. V.; Bohn, P. W., Nanofluidics in chemical analysis. *Chemical Society Reviews* **2010**, 39 (3), 1060-1072.
6. Pennathur, S.; Santiago, J. G., Electrokinetic Transport in Nanochannels. 1. Theory. *Anal. Chem.* **2005**, 77, 6772-6781.
7. Weerakoon-Ratnayake, K. M.; Uba, F. I.; Oliver-Calixte, N. J.; Soper, S. A., Electrophoretic Separation of Single Particles Using Nanoscale Thermoplastic Columns. *Analytical chemistry* **2016**, 88 (7), 3569-3577.
8. Oneil, C. E.; Jackson, J. M.; Shim, S.-H.; Soper, S. A., Interrogating Surface Functional Group Heterogeneity of Activated Thermoplastics Using Super-Resolution Fluorescence Microscopy. *Analytical Chemistry* **2016**, 88 (7), 3686-3696.
9. Uba, F. I.; Pullagurla, S. R.; Sirasunthorn, N.; Wu, J.; Park, S.; Chantiwas, R.; Cho, Y.-K.; Shin, H.; Soper, S. A., Surface charge, electroosmotic flow and DNA extension in chemically modified thermoplastic nanoslits and nanochannels. *Analyst* **2015**, 140 (1), 113-126.
10. Napoli, M.; Atzberger, P.; Pennathur, S., Experimental study of the separation behavior of nanoparticles in micro-and nanochannels. *Microfluidics and Nanofluidics* **2011**, 10 (1), 69-80.
11. Booth, F. In *The cataphoresis of spherical, solid non-conducting particles in a symmetrical electrolyte*, 1950; The Royal Society: pp 514-533.
12. Wiersema, P. H.; Loeb, A. L.; Overbeek, J. T. G., Calculation of the electrophoretic mobility of a spherical colloid particle. *Journal of Colloid and Interface Science* **1966**, 22 (1), 78-99.
13. Napoli, M.; Atzberger, P.; Pennathur, S., Experimental study of the separation behavior of nanoparticles in micro- and nanochannels. *Microfluid Nanofluid* **2011**, 10 (1), 69-80.
14. Novak, B. R.; Moldovan, D.; Nikitopoulos, D. E.; Soper, S. A., Distinguishing Single DNA Nucleotides Based on Their Times of Flight Through Nanoslits: A Molecular Dynamics Simulation Study. *The Journal of Physical Chemistry B* **2013**, 117 (12), 3271-3279.
15. Xia, K.; Novak, B. R.; Weerakoon-Ratnayake, K. M.; Soper, S. A.; Nikitopoulos, D. E.; Moldovan, D., Electrophoretic Transport of Single DNA Nucleotides through Nanoslits: A Molecular Dynamics Simulation Study. *The Journal of Physical Chemistry B* **2015**.
16. Branton, D.; Deamer, D. W.; Marziali, A.; Bayley, H.; Benner, S. A.; Butler, T.; Di Ventra, M.; Garaj, S.; Hibbs, A.; Huang, X.; Jovanovich, S. B.; Krstic, P. S.; Lindsay, S.; Ling, X. S.; Mastrangelo, C. H.; Meller, A.; Oliver, J. S.; Pershin, Y. V.; Ramsey, J. M.; Riehn, R.; Soni, G. V.; Tabard-Cossa, V.; Wanunu, M.; Wiggin, M.; Schloss, J. A., The potential and challenges of nanopore sequencing. *Nat Biotech* **2008**, 26 (10), 1146-1153.

17. Branton, D. e. a., The potential and challenges of nanopore sequencing. *Nature Biotechnology* **2008**, *26*, 1146-1153.
18. Deamer, D. W.; Akeson, M., Nanopores and nucleic acids: prospects for ultrarapid sequencing. *Trends in Biotechnology* **2000**, *18* (4), 147-151.
19. Meller, A. B., D., Single molecule measurements of DNA transport through a nanopore. *Electrophoresis* **2002**, *23*, 2583-2591.
20. Storm, A. J. C., H.; Ling, S.; Zandbergen, W.; Dekker, C., Fabrication of solid state nanopores with single-nanometre precision. *Nature Materials* **2003**, *2* (537-540).
21. Deamer, D. W.; Branton, D., Characterization of Nucleic Acids by Nanopore Analysis. *Accounts of Chemical Research* **2002**, *35* (10), 817-825.
22. Clarke, J. W., H.C.; Jayasinghe, L.; Patel, A.; Reid, S.; Bayley, H., Continuous base identification for single-molecule nanopore DNA sequencing. *Nature Nanotechnology* **2009**, *4*, 265-270.
23. Novak, B. R.; Moldovan, D.; Nikitopoulos, D. E.; Soper, S. A., Distinguishing Single DNA Nucleotides Based on Their Times of Flight Through Nanoslits: A Molecular Dynamics Simulation Study. *Journal of Physical Chemistry B* **2013**, *117* (12), 3271-3279.
24. Xia, K.; Novak, B. R.; Weerakoon-Ratnayake, K. M.; Soper, S. A.; Nikitopoulos, D. E.; Moldovan, D., Electrophoretic Transport of Single DNA Nucleotides through Nanoslits: A Molecular Dynamics Simulation Study. *Journal of Physical Chemistry B* **2015**, *119*, 11443-11448.
25. Oliver-Calixte, N. J.; Uba, F. I.; Battle, K. N.; Weerakoon-Ratnayake, K. M.; Soper, S. A., Immobilization of Lambda Exonuclease onto Polymer Micropillar Arrays for the Solid-Phase Digestion of dsDNAs. *Analytical Chemistry* **2014**, *86* (9), 4447-4454.
26. Schindelin, J.; Arganda-Carreras, I.; Frise, E.; Kaynig, V.; Longair, M.; Pietzsch, T.; Preibisch, S.; Rueden, C.; Saalfeld, S.; Schmid, B.; Tinevez, J.-Y.; White, D. J.; Hartenstein, V.; Eliceiri, K.; Tomancak, P.; Cardona, A., Fiji: an open-source platform for biological-image analysis. *Nat Meth* **2012**, *9* (7), 676-682.
27. Yuan, Z.; Garcia, A. L.; Lopez, G. P.; Petsev, D. N., Electrokinetic transport and separations in fluidic nanochannels. *Electrophoresis* **2007**, *28* (4), 595-610.
28. Weerakoon-Ratnayake, K. M.; O'Neil, C. E.; Uba, F. I.; Soper, S. A., Thermoplastic nanofluidic devices for biomedical applications. *Lab on a Chip* **2017**, *17*, 362-381.
29. Xuan, X.; Li, D., Electrokinetic transport of charged solutes in micro- and nanochannels: the influence of transverse electromigration. *Electrophoresis* **2006**, *27* (24), 5020-31.
30. Xuan, X., Ion separation in nanofluidics. *Electrophoresis* **2008**, *29*, 3737-3743.
31. Rice, C. L.; Whitehead, R., Electrokinetic flow in a narrow cylindrical capillary. *The Journal of Physical Chemistry* **1965**, *69* (11), 4017-4024.
32. Baker, D., *Capillary Electrophoresis*. John Wiley and Sons Inc: New York, NY, 1995.
33. Geldart, S. E.; Brown, P. R., Analysis of nucleotides by capillary electrophoresis. *Journal of Chromatography A* **1998**, *828* (1-2), 317-336.
34. Shih, P.; Pedersen, L. G.; Gibbs, P. R.; Wolfenden, R., Hydrophobicities of the nucleic acid bases: distribution coefficients from water to cyclohexane. *Journal of molecular biology* **1998**, *280* (3), 421-430.
35. Jorgenson, J. W.; Lukacs, K. D., ZONE ELECTROPHORESIS IN OPEN-TUBULAR GLASS-CAPILLARIES. *Analytical Chemistry* **1981**, *53* (8), 1298-1302.

36. Grossman, P. D., CHAPTER 1 - Factors Affecting the Performance of Capillary Electrophoresis Separations: Joule Heating, Electroosmosis, and Zone Dispersion. In *Capillary Electrophoresis*, Academic Press: San Diego, 1992; pp 3-43.
37. Jorgenson, J. W.; Lukacs, K. D., Capillary Zone Electrophoresis. *Science* **1983**, 222 (4621), 266-272.
38. Henry, A. C.; Tutt, T. J.; Galloway, M.; Davidson, Y. Y.; McWhorter, C. S.; Soper, S. A.; McCarley, R. L., Surface modification of poly(methyl methacrylate) used in the fabrication of microanalytical devices. *Analytical Chemistry* **2000**, 72 (21), 5331-5337.
39. Soper, S. A.; Ford, S. M.; Qi, S.; McCarley, R. L.; Kelly, K.; Murphy, M. C., Polymeric microelectromechanical systems. *Analytical Chemistry* **2000**, 72 (19), 642A-651A.
40. Vaidya, B.; Soper, S. A.; McCarley, R. L., Surface modification and characterization of microfabricated poly(carbonate) devices: manipulation of electroosmotic flow. *Analyst* **2002**, 127 (10), 1289-1292.
41. McCarley, R. L.; Vaidya, B.; Wei, S. Y.; Smith, A. F.; Patel, A. B.; Feng, J.; Murphy, M. C.; Soper, S. A., Resist-free patterning of surface architectures in polymer-based microanalytical devices. *Journal of the American Chemical Society* **2005**, 127 (3), 842-843.
42. Napoli, M.; Eijkel, J. C. T.; Pennathur, S., Nanofluidic technology for biomolecule applications: a critical review. *Lab on a Chip* **2010**, 10 (8), 957-985.
43. Stein, D.; Kruithof, M.; Dekker, C., Surface-Charge-Governed Ion Transport in Nanofluidic Channels. *Physical Review Letters* **2004**, 93 (3), 035901.
44. Stein, D.; van der Heyden, F. H. J.; Koopmans, W. J. A.; Dekker, C., Pressure-driven transport of confined DNA polymers in fluidic channels. *Proceedings of the National Academy of Sciences* **2006**, 103 (43), 15853-15858.
45. Rani, S. D.; You, B. H.; Soper, S. A.; Murphy, M. C.; Nikitopoulos, D. E., Influence of material transition and interfacial area changes on flow and concentration in electro-osmotic flows. *Analytica Chimica Acta* **2013**, 770, 103-110.
46. Davis, L. M.; Fairfield, F. R.; Harger, C. A.; Jett, J. H.; Keller, R. A.; Hahn, J. H.; Krakowski, L. A.; Marrone, B. L.; Martin, J. C.; Nutter, H. L.; Ratliff, R. L.; Shera, E. B.; Simpson, D. J.; Soper, S. A., Rapid DNA Sequencing Based Upon Single Molecule Detection. *Genet. Anal.-Biomol. Eng.* **1991**, 8 (1), 1-7.
47. Jia, Z.; Choi, J.; Amarasekara, C. A.; Weerakoon-Ratnayake, K. M.; Soper, S. A.; Park, S., Sensing Single Deoxynucleotide Monophosphates (dNMPs) using In-Plane Nanopores. **2018**, (*manuscript in preparation to publish in Nature Nanotechnology*).

**Chapter 3: Open-tubular Nanoelectrochromatography: (OT-NEC) Gel-free Separation
of Single Stranded DNAs in Thermoplastic Nanochannels**

3.1 Introduction

Nucleic acid separations continue to represent an important area in research, forensic, and clinical laboratories because many applications in each laboratory setting requires identification of molecular biological reaction products using a separation step whether it be chromatographic and/or electrophoretic. For example, much emphasis has been placed on precision medicine (<https://www.whitehouse.gov/precision-medicine>), where diagnosis, treatment, and prevention are tailored to an individual's genetic makeup of their disease.¹ DNA biomarkers that can be used as diagnostic and prognostic indicators of disease include, but are not restricted to, single nucleotide polymorphisms (SNP), deletions, insertions and other sequence variations and in forensics to find short tandem repeats (STR). STRs are used in forensic applications for human identification where the assay typically incorporating a PCR step followed by capillary gel electrophoresis.²

Single-stranded DNAs (ssDNA) can be the product of the biological reaction, such the ligase detection reaction (LDR), which can detect known point mutations with high sensitivity, even at the single molecule level.³ Thus, an increased demand to analyze and separate ssDNA with high resolution in clinical settings is becoming very important.⁴⁻⁶ For example, in LDRs the sequence content of the primers serve to define the particular SNP (biomarker) to be queried with changes in the lengths of the primers used to allow for multiplexing (*i.e.*, analyzing multiple mutations simultaneously), with the resultant products sorted via electrophoresis.⁷⁻⁹

The growing need for higher throughput, and separations with higher efficiency that result in better resolving power to increase the multiplexing capacity of the assay are still needed. The workhorse for sorting ssDNAs continues to be capillary gel electrophoresis and much work over the last 20 years have focused on developing new surface coatings for capillary columns to

suppress the electroosmotic flow (EOF) and gel formulations that can be used to electrophoretically sort DNA fragments;(REF) due to the free draining behavior of DNA, they comigrate in free solution irrespective of size.(REF) Unfortunately, the need for column coatings and gels can limit the utility of current gel-based electrophoretic methods, especially in clinical settings.¹⁰

Development of DNA separation methods for clinical applications are trending toward miniaturization and methods that can support point-of-care testing.¹¹ With advances in design and fabrication of microfluidic “lab-on-a-chip” (LOC) devices over the last two decades, there have been numerous reports on microscale electrophoretic separations of DNA.¹² However, the majority of these methods still utilize a gel-based matrix for the separation due to the length independent mobility of DNA for both double stranded and single stranded forms in free solution.^{13, 14} Employing automated chip-based gel electrophoresis systems for DNA separations still remains challenging due to the limitations imposed by the requirement of gel loading and replacement in microchip electrophoresis as well as wall-coatings to suppress the EOF.¹⁵⁻¹⁸ Due to the high EOF in glass devices induced by the high surface charge density, wall-coatings are required such as linear polyacrylamides that are covalently anchored to the wall of the microchannel or dynamic coatings.^{19, 20} If the separation could be performed in free solution, challenges associated with the need for gel matrices would be eliminated.

End-labeled free solution electrophoresis is a technique where ssDNA and dsDNA separations are performed in free solution by attaching to the DNA a large uncharged molecule known as a drag tag. Limited resolution for long DNA fragments and the requirement of DNA modification by the drag tag are disadvantages of this method.²¹⁻²⁴

On the other hand, nanofluidic-based separations have garnered attention due to nanoscale phenomena, such as electric double layer effects and transverse electromigration leading to unique separation modalities.²⁵⁻²⁷ In addition, advantages of nanofluidic separations include low sample and reagent consumption, ultrafast separations, and ease of integration to LOC devices to allow for sample pre-processing before the separation. The increased surface area-to-volume ratio in nanofluidic channels also allows for solute/wall interactions that can influence the electrokinetic transport of analytes through nanochannels. Field-dependent mobilities are observed as well due to intermittent motion of solutes through nanochannels when surface roughness is comparable to the critical dimension of the nanochannel.²⁸ Moreover, adsorption/desorption events between analytes and the column wall can be prominent in nanochannels compared to microchannels due to scaling effects. Kitamori *et al.*²⁹ utilized these adsorption/desorption effects in nanochannels to demonstrate open tubular chromatographic separations, which he coined as extended nanochromatography.³⁰ They performed a wide range of chromatographic separations by using pressure driven flow in glass nanofluidic devices with channel dimensions of 100 nm in depth, 100 nm in width and 4 cm in length. Reverse phase chromatographic separation of amino acids was performed by chemically modifying the nanochannel surface with a C18 stationary phase.³¹ Moreover, in a recent review on nanoscale electrophoresis by Santiago *et al.*,^{32, 33} he reported the effects of wall interactions, which can be more dominate compared to electrophoretic effects, indicating that separations in nanoscale columns can be considered to be more chromatographic in nature than electrophoretic.

Moldovan *et al.*^{33, 34} performed a computational molecular dynamics study and revealed that adsorption/desorption behavior of deoxynucleotide monophosphates (dNMPs) determined the

migration rate of these molecules when driven electrokinetically through thermoplastic nanoslits with the rate of migration determined by the molecular-dependent hydrophobicity of the dNMPs.

Recent publications of DNA separations have demonstrated unique nanoscale phenomena for free solution electrokinetic length-based separations of double-stranded (ds) DNA in glass and silicon nanofluidic devices. Cross *et al.*³⁵ showed that the length dependent mobility of DNA strands (2 kb-10 kb) electrically driven through slit-like nanochannels (19 nm and 70 nm depths). They claimed that surface interactions with channel walls and confinement played an essential role leading to the length-dependent separation. Peterson *et al.*³⁶ showed that oligonucleotides could be separated via nanochannel electrophoresis and proposed steric effects alone contributed to the residence time distribution of 100-1000 base pair (bp) oligonucleotides. Pennathur *et al.*³⁷ showed the free solution electrokinetic separations of dsDNAs in simple cross and double T glass nanofluidic channels (40 nm, 100 nm, and 1560 nm depths), where they investigated ionic strength and channel dimension effects on the separation of dsDNA from 10 bp – 100 bp in length. They suggested that separation efficiency was dependent on the finite electrical double layer (EDL) thickness with respect to the slit dimensions. The corresponding contour lengths, 3.4 – 34 nm, of the dsDNA fragments were smaller than both the persistence length and channel heights. The molecules were end-labeled with fluorescein or contained fluorescein-12-dUTP. According to their observations, the migration times of dsDNA depended on the ratio of the EDL thickness to channel half depth and the ratio of the length of the molecule to channel half depth. The best separation for these fragments were achieved in 100 nm nanochannels using sodium borate buffers at 1 mM to 10 mM; ratio of the channel critical dimension/thickness of EDL (d/λ_d) was 33.

Unfortunately, in terms of clinical applications, utilization of glass-based nanofluidic devices is challenged by the fact that they require sophisticated device fabrication techniques that are time consuming and high in cost, which can impede the use of nanochannel electrophoresis requiring disposable devices as would be the case in clinical or forensic applications. Recently, thermoplastics have become a viable substrate for nanofluidics due to their biocompatibility, optical properties comparable to glass, and their ability to be manufactured in large scale at low-cost using replication techniques, such as nanoimprint lithography (NIL).^{28, 38-40} Another benefit of thermoplastics for nanofluidics is their diverse surface chemistries, which are determined by the monomers comprising the polymer chains. For example, poly(methylmethacrylate), PMMA, possesses methyl esters. In addition, a diverse range of surface activation methods can be used to generate surface functional groups that can alter the surface chemistry of the polymer, for example changing its wettability and altering the EOF.⁴¹ UV/O₃ or O₂ plasma activation are methods that have been reported to generate oxygen-containing species for many plastics, such as carbonyls (aldehydes, ketones, carboxylic acids) and alcohols through free radical photo-initiated oxidation.^{42, 43}

There have been a limited number of studies on nanoscale separations using thermoplastic nanofluidic devices.^{4, 44} Weerakoon-Ratnayake *et al.*⁴⁵ showed the electrokinetic transport of silver nanoparticles (AgNPs) using PMMA nanoslits (only one dimension in the nanoscale). The authors were able to demonstrate size-dependent mobilities of AgNPs in free solution, which was not possible using microscale columns. Differences in the mobilities were observed for 60 nm and 100 nm AgNPs at high electric field strengths, where no intermittent motion was observed. Most recently, O’Neil *et al.*⁴⁴ showed the separation of dNMPs in free solution using thermoplastic

nanochannel devices fabricated in PMMA substrates with COC (cyclic olefin copolymer) cover plates. High electric field strengths provided better separations. In addition, the mobility order of the dNMPs was closely related to the hydrophobicity of each dNMP. However, the separation was dominated by electrophoresis compared to chromatographic mechanisms.

The majority of nanoscale separations noted above were performed on double stranded DNAs (dsDNA) utilizing glass-based nanofluidic devices. Compared with dsDNA, ssDNA is highly flexible, thermodynamically less stable and more hydrophobic.^{46,47} Published literature discussing the flexibility of ssDNA reveals a large range of persistence lengths spanning from 1– 6 nm under a variety of conditions.⁴⁸⁻⁵⁰ The base-to-base spacing is 0.43 nm compared to 0.34 nm for dsDNA. ssDNA is also amphophilic, where the nucleobases are hydrophobic, and the phosphodiester backbone is hydrophilic. Hydrogen bonding, hydrophobic interactions, and van der Waals interactions are the largest contributors to DNA-surface interactions.⁵¹ Due to the high flexibility of ssDNA, they have the ability to expose either nucleobases or the phosphodiester backbone depending on the nature of the surface the molecule is in contact with.⁵² Therefore, in nanoconfined environments where surface interactions are prominent these molecules can behave differently compared dsDNA.

In this work, we report the use of thermoplastic nanochannels (100 nm x 100 nm in depth and width, respectively) fabricated in PMMA for the free-solution electrokinetically driven separation of ssDNAs. The motivation for utilizing nanoscale electrophoresis of ssDNAs is to accommodate a nanosensor we are developing that seeks to identify low abundant point mutations using LDR. The ligated products are ssDNAs with lengths <150 bases. The nanosensor performs a solid-phase LDR and then, utilizes nanoscale electrokinetics to size-separate the LDR products specifically for

multiplexing (identify multiple point mutations in a single assay). Therefore, it is essential to optimize the separation of ssDNAs through the use of thermoplastic nanochannels with the identification efficiency dependent on the resolution between a series of ssDNA fragments. However, the results secured herein will be useful in a variety of other applications as well, which require the analysis of gel-free separations of both ds- and ssDNA fragments, especially when multiplexing is necessary.

To track the motion of ssDNA fragments labeled with ATTO 532 through the polymer nanochannels (PMMA-COC hybrid devices), laser-induced epifluorescence microscopy was used. The thermoplastic devices were fabricated by nanoimprint lithography, NIL. We found that we could separate oligonucleotides in free solution with an effective migration time that was inversely related to the length of the oligonucleotide indicating that the separation was affected by solute/wall interactions. Unique to these separations is that no monolayer coating of the polymer substrate was required and also, the channel critical dimension was much larger than the double layer thickness. Therefore, we define our separation as open tubular nanoelectrochromatography (OT-NEC). We will present results on the use of different electrochromatographic parameters and their effect on the resolution of the separation including electric field strength, effective column length, and type of PMMA.

3.2 Materials and Methods

3.2.1 Reagent and Materials

Silicon $\langle 100 \rangle$ (Si) wafers were purchased from University Wafers (Boston, MA). Impact modified (IM) and non-impact modified (NIM) PMMA substrates were purchased from ePlastics (San Diego, CA) and Good Fellow (Berwyn, PA), respectively. Cyclic olefin copolymer (COC

8007) was purchased from TOPAS Advanced Polymers (Florence, KY). COC 6015 was purchased from Knightsbridge Plastics, Inc. (Fremont, CA). UV curable polyurethane (PUA) resin was purchased from Chansung Sheet Co. Ltd. (Chuncheognam-do, Korea) ATTO 532 end labeled ssDNA with three different lengths (Oligo35, Oligo50, Oligo70) were purchased from Integrated DNA technologies (San Jose, CA) (see supporting information for sequences). 10X Ultra-pure trisborate EDTA buffer (TBE) and molecular biology grade water was purchased from Thermo Scientific (Waltham, MA).

3.2.2 Fabrication of microchannel devices

T-shaped (50 μm depth x 100 μm width and 5 cm long) microfluidic devices were hot embossed using a hot embossing machine (Wabash P3H-15-CLX, IN, USA) into PMMA. The upper platen was kept at 155°C and lower platen was kept at 80°C with 1250 psi pressure applied for 3 min. Embossed devices were diced using a bandsaw and reservoirs were mechanically drilled. Then, the devices were cleaned with 5% Micro-90, IPA, and nanopure water. Following embossing and hole drilling, the substrates were UV/O₃ treated for 16 min at 22 mW/cm² and sealed with a 150 μm thick PMMA sheet by using thermal fusion bonding at 105°C for 1 h. Microchannel dimensions were measured before and after bonding using a rapid laser-scanning confocal microscope (VK-X250, Keyence, IL, USA).

3.2.3 Free solution separation of oligonucleotides by microchip electrophoresis

The microfluidic device was primed with 50% methanol/water mixture for 5 min. Then it was filled with TBE buffer at pH 8.3. Separation was carried out using a normal mode with the injection end set as the anode, and the detection end as the cathode. Injection was initiated by applying a positive voltage to the sample reservoir and grounding the sample waste reservoir for the amount

of time required to completely fill the cross channel. The remaining reservoirs were floating during injection. After injection, a positive voltage was applied to the electrophoresis buffer reservoir and the electrophoresis waste reservoir was grounded. Detection was done 4.0 cm from injection cross using a home-built laser-induced fluorescence detector equipped with a single photon counting module.

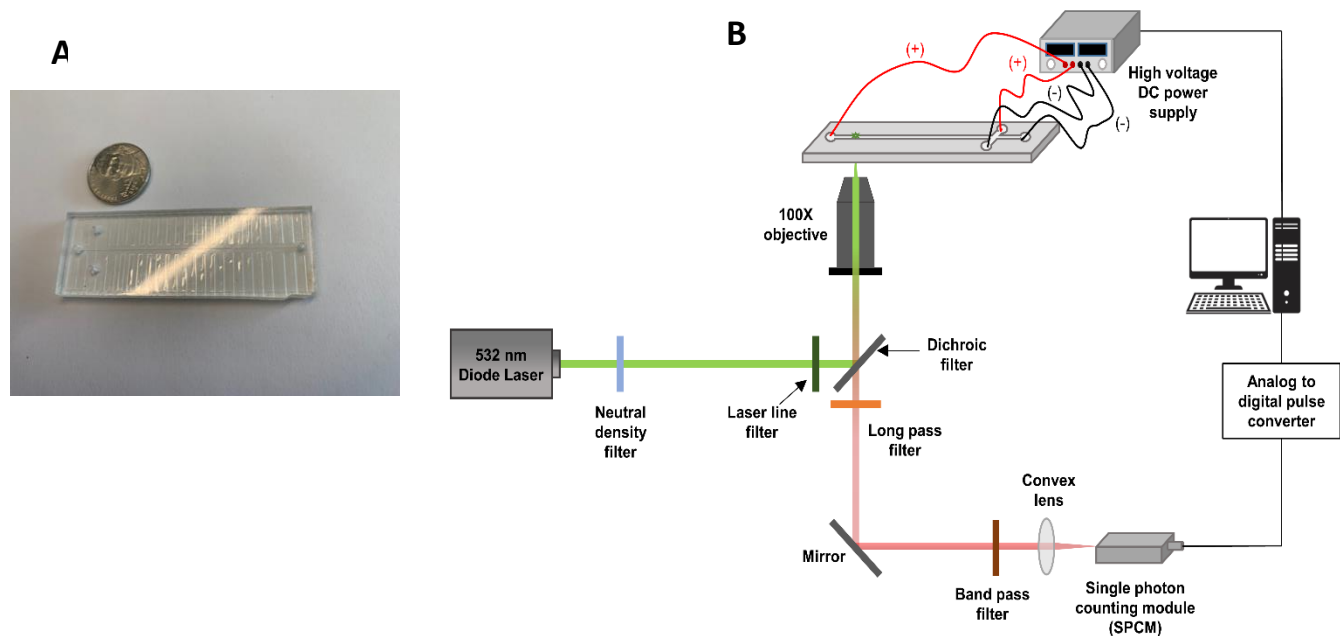


Figure 3.1: **A)** An image of the T-chip used for the microscale electrophoresis. The chip was made via hot embossing into PMMA. **B)** Schematic diagram of the in-house built microchip electrophoresis laser-induced fluorescence detector that utilized a 20 mW 532 nm excitation laser with edge filter. The detector contained a 560 nm long pass filter, 532 nm dichroic filter and SPCM-AQR single photon counting module within the optical train. A 100X high numerical aperture ($NA = 1.3$) microscope objective was used to focus the laser beam onto the microchannel and collect the fluorescence.

The laser-induced fluorescence (LIF) detector illustrated in Figure 3.1 was configured in an epillumination format having a 532 nm, 20 mW excitation laser (LaserGlow Technologies, Toronto, Ontario, Canada), XF 3085 edge filter (Horiba Scientific, Middlesex, UK), 560 nm long pass filter (Omega Optical, Brattleboro, VT), a 532 nm dichroic filter (Omega Optical Brattleboro,

VT) and a SPCM-AQR single photon counting module (Perkin Elmer Optoelectronics, Waltham, MA). A 100X high numerical aperture (NA = 1.3) microscope objective from Nikon (Natick, MA) was used to focus the laser beam onto the microchip and collect the fluorescence.

3.2.4 Fabrication of nanochannel devices

Fabrication of nanochannel devices were done by following a procedure previously reported by our group with slight modifications.^{28, 53} Access microchannels were fabricate in a Si wafer through photolithography followed by wet etching. Then, nanochannels were fabricated by focused ion beam milling into the Si wafer. Resin stamps were produced from Si master by UV curing of a PUA resin for 3 min onto a COC plate coated with a NOA72 adhesive. Next, the structures on the resin stamp were thermally imprinted onto PMMA substrates using nanoimprint lithography with a Nanonex 2500 nanoimprinting machine using air cushion press thermal imprinting. Unlike the pressing method for imprinting where solid parallel plates are used, air cushion press methods have improved uniformity in pressure and imprinting speed. The conditions used for imprinting are given in Table 3.1 for different PMMA substrates used in the experiments. Metrology of the devices were done by SEM imaging (see Figure 3.2). The depths of the nanochannels imprinted in different PMMAs were measured using a scanning probe microscope, SPM (SPM-9700HT, SHIMADZU, Japan) and are given in Table 3.1.

Table 3.1. Conditions used to imprint nanochannel devices on two different PMMA substrates using the Nanonex 2500.

Material	Tg /°C	Imprinting temp / °C	Pressure /psi	Time /s	Depth of channel/nm
IM-PMMA	105	130	300	300	112.2 nm
NIM-PMMA	122	140	300	300	114.7 nm

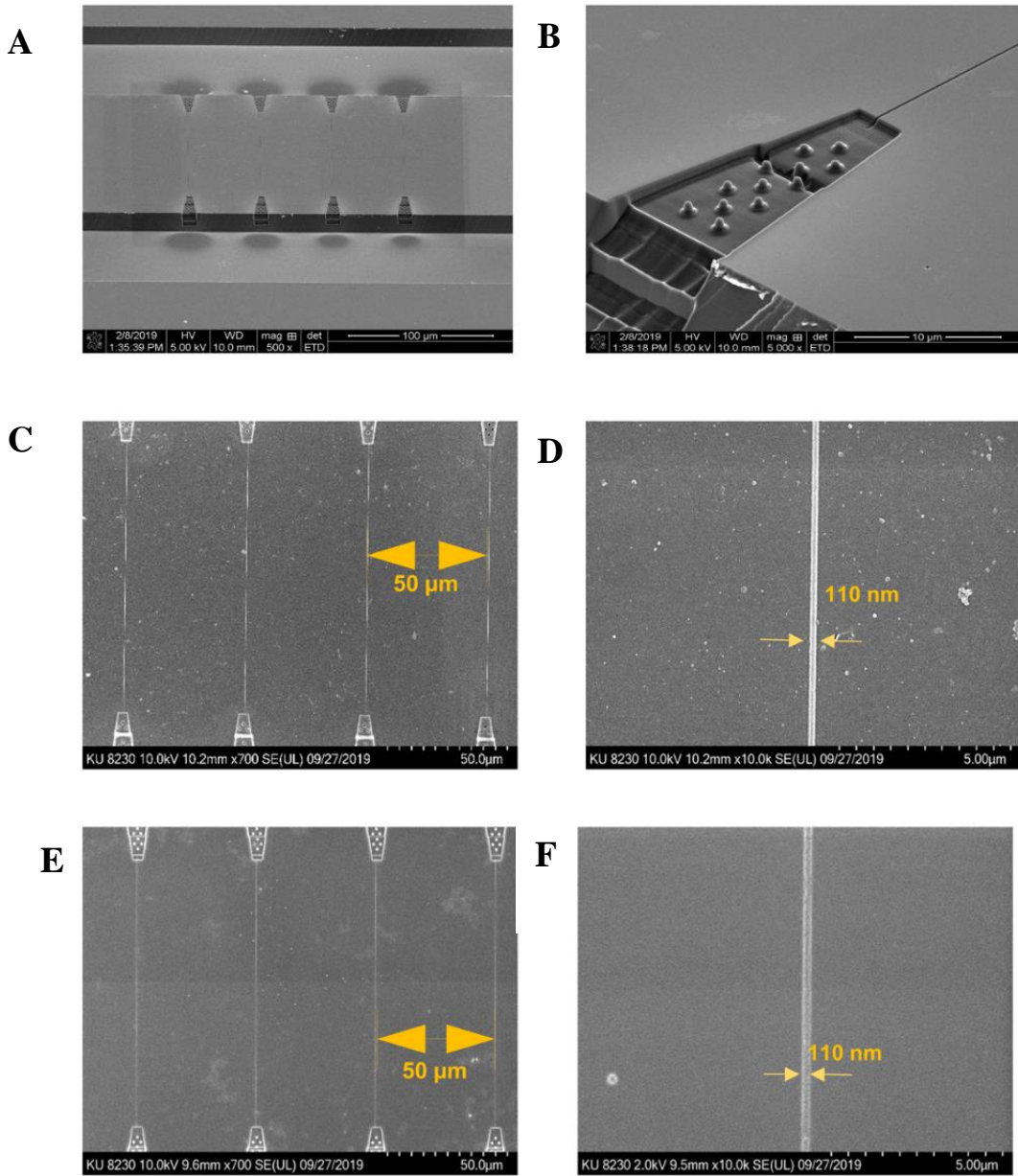


Figure 3.2. SEM images of the Si master, resin stamp, and imprinted device. **A)** An SEM of the Si master at 500X magnification. **B)** Enlarged area of the entrance funnel formed in the Si master. **C)** UV-imprinted nanochannel device to form the resin stamp with PUA. **D)** Enlarged nanochannel area in the resin stamp. **E)** Nanochannels thermally imprinted into PMMA substrate. **F)** Enlarged area of nanochannel imprinted into PMMA

After imprinting the nanochannel device, sealing was done using a COC coverplate (100 μm in thickness) using the conditions mentioned in Table 3.2

Table 3.2. Bonding conditions used to seal the nanochannel devices imprinted on two different PMMA substrates with COC8007 cover plate in Nanonex2500. Both cover plate and substrate were oxygen plasma treated prior to bonding.

Substrate-coverplate	Bonding conditions (°C, psi, min)
IM-PMMA-COC	70, 110, 15
NIM-PMMA-COC	70, 100, 15

The bond strength between the cover plate and substrate of IM-PMMA and NIM-PMMA was evaluated using a crack opening method.^{54,55} The bond strength was determined by placing a razor blade of known thickness t_b between bonded substrate and cover plate to induce an interfacial fracture with a length of L from the edge of the razor blade. If the elastic moduli of the cover plate and substrate are E_p and E_s , respectively, the bond strength is determined using equation (3.1), where t_s and t_p are the thickness of the cover plate and substrate, respectively. The elastic moduli of IM-PMMA was 1.6 GPa and for NIM-PMMA it was 3.3 GPa that was obtained experimentally using a Q800 dynamic mechanical analyzer (TA instruments, New Castle, DE). The elastic moduli of the COC 8007 cover plate was 3.0 GPa, which was provided by the manufacturer. All measurements were performed five times and the average bond strength is reported along with the standard deviation in measurements in Table 3.3. According to bond strength data there is no

significant difference between the bond strength of IM-PMMA-COC devices and NIM-PMMA-COC devices

$$\gamma = \frac{3t_b^2 E_s t_s^3 E_p t_p^3}{16L^4(E_s t_s^3 + E_p t_p^3)} \quad (3.1)$$

Table 3.3. Calculated bond strength by crack test for IM-PMMA and NIM-PMMA using equation (3.1).

Assembled device	NIM-PMMA	IM-PMMA
Bond strength (mJ/cm ²)	0.086±0.014	0.084±0.018

3.2.5 Surface roughness measurements by AFM

To determine surface roughness of IM-PMMA and NIM-PMMA, an AFM analysis was conducted. The tip used for imaging was operated at a frequency of 300 kHz and a radius below 15 nm. Tapping mode was used with a scanning frequency of 1 Hz. First, IM-PMMA and NIM-PMMA surfaces (1 cm x 1 cm) were imaged by AFM to measure roughness without exposing to oxygen plasma. Then, both PMMA surfaces were exposed to oxygen plasma at 50 mW power for 1 min and surface roughness was measured by AFM and RMS (root mean square roughness) was reported for each of these different surfaces.

3.2.6 EOF measurements

The current monitoring method described by Huan *et al.*³⁴ was used to measure the EOF in fabricated nanochannel devices.³⁴ A nanochannel device possessing a single nanochannel (107 µm long, 100 nm deep and 100 nm wide) connecting two access microchannels was fabricated as described previously. The chip was first primed with 50% v/v water/methanol, then drained, and flushed with nuclease free water. Then, the device was filled with 45.0 mM TBE buffer and allowed to equilibrate for 4 min under a 1 V DC bias. After achieving a constant current trace, one reservoir was replaced by 48.0 mM TBE. Pt electrodes were placed in the reservoirs at each end of the nanochannel under a 1 V DC bias. Signals were acquired using pClamp10 software and Digidata 1440B low noise digitizer set at a rate of 10 kHz sampling frequency.

3.2.7 Detection system for the nanoelectrochromatography

All fluorescence imaging was done using Nikon TE2000 inverted microscope (Nikon, Minato-ku, Tokyo, Japan), which was equipped with a 100x oil immersion objective (NA-1.3). A Keplerian beam expander was used to expand the Gaussian laser beam to completely backfill the microscope objective. The lower intensity wings were knocked out using an iris to ensure uniform laser intensity within the microscope's field-of-view. Kohler epillumination was used to focus the laser beam to the back of a microscope objective to allow uniform irradiation of the entire field-of-view. The excitation beam was passed through a 532 nm laser line filter (F1) and dichroic filter (DF). The emission signal was collected by the microscope objective, passed though the dichroic filter, spectrally selected using a long pass filter (F2), band pass filter (F3), and imaged onto an iXon 897 EMCCD camera (Andor Technologies Ltd, Belfast, United Kingdom), which was controlled by Metamorph software. See Figure 3.3.

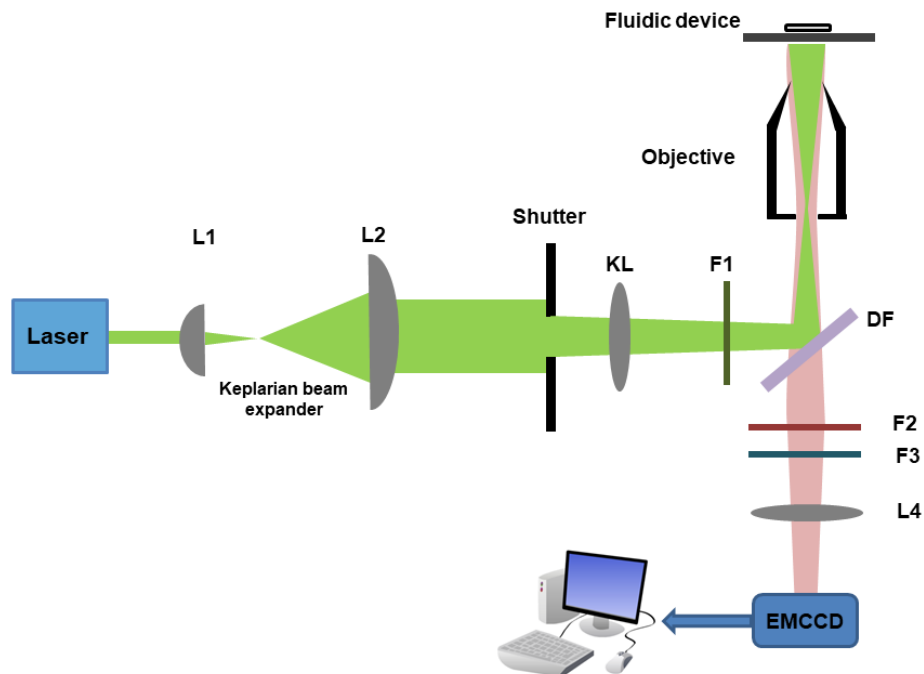


Figure 3.3: The optical setup of the fluorescence imaging system. The Gaussian beam from the laser (Nd:YAG; $\lambda_{ex} = 532$ nm; $P = 0.01\text{-}5$ W; 2.2 mm beam diameter) was expanded 10x using a Keplerian beam expander and the wings were knocked out with an iris that ensured uniform laser intensity in the field-of view and complete backfilling of the objective (OBJ). The beam was focused into the back of a 100x oil immersion objective

3.2.8 Nanoelectrochromatographic separation of ssDNAs

Assembled nanochannel devices were primed with 50 % methanol for 5 minutes. Then using a vacuum pump, the methanol was removed from the nanofluidic device. Then it was filled with 45 mM TBE buffer at pH 8.3 and allowed to equilibrate for 10 minutes. ATTO532 labeled oligonucleotides solutions of 200 nM were prepared in 45mM TBE. Next carrier electrolyte in one of the reservoirs connecting microchannels was replaced with oligonucleotide solution. Afterwards the carrier electrolyte in the opposite side of same microchannel was removed and vacuum was applied to make sure it was completely filled. Once microchannel was filled, all the

other reservoirs were filled with same volume of carrier electrolyte. Finally, square voltage (V_{pp}) was applied using an ATTEN ATF20B function waveform generator for a period of 10 s to allow for multiple injections of the dye labeled oligonucleotides to nanochannels. Events were recorded for 18000 frames allowing multiple events to be analyzed.

3.2.9 Data analysis

ImageJ software⁵⁶ was used to analyze the fluorescence intensity generated by the ATTO 532-labeled ssDNAs as they migrated through the plastic nanochannels. Videos collected using the imaging microscope's EMCCD camera were imported into ImageJ software and the time for the dye front to move between two detection windows placed at the entrance and exit of nanochannel was determined. The data was then exported into Origin pro 8.5, where the data was smoothed and the time of the fluorescence front reaching the entrance (peak 1) and the exit (peak 2) evaluated. The time difference (Δt) between peaks 1 and 2 was taken as the migration time (see Figure 3.4) for each of the ssDNAs.

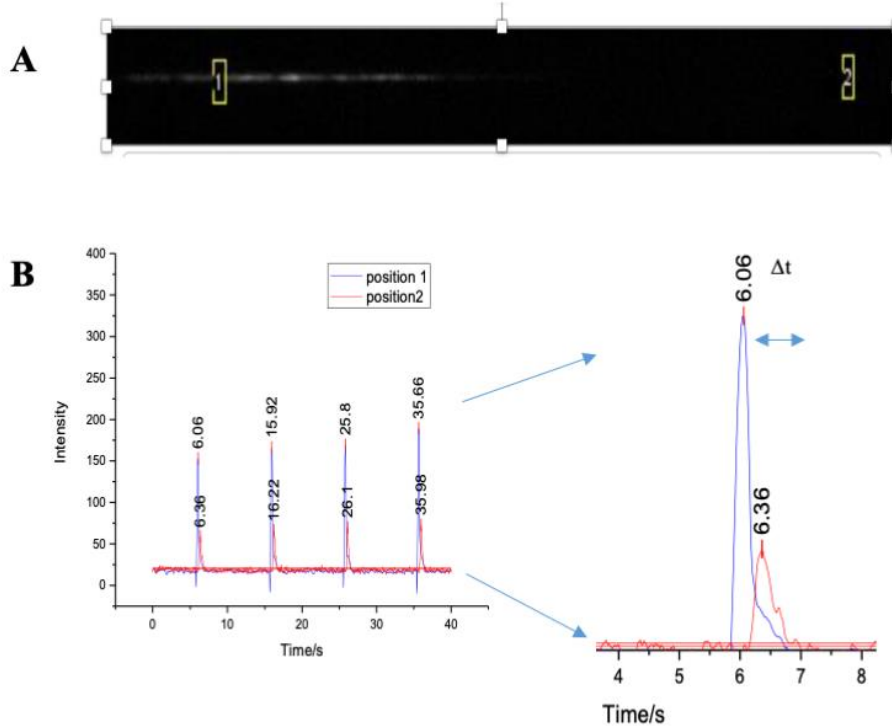


Figure 3.4. Representation of how the nanochannel electrochromatography and data analysis were performed. **A)** A of picture a fluorescently labeled ss-DNA migrating through a thermoplastic nanochannel. The yellow boxes indicate Positions (Pos) 1 and 2. **B)** The fluorescence intensity profile of one injection event was enlarged at Pos1 and 2.

The time difference was used to calculate the effective mobility given below using equation (3.2);

$$\mu_{\text{eff}} = (lL/\Delta tV) \quad (3.2)$$

where l is the distance between two detection windows, L is the total nanochannel length, and V is the applied voltage (Figure 3.5).

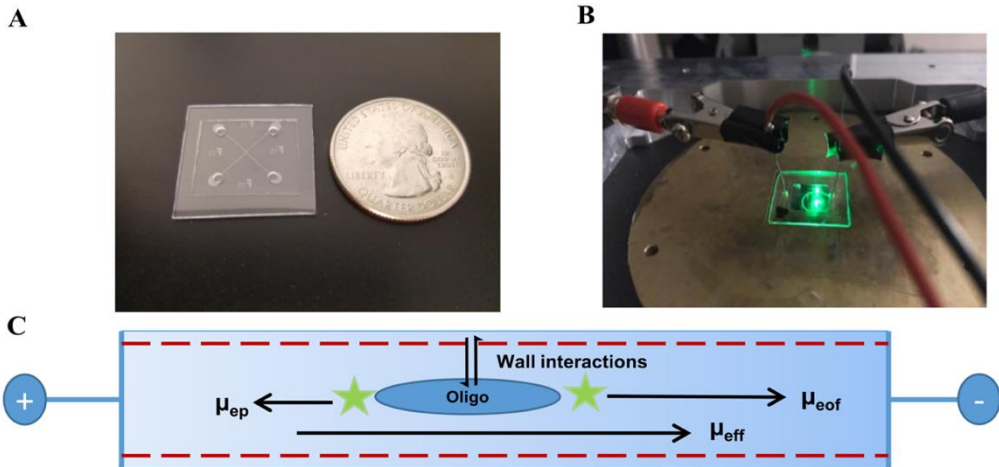


Figure 3.5. **A)** Image of a PMMA/COC nanochannel device (100 nm x 100 nm x 107 μm in depth, width, and length, respectively). **B)** Experimental setup for nanoelectrochromatography experiment where anode (red) is at the sample input reservoir and the cathode at the waste reservoir. **C)** Schematic of a nanochannel when an external electric field was applied. Electroosmotic flow (μ_{eof}) was from anode to cathode while the electrophoretic mobility (μ_{ep}) of negatively charged dye-labeled ssDNA was toward the anode. In addition to μ_{ep} and μ_{eof} , the ssDNA can interact with wall of the channel giving rise to μ_{eff} .

3.3 Results and Discussion

3.3.1 Microscale separation of ssDNAs

To understand separation of ssDNA scaling effects with respect to channel dimensions (width and depth; microchannel versus nanochannel), we first investigated the free solution electrokinetic separation of dye-labeled ssDNAs of different lengths (35mer, 50mer, 70mer) in 45 mM TBE buffer (pH 8.3) using a PMMA microchannel device (column length was 5 cm, width = 100 μm , and depth = 50 μm). The ssDNAs migrated from anode to cathode in the same direction as the EOF. As seen in Figure 3.6, all three ssDNAs comigrated with an apparent mobility of $1.80 \times 10^{-5} \text{ cm}^2/\text{Vs}$. Here, the free draining behavior of the ssDNA occurred, which resulted in the

electrophoretic mobility to be independent of the ssDNA length. Thus, electrophoresis was the dominate separation mechanism. For ssDNAs, it has been shown that the electrophoretic mobility increases with increasing nucleotides to ~10 nucleotides and then the mobility becomes insensitive to increasing nucleotide length in free solution using fused silica capillaries.⁵⁷ This is in agreement with our observations in which the ssDNA comigrated in free solution even using a PMMA microchip, which has different surface chemistry compared to fused silica and different EOFs.

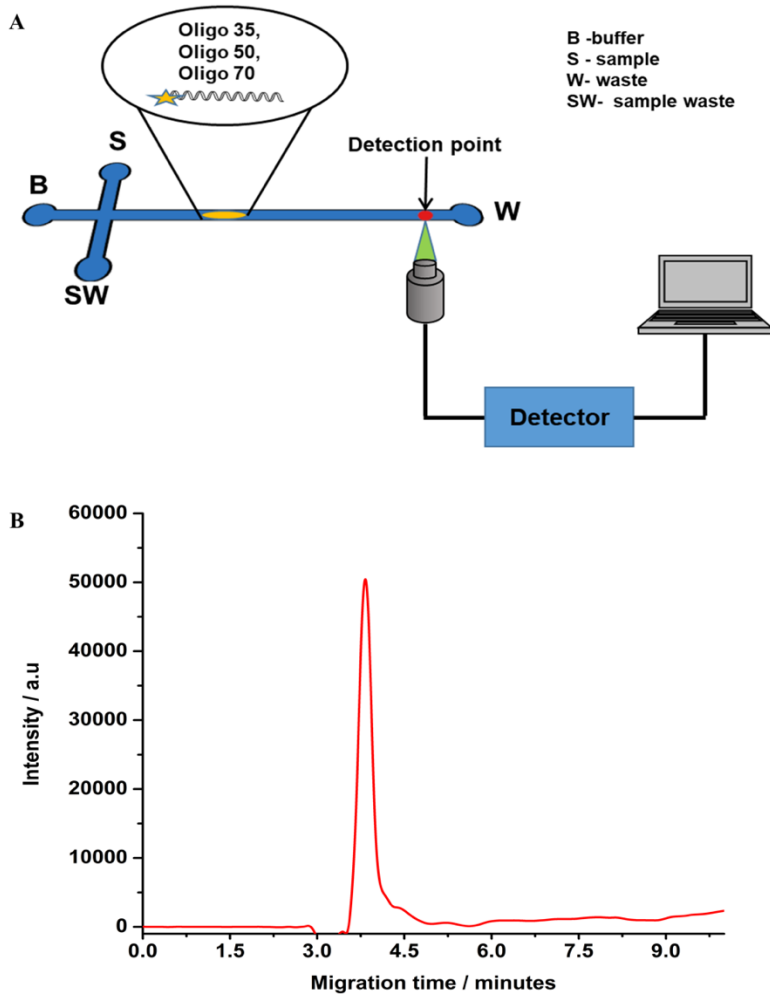


Figure 3.6.A) Schematic diagram of experimental set up used for the microscale electrophoresis, where a T shaped microchip is used. A sample plug was electrokinetically introduced into the separation channel by applying a potential across the S and SW reservoirs. A photon avalanche detector was used to capture the fluorescence signal at the detection point. **B)** Electropherogram obtained for the free solution microchip (PMMA) electrophoresis of ssDNAs with microchannel dimensions of 50 μm x 100 μm (depth and width respectively) and 5.0 cm in length. The applied voltage for the electrophoresis was 5 kV (1000 V/cm) with a 45 mM TBE buffer (pH 8.3) used as the background electrolyte. The of ssDNAs (5 μM) were injected electrokinetically into the separation channel.

3.3.2 Material effects on EOF and ssDNA separations

3.3.2.1 Material effects on electroosmotic flow

Nanochannels were fabricated using two different types of PMMA substrates to understand material effects on the nanoscale separation of ssDNAs. PMMA is a brittle thermoplastic with excellent optical properties. Two types of sheet PMMA that were evaluated were impact modified PMMA (IM-PMMA) and non-impact modified PMMA (NIM-PMMA). Because NIM-PMMA has a low impact strength meaning that it has a low capacity to absorb energy during deformation, to improve the impact strength acrylic modifiers are blended with the polymer matrix without degrading its optical transparency; this is called IM-PMMA.⁵⁸ These two materials were tested because each PMMA plastic is activated using O₂ plasma and this activation process will alter the surface charge through photo-oxidation reactions creating carboxylic acids groups as we have shown in our previous work.^{28, 59} Because the extent of surface carboxylic acids formed is dependent on the material as well as the distribution of charges on the surface, it was hypothesized that the presence of the acrylic modifiers could affect the separation performance using nanoscale electrophoresis.⁵⁹

Surface roughness in nanofluidic devices may occur either during replication due to imperfections in the molding tool,⁶⁰ or following activation with an O₂ plasma.²⁸ Molecular dynamic (MD) studies have discovered that surface roughness has a large influence on the EOF and surface wettability depending on the magnitude of the roughness height (h_r). The EOF can be significantly different for a situation where $\lambda_d/h_r \ll 1$ compared to a situation where $\lambda_d/h_r \sim 1$ and when surface roughness is comparable to the thickness of the EDL it can affect the magnitude of the EOF⁶¹ and streaming potential.⁶² However, the effect becomes insignificant when the thickness

of the EDL is larger than the roughness height.⁶³ According to Zhang *et al.*⁶⁴ the fluid flow experiences great resistance on rough surfaces causing molecules to adsorb onto the surface of the nanochannel. In addition, their simulations indicated a decrease in the zeta potential and EOF with increasing roughness, which agreed with other MD simulation studies.⁶⁵ We also hypothesized that the presence of the acrylic modifiers may also affect the surface roughness compared to PMMA without the acrylic modifiers following O₂ plasma activation, which would affect the EOF.

We first measured the surface roughness of sheet IM-PMMA and NIM-PMMA before and after O₂ plasma activation to serve as a model for our nanochannel devices. Surface topographical profiling was done using sheet PMMAs due to the difficulties associated with using AFM profiling of nanochannels arising from AFM tip-wall interactions. Figures 3.7A and 3.7B show AFM images of IM-PMMA and NIM-PMMA without O₂ plasma activation, where Figures 3.7 C and D show AFM images of IM-PMMA and NIM-PMMA after O₂ plasma activation respectively. After exposing to O₂ plasma the root mean square roughness (RMS) of the surface increased for both materials. (see Figure 3.7E) O₂ plasma not only modified the surface chemically, but also created sub-nanometer and nanometer surface roughness features through slight etching of the surface during the activation process.⁶⁰ The surface roughness of IM-PMMA prior to and after O₂ plasma activation was much higher than that of NIM-PMMA. Higher RMS roughness for IM-PMMA may be due to the acrylic modifiers present in IM-PMMA; after O₂ plasma treatment, difference in etching rates for the additives and PMMA in IM-PMMA will enhance its roughness with respect to NIM-PMMA. Thus, the surface of NIM-PMMA nanochannel devices would be expected to be smoother than that of IM-PMMA nanochannels.

The EOF of nanochannel devices was measured by the buffer replacement method.³⁴ For these experiments, we used O₂ plasma modified nanochannel devices using both IM-PMMA and NIM-PMMA substrates. According to our previous studies, the majority of surface functionalities following O₂ plasma activation of PMMA are carboxylic acid groups, which provide a negatively charged surface at pH 8.3 due to deprotonation of the carboxy groups.^{28, 66} The thickness of the EDL in these experiments was estimated to be ~1.3 nm at the TBE buffer concentrations used herein. The zeta potential was calculated using equation (3.3);

$$\mu_{eof} = \varepsilon\zeta / 4\pi\eta \quad (3.3)$$

As seen in Figure 3.7F, the EOF and zeta potential were smaller for IM-PMMA compared to that of NIM-PMMA. These observations are in agreement with the aforementioned molecular dynamic simulation results, which indicated increased surface roughness typically reduces the EOF. In addition, IM-PMMA also showed lower zeta potential compared to NIM-PMMA, which could mean that the acrylic modifiers are less prone to undergo surface photo-oxidation during O₂ plasma treatment. The EOF mobility measured for NIM-PMMA (4.1×10^{-4} cm²/Vs) and IM-PMMA (2.2×10^{-4} cm²/Vs) is higher than the experimentally measured EOF reported by Uba *et al.*²⁸ (1.02×10^{-4} cm²/Vs), but in closer agreement with their expected EOF mobility (4.74×10^{-4} cm²/Vs) calculated using surface charge data.^{28, 67}

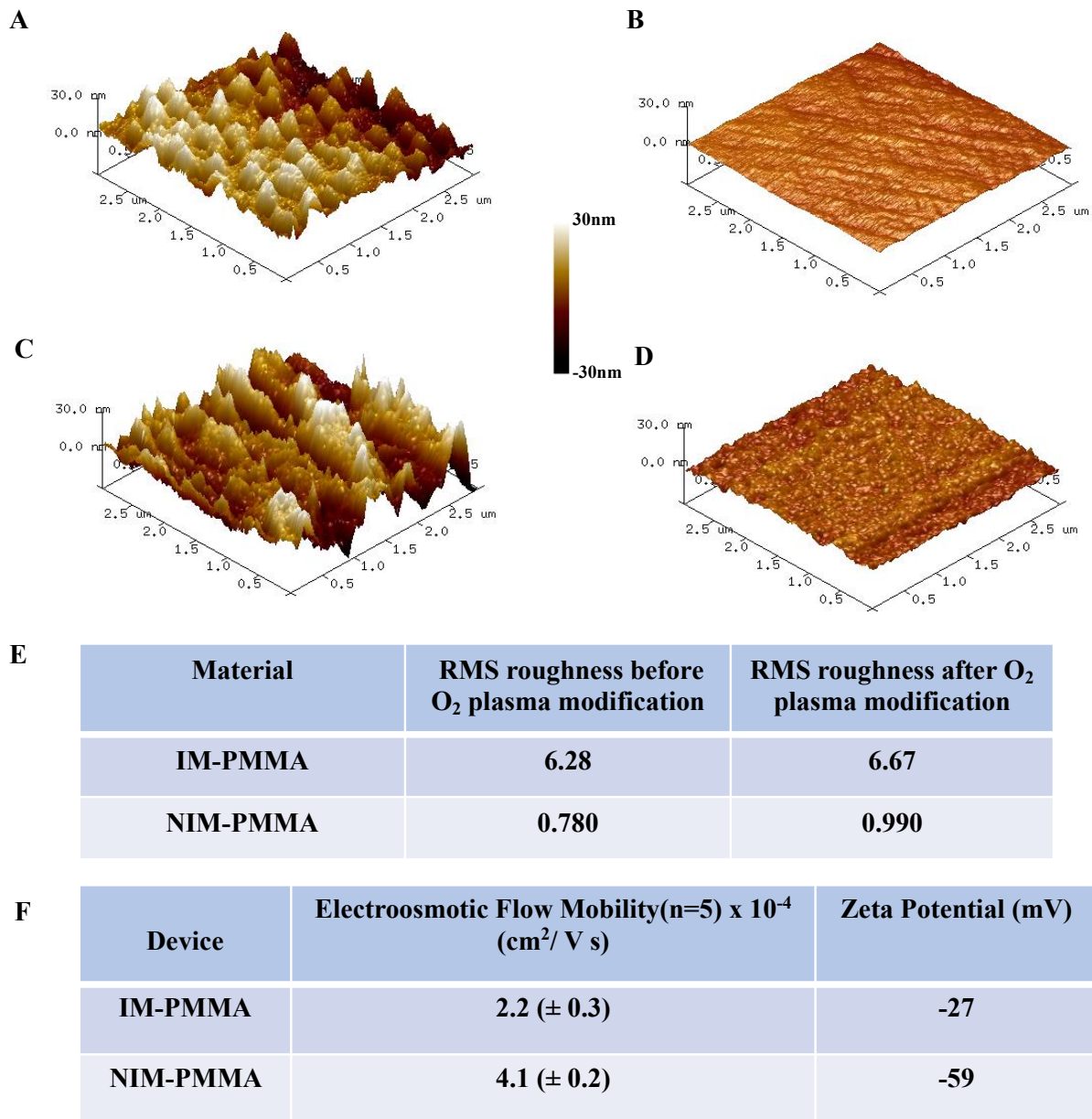


Figure 3.7. Characterization of surface roughness by AFM for IM-PMMA and NIM-PMMA surfaces before and after O₂ plasma activation. Shown are AFM images of: **A**) IM-PMMA; **B**) NIM-PMMA; **C**) O₂ plasma treated IM-PMMA; and **D**) O₂ plasma treated NIM PMMA. Plasma activation was done at 50 mW for 1 min, which is similar to conditions used during bonding of nanochannel devices.²⁸ These images were taken by scanning an area of 3 μ m x 3 μ m. **E**) Comparison of the measured root mean square (RMS) roughness of both PMMA types before and after O₂ plasma activation. **F**) The measured EOF for NIM-PMMA and IM-PMMA nanochannel devices as well as the zeta potential following O₂ plasma activation (EOF measured at pH = 8.3).

3.3.3 Open-tubular nanoelectrochromatography (OT-NEC) separation of ssDNAs

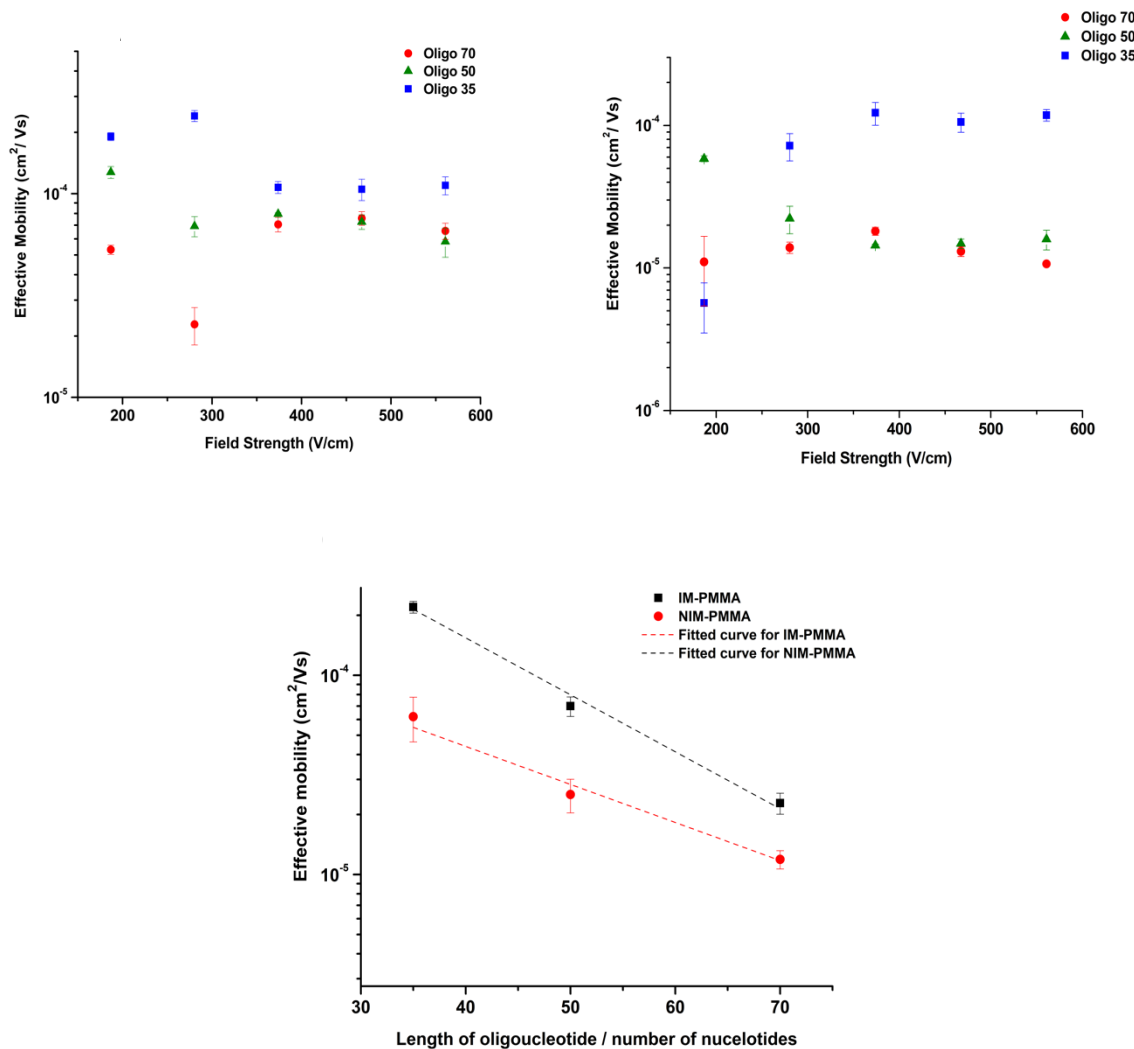


Figure 3.8. A) Effective mobility of oligonucleotides vs. the field strength in NIM-PMMA (substrate) – COC 8007 (cover plate) nanochannels (100 nm depth x100 nm width and 104 μ m length). B) Effective mobility of oligonucleotides vs. the field strength in IM-PMMA (substrate)-COC8007 (cover plate) nanochannels (100 nm depth x100 nm width and 104 nm length) C) semilog plot of effective mobility vs length of oligonucleotides in NIM-PMMA and IM-PMMA.

Because the free solution electrokinetic separation of the ssDNAs were not observed using PMMA-based microchip devices, we sought to determine if reducing the size of the channel could result in the ability to electrokinetically sort the model ssDNAs in free solution using thermoplastic nanochannels (dimensions were 110 nm x 110 nm in depth and width, respectively). Figure 3.8 shows the effective mobilities at varying field strengths. The background electrolyte concentration used here was 45 mM TBE resulting in a thickness of the EDL of 1.3 nm. With this EDL thickness, the ratio of the channel height to EDL thickness (d/λ_d) was ~80, which would suggest a plug-like flow profile,⁴ indicating that transverse electromigration would not be in effect here.⁶⁸ But, as can be seen in Figure 3.8A and 3.8B, each of the ssDNA models have different effective mobilities indicating that they could be separated using nanocolumns in both IM-PMMA and NIM-PMMA. So why is not the same type of separation observed in microchip electrophoresis (see Figure 3.6)? Because the nanochannel dimensions (depth and width) are much smaller than in the case of the microchannel resulting in a significantly higher surface area-to-volume ratio in nanochannel (~1000 times higher), the nanochannel allows for frequent solute-wall interactions and thus, the separation can be influenced by potential chromatographic effects. In contrast, the microchannel due to its larger size allows for very infrequent interactions between the solutes and the PMMA wall. Because significantly fewer wall interactions are expected in the microchannel, the electrokinetic transport of the model ssDNAs are dominated by electrophoretic effects which result in no observable separation due to the free draining behavior of DNAs in free solution.

Therefore, we define the nanoscale separation observed here to be open tubular nanoelectrochromatography (OT-NEC) and thus use the term effective mobility typically used in conventional capillary electrochromatography (CEC), where analytes are separated according to

their partitioning between both the liquid and stationary phase and electrophoretic mobilities.^{69, 70} The flat flow profile of the EOF provides better efficiencies than that associated with the parabolic flow profiles obtained using pressure-driven flows. In our experiment, the dimensions of the separation column are in the nanoscale and the background carrier electrolyte acts as the mobile phase, which is driven through the nanochannel by the EOF. Instead of a capillary in which the wall is coated with a stationary phase or the column is packed with silica particles coated with a stationary phase, we utilized here an open nanochannel with the surface carboxyl groups formed during O₂ plasma activation of the thermoplastic serving as the stationary phase. As such, for our OT-NEC we can forgo the chemical steps of forming the stationary phase or packing the column.

The velocity (V) of an analyte moving through the nanochannel is defined by equation 3.4, where k' is the capacity factor:⁶⁹

$$V = \left(\frac{1}{1+k'} \right) V_{app} \quad (3.4)$$

For a given solute, V_{app} (apparent velocity) is the sum of the EOF velocity and the electrophoretic velocity of a particular solute. The effective mobility (μ_{eff}) for a solute migrating through the thermoplastic nanochannel can be deduced by dividing equation (3.4) by the electric field strength (E ; V cm⁻¹) is given by equation (3.5). In OT-NEC, solutes with similar apparent mobilities [μ_{app} - see equation (3.6)] can have different effective mobilities depending on the degree of wall interactions they experience within the nanochannel.

$$\mu_{eff} = \left(\frac{1}{1+k} \right) \mu_{app}. \quad (3.5)$$

$$\mu_{app} = \mu_{eof} + \mu_{ep} \quad (3.6)$$

3.3.2.2 Effect of electric field strength on the effective mobility

The radius of gyration (R_g) of each ssDNA is calculated by $R_g = \sqrt{\sigma L/3}$ ⁵⁷ where σ is the persistence length (5 nm)⁷¹ of the ssDNA and L is the contour length (L= number of nucleotides x distance between two adjacent nucleotides - 0.43 nm). The values of the R_g for each of the model ssDNAs are given in Table 3.4. According to the calculated R_g values for these ssDNA, $R_g <$ channel dimension (h) in all cases and the persistence length of ssDNA<< channel depth, and thus, we can assume that these ssDNA migrate through the nanochannel as randomly coiled molecules.

Table 3.4. Calculated radius of gyration of ssDNA by using the equation $R_g = \sqrt{\sigma L/3}$ where σ is the persistence length (5 nm)⁷¹ of the ssDNA and L is the contour length. [L= number of nucleotides x length per (0.43 nm)].

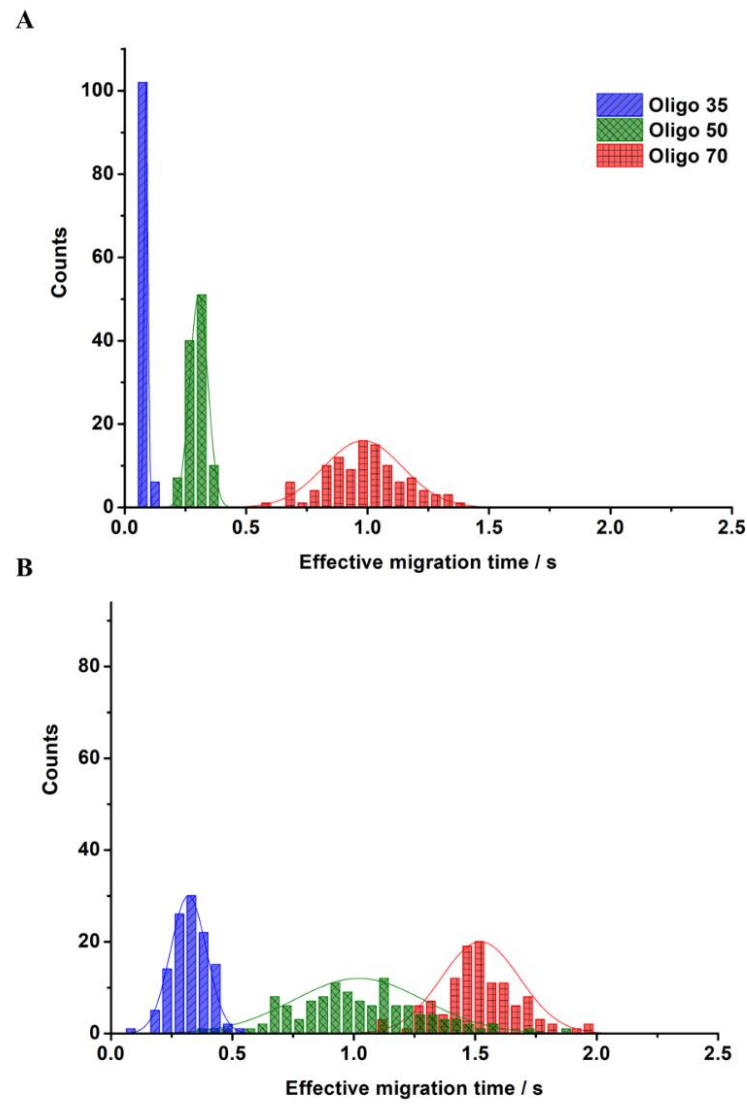
Radius of gyration (R_g) /nm	
Oligo 35	5.0
Oligo 50	5.9
Oligo 70	7.1

As evident from Figures 3.8A and 3.8B, the effective mobility of each ssDNA does not depend on the electric field strength in both materials except for the electric field strengths < 280 V/cm. The field strength dependency of the apparent mobility has been reported for the electrokinetic transport of molecules in nanochannels and arises from intermittent motion^{28, 44, 45}. Intermittent motion can be due to either solute/wall interactions or dielectrophoretic trapping induced by inhomogeneous electric fields caused by surface roughness. At low electric field strengths, the

molecules migrate slower than the high electric field strengths and have more time to interact with the nanochannel wall. We believe similar effects are responsible for the field dependent mobility observed in these ssDNA at the electric field strengths ≤ 280 V/cm. In addition to the field independent mobility observed at electric fields > 280 V/cm, the effective mobility difference among different length of ssDNA is lost. For example, the apparent mobility of Oligo 50 and Oligo 70 approach each other in both PMMA substrates. This may have resulted from the lack of interactions of ssDNA with the nanochannel walls due to higher EOF velocities at high electric field strength ($V_{eof} = \mu_{eof} E$).

In Figure 3.8C we present the relationship between the effective mobility and the length of the ssDNA at 280 V/cm for both IM-PMMA and NIM-PMMA. The effective mobility and the length of the ssDNA are related through an exponential function $y = 0.002e^{(-0.064x)}$ where y is the effective mobility and x is the length of the ssDNA for NIM-PMMA. In the case of IM-PMMA this relationship was found to be $y = 0.003e^{(-0.047x)}$. By using the average standard deviation of the effective mobility of 3 ssDNA, the smallest distinguishable nucleotide length difference is ~ 3 nucleotide for both NIM-PMMA and IM-PMMA.

3.3.2.3 Separation of oligonucleotides in IM-PMMA and NIM-PMMA



	Oligo 35		Oligo 50		Oligo 70	
	IM- PMMA	NIM-PMMA	IM-PMMA	NIM-PMMA	IM- PMMA	NIM-PMMA
Oligo 35	-	-		2.6	2.4	2.8
Oligo 50	0.9	2.6	-	-	0.6	1.8
Oligo 70	2.4	2.8	0.6	1.8	-	-

Figure 3.9 **A)** Histogram of effective migration time of Oligo 35, Oligo 50 and Oligo 70 at a field strength of 280 V/cm that were separated in NIM-PMMA-COC8007 device. **B)** Histogram of effective migration time of Oligo 35, Oligo 50 and Oligo 70 at a field strength of 280 V/cm that were separated in IM-PMMA-COC 8007 device. Histograms were fitted in to a Gaussian distribution and each bin represent 0.05 s for n=100 events. **C)** Calculated separation resolution between the 3 ssDNA.

Figure 3.9 shows histograms of the effective migration time of the model ssDNAs in IM-PMMA and NIM-PMMA nanochannel devices at an electric field strength of 280 V/cm ($E = 280$ V/cm). Figures 3.9A and 3.9B show histograms of effective migration times for the ATTO 532 labeled ssDNAs in NIM-PMMA and IM-PMMA at a field strength of 280 V/cm. This field strength was selected because it provided the best separation in terms of resolution for all ssDNAs in both IM-PMMA and NIM-PMMA nanochannel devices. The migration order of the ssDNAs in both materials was similar; Oligo35 < Oligo50 < Oligo70, where the number indicates the number of nucleotides in the ssDNA. The migration time increased with increasing chain length of these ssDNAs. These thermoplastic nanochannels were activated with O_2 plasma to give carboxylic acid groups on their surface. At pH 8.3, these groups are expected to be deprotonated leading to a hydrophilic surface and producing an EOF that travels from anode to cathode.

ssDNAs are amphiphilic and because of their high single strand character they have the ability to expose either their phosphodiester backbone or nucleobases to the surface. Therefore, these ssDNA can interact with the surface through electrostatic interactions, van der Waals interactions, hydrogen bonding, and/or hydrophobic interactions.²⁸ Because the nanochannel surface is negatively charged, the question arises: Can the ssDNAs overcome electrostatic effects arising from the channel surface to allow sufficient interactions with the wall either through hydrogen bonding and/or hydrophobic interactions to allow separation? Previous studies of DNA adsorption to silica surfaces have shown that even though electrostatic repulsions exist between the negatively charged DNA and the negatively charged silica surface when the solution pH is greater than the pKa of the surface silanol groups, the phosphate/silanol and hydrophobic interactions are sufficiently strong to overcome electrostatic repulsions.⁷² In addition to the aforementioned

interactions, several investigators have proposed that ssDNA adsorption to silica surfaces can occur through hydrogen bonding via the exposed nucleobases and the silica surface. In light of these observations, we believe that ssDNA when moving electrokinetically through thermoplastic nanochannels will overcome electrostatic repulsions arising from the negatively charged carboxylated surface and interact with the channel wall via hydrogen bonding and/or hydrophobic interactions. If this is indeed the case, then the longer ssDNAs should show a longer effective migration time than the shorter ssDNAs. If the transport was solely arising from the electrophoretic mobility of the oligonucleotides, they should have identical mobilities as electrophoretic mobilities of oligonucleotides are similar regardless of their length, especially for $d/\lambda_d = 80$ (plug-like flow). However, previous research has shown that DNA can be separated in free solution using glass-based devices when d/λ_d is close to unity.⁴

The resolution of adjacent peaks was calculated using $R = 1.18(t_{m2}-t_{m1}) / (w_{0.51}+w_{0.52})$, where t_m and t_{m2} are migration times of the peak pair and $w_{0.51}, w_{0.52}$ are the full width at half maximum for each of the Gaussian peaks. The separation resolution between three oligonucleotides in NIM-PMMA ranged from 1.8- 2.6 (Figure 3.9 C), which exceeded the baseline resolution ($R=1.5$). The separation resolution between three ssDNA in IM-PMMA ranged from 0.6-2.4.(Figure 3.9B). Only the separation resolution between Oligo 35 and Oligo 70 ($R=2.4$) exceeded the baseline separation in IM-PMMA. A recent study by O’Neil *et al.*⁷³ on surface charge mapping of IM-PMMA via super resolution imaging showed that there is a heterogeneous distribution of surface charge groups on these surfaces after oxygen plasma activation. This heterogeneous surface charge distribution in IM-PMMA created “patches” of unmodified polymer on the surface. These hydrophobic “patches” on the surface of IM-PMMA can increase the hydrophobic interactions

with the exposed nucleobases in ssDNA in addition to hydrogen bonding and van der Waal interactions (exposed nucleobases in ssDNA are hydrophobic in nature favor hydrophobic surfaces). This could increase the adsorption and desorption of the ssDNA through hydrophobic interactions leading to broader peaks compared to the NIM-PMMA. The more hydrophilic nanochannel wall in NIM-PMMA, do not have a favorable hydrophobic surface to interact, with the nucleobases in ssDNA therefore in here ssDNA will prefer to form hydrogen bonds and van der Waals interactions with the surface leading to length -based separation of DNA. In addition, broad peaks observed for the separation in IM-PMMA with lower resolution could be due to the increased surface roughness observed in IM-PMMA surface compared to NIM-PMMA because, rough surface or the variation in channel profile effectively increase the distance of the ssDNA molecule near the channel wall must travel while subject to a smaller field with respect to ssDNA molecule in the bulk flow.

The retention factor(k') is another parameter that measures the partitioning of a solute with the stationary phase, which in this case is the PMMA nanochannel wall that has been O₂ plasma activated. The retention factor for a charged analyte in NEC can be deduced from the equation (3.7),^{69, 74} where t_{eff} is the effective migration time of a charged analyte, t_{eof} migration time of a non-retained analyte and k_e'' is the velocity factor. k_e'' can be obtained by equation (3.8) where μ_{ep} is the electrophoretic mobility of an analyte with no wall interactions and μ_{eof} is the EOF mobility. In the absence of wall interactions condition, all oligonucleotides migrate with the same electrophoretic mobility due to the free draining behavior of ssDNAs as explained by Figure 3.6 in the main text. Therefore, $\left(\frac{\mu_{ep}}{\mu_{eof}}\right)$ is constant for all oligonucleotides. Hence k' can be calculated

using equation (3.9). Calculated retention factors for the 3 ssDNAs, using equation (3.9), are given in Table 3.5

$$k' = \frac{t_{eff}(1+k_e'') - t_{eof}}{t_{eof}} \quad (3.7)$$

$$k_e'' = -\left(\frac{\mu_{ep}}{\mu_{eof}}\right) \quad (3.8)$$

$$k' \sim \frac{t_{eff} - t_{eof}}{t_{eof}} \quad (3.9)$$

Table 3.5. Retention factors of oligonucleotides in IM-PMMA and NIM-PMMA.

	Retention factor (k')	
	IM-PMMA	NIM-PMMA
Oligo 35	2.1	0.7
Oligo 50	9	5
Oligo 70	14	18

The retention factor increased with increasing length of the ssDNA in both materials. For IM-PMMA, retention factors ranged from 2.1 – 14 and NIM-PMMA retention factors ranged from 0.7 – 18. Oligo35 had the lowest retention factor in both materials while Oligo70 showed the highest retention factor. These results are in agreement with molecular dynamic simulations done by Monserud *et al.*, ⁷⁵ where the residence time of oligonucleotides increased with increasing length of DNA due to increased interactions with a hydrophilic surface. One can anticipates that larger

molecules will have greater stationary phase interactions. Regardless of whether the molecular conformation is extended, or randomly coiled, the interaction strength between a ssDNA and a nanochannel surface with the appropriate chemistry will increase with molecular length due to increasing van der Waals contacts or other interactions.

3.3.3 Effect of column length on separation performance

Because we observed better separation in NIM-PMMA, we investigated the separation behavior of the 3 ssDNAs at different effective column lengths. Thus, we compared separation column lengths of 30 μm (see Figure 3.10) with our previous results that used a 60 μm effective length. Histograms of the effective migration time were all taken at a field strength of 280 V/cm. Theoretical plates per meter were calculated using $[5.54(\text{teff}/w_{0.5})] \times [100/\text{column length in cm}]$. As in every chromatographic system, the separation resolution is determined by the number of theoretical plates, retention factor and the selectivity of a particular solute as is the case in CEC and is expressed by the equation (3.10) given below (Purnell's equation).⁵¹

$$R = \left(\frac{\sqrt{N}}{4} \right) \left(\frac{k}{k+1} \right) \left(\frac{\alpha}{\alpha-1} \right) \quad (3.10)$$

According to Figures 3.10 and 3.10B, the resolution for the 30 μm length column decreased significantly compared to the 60 μm column length for all 3 ssDNAs (resolution at 30 μm length ranged from 0.5 – 1.8). In contrast to electrophoresis where the resolution is not affected by column length,⁵² in electrochromatography the efficiency decreases with decreasing column length as the number of theoretical plates are directly proportional to the column length ($N = L/H$, where L is

column length and H is the height equivalent to theoretical plate). The number of theoretical plates at 30 μm effective column length was lower for Oligo35 and Oligo50 than that for the 60 μm effective column length as shown in Figure 3.10. However, for Oligo70 we noticed an increase in number of theoretical plates at a shorter column length. This could be due to short time for the surface interaction that led for low dispersion.

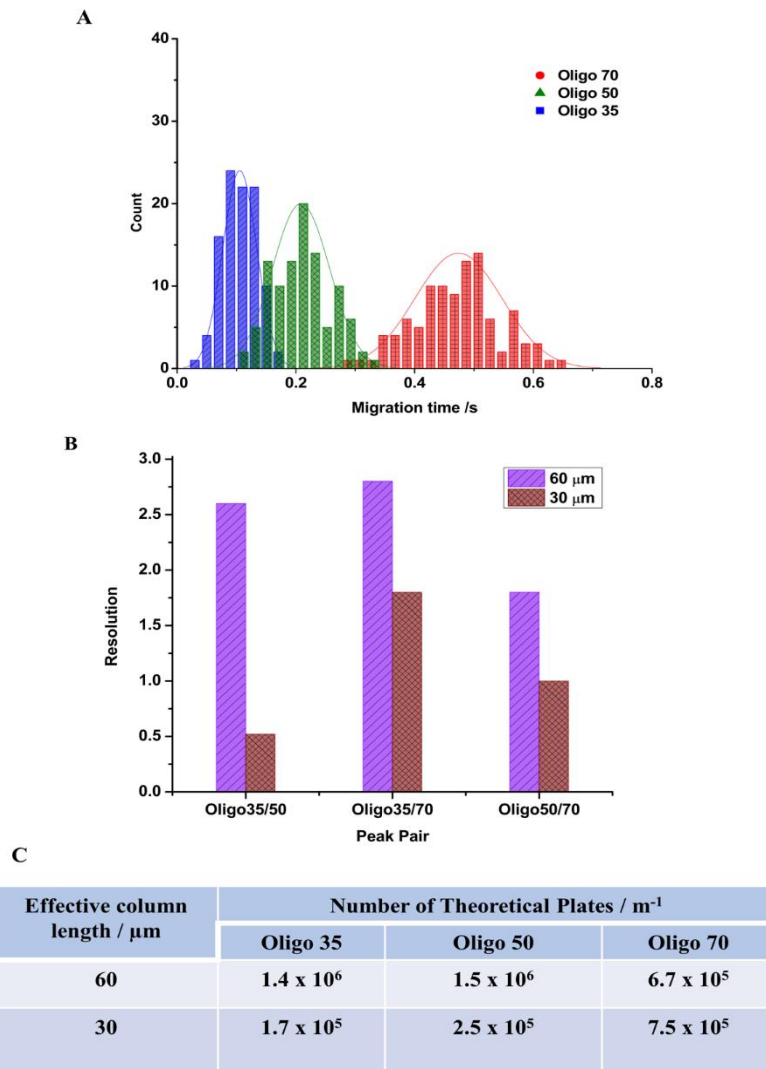


Figure 3.10 **A)** Histogram of migration time for ssDNAs at an effective column length of 30 μm through a 100 nm x 100 nm NIM-PMMA nanochannel at a field strength of 280 V/cm. Histograms were fit to a Gaussian and each histogram represents 100 events. **B)** Comparison of peak resolution at an effective column length of 60 μm and 30 μm. **C)** Calculated theoretical plates for ssDNAs at effective column lengths of 30 μm and 60 μm. $N = 5.54 (t_m/w_{0.5})^2$ was used to calculate the number of theoretical plates and $\frac{N \times 100}{\text{column length (cm)}}$ to obtain theoretical plates in units of m⁻¹.

3.4 Conclusions

The primary result of this study is the free solution separation of short single stranded DNA oligonucleotides in thermoplastic nanochannels with finite electric double layer. We were able to observe a new separation mechanism involved in these thermoplastic nanochannels which is a

combination of electrokinetic transport and surface interactions driven separation involved in nanoscale due to high surface area to volume ratio which is defined as open-tubular nanoelectrochromatography (OT-NEC). We were able to achieve separation resolutions above base line separation for Oligo 35, Oligo 50 and Oligo 70 in NIM-PMMA device which were not achievable in microscale thermoplastic columns. Length-based surface interactions played a major role in determining the migration time of each oligonucleotides through thermoplastic nanochannels. Separation resolution of these oligonucleotides were dependent on the materials surface roughness and the surface charge heterogeneity due to the intermittent motion and fluid recirculation consistent with our previous studies. It is evident that our data shows a significant influence by surface roughness towards electroosmotic flow and zeta potential thus, the separation is not only based on electrophoresis phenomena but includes a chromatographic characteristic as well . Separation efficiency is affected by effective column length where longer columns provided better separation resolution.

These results suggest that we can utilize this method to separate the LDR products generated in our envisioned nanosensor for SNP identification of stroke and cancer. Even though we utilized fluorescently tagged oligonucleotides for the ease of tracking these molecules during their transport through nanochannels, in our proposed nanosensor, a label free approach will be used for length base identification of ss-DNA oligonucleotides between dual nanopore system connected through a nanochannel using both the resistive pulse sensing signal and the time of flight of molecules.

3.5 References

1. Ginsburg, G. S.; Phillips, K. A., Precision Medicine: From Science To Value. *Health Aff (Millwood)* **2018**, 37 (5), 694-701.
2. Buel, E.; Schwartz, M. B.; LaFountain, M. J., Capillary electrophoresis STR analysis: comparison to gel-based systems. *Journal of Forensic Science* **1998**, 43 (1), 164-170.
3. Barany, F.; Gerry, N. P.; Witowski, N. E.; Day, J.; Hammer, R. P.; Barany, G., Detection of nucleic acid sequence differences using the ligase detection reaction with addressable arrays. Google Patents: 2003.
4. Ramakers, C.; Ruijter, J. M.; Deprez, R. H. L.; Moorman, A. F., Assumption-free analysis of quantitative real-time polymerase chain reaction (PCR) data. *Neuroscience letters* **2003**, 339 (1), 62-66.
5. Khanna, M.; Cao, W.; Zirvi, M.; Paty, P.; Barany, F., Ligase detection reaction for identification of low abundance mutations. *Clinical Biochemistry-New York* **1999**, 32 (4), 287-290.
6. Hashimoto, M.; Barany, F.; Soper, S. A., Polymerase chain reaction/ligase detection reaction/hybridization assays using flow-through microfluidic devices for the detection of low-abundant DNA point mutations. *Biosensors and bioelectronics* **2006**, 21 (10), 1915-1923.
7. Lowe, A. J.; Huh, Y. S.; Strickland, A. D.; Erickson, D.; Batt, C. A., Multiplex single nucleotide polymorphism genotyping utilizing ligase detection reaction coupled surface enhanced Raman spectroscopy. *Analytical chemistry* **2010**, 82 (13), 5810-5814.
8. Iannone, M. A.; Taylor, J. D.; Chen, J.; Li, M. S.; Rivers, P.; Slentz-Kesler, K. A.; Weiner, M. P., Multiplexed single nucleotide polymorphism genotyping by oligonucleotide ligation and flow cytometry. *Cytometry: The Journal of the International Society for Analytical Cytology* **2000**, 39 (2), 131-140.
9. Sinville, R.; Coyne, J.; Meagher, R. J.; Cheng, Y. W.; Barany, F.; Barron, A.; Soper, S. A., Ligase detection reaction for the analysis of point mutations using free-solution conjugate electrophoresis in a polymer microfluidic device. *Electrophoresis* **2008**, 29 (23), 4751-4760.
10. Sonker, M.; Kim, D.; Egatz-Gomez, A.; Ros, A., Separation Phenomena in Tailored Micro-and Nanofluidic Environments. *Annual Review of Analytical Chemistry* **2019**, 12.
11. Roda, A.; Michelini, E.; Caliceti, C.; Guardigli, M.; Mirasoli, M.; Simoni, P., Advanced bioanalytics for precision medicine. *Analytical and bioanalytical chemistry* **2018**, 410 (3), 669-677.
12. Khandurina, J.; Guttmann, A., Microscale separation and analysis. *Current Opinion in Chemical Biology* **2003**, 7 (5), 595-602.
13. Grossman, P. D.; Colburn, J. C., Capillary electrophoresis : theory & practice. **1992**.
14. Mayer, P.; Slater, G. W.; Drouin, G., Theory of DNA Sequencing Using Free-Solution Electrophoresis of Protein-DNA Complexes. *Analytical Chemistry* **1994**, 66 (10), 1777-1780.
15. Bae, Y. C.; Soane, D., Polymeric separation media for electrophoresis: Cross-linked systems or entangled solutions. *Journal of Chromatography A* **1993**, 652 (1), 17-22.
16. Barron, A. E.; Soane, D. S.; Blanch, H. W., Capillary electrophoresis of DNA in uncross-linked polymer solutions. *Journal of Chromatography A* **1993**, 652 (1), 3-16.
17. Fang, Y.; Zhang, J. Z.; Hou, J. Y.; Lu, H.; Dovichi, N. J., Activation energy of the separation of DNA sequencing fragments in denaturing noncross-linked polyacrylamide by capillary elecrophoresis. *ELECTROPHORESIS* **1996**, 17 (9), 1436-1442.

18. Viovy, J.-L., Electrophoresis of DNA and other polyelectrolytes: Physical mechanisms. *Reviews of Modern Physics* **2000**, 72 (3), 813.
19. Dolník, V., Wall coating for capillary electrophoresis on microchips. *ELECTROPHORESIS* **2004**, 25 (21-22), 3589-3601.
20. Doherty, E. A.; Meagher, R. J.; Albarghouthi, M. N.; Barron, A. E., Microchannel wall coatings for protein separations by capillary and chip electrophoresis. *Electrophoresis* **2003**, 24 (1-2), 34-54.
21. Duong, T. T.; Kim, G.; Ros, R.; Streek, M.; Schmid, F.; Brugger, J.; Anselmetti, D.; Ros, A., Size-dependent free solution DNA electrophoresis in structured microfluidic systems. *Microelectronic Engineering* **2003**, 67, 905-912.
22. Lau, H. W.; Archer, L. A., Electrophoresis of end-labeled DNA: Theory and experiment. *Physical Review E* **2010**, 81 (3), 031918.
23. Sun, Y.; Kwok, Y. C., Polymeric microfluidic system for DNA analysis. *Analytica Chimica Acta* **2006**, 556 (1), 80-96.
24. Tegenfeldt, J. O.; Prinz, C.; Cao, H.; Huang, R. L.; Austin, R. H.; Chou, S. Y.; Cox, E. C.; Sturm, J. C., Micro-and nanofluidics for DNA analysis. *Analytical and bioanalytical chemistry* **2004**, 378 (7), 1678-1692.
25. Napoli, M.; Eijkel, J. C.; Pennathur, S., Nanofluidic technology for biomolecule applications: a critical review. *Lab on a Chip* **2010**, 10 (8), 957-985.
26. Pennathur, S.; Santiago, J. G., Electrokinetic transport in nanochannels. 2. Experiments. *Analytical Chemistry* **2005**, 77 (21), 6782-6789.
27. Pennathur, S.; Santiago, J. G., Electrokinetic transport in nanochannels. 1. Theory. *Analytical Chemistry* **2005**, 77 (21), 6772-6781.
28. Uba, F. I.; Pullagurla, S. R.; Sirasunthorn, N.; Wu, J.; Park, S.; Chantiwas, R.; Cho, Y.-K.; Shin, H.; Soper, S. A., Surface charge, electroosmotic flow and DNA extension in chemically modified thermoplastic nanoslits and nanochannels. *Analyst* **2015**, 140 (1), 113-126.
29. Mawatari, K.; Kazoe, Y.; Shimizu, H.; Pihosh, Y.; Kitamori, T., Extended-nanofluidics: fundamental technologies, unique liquid properties, and application in chemical and bio analysis methods and devices. ACS Publications: 2014.
30. Shimizu, H.; Toyoda, K.; Mawatari, K.; Terabe, S.; Kitamori, T., Femtoliter Gradient Elution System for Liquid Chromatography Utilizing Extended Nanofluidics. *Analytical Chemistry* **2019**, 91 (4), 3009-3014.
31. Smirnova, A.; Shimizu, H.; Mawatari, K.; Kitamori, T., Reversed-phase Chromatography in an Extended Nanospace: Separating Amino Acids in Short and Long Nanochannels. *Analytical Sciences* **2015**, 31 (11), 1201-1204.
32. Baldessari, F.; Santiago, J. G., Electrophoresis in nanochannels: brief review and speculation. *Journal of Nanobiotechnology* **2006**, 4 (1), 12.
33. Xia, K.; Novak, B. R.; Weerakoon-Ratnayake, K. M.; Soper, S. A.; Nikitopoulos, D. E.; Moldovan, D., Electrophoretic Transport of Single DNA Nucleotides through Nanoslits: A Molecular Dynamics Simulation Study. *The Journal of Physical Chemistry B* **2015**, 119 (35), 11443-11458.
34. Huang, X.; Gordon, M. J.; Zare, R. N., Current-monitoring method for measuring the electroosmotic flow rate in capillary zone electrophoresis. *Analytical Chemistry* **1988**, 60 (17), 1837-1838.

35. Cross, J. D.; Strychalski, E. A.; Craighead, H., Size-dependent DNA mobility in nanochannels. *Journal of Applied Physics* **2007**, *102* (2), 024701.
36. Svec, F.; Fréchet, J.; Hilder, E.; Peterson, D.; Rohr, T., In Micro Total Analysis Systems 2002, Baba Y., van den Berg A. Kluwer Academic Publishers, Dordrecht: 2002.
37. Pennathur, S.; Baldessari, F.; Santiago, J. G.; Kattah, M. G.; Steinman, J. B.; Utz, P. J., Free-Solution Oligonucleotide Separation in Nanoscale Channels. *Analytical Chemistry* **2007**, *79* (21), 8316-8322.
38. Chantiwas, R.; Hupert, M. L.; Pullagurla, S. R.; Balamurugan, S.; Tamarit-López, J.; Park, S.; Datta, P.; Goettert, J.; Cho, Y.-K.; Soper, S. A., Simple replication methods for producing nanoslits in thermoplastics and the transport dynamics of double-stranded DNA through these slits. *Lab on a Chip* **2010**, *10* (23), 3255-3264.
39. Chantiwas, R.; Park, S.; Soper, S. A.; Kim, B. C.; Takayama, S.; Sunkara, V.; Hwang, H.; Cho, Y.-K., Flexible fabrication and applications of polymer nanochannels and nanoslits. *Chemical Society Reviews* **2011**, *40* (7), 3677-3702.
40. Weerakoon-Ratnayake, K. M.; O'Neil, C. E.; Uba, F. I.; Soper, S. A., Thermoplastic nanofluidic devices for biomedical applications. *Lab on a Chip* **2017**, *17* (3), 362-381.
41. What is precision medicine. <https://ghr.nlm.nih.gov/primer/precisionmedicine/definition> (accessed 09/15/2019).
42. Chai, J.; Lu, F.; Li, B.; Kwok, D. Y., Wettability interpretation of oxygen plasma modified poly (methyl methacrylate). *Langmuir* **2004**, *20* (25), 10919-10927.
43. Xu, F.; Datta, P.; Wang, H.; Gurung, S.; Hashimoto, M.; Wei, S.; Goettert, J.; McCarley, R. L.; Soper, S. A., Polymer microfluidic chips with integrated waveguides for reading microarrays. *Analytical chemistry* **2007**, *79* (23), 9007-9013.
44. O'Neil, C.; Amarasekara, C. A.; Weerakoon-Ratnayake, K. M.; Gross, B.; Jia, Z.; Singh, V.; Park, S.; Soper, S. A., Electrokinetic transport properties of deoxynucleotide monophosphates (dNMPs) through thermoplastic nanochannels. *Analytica chimica acta* **2018**, *1027*, 67-75.
45. Weerakoon-Ratnayake, K. M.; Uba, F. I.; Oliver-Calixte, N. J.; Soper, S. A., Electrophoretic Separation of Single Particles Using Nanoscale Thermoplastic Columns. *Analytical Chemistry* **2016**, *88* (7), 3569-3577.
46. Arumay, P.; Yaakov, L., Structure, stability and specificity of the binding of ssDNA and ssRNA with proteins. *PLoS Computational Biology* **2019**, *15* (4), e1006768.
47. Liautard, J. P., Rapid separation of single-stranded DNA from double-stranded DNA by reversed-phase high-performance liquid chromatography. *Journal of Chromatography A* **1984**, *285*, 221-225.
48. Tinland, B.; Pluen, A.; Sturm, J.; Weill, G., Persistence length of single-stranded DNA. *Macromolecules* **1997**, *30* (19), 5763-5765.
49. Chen, H.; Meisburger, S. P.; Pabit, S. A.; Sutton, J. L.; Webb, W. W.; Pollack, L., Ionic strength-dependent persistence lengths of single-stranded RNA and DNA. *Proceedings of the National Academy of Sciences* **2012**, *109* (3), 799.
50. Mills, J. B.; Vacano, E.; Hagerman, P. J., Flexibility of single-stranded DNA: use of gapped duplex helices to determine the persistence lengths of poly (dT) and poly (dA). *Journal of molecular biology* **1999**, *285* (1), 245-257.
51. Melzak, K. A.; Sherwood, C. S.; Turner, R. F.; Haynes, C. A., Driving forces for DNA adsorption to silica in perchlorate solutions. *Journal of colloid and interface science* **1996**, *181* (2), 635-644.

52. Maheswari, P. U.; Rajendiran, V.; Palaniandavar, M.; Thomas, R.; Kulkarni, G., Mixed ligand ruthenium (II) complexes of 5, 6-dimethyl-1, 10-phenanthroline: the role of ligand hydrophobicity on DNA binding of the complexes. *Inorganica chimica acta* **2006**, 359 (14), 4601-4612.
53. Uba, F. I.; Hu, B.; Weerakoon-Ratnayake, K.; Oliver-Calixte, N.; Soper, S. A., High process yield rates of thermoplastic nanofluidic devices using a hybrid thermal assembly technique. *Lab on a Chip* **2015**, 15 (4), 1038-1049.
54. Ramm, P.; Lu, J. J.-Q.; Taklo, M. M., *Handbook of wafer bonding*. John Wiley & Sons: 2011.
55. Tsao, C.; Hromada, L.; Liu, J.; Kumar, P.; DeVoe, D., Low temperature bonding of PMMA and COC microfluidic substrates using UV/ozone surface treatment. *Lab on a Chip* **2007**, 7 (4), 499-505.
56. Schindelin, J.; Arganda-Carreras, I.; Frise, E.; Kaynig, V.; Longair, M.; Pietzsch, T.; Preibisch, S.; Rueden, C.; Saalfeld, S.; Schmid, B.; Tinevez, J.-Y.; White, D. J.; Hartenstein, V.; Eliceiri, K.; Tomancak, P.; Cardona, A., Fiji: an open-source platform for biological-image analysis. *Nat Methods* **2012**, 9 (7), 676-682.
57. Stellwagen, E.; Lu, Y.; Stellwagen, N. C., Unified description of electrophoresis and diffusion for DNA and other polyions. *Biochemistry* **2003**, 42 (40), 11745-11750.
58. Cho, K.; Yang, J.; Park, C. E., The effect of rubber particle size on toughening behaviour of rubber-modified poly (methyl methacrylate) with different test methods. *Polymer* **1998**, 39 (14), 3073-3081.
59. Oneil, C. E.; Jackson, J. M.; Shim, S.-H.; Soper, S. A., Interrogating Surface Functional Group Heterogeneity of Activated Thermoplastics Using Super-Resolution Fluorescence Microscopy. *Analytical Chemistry* **2016**, 88 (7), 3686-3696.
60. Hu, Y.; Werner, C.; Li, D., Electrokinetic transport through rough microchannels. *Analytical Chemistry* **2003**, 75 (21), 5747-5758.
61. Ziarani, A.; Mohamad, A., Effect of Wall Roughness on the Slip of Fluid in a Microchannel. *Nanoscale and microscale thermophysical engineering* **2008**, 12 (2), 154-169.
62. Park, H.; Lee, H., Effects of wall roughness and velocity slip on streaming potential of microchannels. *International Journal of Heat and Mass Transfer* **2012**, 55 (11-12), 3295-3306.
63. Qiao, R., Effects of molecular level surface roughness on electroosmotic flow. *Microfluidics and Nanofluidics* **2007**, 3 (1), 33-38.
64. Zhang, C.; Lu, P.; Chen, Y., Molecular dynamics simulation of electroosmotic flow in rough nanochannels. *International Communications in Heat and Mass Transfer* **2014**, 59, 101-105.
65. Qiao, R.; Aluru, N. R., Atomistic simulation of KCl transport in charged silicon nanochannels: Interfacial effects. *Colloids and Surfaces A: Physicochemical and Engineering Aspects* **2005**, 267 (1), 103-109.
66. Henry, A. C.; Tutt, T. J.; Galloway, M.; Davidson, Y. Y.; McWhorter, C. S.; Soper, S. A.; McCarley, R. L., Surface Modification of Poly(methyl methacrylate) Used in the Fabrication of Microanalytical Devices. *Analytical Chemistry* **2000**, 72 (21), 5331-5337.
67. O'Neil, C. E.; Taylor, S.; Ratnayake, K.; Pullagurla, S.; Singh, V.; Soper, S. A., Characterization of activated cyclic olefin copolymer: effects of ethylene/norbornene content on the physicochemical properties. *Analyst* **2016**, 141 (24), 6521-6532.

68. Rogers, B.; Adams, J.; Pennathur, S., *Nanotechnology: understanding small systems*. Crc Press: 2014.
69. Lelièvre, F.; Yan, C.; Zare, R. N.; Gareil, P., Capillary electrochromatography: operating characteristics and enantiomeric separations. *Journal of Chromatography A* **1996**, 723 (1), 145-156.
70. Xiang, R.; Horváth, C., Fundamentals of Capillary Electrochromatography: Migration Behavior of Ionized Sample Components. *Analytical Chemistry* **2002**, 74 (4), 762-770.
71. Qian, W.; Doi, K.; Kawano, S., Effects of polymer length and salt concentration on the transport of ssDNA in nanofluidic channels. *Biophysical journal* **2017**, 112 (5), 838-849.
72. Wu, J.; Wang, H.; Zhu, A.; Long, F., Adsorption kinetics of single-stranded DNA on functional silica surfaces and its influence factors: an evanescent-wave biosensor study. *ACS omega* **2018**, 3 (5), 5605-5614.
73. Jackson, J. M.; Witek, M. A.; Hupert, M. L.; Brady, C.; Pullagurla, S.; Kamande, J.; Aufforth, R. D.; Tignanelli, C. J.; Torphy, R. J.; Yeh, J. J.; Soper, S. A., UV activation of polymeric high aspect ratio microstructures: ramifications in antibody surface loading for circulating tumor cell selection. *Lab on a chip* **2014**, 14 (1), 106-117.
74. Wiedmer, S. K.; Jussila, M.; Hakala, R. M. S.; Pystynen, K.-H.; Riekkola, M.-L., Piperazine-based buffers for liposome coating of capillaries for electrophoresis. *ELECTROPHORESIS* **2005**, 26 (10), 1920-1927.
75. Monserud, J. H.; Schwartz, D. K., Effects of molecular size and surface hydrophobicity on oligonucleotide interfacial dynamics. *Biomacromolecules* **2012**, 13 (12), 4002-4011.

**Chapter 4. Electrokinetic Separation of Ribonucleotide Monophosphates
(rNMPs) in Thermoplastic Nanochannels**

4.1 Introduction

The flow of information coded in genes as DNA (deoxyribonucleic acid) to RNA(ribonucleic acid) and then to functional proteins is described by the central dogma of molecular biology, where transfer of information from DNA to RNA is known as transcription and transfer of information from RNA to proteins is referred to as translation.¹ Transcription of genes into complementary RNA molecules regulates the biological activity within the cell. The entire RNA molecules that transcribe all genes of the genome are together known as the transcriptome and understanding the transcriptome is essential for interpreting the functional elements of the genome and understanding development of diseases.² The transcriptome is highly complex and encompasses multiple types of coding and noncoding RNA species. In general, RNA molecules are referred as the simple intermediate between genes and proteins, as encapsulated in the central dogma of molecular biology. Therefore, messenger RNA (mRNA) are the most frequently studied RNA species because they encode proteins through the corresponding genetic code. In addition to coding mRNA, there is a diverse group of noncoding RNA molecules that are functional. These non-coding RNAs include ribosomal RNA(rRNA), transfer RNA (tRNA), which are involved in translation of mRNA, small nucleolar RNA (snoRNA) and microRNAs (sequence-specific regulators of post-transcriptional gene expression in many eukaryotes).³⁻⁵

Analysis of the transcriptome (RNA analysis) has garnered a lot of attention recently as it offers many advantages over whole-genome analysis. Whole-genome sequencing provides a static view of an organism's genetic and regulatory information, but transcriptome analysis allows assessment of dynamic changes in gene expression in response to various stimuli.^{6,7} In addition, identification of unique transcripts such as alternative splice variants, single-nucleotide polymorphisms, and

fusion to enhance understanding of the underlying mechanisms governing the changes in gene expression that underlie health and disease are obtained through quantitative analysis of gene expression. Moreover, with the development of precision medicine, RNA analysis will increasingly be used for biomarker discovery and in the identification of molecular signatures that define various disease subtypes and responses to pharmacologic therapy.⁸⁻¹⁰

RNA analysis was first done by utilizing hybridization-based microarray technologies, which provide high throughput analysis at relatively low cost.^{11, 12} Though microarray-based methods have been utilized for over a decade as the sole method for RNA analysis, it has numerous limitations that made them far from being an ideal tool for analyzing the transcriptome. These include cross-hybridization artifacts in the analysis of highly similar sequences; need of separate array designs for each species; variation of results in different platforms and thus inability of direct comparison of results; and integration and low accuracy in quantification of low expressed and very high expressed genes.¹³⁻¹⁵

The advent of high throughput next generation sequencing (NGS) platforms revolutionized the understanding of the complex and dynamic nature of the transcriptome by allowing RNA analysis through complementary DNA (cDNA) sequencing at a massive scale. This method is known as RNA sequencing (RNA-seq).¹⁶ RNA-seq promised to eliminate most of the challenges posed in microarray technologies by measuring the transcriptomes at base pair resolution, using essentially the same protocol for any species with increased dynamic range and minimal noise. RNA-seq provides a detailed and quantitative view of gene expression, allele-specific expression, and alternative splicing.² With recent advances in the RNA-seq workflow, it has enabled deep profiling

of the transcriptome and the ability to elucidate differences in physiological and pathological conditions.¹⁷

Even though the accomplishments are impressive in RNA-seq, there are numerous challenges that prevent the understanding of the real nature of the transcriptome. These limitations are: The propensity of various reverse transcriptases (RT) to generate spurious second complementary DNA (cDNA) strands due to their DNA-dependent polymerase activities; artifactual cDNA generation due to template switching or contaminating DNA and primer independent cDNA synthesis; low amount of cDNA due to the inefficient nature of RT and biases introduced during amplification and ligation steps.¹⁸ These limitations during the conversion of RNA to cDNA results in the loss of the majority of transcripts present in each cell, leading to a high level of noise and stochasticity in the RNA-seq process. Therefore, it is necessary to develop new sequencing platforms to address the aforementioned limitations, which includes methods capable of sequencing full length transcripts without amplification.

Recently, single-molecule sequencing (SMS), some of which are based on nanopore readout, has become an attractive alternative to ensemble-based sequencing as it can eliminate the need for polymerases used in traditional sequencing modalities, as well as potentially provide longer read lengths.^{19, 20} Unlike the NGS techniques, nanopore sequencing does not require fluorescent labelling as the sequencing is done by measuring the current blockade characteristics of each nucleotide as it moves through a narrow constriction. This significantly reduces the cost and time needed for sequencing.¹⁹ Currently, nanopore sequencing is done using two major approaches, strand sequencing^{21, 22} and exosequencing.^{20, 23, 24} Ayub *et al.*²⁰ showed the use of polynucleotide phosphorylase (PNPase), which processively cleaves ssRNA in the 3'-to-5'

direction using inorganic phosphate (P_i) to cleave the phosphoester linkage and release ribonucleotide diphosphates (rNDPs) that can subsequently pass through an engineered α HL (HL = hemolysin) pore containing cyclodextrin adapters that are non-covalently bound to the pore. The signal from the rNDPs are obtained through resistive pulse sensing. The authors claimed that the additional charge on the rNDPs allow it to be captured by the nanopore more efficiently than ribonucleotide monophosphates (rNMPs). However, diffusional misordering is a limitation of this approach.²⁵ Moreover, single nucleotide detection approaches are also limited by high error rates as nucleotide bases are identified using current blockage events, which show poor discrimination of the nucleotide bases.¹⁹

To overcome these challenges, we are developing an innovative SMS strategy that is based on the exosequencing approach, and enzymatically cleaves RNAs using a processive enzyme to generate individual rNMPs.²⁶ This is achieved via a clipping enzyme such as exoribonuclease 1(XRN-1) tethered to the solid nanopillar support that can processively clip the RNA strand into their constituent rNMPs when activated by the introduction of Mg^{2+} into the enzymatic reactor. Then, the released rNMPs are electrokinetically transported through a nanochannel with the travel time determined by the applied electric field, the length of the flight tube, and channel wall interactions. Identification of the nucleobases is enabled by molecular-dependent flight times of rNMPs within nanochannels (*i.e.*, apparent electrophoretic mobility). Therefore, a thorough understanding of the translocation of rNMPs through nanochannels along with parameters which we can enhance resolution between rNMPs to allow for high identification accuracy will be required.

Separation of rNMPs has been achieved using conventional electrophoresis methods, most commonly using alkaline solutions as the carrier electrolyte.²⁷⁻²⁹ Alkaline solutions provide a stable EOF, thus coated capillaries are not necessary to eliminate or stabilize the EOF.²⁹ Sodium borate is the most commonly used alkaline buffer for rNMP electrophoretic separations.^{27, 30} In addition to sodium borate, other researchers have used sodium and ammonium carbonate buffers, which provide a stable baseline and adequate resolution.³¹ In addition to capillary electrophoresis, several researchers have used liquid chromatographic methods to separate rNMPs.³²⁻³⁴

Although conventional capillary electrophoresis and chromatography has had success in the separation of rNMPs, nanofluidics have garnered attention recently due to the unique separation modalities observed compared to microscale electrophoretic separations. It was determined that electrokinetic separations in nanochannels depend on ion valence, ζ (zeta potential), ion mobility, and thickness of the electric double layer (λ_D).³⁵⁻³⁸ The increased surface area-to-volume ratio also allows for a host of solute/wall interactions, which in turn allows for separations based on hydrophobic, electrostatic, hydrogen bonding and van der Waals interactions in addition to the electrophoretic ones.³⁹ However, the majority of these separations were done in glass/silicon based nanofluidic devices, which make these separations not ideal for clinical needs as the fabrication of these devices is associated with high cost, time consuming and sophisticated fabrication methods.^{40, 41}

There are, however, scale-dependent processes that can degrade the performance of using nanoscale columns, such as intermittent motion of analytes due to dielectrophoretic trapping artifacts generated by surface roughness. This surface roughness creates inhomogeneous electric fields inside the fluidic channel and traps the molecules by localized dielectric fields.^{42, 43} Others

include electric double layer (EDL) overlap, concertation polarization, and increased surface interactions due to high surface area-to volume ratio.

Thermoplastic nanofluidic devices have garnered attention as an alternative to glass/silicon devices due to their diverse physiochemical properties and the fabrication techniques available to design the prerequisite structures.^{42, 44} Thermoplastic nanofluidic devices can be fabricated using nanoimprint lithography (NIL), where it takes advantage of the deformability of the substrate at temperatures above the glass transition temperature (T_g) of the substrate to produce multi-scale structures in a relatively high production mode over large areas at moderate cost.^{6, 44} The diversity in their surface chemistry, which is determined by the identity of the monomer units comprising the polymer chains, is another advantage of using thermoplastics as column materials. In addition, a diverse range of simple activation techniques can be employed to generate functional groups that alter the surface chemistry of these nanochannel walls.^{43, 45, 46}

There have been a limited number of studies on nanoscale separations using thermoplastic nanofluidic devices.⁴⁶⁻⁴⁸ Weerakoon-Ratnayake *et al.*⁴⁷ investigated the separation of silver nanoparticles (AgNP) within nanoscale PMMA columns. AgNPs within these devices were detected by dark field microscopy with varying slit dimensions, ionic strength of the buffer, and applied electric field strengths. The authors demonstrated size-based separation of AgNPs without buffer additives in the carrier electrolyte (*i.e.*, sodium dodecyl sulfate micelles), which was not possible within microscale columns. High resolution was observed for 60 nm and 100 nm AgNP at high electric field strengths where the influence of stick-slip motion was minimal. O’Neil *et al.*⁴⁶ demonstrated differences in the electromigration of 20 nm polystyrene (PS) beads traveling through PMMA nanoslits at varying field strengths. At low electric field strengths (200 V/cm), the PS beads had high numbers of wall interactions resulting in increased electrophoretic migration

time and increased peak dispersion. However, a 50% increase in the electric field strength (300 V/cm) generated a 600% decrease in the electrophoretic migration time. Further, the relative dispersion in the migration times were reduced from 40% at 200 V/cm to 8% at 300 V/cm, a 5-fold decrease. O’Neil *et al.*⁴⁸ recently showed the separation of deoxynucleotide monophosphates (dNMPs) through thermoplastic nanochannels made with PMMA and COC. In their study, they observed field-dependent mobilities of dNMPs at low electric field strength due to recirculation of solutes arising from non-uniform surface charge. They showed that increasing the pH of the carrier electrolyte increased the separation resolution while low ionic strength conditions where the EDL is thick, led to poor separation resolution. They also observed at very high pH (pH>10.3), delamination of the PMMA-COC nanofluidic device limited the use of higher pH electrolytes to possibly further improve the electrophoretic resolution.

In this work, we report the separation of rNMPs in thermoplastic nanofluidic channels. We fabricated COC/COC monolithic thermoplastic nanochannel devices with the ability to control the EOF through post assembly UV/O₃ surface modification. Furthermore, these COC/COC devices showed significantly high bond strength compared to PMMA/COC devices. We investigated the separation resolution of the rNMPs under different conditions including the carrier electrolyte pH, electric field strength, and the material type. We were able to separate all rNMPs in free solution with identification accuracies, which were based on mobility matching, >99.99 % in COC/COC devices and >99.76 in PMMA/COC devices. In addition, the separation mechanism changed with the thermoplastic material used; COC/COC devices the separation mechanism was primarily electrophoretic in nature, while for PMMA/COC devices it was primarily electrochromatographic.

4.2 Materials and Methods

4.2.1 Materials and reagents

Silicon $\langle 100 \rangle$ (Si) wafers were purchased from University Wafers (Boston, MA). Impact modified (IM) and non-impact modified (NIM) PMMA substrates were purchased from ePlastics (San Diego, CA) and Good Fellow (Berwyn, PA), respectively. Cyclic olefin copolymer (COC 8007 and COC 5010) were purchased from TOPAS Advanced Polymers (Florence, KY). COC 6015 was purchased from Knightsbridge Plastics Inc. (Fremont, CA). UV curable polyurethane resin was purchased from Chansang sheet Co Ltd. ATTO532 was purchased from ATTO 532 dye was purchased from Atto-Tec (Siegen, Germany). Uridine 5'-monophosphate disodium salt, cytidine 5'-monophosphate disodium salt, adenosine 5'-monophosphate disodium salt and guanosine 5'- monophosphate disodium salt, were purchased from Sigma-Aldrich (St. Louis, MO). Molecular biology grade water was purchased from Thermo Scientific (Waltham, MA).

4.2.2 Fabrication of nanochannel devices

Nanofluidic structures were fabricated in thermoplastic substrates using a method described earlier by our group. Briefly, microchannels were fabricated in a Si wafer (master) via optical lithography followed by wet etching. Then nanochannels were fabricated using focused-ion beam milling. Next, the resin stamps were produced from the Si master by curing a UV curable polyurethane (PUA) resin. COC6015 coated with NOA72 adhesive was used as the backplate of resin. After that, nanochannels were imprinted on COC5010 substrate which had a T_g of 108 °C and non-impact modified PMMA (NIM-PMMA) using the Nanonex 2500 nanoimprinting machine. A

schematic diagram of the imprinting/bonding scheme using Nanonex 2500 is shown in Figure 4.1A.

Nanonex 2500 uses an air cushion press method (ACP). In this method, an inert gas is used to press the patterned mold and the substrate against each other in an enclosed chamber rather than solid parallel plates. (Figure 4.1A) This method has several advantages over the solid plate parallel method including: a) isotopically applied gas pressure eliminates lateral shift or rotation and reduce the damage to the mold; b) ACP has much more uniform pressure which eliminates hot spots in the imprinting; c) The conformable gas (or fluid) layers in ACP eliminate direct contact between the solid plates and samples (mold and/or substrate), and thus removes any effects related to the imperfection of the solid plates; d) ACP is immune to dust and topological variations on the backside of the mold or substrate; e) The smaller thermal mass in ACP provides faster thermal imprinting.^{49, 50}

Figure 4.1B shows the temperature-pressure process program used for the imprinting of nanofluidic devices and the bonding of devices. The temperature and pressure conditions for imprinting and bonding will depend on the substrates used. Details on COC/COC device fabrication is discussed in section 4.3.1. As shown in Figure 4.1B the temperature-pressure process program consists of seven segmented processes.

1) Pump down stage – A silicon rubber bag consisting of a substrate and stamp are placed within an enclosed chamber. The first step is the evacuation of this chamber. We used 3 min pump down time to achieve this.

- 2) Pre-pressure stage – After the chamber was pumped down, the chamber pressure was raised to a pre-pressure before heating the system, which takes about 1 min. In the Nanonex 2500, nitrogen is used as the gas for ACP.
- 3) Heating stage – Once the chamber reached pre-pressure, heating of the chamber occurred. The heating in Nanonex was achieved using infrared lamps below the Si wafer. The use of a Si wafer facilitates the heat conduction to the thermoplastic substrate.
- 4) Pressure stage – Once the desired imprinting/bonding temperature is reached, the pressure is immediately raised to the intended final pressure. This final pressure is determined depending on the bonding or imprinting and material used for substrates.
- 5) Hold stage – In this step, the desired temperature and pressure are maintained. For imprinting the holding time is 5 min. For bonding the hold time is 15 min.
- 6) Cool down stage – Once imprinting/bonding is complete, the temperature of the chamber starts to decrease gradually to 45°C at a rate of 2.5°C/s while holding the device imprinting/bonding pressure. This reduces the stress imposed on the substrate/cover plate and lowers channel deformation.
- 7) Demolding stage – After the cooling process, the chambers release the gas pressure and separate.

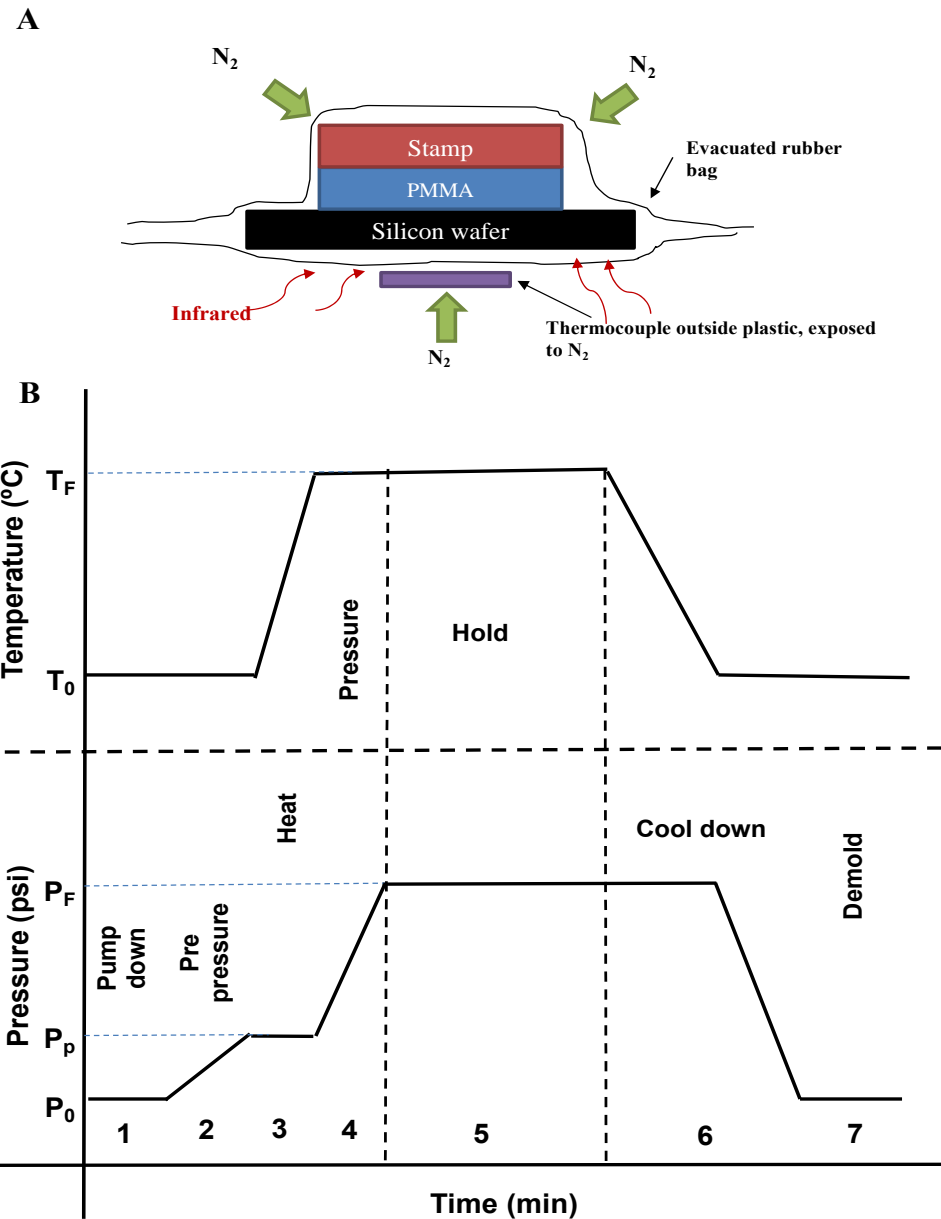


Figure 4.1. **A)** Schematic illustration of the device assembly using the Nanonex2500. **B)** Temperature-pressure process profile showing the seven stages for the imprinting and bonding cycle. An imprinting cycle is 10 min (5 min imprinting time) and bonding cycle is 25 min (15 min bonding time).

Imprinting of the nanofluidic channels into COC and NIM-PMMA is a critical step in device fabrication. Preliminary tests were conducted to optimize the imprinting pressure, imprinting temperature, and imprinting time. The imprinting temperature was kept higher than the glass

transition temperature of the thermoplastic substrate. For NIM-PMMA devices, we used the same imprinting conditions mentioned in Chapter 3 (130° C temperature, 300 psi pressure and 5 min imprinting time).

The imprinting of nanofluidic structures on COC5010 substrate was done by keeping the imprinting pressure (300 psi) and time (5 min) constant while optimizing the imprinting temperature. The optimized conditions for the imprinting are given in Table 4.1 for both COC5010 and PMMA. The imprinted nanofluidic devices with optimized conditions were then characterized using SEM imaging and SPM.(see Figure 4.2)

Table 4.1. The optimized imprinting conditions for NIM-PMMA and COC5010 110 x 110 nm nanochannels in Nanonex 2500; Width and depth of the imprinted nanochannel measured by SEM (Hitachi SU8230 Field emission scanning electron microscopy)and SPM (Schimadzu SPM-9700HT), respectively.

Substrate	Imprinting conditions (temp., pressure, time)	Width and depth of the imprinted device
NIM-PMMA	130°C, 300 psi, 5min	110 (± 1.4) nm x 112.1 (± 1.6) nm
COC5010	135°C, 300 psi, 5min	110 (± 0.9) nm x 109.3 (± 1.3) nm

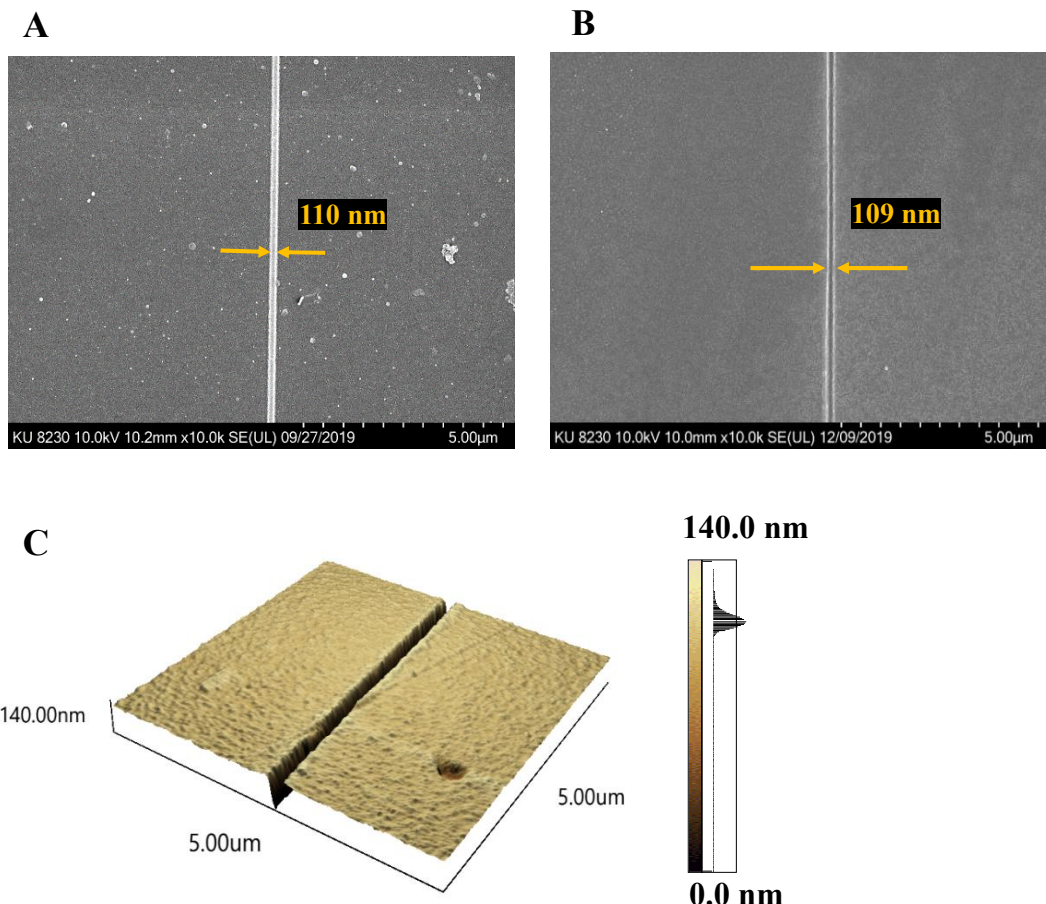


Figure 4.2. **A)** An SEM image of nanochannel replicated onto polyurethane (PUA) resin. **B)** An SEM image of nanochannel imprinted into COC5010 substrate. **C)** An SPM image of the nanochannel imprinted in to COC5010 and the depth was measured as 110 nm by SPM.

It is necessary to seal the nanofluidic device after thermal imprinting using a coverplate. Thermal fusion bonding is used for the sealing of nanochannel devices. Bonding of NIM-PMMA/COC devices were done according to a method described by Uba *et al.*⁵¹ with 1 minute oxygen plasma for both substrate and coverplate at 50 mW oxygen plasma power. We tried a similar protocol to bond COC/COC devices by modifying the both substrates and coverplate by oxygen plasma, but we were not successful in obtaining a well-sealed device. Therefore, we tried bonding these

COC5010 and 8007 without plasma treatment. Successful bonding was achieved between COC5010 and 8007 at 110 psi bonding pressure, 70 °C for 15 minutes. (Table 4.2)

Table 4.2. Optimized bonding conditions for NIM-PMMA and COC 5010 110 x110 nm nanochannels using the Nanonex 2500.

Substrate	Plasma modification	Bonding conditions (temp., pressure, time)
NIM-PMMA	1 min. at 50 mW	70°C, 110 psi, 15min
COC 5010	No modification	70°C, 100 psi, 15min

4.2.3 Bond strength measurements of nanochannel devices

The bond strength of COC nanochannel devices was evaluated by using crack opening method.^{52, 53} Here a razor blade of known thickness t_b is inserted between bonded substrate and cover plate to induce an interfacial fracture with a length of L from the edge of the razor blade. If elastic moduli of cover plate and substrate are E_p and E_s respectively, the bond strength is represented by equation (1). where t_s and t_p are the thickness of cover plate and the thickness of substrate. The elastic moduli of NIM-PMMA is 3.3 GPa, which was obtained experimentally by Q800 dynamic mechanical analyzer (TA instruments, New Castle, DE). The elastic moduli of COC5010 substrate is 3.0 GPa provided by manufacturer. The elastic moduli of COC8007 cover plate is 2.6 GPa provided by manufacturer. In this work, all tests were performed using a stainless steel single edge razor blade with a thickness of 0.009" and the crack lengths were measured using a calibrated upright microscope with a 10X objective lens. Bond strengths were calculated using

equation (4.1) All measurements were replicated five times and the average of bond strength was represented with the standard deviation of measurements.

$$\gamma = \frac{3t_b^2 E_s t_s^3 E_p t_p^3}{16L^4(E_s t_s^3 + E_p t_p^3)} \quad (4.1)$$

4.2.4 Evaluation of pH stability of fabricated nanochannel devices

Fabricated COC/COC and NIM-PMMA/COC nanochannel devices were first filled with Rhodamine B solution in ultrapure water at pH 7.0 and fluorescence images were captured including funnel area and nanochannel to make sure there is no channel deformation after bonding. Then the solution was removed using vacuum suction and washed with 50 % methanol/water mixture and added Rhodamine solution made in glycine buffer at pH 10.0. Fluorescence images were captured at t=0, t=0.5 h, and t=3 h to observe any deformation or leaking of fluorescence by delamination of coverplate.

4.2.5 Electroosmotic flow (EOF) measurement

Current monitoring method described by Huan *et al.*⁵⁴ was used to measure EOF in fabricated nanochannel device. A nanochannel device possessing a single nanochannel (107 μm long, 100 nm deep and 100 nm wide) connecting two access microchannels was fabricated as described earlier in text. First, the entire chip was primed with 50% (v/v water/methanol), then drained, and flushed with nuclease free water. After that, the device was filled with 1X NE (New England) buffer 3 (composition of NE buffer is given in Table 4.3) and allowed to equilibrate for 4 min. under a 500 mV DC bias. After confirming the equilibrium by a constant current trace, one reservoir was replaced by 0.94X NE buffer. Pt electrodes were placed in the reservoirs across the

channels under a 500mV DC bias. Signals were acquired using pClamp10 software and Digidata 1440B low noise digitizer set at a rate of 10 kHz sampling frequency. Electroosmotic flow was measured by changing the UV/O₃ dose through the coverplate of COC nanochannel device. The NE buffer is used as the stabilizing buffer for XRN-1. Therefore, we used same buffer for all of our experiments to match with enzyme conditions.

Table 4.3. Chemical composition of 1X NE buffer 3.

Component	Concentration (mM)
Sodium Chloride (NaCl)	100
Magnesium Chloride (MgCl₂)	10
Tris-HCl	50
Dithiothreitol (DTT)	1

4.2.6 Microscale electrophoresis of rNMPs

Fabrication of T-shaped microfluidic device (50μm depth x 100μm width and 5 cm long) was done by a hot embossing (Wabash P3H-15-CLX, IN, USA) into PMMA according to a method described by our group.⁵⁵ Embossed devices were diced using a bandsaw and reservoirs were drilled. Next, the devices were cleaned with 5% Micro-90, IPA and nanopure water. Finally, sealing of these devices were done using thermal fusion bonding to a 150 μm thick PMMA sheet at 105 °C for an hour. Before bonding the T-shaped chip was UV/O₃ treated at 22 mW for 16 min. Microchannel dimensions were measured before and after bonding by rapid laser-scanning optical profilometry (VK-X250, Keyence, IL, USA).

First the microfluidic device was primed with 50 % methanol/water mixture for 5 min. Then it was filled with 1X NE buffer 3 at pH 7.9. Separation was carried out at normal mode where the injection end is anodic, and the detection end is cathodic. Injection was initiated by applying a positive voltage to the sample reservoir and grounding the sample waste reservoir for the amount of time required to completely fill the cross channel. The remaining reservoirs were let to float during injection. After injection, a positive high voltage was applied to the electrophoresis buffer reservoir and the electrophoresis waste reservoir was grounded allowing the separation. Detection was done 4.0 cm away from injection point sing a home-built laser induced fluorescence detection system equipped with a single-photon counting module.

Figure 4.3 shows the LIF detector which was configured in an epillumination format having a 532 nm, 20 mW excitation laser (LaserGlow Technologies, Toronto, Ontario, Canada), XF 3085 edge filter (Horiba Scientific, Middlesex, UK), 560 nm long pass filter (Omega Optical, Brattleboro, VT), a 532 nm dichroic filter (Omega Optical Brattleboro, VT) and a SPCM-AQR single photon counting module (Perkin Elmer Optoelectronics, Waltham, MA). A 100X high numerical aperture (NA = 1.3) microscope objective from Nikon (Natick, MA) was used to focus the laser beam onto the microchip and collect the fluorescence.

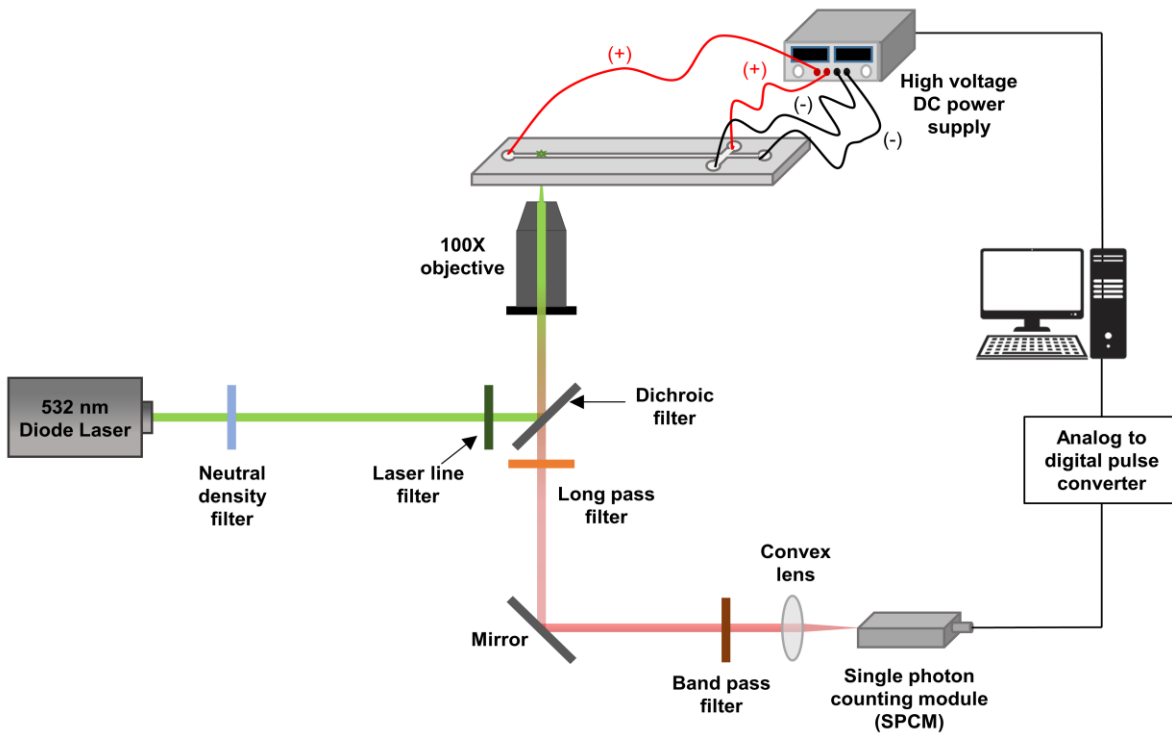


Figure 4.3. A schematic diagram of microscale electrophoresis set up with the T-shaped microchip fabricated in PMMA having the dimensions of 100 μm in width and 50 μm depth. The length of the separation channel is 5 cm.

4.2.7 Electrokinetic separation of rNMPs in nanochannels

Assembled COC/COC nanochannel devices were UV/O₃ treated through the COC coverplate at 22 mW for 15 min with highest EOF.⁴⁶ For NIM-PMMA/COC devices no UV/O₃ activation is done. Then nanochannel devices were primed with 50 % methanol for 5 min. Next using a vacuum pump, the methanol was removed from the nanofluidic device. After that it was filled with 1X NE buffer 3 at pH 7.9 and allowed to equilibrate for 10 min. ATTO532 labeled rNMPs of 200 nM were prepared in 1X NE buffer 3. Next, carrier electrolyte in one of the reservoirs connecting microchannels was replaced with rNMP solution. Afterwards the carrier electrolyte in the opposite side of same microchannel was removed and vacuum was applied to make sure it was completely

filled. Once the microchannel was filled, all the other reservoirs were filled with the same volume of carrier electrolyte. Finally, square voltage (V_{pp}) was applied using an ATTEN ATF200B function waveform generator for a period of 20 s to allow for multiple injections of the dye labeled oligonucleotides to nanochannels. Events were recorded for 6000 frames allowing multiple events to be analyzed.

All fluorescence imaging was done using Nikon TE2000 inverted microscope (Nikon, Minato-ku, Tokyo, Japan) equipped with 100x oil immersion objective (NA-1.3). A Keplerian beam expander was used to expand the Gaussian laser beam to completely backfill the objective. The lower intensity wings were whacked using an iris to ensure uniform laser intensity in the microscope's field of view. Kohler epiillumination was used to focus the beam to the back of microscope objective to allow irradiation of entire field-of-view and passed through 532 laser line filter (F1) and dichroic filter (DF). The emission signal was collected by the objective, passed through the dichroic filter, spectrally selected long pass filter (F2), band pass filter (F3) and imaged onto an iXon 897 EMCCD camera (Andor technologies Ltd, Belfast, United Kingdom) controlled by Metamorph software (see Figure 4.4).

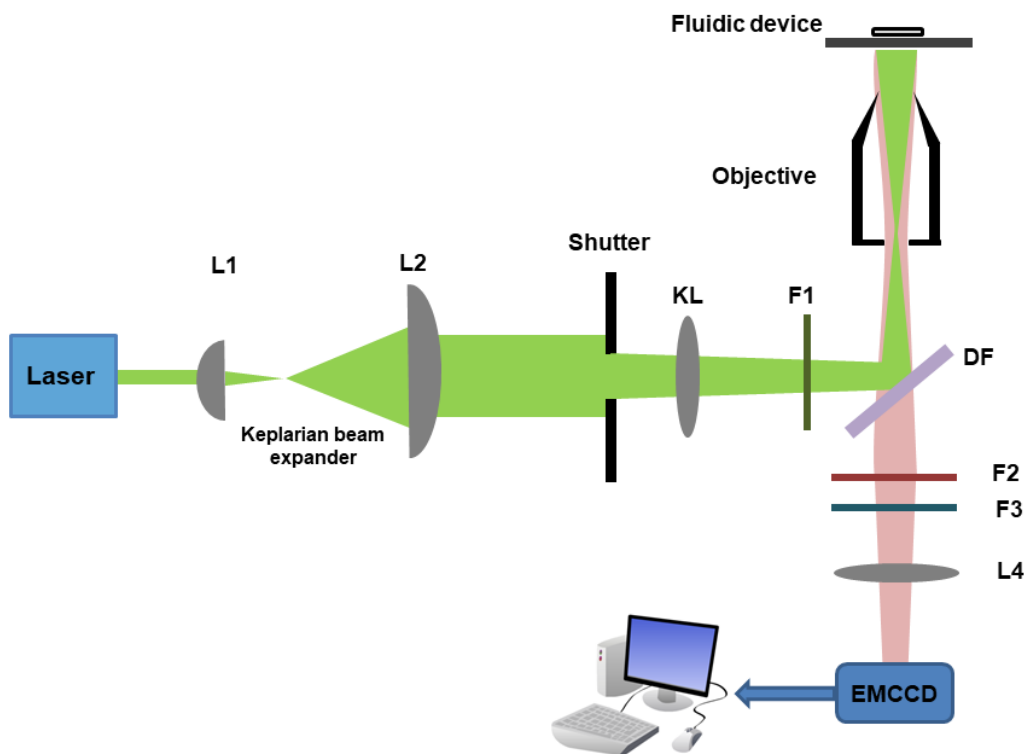


Figure 4.4. (A) Optical set-up of the fluorescence imaging system. The Gaussian beam from the laser (Nd:YAG; $\lambda_{\text{ex}} = 532 \text{ nm}$; $P = 0.01\text{-}5 \text{ W}$; 2.2 mm beam diameter) was expanded 10x using a Keplerian beam expander and the wings were knocked out with an iris that ensured uniform laser intensity in the field-of-view and complete back-filling of the objective (OBJ). The beam was focused into the back of a 100x oil immersion objective

4.2.8 Data analysis

ImageJ software⁵⁶ was used to analyze the fluorescence intensity data relevant to nanoscale separations. Collected videos were imported to image software and two detection windows of $1\mu\text{m}^2$ were placed at the entrance and exit of nanochannel. Fluorescence intensity of these two detection windows were recorded using ImageJ software. These data were then exported to data analysis software Origin pro 8.5. The first derivative was taken of each data set to find the two peaks representing the time at which the maximum intensity was reached at both the entrance and

exit of the nanochannel. The time between peak 1 and peak 2 is the ΔT for each rNMPs and the apparent mobility can be determined from this value as following equation (4.2). Where l is the distance between two detection windows, L total length of nanochannel and V is the applied electric potential.

$$\mu_{app} = (lL/\Delta TV) \quad (4.2)$$

4.3 Results and discussion

4.3.1 Bond strength and pH stability of COC/COC devices

Thermal bonding is an essential step for obtaining enclosed nanochannels in nanofluidic devices. Therefore, we studied the bond strength of thermally bonded COC/COC devices and NIM-PMMA/COC devices using the crack opening method described in previous sections. The advantage of using thermal bonding for sealing was that nanochannels with homogeneous channel surfaces with uniform properties (i.e., surface charge and wetting angles) can be obtained. Preliminary tests were conducted to optimize the bonding pressure and bonding time at a bonding temperature of 70°C, which is close to the glass transition temperature of the cover plate, to avoid undesirable deformation of the nanochannels during thermal sealing because the substrate, which contains the nanochannels, has a much higher glass transition temperature. The optimized bonding parameters (see Table 4.2) were utilized to prepare sealed nanochannel devices to obtain bond strengths. As shown in Figure 4.5A, the bond strength of COC/COC devices were significantly higher than that of NIM-PMMA/COC devices. This suggests that interfacial adhesion of similar materials is greater than that of dissimilar materials.

pH stability is another important parameter to evaluate in these COC/COC devices and NIM-PMMA/COC devices because we wanted to check whether this device is usable at pH >9 that may result in optimal rNMP electrophoretic separations. In these experiments to check for cover plate delamination from the substrate, the device was flooded with different pH buffers and then the device was filled with a Rhodamine dye test and using fluorescence imaging, determine if leaking of the dye solution occurred. A fluorescent image of the dye-filled chip was first taken at neutral pH to make sure that the bonded device had no leakage prior to adding the high pH Rhodamine B solution. After 30 min, the NIM-PMMA/COC devices leaked as fluorescence appeared near the inlets of the nanochannels indicating the delamination of the cover plate from the substrate. However, for COC/COC devices, even after 3 h we did not observe leaking or delamination. (see Figure 4.5 B and C respectively). According to this observation, NIM-PMMA/COC devices are less stable at high pH conditions. When considering on the chemical resistance of NIM-PMMA and COC, NIM-PMMA shows lower base resistance (There can be slight swelling and dissolving of PMMA when exposed to bases).^{57, 58} This might be the reason for the observed delamination of cover plate from the substrate in NIM-PMMA/COC devices compared to COC/COC devices.

A	Assembled device	NIM-PMMA / COC8007	COC5010 / COC8007
Bond strength (mJ/cm ²)	0.086 ± 0.014	8.533 ± 1.125	

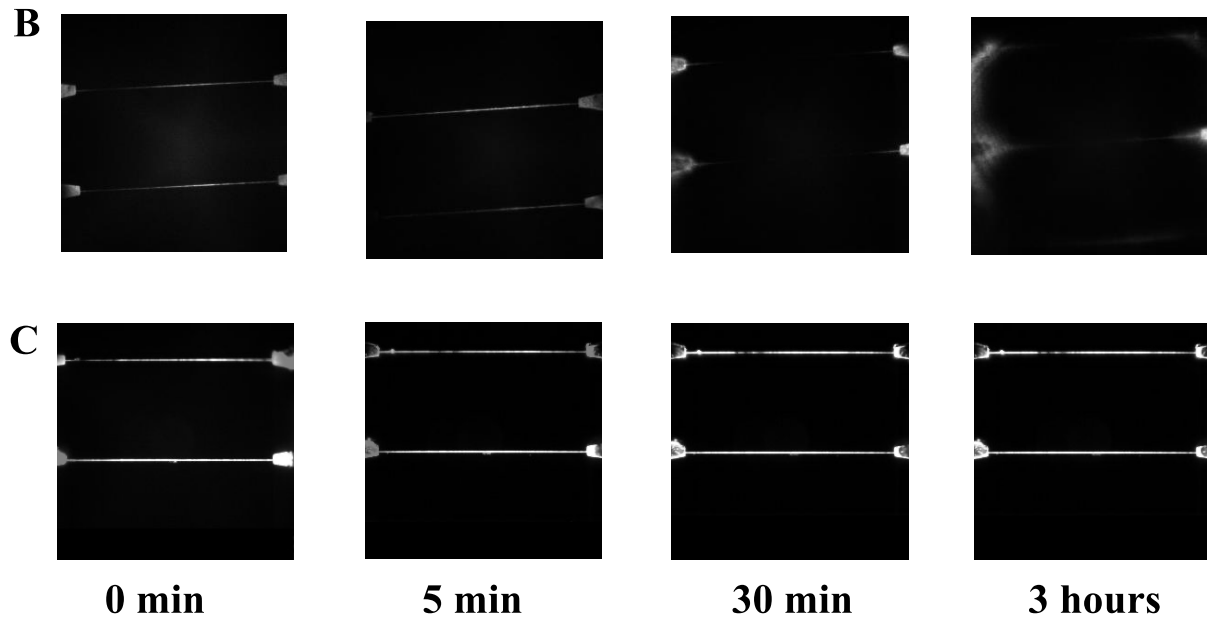


Figure 4.5. **A)** The bond strength calculated for thermally bonded COC/COC devices and NIM-PMMA/COC devices. Bonding of COC/COC devices was done without plasma treatment and NIM-PMMA/COC was done by treating both substrate and coverplate under 50 mW O₂ plasma for 1 min Standard deviation is given for n=5 measurements. **B)** pH stability of NIM-PMMA/COC devices with time. **C)** pH stability of COC/COC devices with time. All fluorescence images were adjusted to the same intensity scale.

4.3.2 Water contact angle and EOF mobility of COC/COC devices

Water contact angle measurements can serve as a measure of the hydrophilicity of a surface, although it does not provide an insight into the functional group identity. Contact angle data evaluate the hydrophilicity/hydrophobicity of the surfaces, which is indicative of the formation of polar functional groups on the surface generated after surface activation. Figure 4.6A shows the

contact angle measured at different UV/O₃ exposure times for a COC 5010 substrate with a COC 8007 cover plate. The contact angle decreased with increasing time up to 15 min. This indicated that the COC surface had become more hydrophilic due to polar functional groups generated during the process of UV/O₃ activation. The contact angle did not change with further increasing UV/O₃ exposure time after 15 min as shown in Figure 4.6 A(p = 0.3474 for n=5 contact angle data for 15 min UV exposure vs. 20 min UV exposure).

Another important parameter to be considered is the EOF in these nanofluidic devices. Therefore, we measured the EOF with UV/O₃ exposure time in a sealed COC/COC nanochannel device, and the device was exposed to UV/O₃ through the cover plate. According to the data presented in Figure 4.6B, The EOF mobility remained constant ($1.40 \times 10^{-5} \text{ cm}^2/\text{Vs}$) until 10 min exposure time, but at 15 min exposure, there was a significant increase in the EOF (~10-fold increase) and then at 20 min exposure, the EOF remains the same (p=0.87 for EOF value at 15 min exposure vs 20 min exposure). At low λ_D (here ~0.3 nm), μ_{eof} can be represented in terms of the bulk solvent viscosity η_0 , and the zeta potential ζ by the Helmholtz-Smoluchowski equation where ϵ_0, ϵ_r are the permittivity of air and the relative permittivity of the buffer, respectively.

$$\mu_{eof} = \frac{\epsilon_0 \epsilon_r \zeta}{\eta_0} \quad (4.3)$$

Furthermore, the zeta potential can be represented in terms of σ_s (surface charge) and λ_D (electric double layer thickness) for different electrolyte solutions using the equation (4.4).⁴³

$$\zeta = \frac{2 k_B T}{e} \ln \left[\frac{2 e \sigma_s \lambda_D}{\epsilon_r \epsilon_0 k_B T} + \sqrt{1 + \left[\frac{(e \lambda_D / \epsilon_r \epsilon_0 k_B T)^2}{4} \right]} \right] \quad (4.4)$$

In equation (4.3), ϵ_0 and ϵ_r are permittivity of air and the relative permittivity of buffer and are constants for a given carrier electrolyte. The parameters that can change σ_s , ζ , λ_D , or η will alter the magnitude of the EOF. Here, the same buffer concentration was used and therefore, or η does not change as a function of UV/O₃ dose. Only σ_s is changing, therefore the EOF changes due to the increasing number of -COOH groups on the plastic surface generated during UV/O₃ activation. However, similar to contact angle data the EOF levels off after 15 min UV/O₃ exposure. Both of these observations suggest that there is no further increase in the surface -COOH functional groups. O'Neil *et al.*⁴⁶, whom mapped the distribution and number density of surface -COOH groups in COC by superresolution microscopy, observed a reduction of -COOH groups at 20 min UV/O₃ exposure time compared 15 min. This is different compared to our observation, where we did not observe a change in the surface -COOH groups at 15 min and 20 min UV/O₃ exposure time. This nearly constant -COOH density is most likely due to the scission of the polymer chains and etching of the surface during prolonged exposure to UV/O₃ in addition to the generated -COOH groups.^{59, 60}

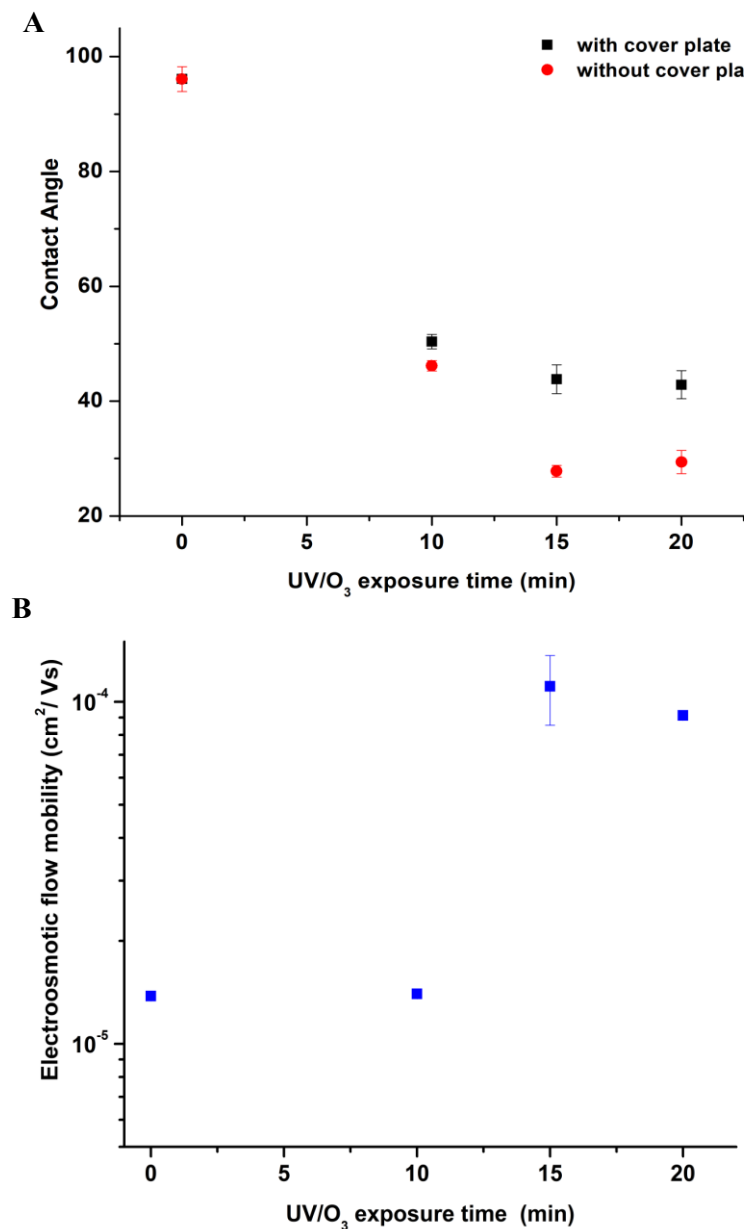


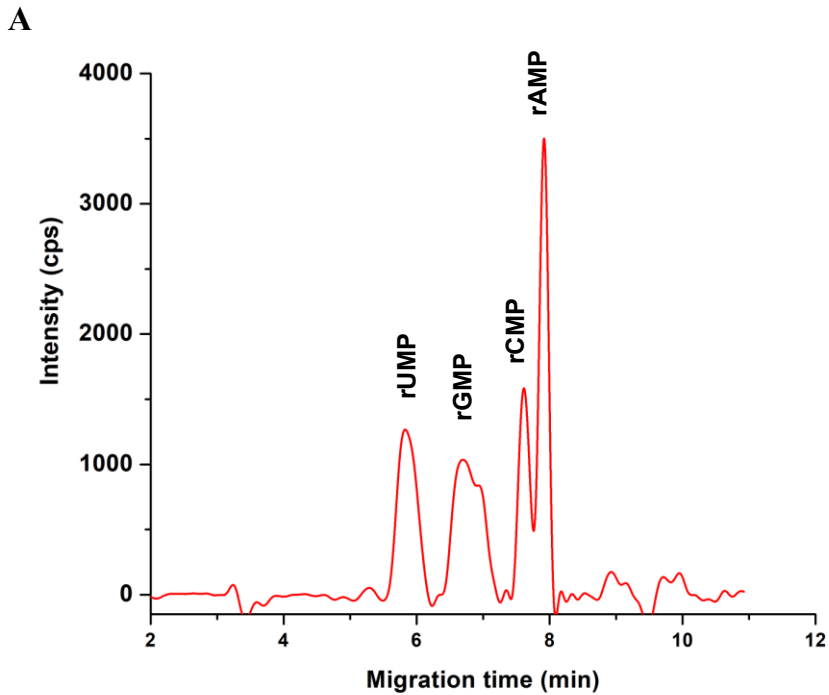
Figure 4.6. **A)** Water contact angle of COC 5010 surface measured at different UV/O₃ exposure times at 22 mW/cm². The data points named as with cover plate were obtained by keeping a cover plate on top of the substrate and then exposing it with UV/O₃. After exposure, the contact angle of the underlying substrate was measured. **B)** EOF mobility of COC/COC nanochannel devices. The dimensions of the nanochannels were 110 nm x 110 nm depth and width respectively (length – 107 μm). Substrate is COC5010 and sealed with COC8007 coverplate. The activation was done though the coverplate side. Error bars represent the standard deviation of contact angle and EOF for n=5.

4.3.3 Microscale electrophoretic separation of rNMPs

We carried out microscale separations of the rNMPs using a T-shaped microchip fabricated in PMMA (depth = 50 μm ; width = 100 μm effective length = 5 cm) to understand the effects of scaling for the separation. The free solution electrophoretic separations of the rNMPs was done in 1X NE buffer 3 at pH 7.9. During the microscale electrophoresis, rNMPs migrated from anode to cathode in spite of their anionic nature. As shown in Figure 4.7A, at pH 7.9 we could separate all four rNMPs in free solution by electrophoresis. The apparent mobilities of the rNMPs were calculated using equation 4.5 and are presented in Figure 4.7B. In this case, l is the distance to the detector from injection point (4.0 cm), t_m is the migration time of rNMPs, and E is the electric field strength (1,000 V/cm). The apparent mobility order of rNMPs were rAMP < rCMP < rGMP < rUMP, which was the opposite of the migration time order.

$$\mu_{app} = \frac{l}{t_m E} \quad (4.5)$$

Uhrova *et al.*²⁷ showed the separation of ribonucleotide monophosphates in a fused silica capillary without suppressing the EOF by free solution electrophoresis using borate buffer at pH 8 and observed similar migration order except for rUMP, where they observed a higher migration time for rUMP. Baseline separation (resolution >1.5) was obtained for rGMP and rUMP, but for rAMP and rCMP no baseline separation was observed (see Figure 4.7C).



B

rNMPs	Apparent mobility $\times 10^{-5}$ (cm ² /Vs)
rUMP	1.50
rGMP	1.20
rCMP	1.09
rAMP	1.05

C

Peak Pair	Separation resolution
rUMP/rGMP	1.74
rGMP/rCMP	2.00
rCMP/rAMP	1.15

Figure 4.7. **A)** The electropherogram for the separation of rNMPs by microscale electrophoresis in PMMA microchannels having dimensions of 50 $\mu\text{m} \times 100 \mu\text{m}$ (depth and width, respectively) with 5 cm separation length. **B)** Calculated apparent mobilities of rNMPs using equation (4.5). **C)** Resolutions (R) calculated for adjacent peak pairs using the electropherogram shown in (A). $R = 1.18(t_{m2}-t_{m1}) / (w_{0.5}+w_{0.5})$ where t_{m1} and t_{m2} are migration times and w_1 and w_2 corresponds to the peak widths at the base of the peaks.

4.3.4 Effect of material type for the nanoelectrokinetic separation of ATTO 532-labeled rNMPs

In sections 4.3.1 and 4.3.2 we compared the mechanical and chemical properties of fabricated nanochannel devices in COC/COC and NIM-PMMA/COC. In here we studied the separation of rNMPs in NIM-PMMA/COC nanochannel devices to those in COC/COC devices. Upon changing the substrate, we changed the nanochannel wall and thus the surface charge and EOF become different compared to COC/COC devices. The EOF mobility for NIM-PMMA devices were reported in Chapter 3, which was $4.2 \times 10^{-4} \text{ cm}^2 / \text{Vs}$. The EOF of NIM-PMMA devices were ~4 times higher than that of COC/COC nanochannel devices and thus, herein we sought to understand the effect of material type for the separation.

4.3.4.1 Separation of rNMPs in NIM-PMMA/COC nanochannel devices

Figure 4.8A shows the apparent mobility versus electric field strength for the four rNMPs using a 110 nm x 110 nm nanochannel fabricated in NIM-PMMA/COC with a carrier electrolyte consisting of 1x NE buffer 3 (ionic strength 145 mM) at pH 7.9. At pH 7.9, all ATTO 532-labeled rNMPs have a net charge of -3; the ATTO-532 dye contributes a -2 charge and the phosphate contributes -1 (see Figure 4.8B) with all nucleobases not carrying a charge at this pH. The apparent mobility is a sum of the EOF (μ_{eof}) and the electrophoretic mobility of the rNMP (μ_{ep}). In this case, the electrophoretic mobility of the dye/rNMP conjugate is opposite in direction to the EOF and thus, an increase in μ_{ep} results in a decrease in the apparent mobility. Because all rNMPs have the same charge at this pH, the differences in the apparent mobility could arise due to differences in their size, which in this case arises from the nucleobase if the separation mechanism is merely

electrophoretic. We could only do the separations at electric field strengths less than 464 V/cm in these nanochannel devices due to the fast movement of rNMP at electric field strengths >464V/cm without experiences significant peak slewing due the limited frame rate of the EMCCD camera. As seen in Figure 4.8A there is a field dependent apparent mobility for rCMP and rAMP but not for rUMP and rGMP whereas on the dNMPs separation⁴⁸, all dNMPs showed field dependent apparent mobility. At this point we are not exactly sure why field dependent apparent mobilities are observed for some of the rNMPs.

Figure 4.8C shows histograms of the apparent mobility for the ATTO 532 labeled rNMPs at 280 V/cm in NIM-PMMA/COC devices. This electric field was selected as it provided the optimal resolution between the rNMPs with minimum standard deviations. These histograms were fit to a Gaussian function and the resolution and identification accuracies were calculated. The apparent mobility order here is rUMP < rGMP < rCMP < rAMP. The observed apparent mobility order here is different than the apparent mobility order we observed in microscale CE with no wall interactions (in the microchannel due to its larger size allows for very infrequent interactions between the solutes and the PMMA wall). Therefore, the difference observed in the apparent mobility order could be due to the scaling effects that arose in nanoscale compared to microscale. When the channel dimensions are decreased to nanometers, the surface area-to-volume ratio increases, and thus, surface interactions of analytes with channel walls become prominent. Increased surface interactions of rNMPs with nanochannel walls can contribute to the electrophoretic separation of rNMPs leading to a difference in the apparent mobility order in nanoscale.⁴⁸ The average separation resolution is 4.3. (separation resolutions ranged from 1.4-7.8) Another important metric for the utilization of mobility matching for the identification of mononucleotides is the identification accuracy, which is related to the separation resolution

between the nucleotides. We define the “identification accuracy” as the amount of overlap of two adjacent Gaussian fits to the histograms of the ATTO 532-rNMPs’ apparent mobilities. The percent overlap of the Gaussian peak was calculated using a previously described method and is related to separation resolution.⁶¹ The average identification accuracy for the separation of rNMPs in NIM-PMMA/COC devices was >99.955%.

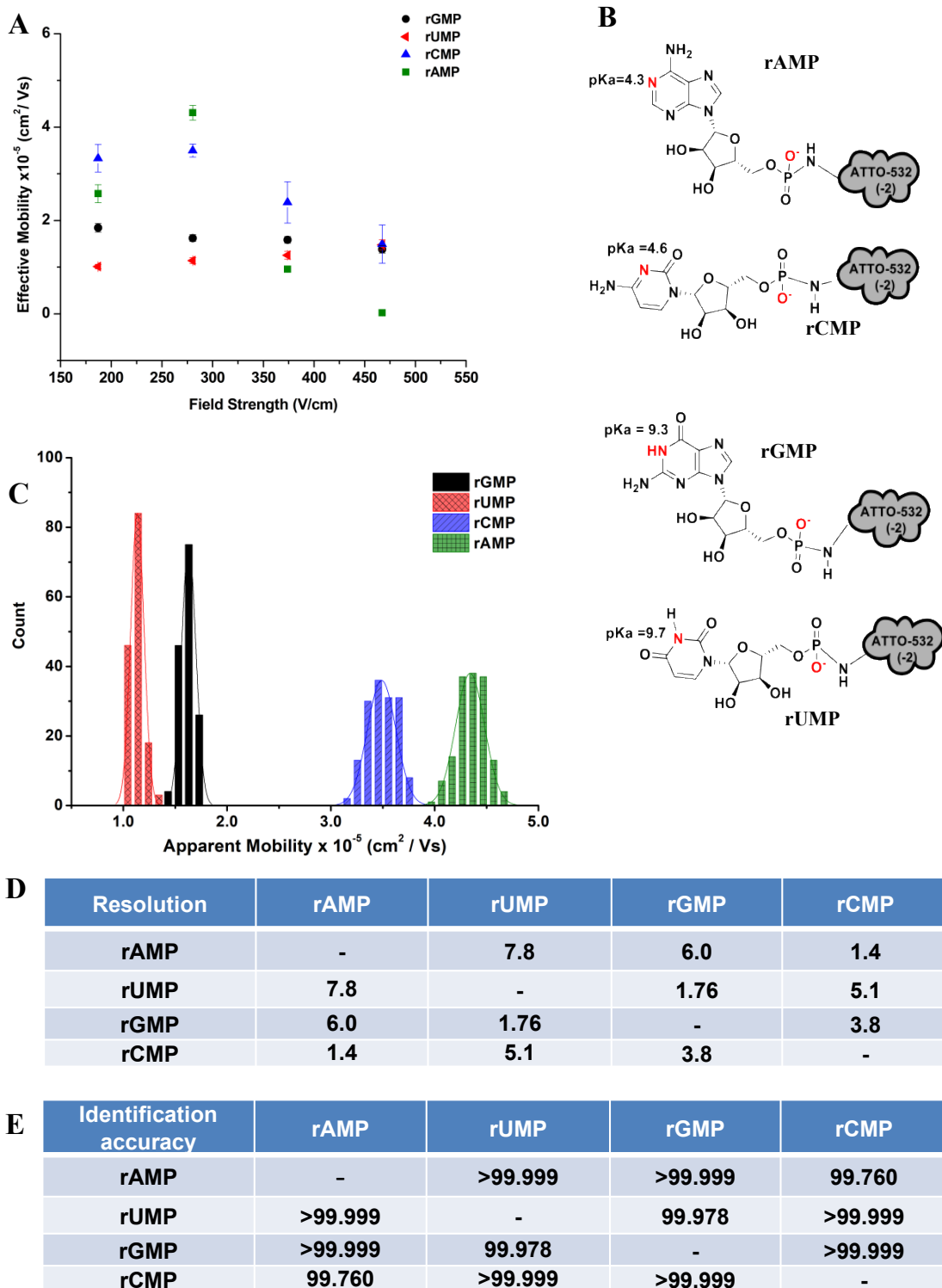
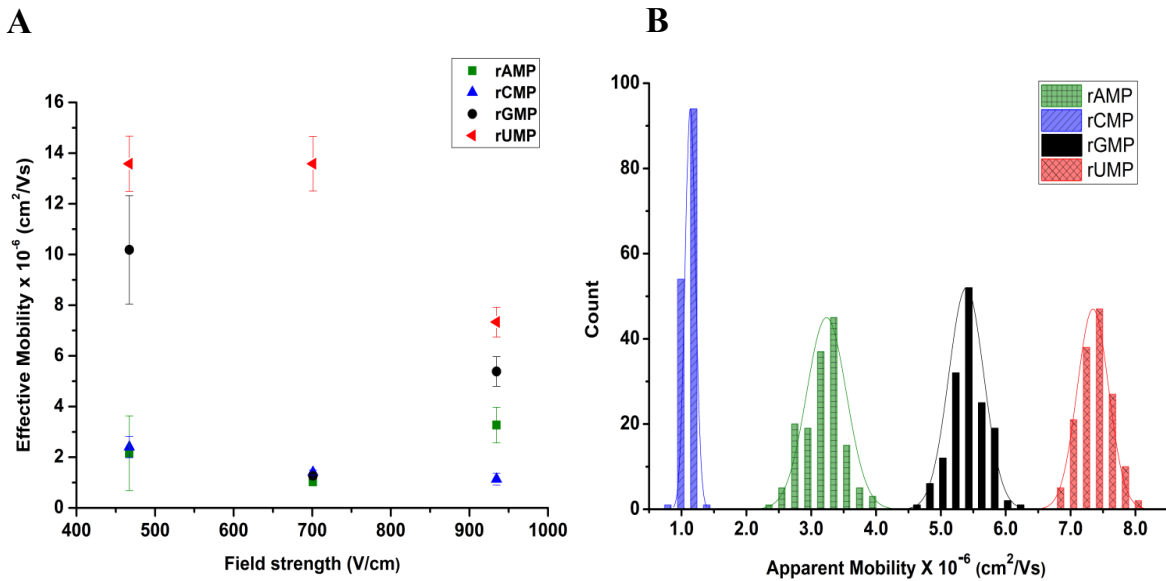


Figure 4.11. A) Apparent mobility vs electric field strength of rNMPs in 110 nm x 110 nm nanochannels fabricated in NIM-PMMA/COC nanochannels using 1X NE buffer 3 at pH 7.9 as carrier electrolyte. B)

schematic diagram of rNMPs with attached dye and the pKa of the nucleobases. **C)** Histogram of apparent mobilities of rNMPs at 280 V/cm in 110 x 100 nm NIM-PMMA/COC nanochannel devices using 1X NE buffer 3 at pH 7.9 as the carrier electrolyte. The histograms were fit in to gaussian function and each bin represent $2 \times 10^{-6} \text{ cm}^2/\text{Vs}$. **C)** The resolution of peaks was calculated using $R = 1.18 (\Delta\mu/w_{0.5} + w_{0.5})$ where $w_{0.5}$ correspond to the full width at half maximum of the gaussian peaks. **D)** Identification accuracies of rNMPs calculated from Gaussian peak overlap. Identification accuracy = area of non-overlapped/total peak area.

4.3.4.2 Separation of rNMPs in COC/COC nanochannel devices

In the previous section, we investigated the separation of rNMPs in NIM-PMMA/COC nanochannel devices, and here we investigated the separation of rNMPs in COC/COC devices. Upon changing the substrate, we changed the nanochannel wall and, thus, the surface charge and EOF compared to NIM-PMMA/COC devices. The EOF mobility for COC/COC devices(was $1.1 \times 10^{-4} \text{ cm}^2 / \text{Vs}$) is ~4 times smaller than that of NIM-PMMA/COC devices (reported in Chapter 3, which was $4.2 \times 10^{-4} \text{ cm}^2 / \text{Vs}$). Therefore, the overall magnitude of μ_{app} is lower in COC/COC devices compared to NIM-PMMA/COC devices. Figure 4.9A shows the apparent mobility vs. Field strength of rNMPs in the COC/COC nanochannel device. In contrast to the data shown in Figure 4.8A, here we could only do the separation at higher electric field strengths because at electric field strength <464 V/cm we observed nonspecific adsorption of rNMPs to the nanochannel and could not imagine the movement of dye front accurately to calculate the apparent mobilities. At electric field strengths < 934 V/cm majority of the rNMPs comigrated. Moreover, the dependent field mobility is observed here only for rUMP and rGMP, which was the opposite in NIM-PMMA/COC devices. However, at this point, we don't know the exact reasons for these observations.



C

Resolution	rAMP	rUMP	rGMP	rCMP
rAMP	-	3.72	1.94	2.69
rUMP	3.72	-	1.96	8.88
rGMP	1.94	1.96	-	6.10
rCMP	2.69	8.88	6.10	-

D

Base call accuracy	rAMP	rUMP	rGMP	rCMP
rAMP	-	>99.999	99.995	>99.999
rUMP	>99.999	-	99.996	>99.999
rGMP	99.995	99.996	-	>99.999
rCMP	>99.999	>99.999	>99.999	-

Figure 4.9. **A)** Apparent mobility vs electric field strength of rNMPs in 110 nm x 110 nm nanochannels fabricated in COC/COC nanochannels using 1X NE buffer 3 at pH 7.9 as the background carrier electrolyte **B)** Histogram am of apparent mobilities of rNMPs at 934 V/cm in 110 x 100 nm COC/COC nanochannel devices using 1X NE buffer 3 at pH 7.9 as the carrier electrolyte. The histograms were fit into gaussian function and each bin represent $2 \times 10^{-6} \text{ cm}^2/\text{Vs}$. **C** The resolution of peaks was calculated using $R = 1.18 (\Delta\mu/w_{0.5} + w_{0.5})$ where $w_{0.5}$ correspond to the full width at half maximum of the gaussian peaks. **D)** Identification accuracies of rNMPs calculated from Gaussian peak overlap. Identification accuracy was calculated as mentioned in Figure 4.8.

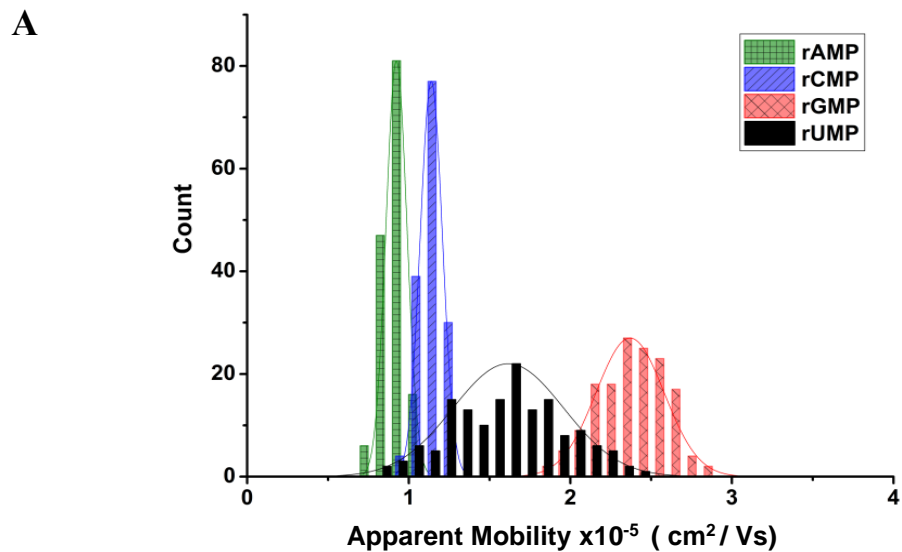
Figure 4.9B shows histograms of the apparent mobility for the ATTO 532-labeled rNMPs at 934 V/cm, which was selected because it provided optimal separation resolution between the rNMPs. The resolution for these rNMPs was determined from the Gaussian fits to the histograms. Figure 4.9C shows the separation resolution between rNMP Gaussian fit pairs using 1X NE buffer 3 at pH 7.9. The apparent mobility order is rCMP < rAMP < rGMP < rUMP and is different than the apparent mobility order observed in NIM-PMMA/COC nanochannel devices. However, the apparent mobility order observed here is similar to the apparent mobility order seen in microscale CE except for the apparent mobility order of rAMP. At the carrier electrolyte pH 7.9 and the field strength of 934 V/cm ($\lambda_d = 0.3$ nm), the average separation resolution of rNMPs is 4.2 (ranged from 1.94 to 8.88, see Figure 4.9 C). This implies that the average separation resolution is not significantly different than that of NIM-PMMA/COC devices. Figure 4.9D shows the calculated identification accuracies for the nucleotides at the above experimental conditions. As can be seen from this data, the identification the average identification accuracy for the separation of rNMPs in COC/COC devices was >99.997. The average identification accuracy of rNMPs in COC/COC devices was higher than that of NIM-PMMA/COC devices. The average identification accuracy was high for the rNMPs in both materials compared to our previous separation on the dNMPs (deoxynucleotide monophosphates) where average identification accuracy was >95 %.⁴⁸ This implies that the separation of rNMPs is better in nanochannels than that of the dNMPs. Although we are not exact about what makes this difference, we suggest that the changed surface interactions of rNMPs with nanochannels might have contributed to this change.

4.3.4.3 Effect of pH on the nanoelectrokinetic separation of ATTO 532-labeled rNMPs in COC/COC devices

We explored the separation of the rNMPs at pH 10.3, because a majority of the ribonucleotide monophosphate separations showed better resolution at high pH (pH >9). For the high pH experiment, the same carrier electrolyte was used with slight modifications. Tris-HCl in 1X NE buffer 3 was replaced with glycine, but the ionic strength was kept a constant. Glycine has the proper buffer capacity at pH 10.3 (pK_a 9.6) and therefore, the pH of the carrier electrolyte is maintained properly during the course of the experiment.

Figure 4.10A shows histograms of apparent mobility of rNMPs at pH 10.3 using COC/COC nanochannels at a field strength of 934 V/cm. The apparent mobility order at this pH was rAMP < rCMP < rGMP < rUMP. As seen in the Figure 4.9 where the separation was carried out at pH 7.9, the overall magnitude of the μ_{app} for all rNMPs increased. Increasing the carrier electrolyte pH had a two-fold effect: (1) Increasing the EOF due to increased ionization of the surface functional groups (the pK_a of the surface -COOH groups are ~ 6.9)⁴³ and the percent ionization of the surface -COOH groups can be calculated using the Henderson-Hasselbalch equation at different carrier electrolyte pHs.⁶² The calculation at pH 7.9 resulted in 90% ionization of the surface -COOH groups, while pH 10.3 resulted in 99.99% ionization. The EOF mobility measured at this pH was $7.5 \times 10^{-4} \text{ cm}^2/\text{Vs}$, which was approximately seven times higher compared to the EOF observed at pH 7.9 ($1.1 \times 10^{-4} \text{ cm}^2/\text{Vs}$). (2) Changing the charge status on some rNMPs. In this case, we would expect rGMP and rUMP to have the lowest μ_{app} compared to the other two rNMPs. However, the experimental observations do not support for this argument. At pH 10.3, the separation resolution was reduced compared to pH 7.9 partly due to the increased peak width of rGMP and rUMP. In

our previous paper,⁴⁸ we observed surface interactions contributed to the nanoscale separation due to the increased surface area-to-volume ratio compared to microscale columns. The change in the charge of rNMPs also can alter potential interactions of the rNMPS with the nanochannel wall. The increased band dispersion of rGMP and rUMP could be due to the contributions arising from increased wall interactions. Figure 4.10B shows the calculated separation resolutions between rNMPs at pH 10.3. Similar to previous experiments, we determined the identification accuracies of rNMPs considering the amount of peak overlap in histograms (Figure 4.10 C). We observed a decrease in the identification accuracies in rNMPs with increasing pH. The average identification accuracy under high pH conditions was >95.620.



B

Resolution	rAMP	rUMP	rGMP	rCMP
rAMP	-	0.81	2.55	0.78
rUMP	0.81	-	0.64	0.82
rGMP	2.55	0.64	-	2.08
rCMP	0.78	0.82	2.08	-

C

Base call accuracy	rAMP	rUMP	rGMP	rCMP
rAMP	-	94.738	>99.999	94.062
rUMP	94.738	-	89.973	94.950
rGMP	>99.999	89.973	-	>99.999
rCMP	94.062	94.950	>99.999	-

Figure 4.10. **A)** Histogram of apparent mobilities of rNMPs at 934 V/cm in 110 x 100 nm COC/COC nanochannel devices using 1X NE buffer 3 at pH 10.3 as the carrier electrolyte. The histograms were fit to Gaussian functions and each bin represents 2×10^{-6} cm^2/Vs . **B)** The resolution of peaks at pH 10.3 was calculated using $R = 1.18 (\Delta\mu/w_{0.5} + w_{0.5})$, where $w_{0.5}$ correspond to the full width at half maximum of the Gaussian peaks. **C)** Identification accuracies of rNMPs calculated from Gaussian peak overlap. Identification accuracy = area of non-overlapped/total peak area at pH 10.3.

4.4 Conclusions

Our proposed SMS method address the limitations of poor base call accuracy of current nanopore sequencing by generating mononucleotides using a processive enzyme from an intact RNA molecule. Identification of the nucleobases would be enabled by molecular-dependent flight times of the rNMPs within nanochannels, which in this case refers to the apparent mobilities of the rNMPs; concept termed Time-of-Flight (ToF) identification. In this work, we sought to understand the electrokinetic properties of the rNMPs in thermoplastic nanochannels under varying pH, material type, and ultimately how these factors contribute to the separation resolution and identification accuracy of rNMPs. We first fabricated COC/COC nanofluidic devices and investigated the change of the contact angle and EOF with UV/O₃ dose. The lowest contact angle and the highest EOF was obtained at 15 min UV/O₃ exposure, further increase of UV/O₃ exposure time did not change the EOF and thus the -COOH group density. The advantage of COC/COC devices was the ability to perform post assembly surface modification and control EOF depending on the UV/O₃ dose, which is not possible in NIM-PMMA/COC devices.

In both COC/COC nanochannel devices and NIM-PMMA/COC nanochannel devices the separation resolutions of rNMPs were >1.5 and the average separation resolutions were about the same. (4.2 for COC/COC devices and 4.3 for NIM-PMMA/COC devices) However, the identification accuracies of rNMPs were higher in COC/COC devices ($\geq 99.997\%$) than that of NIM-PMMA/COC devices (99.955%). In contrast to our separation of dNMPs in thermoplastic nanochannels, increasing pH of the carrier electrolyte decreased the separation resolution of rNMPs ranging from 0.64-2.55. In both materials the separation is primarily due to electrophoresis, but there were some contributions from the surface interactions of rNMPs with the nanochannel

walls for the separation. The successful separation of rNMPs in free solution using thermoplastic nanochannels will be able to be utilized in developing the SMS nanosensor and the advances of this in the future will facilitate the analysis of the transcriptome.

4.5. References:

1. Crick, F., Central dogma of molecular biology. *Nature* **1970**, 227 (5258), 561.
2. Wang, Z.; Gerstein, M.; Snyder, M., RNA-Seq: a revolutionary tool for transcriptomics. *Nat Rev Genet* **2009**, 10 (1), 57-63.
3. Botstein, D., *Decoding the language of genetics*. Cold Spring Harbor Laboratory Press: 2015.
4. Voet, D.; Voet, J. G., *Biochemistry*. John Wiley & Sons: 2010.
5. Pillai, R. S., MicroRNA function: multiple mechanisms for a tiny RNA? *Rna* **2005**, 11 (12), 1753-1761.
6. Abgrall, P.; Low, L.-N.; Nguyen, N.-T., Fabrication of planar nanofluidic channels in a thermoplastic by hot-embossing and thermal bonding. *Lab on a Chip* **2007**, 7 (4), 520-522.
7. Hoeijmakers, W. A.; Bártfai, R.; Stunnenberg, H. G., Transcriptome analysis using RNA-Seq. In *Malaria*, Springer: 2012; pp 221-239.
8. Whitley, S. K.; Horne, W. T.; Kolls, J. K., Research techniques made simple: methodology and clinical applications of RNA sequencing. *Journal of Investigative Dermatology* **2016**, 136 (8), e77-e82.
9. Grada, A.; Weinbrecht, K., Next-generation sequencing: methodology and application. *The Journal of investigative dermatology* **2013**, 133 (8), e11.
10. Ray, M.; Horne, W.; McAleer, J. P.; Ricks, D. M.; Kreindler, J. L.; Fitzsimons, M. S.; Chan, P. P.; Trevejo-Nunez, G.; Chen, K.; Fajt, M., RNA-seq in pulmonary medicine: how much is enough? *American journal of respiratory and critical care medicine* **2015**, 192 (3), 389-391.
11. Schena, M.; Shalon, D.; Davis, R. W.; Brown, P. O., Quantitative monitoring of gene expression patterns with a complementary DNA microarray. *Science* **1995**, 270 (5235), 467-470.
12. Lockhart, D. J.; Dong, H.; Byrne, M. C.; Follettie, M. T.; Gallo, M. V.; Chee, M. S.; Mittmann, M.; Wang, C.; Kobayashi, M.; Norton, H., Expression monitoring by hybridization to high-density oligonucleotide arrays. *Nature biotechnology* **1996**, 14 (13), 1675.
13. Casneuf, T.; Van de Peer, Y.; Huber, W., In situ analysis of cross-hybridisation on microarrays and the inference of expression correlation. *BMC bioinformatics* **2007**, 8 (1), 461.
14. Shendure, J., The beginning of the end for microarrays? *Nature methods* **2008**, 5 (7), 585.
15. Kawasaki, E. S., The end of the microarray Tower of Babel: will universal standards lead the way? *Journal of biomolecular techniques: JBT* **2006**, 17 (3), 200.
16. Mortazavi, A.; Williams, B. A.; McCue, K.; Schaeffer, L.; Wold, B., Mapping and quantifying mammalian transcriptomes by RNA-Seq. *Nature methods* **2008**, 5 (7), 621.

17. Sudhagar, A.; Kumar, G.; El-Matbouli, M., Transcriptome analysis based on RNA-seq in understanding pathogenic mechanisms of diseases and the immune system of fish: a comprehensive review. *International journal of molecular sciences* **2018**, *19* (1), 245.
18. Ari, S.; Arikan, M., Next-generation sequencing: advantages, disadvantages, and future. In *Plant omics: Trends and applications*, Springer: 2016; pp 109-135.
19. Branton, D.; Deamer, D. W.; Marziali, A.; Bayley, H.; Benner, S. A.; Butler, T.; Di Ventra, M.; Garaj, S.; Hibbs, A.; Huang, X., The potential and challenges of nanopore sequencing. In *Nanoscience and technology: A collection of reviews from Nature Journals*, World Scientific: 2010; pp 261-268.
20. Ayub, M.; Hardwick, S. W.; Luisi, B. F.; Bayley, H., Nanopore-based identification of individual nucleotides for direct RNA sequencing. *Nano letters* **2013**, *13* (12), 6144-6150.
21. Cockcroft, S. L.; Chu, J.; Amorin, M.; Ghadiri, M. R., A single-molecule nanopore device detects DNA polymerase activity with single-nucleotide resolution. *Journal of the American Chemical Society* **2008**, *130* (3), 818-820.
22. Lieberman, K. R.; Cherf, G. M.; Doody, M. J.; Olasagasti, F.; Kolodji, Y.; Akeson, M., Processive replication of single DNA molecules in a nanopore catalyzed by phi29 DNA polymerase. *Journal of the American Chemical Society* **2010**, *132* (50), 17961-17972.
23. Bayley, H., Sequencing single molecules of DNA. *Current opinion in chemical biology* **2006**, *10* (6), 628-637.
24. Astier, Y.; Braha, O.; Bayley, H., Toward single molecule DNA sequencing: direct identification of ribonucleoside and deoxyribonucleoside 5'-monophosphates by using an engineered protein nanopore equipped with a molecular adapter. *Journal of the American Chemical Society* **2006**, *128* (5), 1705-1710.
25. Reiner, J. E.; Balijepalli, A.; Robertson, J. W.; Drown, B. S.; Burden, D. L.; Kasianowicz, J. J., The effects of diffusion on an exonuclease/nanopore-based DNA sequencing engine. *The Journal of chemical physics* **2012**, *137* (21), 214903.
26. Astier, Y.; Braha, O.; Bayley, H., Toward Single Molecule DNA Sequencing: Direct Identification of Ribonucleoside and Deoxyribonucleoside 5'-Monophosphates by Using an Engineered Protein Nanopore Equipped with a Molecular Adapter. *Journal of the American Chemical Society* **2006**, *128* (5), 1705-1710.
27. Uhrová, M.; Deyl, Z.; Suchánek, M., Separation of common nucleotides, mono-, di- and triphosphates, by capillary electrophoresis. *Journal of Chromatography B: Biomedical Sciences and Applications* **1996**, *681* (1), 99-105.
28. Mateos-Vivas, M.; Rodríguez-Gonzalo, E.; Domínguez-Álvarez, J.; García-Gómez, D.; Ramírez-Bernabé, R.; Carabias-Martínez, R., Analysis of free nucleotide monophosphates in human milk and effect of pasteurisation or high-pressure processing on their contents by capillary electrophoresis coupled to mass spectrometry. *Food chemistry* **2015**, *174*, 348-355.
29. Geldart, S. E.; Brown, P. R., Analysis of nucleotides by capillary electrophoresis. *Journal of Chromatography A* **1998**, *828* (1-2), 317-336.
30. Liu, H.; Qi, S.; Zhang, Y.; Huang, A.; Sun, Y., Determination of inosine 5'-monophosphate and guanosine 5'-monophosphate in pig feed by capillary zone electrophoresis. *Journal of High Resolution Chromatography* **1997**, *20* (4), 242-244.
31. Geldart, S. E.; Brown, P. R., Separation of purine and pyrimidine bases by capillary zone electrophoresis with carbonate buffers. *Journal of Chromatography A* **1999**, *831* (1), 123-129.

32. Contreras-Sanz, A.; Scott-Ward, T. S.; Gill, H. S.; Jacoby, J. C.; Birch, R. E.; Malone-Lee, J.; Taylor, K. M. G.; Peppiatt-Wildman, C. M.; Wildman, S. S. P., Simultaneous quantification of 12 different nucleotides and nucleosides released from renal epithelium and in human urine samples using ion-pair reversed-phase HPLC. *Purinergic Signal* **2012**, *8* (4), 741-751.
33. Ranogajec, A.; Beluhan, S.; Šmit, Z., Analysis of nucleosides and monophosphate nucleotides from mushrooms with reversed-phase HPLC. *Journal of separation science* **2010**, *33* (8), 1024-1033.
34. Ren, Y.; Chen, X.; Zhang, J.; Li, D.; Song, X., Simultaneous determination of 5'-monophosphate nucleotides in infant formulas by HPLC-MS. *Journal of chromatographic science* **2011**, *49* (4), 332-337.
35. Pennathur, S.; Santiago, J. G., Electrokinetic Transport in Nanochannels. 1. Theory. *Analytical Chemistry* **2005**, *77* (21), 6772-6781.
36. Pennathur, S.; Santiago, J. G., Electrokinetic Transport in Nanochannels. 2. Experiments. *Analytical Chemistry* **2005**, *77* (21), 6782-6789.
37. Xuan, X.; Li, D., Electrokinetic transport of charged solutes in micro-and nanochannels: The influence of transverse electromigration. *Electrophoresis* **2006**, *27* (24), 5020-5031.
38. Garcia, A. L.; Ista, L. K.; Petsev, D. N.; O'Brien, M. J.; Bisong, P.; Mammoli, A. A.; Brueck, S. R.; López, G. P., Electrokinetic molecular separation in nanoscale fluidic channels. *Lab on a Chip* **2005**, *5* (11), 1271-1276.
39. Baldessari, F.; Santiago, J. G., Electrophoresis in nanochannels: brief review and speculation. *Journal of Nanobiotechnology* **2006**, *4* (1), 12.
40. Wang, L.; Shao, P.; van Kan, J.; Ansari, K.; Bettiol, A.; Pan, X.; Wohland, T.; Watt, F., Fabrication of nanofluidic devices utilizing proton beam writing and thermal bonding techniques. *Nuclear Instruments and Methods in Physics Research Section B: Beam Interactions with Materials and Atoms* **2007**, *260* (1), 450-454.
41. Duan, C.; Wang, W.; Xie, Q., Fabrication of nanofluidic devices. *Biomicrofluidics* **2013**, *7* (2), 026501.
42. Chantiwas, R.; Hupert, M. L.; Pullagurla, S. R.; Balamurugan, S.; Tamarit-López, J.; Park, S.; Datta, P.; Goettert, J.; Cho, Y.-K.; Soper, S. A., Simple replication methods for producing nanoslits in thermoplastics and the transport dynamics of double-stranded DNA through these slits. *Lab on a Chip* **2010**, *10* (23), 3255-3264.
43. Uba, F. I.; Pullagurla, S. R.; Sirasunthorn, N.; Wu, J.; Park, S.; Chantiwas, R.; Cho, Y.-K.; Shin, H.; Soper, S. A., Surface charge, electroosmotic flow and DNA extension in chemically modified thermoplastic nanoslits and nanochannels. *Analyst* **2015**, *140* (1), 113-126.
44. Chantiwas, R.; Park, S.; Soper, S. A.; Kim, B. C.; Takayama, S.; Sunkara, V.; Hwang, H.; Cho, Y.-K., Flexible fabrication and applications of polymer nanochannels and nanoslits. *Chemical Society Reviews* **2011**, *40* (7), 3677-3702.
45. Chai, J.; Lu, F.; Li, B.; Kwok, D. Y., Wettability interpretation of oxygen plasma modified poly (methyl methacrylate). *Langmuir* **2004**, *20* (25), 10919-10927.
46. Oneil, C. E.; Jackson, J. M.; Shim, S.-H.; Soper, S. A., Interrogating Surface Functional Group Heterogeneity of Activated Thermoplastics Using Super-Resolution Fluorescence Microscopy. *Analytical Chemistry* **2016**, *88* (7), 3686-3696.

47. Weerakoon-Ratnayake, K. M.; Uba, F. I.; Oliver-Calixte, N. J.; Soper, S. A., Electrophoretic separation of single particles using nanoscale thermoplastic columns. *Analytical chemistry* **2016**, 88 (7), 3569-3577.
48. O'Neil, C.; Amarasekara, C. A.; Weerakoon-Ratnayake, K. M.; Gross, B.; Jia, Z.; Singh, V.; Park, S.; Soper, S. A., Electrokinetic transport properties of deoxynucleotide monophosphates (dNMPs) through thermoplastic nanochannels. *Anal Chim Acta* **2018**, 1027, 67-75.
49. Cabrini, S.; Kawata, S., *Nanofabrication handbook*. CRC Press: 2012.
50. Gao, H.; Tan, H.; Zhang, W.; Morton, K.; Chou, S. Y., Air cushion press for excellent uniformity, high yield, and fast nanoimprint across a 100 mm field. *Nano Letters* **2006**, 6 (11), 2438-2441.
51. Uba, F. I.; Hu, B.; Weerakoon-Ratnayake, K.; Oliver-Calixte, N.; Soper, S. A., High process yield rates of thermoplastic nanofluidic devices using a hybrid thermal assembly technique. *Lab on a Chip* **2015**, 15 (4), 1038-1049.
52. Ramm, P.; Lu, J. J.-Q.; Taklo, M. M., *Handbook of wafer bonding*. John Wiley & Sons: 2011.
53. Tsao, C.; Hromada, L.; Liu, J.; Kumar, P.; DeVoe, D., Low temperature bonding of PMMA and COC microfluidic substrates using UV/ozone surface treatment. *Lab on a Chip* **2007**, 7 (4), 499-505.
54. Huang, X.; Gordon, M. J.; Zare, R. N., Current-monitoring method for measuring the electroosmotic flow rate in capillary zone electrophoresis. *Analytical Chemistry* **1988**, 60 (17), 1837-1838.
55. Hu, W.; Soper, S. A.; Jackson, J. M., Time-Delayed Integration–Spectral Flow Cytometer (TDI-SFC) for Low-Abundance-Cell Immunophenotyping. *Analytical Chemistry* **2019**, 91 (7), 4656-4664.
56. Schindelin, J.; Arganda-Carreras, I.; Frise, E.; Kaynig, V.; Longair, M.; Pietzsch, T.; Preibisch, S.; Rueden, C.; Saalfeld, S.; Schmid, B.; Tinevez, J.-Y.; White, D. J.; Hartenstein, V.; Eliceiri, K.; Tomancak, P.; Cardona, A., Fiji: an open-source platform for biological-image analysis. *Nature methods* **2012**, 9 (7), 676-682.
57. Ali, U.; Karim, K. J. B. A.; Buang, N. A., A review of the properties and applications of poly (methyl methacrylate)(PMMA). *Polymer Reviews* **2015**, 55 (4), 678-705.
58. Nunes, P. S.; Ohlsson, P. D.; Ordeig, O.; Kutter, J. P., Cyclic olefin polymers: emerging materials for lab-on-a-chip applications. *Microfluidics and nanofluidics* **2010**, 9 (2-3), 145-161.
59. Wei, S.; Vaidya, B.; Patel, A. B.; Soper, S. A.; McCarley, R. L., Photochemically patterned poly (methyl methacrylate) surfaces used in the fabrication of microanalytical devices. *The Journal of Physical Chemistry B* **2005**, 109 (35), 16988-16996.
60. Ozgen, O.; Aksoy, E. A.; Hasirci, V.; Hasirci, N., Surface characterization and radical decay studies of oxygen plasma-treated PMMA films. *Surface and interface analysis* **2013**, 45 (4), 844-853.
61. Bidleman, T. F., The relationship between resolution and percent band overlap. *Journal of Chemical Education* **1979**, 56 (5), 293.
62. Po, H. N.; Senozan, N., The Henderson-Hasselbalch equation: its history and limitations. *Journal of Chemical Education* **2001**, 78 (11), 1499.

Chapter 5. Summary, On-going Developments and Future Work

5.1 Summary

Nucleic acid separations have become an important area of research in forensic and clinical laboratories as many applications in each setting requires the identification of molecular biological reaction products using a separation step through chromatography and/or electrophoresis. The emergence of the concept of precision medicine where diagnosis, treatment, and prevention are tailored to an individual's genetic makeup of his or her disease,¹ has increased the use of nucleic acid biomarkers in clinical settings. Therefore, there is a growing need for higher throughput separations with higher efficiency that result in better resolving power to increase the multiplexing capacity of the assay compared to traditional electrophoretic and chromatographic methods,. Nanofluidic-based separations have garnered a lot of attention to address these demands due to unique nanoscale phenomena, such as electric double layer effects and transverse electromigration which are leading to gel free separations.²⁻⁴ Moreover, low sample and reagent consumption, ultrafast separations, and ease of integration to lab on a chip (LOC) devices to allow for sample pre-processing before the separation are the other advantages of using miniaturized nanofluidic systems.

We successfully fabricated a thermoplastic nanochannel devices which were capable of performing nanoscale electrokinetic separation of rNMPs, dNMPs and ss-DNA. We investigated the ability to use different thermoplastic materials for these separations, while understanding the surface properties such as surface roughness and control of EOF through post assembly surface modification methods. Our results indicated that the ability to separate these analytes in free solution (without any gels or additives) in thermoplastic nanochannels by utilizing unique nanoscale phenomena, specifically the increased surface interactions arisen from increased surface area-to-volume ratio. The advantages of our developed nanoscale separation method are: 1) ability to perform gel free separations, 2) low

reagent and sample consumptions, 3) fast separation, and 4) simple methodology and high throughput device fabrication by NIL. Among these advantages, the ability to perform gel free separation is the most attractive advantage because gel loading and gel replacement limitations in conventional electrophoresis based DNA separations are mitigated. This facilitates the use of these separation methods in clinical settings by enhancing the ability for automation.

We used nanochannels fabricated in thermoplastics having two dimensions (110 nm in depth and 110 nm in width) to separate rNMPs, dNMPs and ss-DNA. We observed that the surface roughness in the nanochannel devices affected the EOF and reduced the separation performance by introducing more band overlap in ssDNA separation. Separation of ssDNAs is driven by electrochromatography and thus a separation resolution was sensitive to the nanochannel material. However, the separation of dNMPs and rNMPs is primarily due to electrophoresis and therefore we did not observe any significant difference in the separation with respect to material used to fabricate the nanochannels. In almost all cases, our nanoscale separation method was able to provide a separation resolution >1.5.

To further refine our developed nanoscale separation method, in the future we want use an electrical detection method instead of fluorescence detection because in our envisioned single molecule sequencing approach, labeling of the mononucleotides either before or after exonuclease digestion would be problematic.⁵ However in these studies we utilized fluorescently labeled nucleotides and ssDNA as fluorescence tagging provided a viable approach to carefully understand the transport properties of these analytes to guide optimization of experimental conditions and nanochannel geometry for optimal separation resolution and identification accuracies.

5.2 Ongoing developments and Future directions

The overall goal of this project is to develop a biosensor that utilizes nanofluidics for the real time, rapid and efficient sequencing of DNA and RNA. DNA/ RNA that are cleaved enzymatically by exonucleases will generate mononucleotides that can be identified via their unique electrokinetic time of flight (ToF) through a 2D nanochannel. These mononucleotides are separated based on their electrokinetic transport properties (electrophoretic and electrochromatographic) through the nanochannel and the ToFs are read electrically by using a pair of in-plane nanopores.

The mixed-scale(micro/nano) single molecule sequencing (SMS) platform is fabricated using thermoplastic via nanoimprinting lithography (NIL) in high production mode. The use of polymer substrates with broad range of surface chemistries enables the optimization of mononucleotide/nanochannel interactions to facilitate ToF identification. The simple workflow, high throughput fabrication process and the low cost per chip make this sensor ideal to meet the clinical demands required for DNA/RNA sequencing.

5.2.1 Introduction

The emergence of high throughput next generation sequencing(NGS) platforms have revolutionized the understanding of complex genomics and transcriptomics by allowing the analysis of DNA and RNA through sequencing, in terms of understanding the genetics of various human diseases and quantitative view gene expression levels.⁶⁻⁸ Although the accomplishments of NGS techniques are impressive, there are several challenges associated with it: such as the complex sample preparation steps involving library preparation, which can be time consuming

(exon targeted sequencing using the Illumina TruSight Tumor panel requires ~28 h for library preparation), the requirement of a high nucleic acid mass input, biases and amplification errors associated with polymerase chain reaction(PCR) amplification step and the limited to short read lengths.⁹

Single molecule nanopore based sequencing has been perceived as a good alternative to address the aforementioned issues associated with NGS. Out of the many advantages of single molecule nanopore sequencing, the most exciting are the simple workflow, the promise of longer reads, and no amplification of DNA/RNA.^{10, 11} In addition, this amplification free SMS that does not require fluorescent labels which significantly reduces the time and cost of the analysis.¹⁰ However, the major challenge associated with SMS sequencing is the difficulty of distinguishing the current signal generated from the translocation of nucleotides because the current signal generated can be due to one nucleotide or due to multiple nucleotides because of the higher thickness of the nanopore compared to a single nucleotide (single base spacing of DNA molecules, ~0.34 nm). By sensing current amplitude only has created a limitation in the decrease of call accuracy.¹²⁻¹⁴(single call accuracy of these nanopore sequencers~92%.)¹⁵ Moreover, a large amount of noise is created in the ionic current measurement due to the large unoccupied volume in nanopores.

One way to mitigate the limitations in readout resolution is the use of a processive exonuclease to clip individual nucleotides from an intact DNA/RNA as long as nucleotides maintain their original order following clipping.¹⁶ Improved single base call accuracy has been shown by directing clipped dNMPs through an α -hemolysin nanopore, but issues arose due to the diffusional misordering of the dNMPs once cleaved from the intact DNA.¹⁷ To address these issues, we are developing a SMS strategy that cleaves DNA/RNA using a processive enzyme to generate

individual mononucleotides. These mononucleotides are then identified based on their molecule-dependent flight times through a nanochannel with two in-plane nanopores that allow for a dual detection modality, in which the signature time of flight (ToF) and current perturbation can both be used to reliably identify each mononucleotide.

5.2.1.1 Description of proposed SMS module

The nanofluidic network comprising the X-ToF SMS chip consists of 3 operational components (see Figure 5. 1): 1) An input/output channel network (~50 nm in depth and width) containing in-plane nanopores (~10 nm effective diameter) to transduce the entrance/exit of a single DNA/RNA molecule into/out of the SMS chip. This network also contains an expansion chamber (trap) to allow the injected DNA to be trapped for storage; it can be electrically ejected from the trap on-demand. 2) A solid-phase bioreactor (single pillar ~500 nm in diameter) with surface-immobilized XRN-1 3) Nano-column (<50^x 50 nm, width^x depth; ≥10 μm in length) equipped with in-plane nanopores (2 per nano-column, <5 nm effective diameter).

RNA molecules are first introduced to X-ToF through the input/output channels containing in-plane pores to sense the loading of single RNA molecules and store it for the sequencing run. Then, the sequence content of the RNA is deduced by the sequential clipping of the input molecules using one of the XRN-1 molecules immobilized on the nanopillar in the presence of Magnesium ions (cofactor). Next, the single rNMP molecules that are generated by enzymatic digestion will be electrokinetically transported through the nanochannel with two in-plane nanopores and the rNMPs are identified based on their ToF. As shown in Figure 1, reservoirs 1-8 are used to input electrophoresis buffer (1,8), sample (4) and waste (2,3,5,6,7). During RNA enrichment, a voltage

is applied across reservoirs (3) and (4). After enrichment, a voltage is applied across the reservoirs (4) and (7) to store the RNA molecule in the trap until sequencing step. Successful loading is determined by the current transient signal generated by the sensing pore. Finally, a voltage is applied across reservoirs (3) and (7) to drive this RNA molecule to the bioreactor for sequencing step,

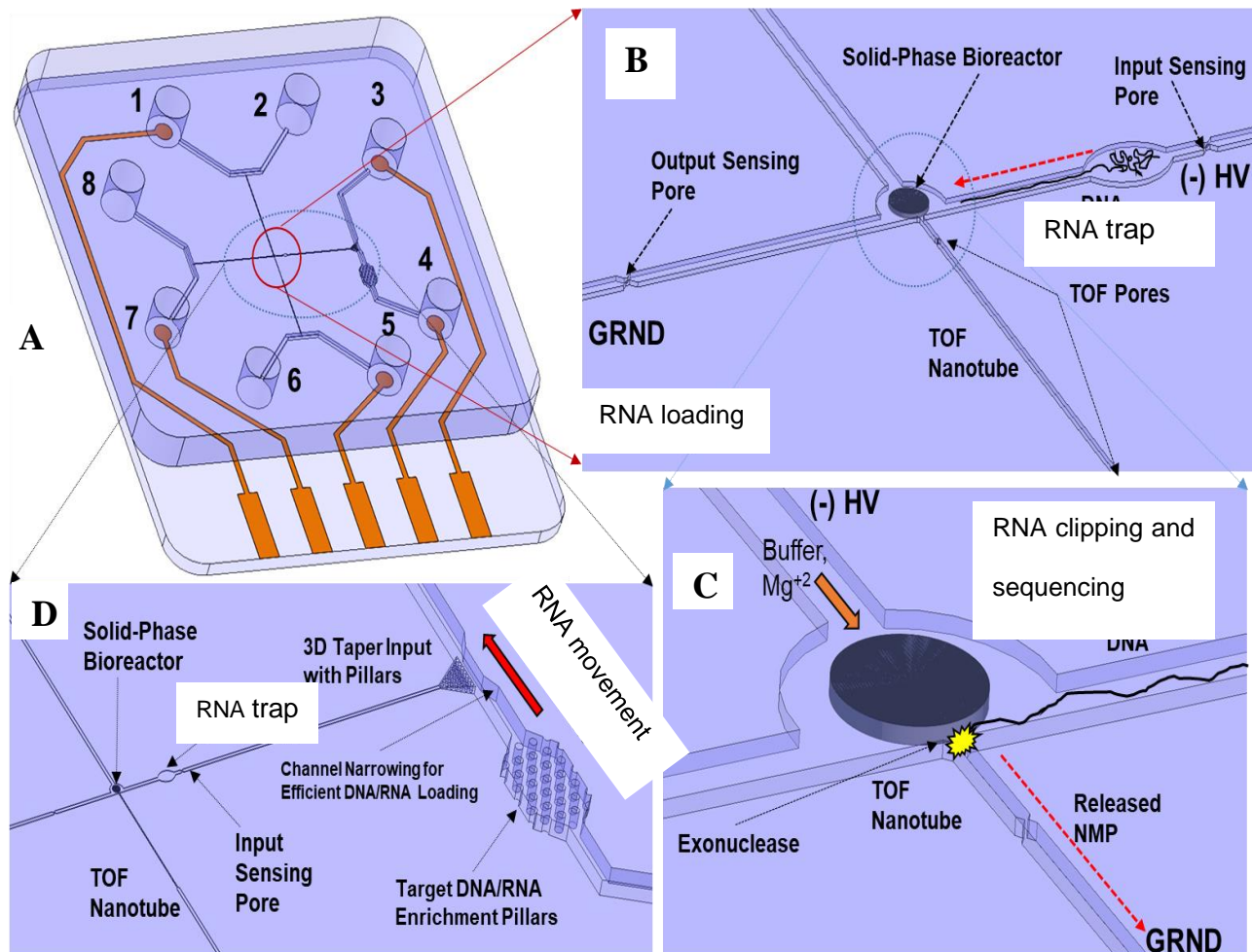


Figure 5.1: A) A schematic diagram of X-ToF. B) An enlarged area of X-ToF with the fluidic network. C) Expanded region of the bioreactor where enzyme digestion of RNA occurs. D) Expanded RNA enriching area of the X-ToF.

5.3 Ongoing developments

Current data presented (chapter 2, and 4) shows the strong potential for the separation of dNMPs and rNMPs within nanochannels due to the unique separation modalities observed in nanoscale. When considering the development of the proposed SMS platform, it is an essential step to understand the enzyme kinetics of the immobilized exonuclease enzymes in to the nanopillar. Exoribonuclease 1 (XRN-1) is a processive enzyme that cleaves RNA and we use this as our model enzyme for RNA sequencing. Therefore, we are analyzing the activity of XRN-1 in solid phase to understand the factors affecting the processivity and clipping rate when tethered on to a pillar in a microfluidic device as the first step. As shown in Figure 2B , we are able to successfully immobilize the XRN-1 enzyme using 3-(3-dimethylaminopropyl) carbodiimide/*N*-hydroxysuccinimide (EDC/NHS) chemistry to a poly(methyl methacrylate) PMMA surface by activating the surface by UV/O₃ to generate carboxylic acid functional groups. We have obtained data for the production of an *in vitro* transcribed RNA (IVT; *FLuc* gene; 1.8 kb) and its digestion using surface immobilized *Xrn1* (Figure 2C). In spite of its secondary structure, *Xrn1* digested this RNA molecule. From this data, *Xrn1* can cleave through secondary structures and thus, can be immobilized directly to the plastic surface without the need for SSB. We have also shown that *Xrn1*, when immobilized, can digest RNA molecules with modified nucleotides (containing a ⁶mA modification; see Figure 2A). In summary, *Xrn1* remained active when immobilized with a cleavage rate of ~60 rNMPs/s

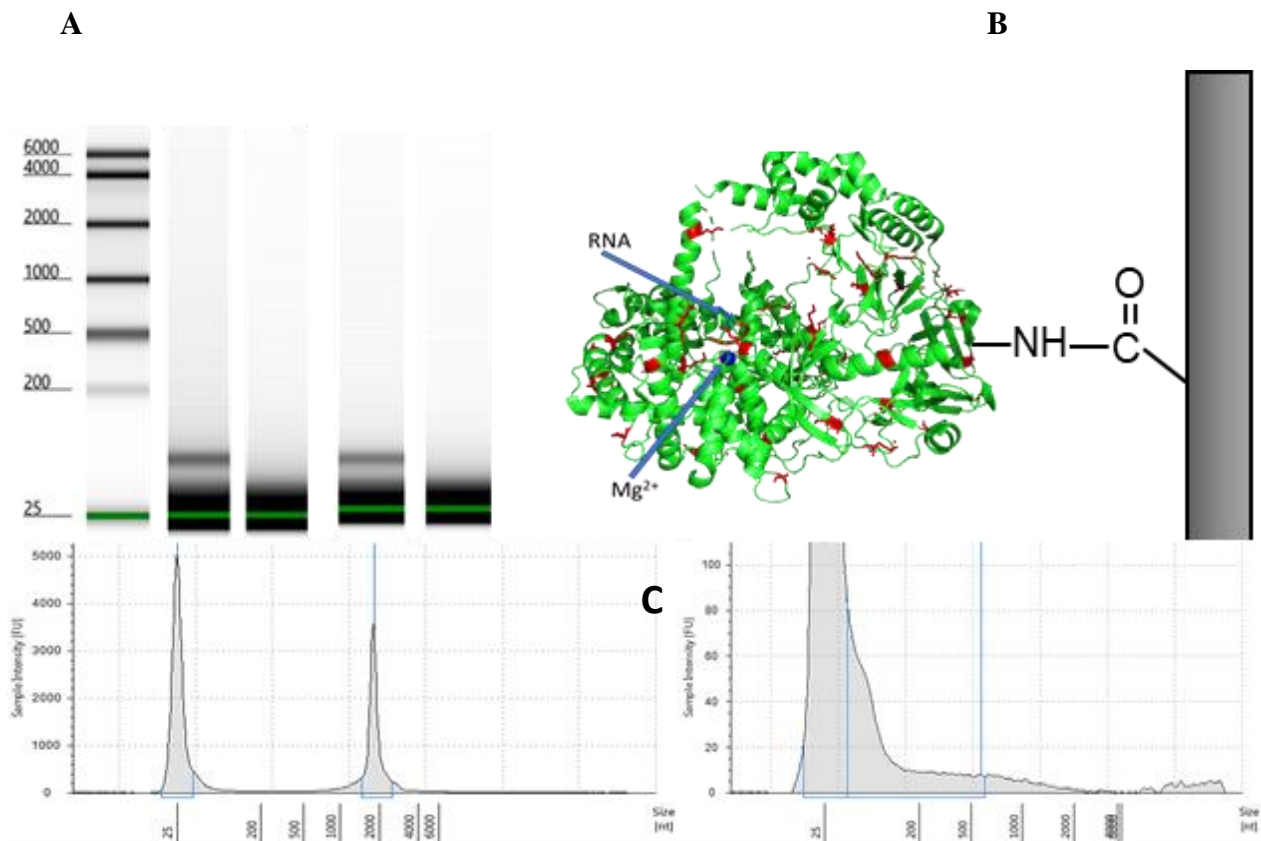


Figure 5.2. **A)** Tapestation traces showing the digestion of 60 mer RNA molecule by XRN-1 tethered to micro fluidic solid phase bioreactor. Lanes: (1) Size markers; 60mer in absence of XRN-1(2) and presence (3) of XRN-1; 60mer containing a ⁶mA residue in absence of (4) and presence (5) of XRN-1. **B)** Immobilization of XRN-1 using direct EDC/NHS coupling to a surface. **C)**Tapestation traces of the FLuc IVT in the absent of (left) and presence of (right) XRN-1.

5.4 Future directions

In previous work, we have demonstrated the ability of the successful function of three components in X-ToF independent (solid-phase bioreactor, nanocolumn with two in-plane nanopores and the input/output fluidic network). Therefore, the future goal is to generate a fully integrated SMS X-ToF device proposed in Figure 1. We will be using RNA template with a known

sequence to investigate the loading efficiency of single RNA into the X-ToF, the efficiency of the XRN-1 digestion in the nanometer domain, and the identification accuracy of rNMPs based of the ToF and current transient amplitudes. The first step of this process will be the fabrication of the integrated X-ToF device. X-ToF device will be fabricated using a method we have reported previously, where a Si master is used to build a resin stamp with micro/nanostructures from which the final devices are replicated to thermoplastics via thermal nanoimprinting lithography. We have started the fabrication of Si master using photolithography to generate microchannels and then focused ion beam milling (FIB) to generate the nanostructures. Figure 5.3 shows the SEM images of the integrated X-ToF device that is fabricated in Si. This **Si** master will then be used to fabricate the X-ToF sensor in COC using NIL . Then, metrology of the device will be done as a quality control step before bonding of the device with a cover plate. Once the fabrication step is complete, immobilization of the XRN-1 enzyme and the necessary activity studies will be done in the integrated X-ToF device.

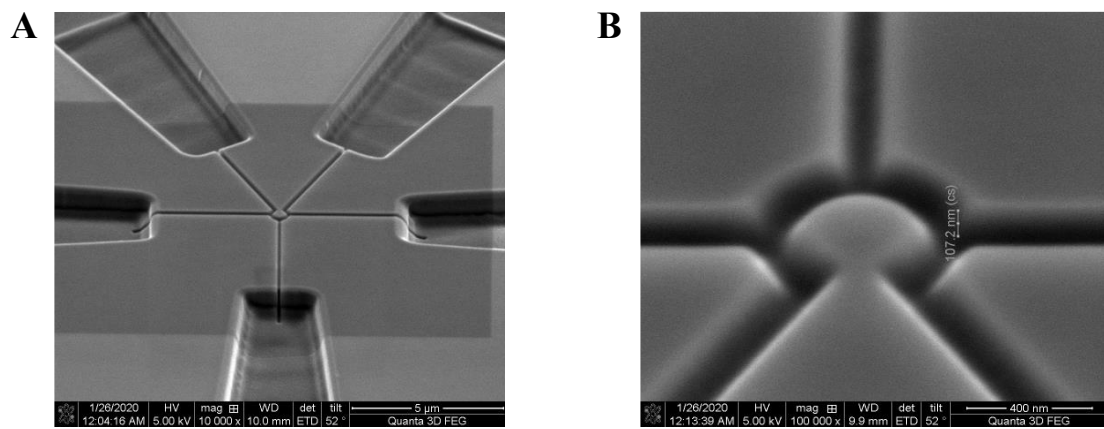


Figure 5.3.A) An SEM image of the footprint of X-ToF fabricated in Si using photolithography and FIB milling. **B)** An enlarged area of the bioreactor in Si master where the XRN-1 will be immobilized in X-ToF sensor.

5.5 References

1. Ginsburg, G. S.; Phillips, K. A., Precision Medicine: From Science To Value. *Health Aff (Millwood)* **2018**, 37 (5), 694-701.
2. Napoli, M.; Eijkel, J. C.; Pennathur, S., Nanofluidic technology for biomolecule applications: a critical review. *Lab on a Chip* **2010**, 10 (8), 957-985.
3. Pennathur, S.; Santiago, J. G., Electrokinetic transport in nanochannels. 2. Experiments. *Analytical Chemistry* **2005**, 77 (21), 6782-6789.
4. Pennathur, S.; Santiago, J. G., Electrokinetic transport in nanochannels. 1. Theory. *Analytical Chemistry* **2005**, 77 (21), 6772-6781.
5. Davis, L. M.; Fairfield, F. R.; Harger, C. A.; Jett, J. H.; Keller, R. A.; Hahn, J. H.; Krakowski, L. A.; Marrone, B. L.; Martin, J. C.; Nutter, H. L.; Ratliff, R. L.; Shera, E. B.; Simpson, D. J.; Soper, S. A., Rapid DNA Sequencing Based Upon Single Molecule Detection. *Genet. Anal.-Biomol. Eng.* **1991**, 8 (1), 1-7.
6. Bonifati, V., Will New Genetic Techniques Like Exome Sequencing and Others Obviate the Need for Clinical Expertise? Yes. *Movement disorders clinical practice* **2017**, 4 (1), 36.
7. Grada, A.; Weinbrecht, K., Next-generation sequencing: methodology and application. *The Journal of investigative dermatology* **2013**, 133 (8), e11.
8. Byron, S. A.; Van Keuren-Jensen, K. R.; Engelthaler, D. M.; Carpten, J. D.; Craig, D. W., Translating RNA sequencing into clinical diagnostics: opportunities and challenges. *Nature Reviews Genetics* **2016**, 17 (5), 257.
9. Ari, S.; Arikan, M., Next-generation sequencing: advantages, disadvantages, and future. In *Plant omics: Trends and applications*, Springer: 2016; pp 109-135.
10. Branton, D.; Deamer, D. W.; Marziali, A.; Bayley, H.; Benner, S. A.; Butler, T.; Di Ventra, M.; Garaj, S.; Hibbs, A.; Huang, X., The potential and challenges of nanopore sequencing. In *Nanoscience and technology: A collection of reviews from Nature Journals*, World Scientific: 2010; pp 261-268.
11. Deamer, D. W.; Branton, D., Characterization of nucleic acids by nanopore analysis. *Accounts of chemical research* **2002**, 35 (10), 817-825.
12. Derrington, I. M.; Butler, T. Z.; Collins, M. D.; Manrao, E.; Pavlenok, M.; Niederweis, M.; Gundlach, J. H., Nanopore DNA sequencing with MspA. *Proceedings of the National Academy of Sciences* **2010**, 107 (37), 16060-16065.
13. Feng, Y.; Zhang, Y.; Ying, C.; Wang, D.; Du, C., Nanopore-based fourth-generation DNA sequencing technology. *Genomics, proteomics & bioinformatics* **2015**, 13 (1), 4-16.
14. Xu, M.; Fujita, D.; Hanagata, N., Perspectives and challenges of emerging single-molecule DNA sequencing technologies. *Small* **2009**, 5 (23), 2638-2649.
15. Xue, P.; Zhao, X.; Qin, M.; Shi, Z.; Zhang, M.; Gu, W., Transcriptome Analysis of Male *Drosophila melanogaster* Exposed to Ethylparaben Using Digital Gene Expression Profiling. *J Insect Sci* **2017**, 17 (4), 87.
16. Clarke, J.; Wu, H.-C.; Jayasinghe, L.; Patel, A.; Reid, S.; Bayley, H., Continuous base identification for single-molecule nanopore DNA sequencing. *Nature nanotechnology* **2009**, 4 (4), 265.
17. Reiner, J. E.; Balijepalli, A.; Robertson, J. W.; Drown, B. S.; Burden, D. L.; Kasianowicz, J. J., The effects of diffusion on an exonuclease/nanopore-based DNA sequencing engine. *The Journal of chemical physics* **2012**, 137 (21), 214903.